UNIVERSITÀ DEGLI STUDI DI UDINE
hic sunt futura

www.uniud.it

Corso di dottorato di ricerca in:

Scienze Biomediche e Biotecnologiche

Ciclo XXXV

Titolo della tesi

"Role of KRAS-Nrf2 axis in regulation of metabolic reprogramming in pancreatic cancer: therapeutic implications".

Dottorando
Himanshi Himanshi

Supervisore
Prof. Luigi E. Xodo

Co-supervisore
Dr. Eros Di Giorgio

2023

Contents

ABSTRACT

The activity of the KRAS oncogene is crucial for the growth of pancreatic cancer. The KRAS oncogene is essential for the development of about 30 % of human tumours, and its targeting is a focus of cancer therapy. The various attempts over the last three decades to develop inhibitors for the protein KRAS or for downstream signalling pathways have not been successful in the clinic, although its importance in cancer has been proven. For this reason, the KRAS oncogene has long been considered as being undruggable. The promoter and the 5'-UTR region of KRAS contain two sequence motifs with high guanine content that enable them to fold into G-quadruplex (G4) structures. The promoter contains two G4 motifs, of which the motif called 32R is well characterised and serves as a hub for the recruitment of transcription factors important for transcription. The 5'-UTR of the mRNA also folds into a complicated tertiary structure in which three non-overlapping G4 motifs near the 5'-cap fold into G4 RNA structures. The 32R-G4 motif of the KRAS promoter forms a G-quadruplex stabilised by three G-tetrads, in equilibrium between two structures called G9T and G25T. We found that both G4s bind to hnRNP A1: a transcription factor essential for transcription of KRAS. 1D NMR analysis suggests that hnRNP A1 binds to the end tetrads of the G4s and unfolds the G25T structure completely and the G9T structure partially. To study the impact of hnRNP A1 on KRAS transcription, we developed a Panc-1 knockout in which hnRNPA1 was deleted by the CRISPR/Cas9 technology. Using Western blot, we discovered that the expression of KRAS was in the knockout cells significantly lower than in the wild-type Panc-1 cells. This proves that hnRNPA1 is crucial for KRAS transcription. In addition, the hnRNP A1 knockout cells have a significantly lower potential for colony formation compared to normal Panc-1 cells. Moreover, by pull-down and western blot experiments, we found that the G4 conformer G25T is a better platform for the formation of the transcription pre-initiation complex with PARP1, Ku70, MAZ and hnRNPA1. I have worked on this project in the first part of my PhD, in collaboration with other researchers, and with an NMR group from University of Bordeaux (France). The results of this work have been published in ACS Omega. 2021 Nov 30;6(49):34092-34106.

Since pancreatic cancer cells are addicted to the KRAS oncogene, the second project I worked on during my PhD aimed to develop a strategy to suppress KRAS with small molecules: cationic porphyrins carrying an alkyl side chain with 14 (2b) or 18 (2d) carbons. The alkyl

porphyrins can be administered either in free form (2d, 2b) or embedded in liposomes of palmitoyl-2-oleoyl-sn-glycero-3-phosphocholine (L-2d, L-2b). Cell cytometry showed that free porphyrins are internalised by pancreatic cancer cells by active (endocytosis) and passive (membrane fusion) transports, whereas L-2d is taken up only by endocytosis. We also found that L-2d partially colocalises with lysosomes and the ER, while free 2d colocalises with lysosomes and the cell membrane. Free 2d accumulates in the cytoplasm and binds with high affinity to G4 RNAs, including those formed in the 5'-UTR of KRAS. Upon exposure to light, the porphyrins produce singlet oxygen and ROS, which degrade the 5'-UTR and thus arrest translation. This strong suppression of KRAS expression is observed at nanomolar concentrations of the porphyrins. Suppression of KRAS by free porphyrins causes inhibition of Nrf2, the master regulator of redox homeostasis, and GPX4, a protein that protects membrane phospholipids from peroxidation. Thus, when KRAS is suppressed, the KRAS-NRF2-GPX4 axis is also repressed, and this leads to the production of lipid ROS, which activate cell death by ferroptosis. In contrast, upon photoactivation, L-2d produces only ROS, which activates cell death mainly by apoptosis. L-2d has little effect on the KRAS-NRF2-GPX4 axis. Overall, our work shows for the first time that cationic alkylporphyrins are potent anticancer drugs for pancreatic cancer cells that activate cell death by ferroptosis and apoptosis, with the predominant type varying depending on the delivery method. The results of this study were published in J Photochem Photobiol B. 2022 Jun;231:112449.

In the last and main part of my PhD, I investigated how the KRAS-Nrf2 axis controls cellular functions including redox homeostasis and metabolic reprogramming in pancreatic cancer cells. To address these issues, we used CRISPR-Cas9 to obtain a knockout of Panc-1 cells in which the two alleles of Nrf2 were deleted by frameshift mutations (Nrf2(-/-) cells). We found that disruption of Nrf2, and thus of the KRAS-Nrf2 axis, leads to an increase in ROS, a decrease in reduced glutathione G-SH and reduced protein thiols, as well as an extensive metabolic reprogramming. RNA-seq analysis, validated by quantitative RT-PCR experiments, showed that key genes encoding enzymes of arginine and medium-chain fatty acid metabolism are upregulated, while genes encoding enzymes of glycolysis, pentose phosphate pathway and glutathione cycle are downregulated, in Nrf2(-/-) cells. This means that under normal conditions pancreatic cancer cells generate ATP and biomass for proliferation through "aerobic glycolysis", i.e. mainly under anaerobic conditions. When the KRAS-Nrf2 axis is

suppressed, as occurs in Nrf2(-/-) cells, the cells lose their ability to utilise glucose but maintain their malignancy by switching to aerobic metabolism and using mainly amino acids, especially arginine, and short-chain fatty acids as nutrients. We found that under conditions of KRAS-Nrf2 deficiency, arginine is diverted into the synthesis of phosphocreatine, forming an energy buffer that enables pancreatic cancer cells to meet the increasing energy demand for proliferation. In addition, arginine is also used for the synthesis of polyamines, compounds that promote cancer progression, and nitric oxide, a molecule that activates mitogenic signalling. The key role that arginine plays in pancreatic cancer cells that have lost the KRAS - Nrf2 pathway is evidenced by the fact that cyclocreatine, which inhibits the phosphocreatine pathway, significantly reduces their capacity of Nrf2(-/-) cells to form spheroid and to produce ATP. Combination treatments that simultaneously target the KRAS-Nrf2 axis and the creatine pathway outperform monotherapies in their ability to fight cancer. Our research reveals the complexity of the metabolism controlled by the KRAS-Nrf2 axis and lays the foundation for the development of new therapy for PDAC. The results of this study are under review in Cell Chemical Biology. Available at https://papers.ssrn.com/sol3/papers.cfm?abstract_id=4318051

In summary, we have investigated the role of oncogenic KRAS in pancreatic cancer cells. Expression of the oncogene is regulated by G4 structures located in the promoter upstream of TSS, which act as a hub for transcription factors, including hnRNP A1 which has the capacity to unfold G4. In addition to the promoter, the 5'-UTR of KRAS mRNA is also rich in guanine and forms G4 RNA structures. These are recognized by cationic porphyrins: photosensitizers that promote RNA degradation and block translation when irradiated with light. Finally, we have investigated the role of the KRAS-Nrf2 axis in reprogramming the metabolism of pancreatic cancer cells. We found that suppression of KRAS, an approach taken by many scientists, switches the cells to aerobic metabolism, thereby maintaining malignancy. This discovery suggests that besides KRAS, pancreatic cancer progression is arrested if also the creatine and polyamine pathways are inhibited by using combination therapies.

Graphical representation

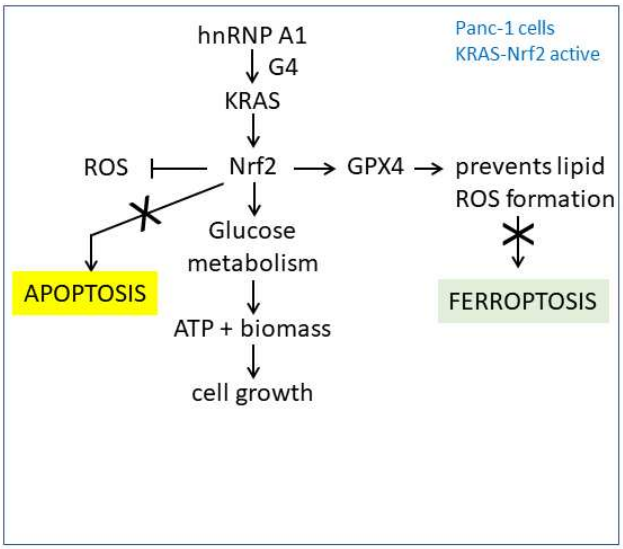

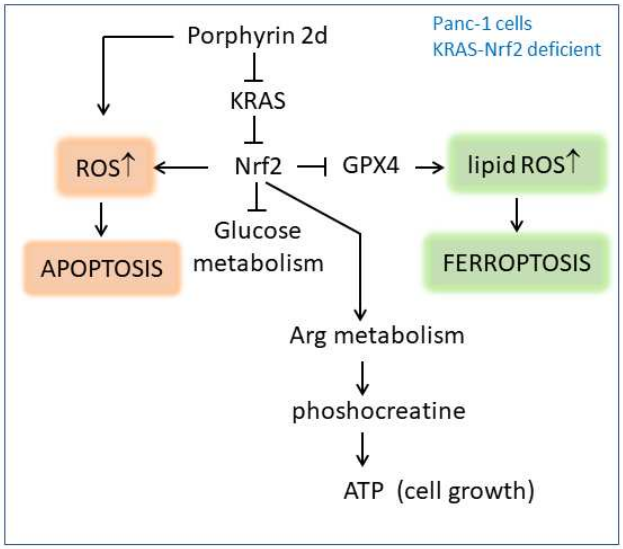

INTRODUCTION

1.The Pancreas

The pancreas is formed in the endodermal germ layer during the developmental process. The ventral and dorsal pancreas arise from the foregut of the embryonic intestine in this germ layer. They grow as two distinct buds and, over time, are repositioned and fuse to form a mature pancreas. The pancreatic progenitor cells develop into endocrine, acinar or ductal cells under the influence of various developmental factors. [1]

The pancreas is an accessory digestive organ located in the upper abdomen between the spleen on the left and the duodenum on the right. Its main function is to regulate glucose homeostasis and digestion.

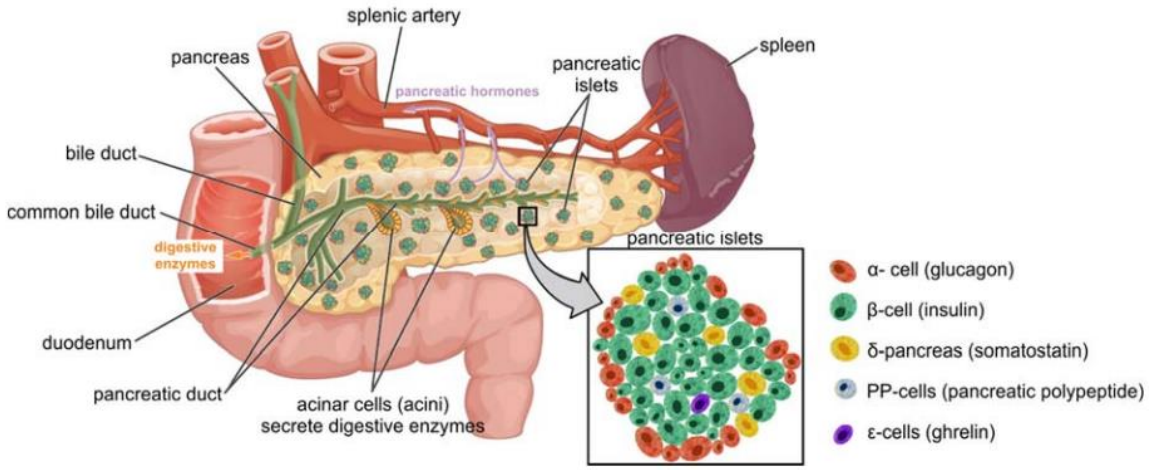

Figure1. An overview of the location and anatomy of the pancreatic. They are located on the C-loop of the duodenum and extend till the spleen. The exocrine and endocrine components of the pancreas each have distinct roles to play. Endocrine islet cluster cells produce certain hormones into the circulation, whereas exocrine acinar cells secrete digestive enzymes into the small intestine via the pancreatic duct system. [2]

The pancreas can be divided into a head, neck, body, and tail (Figure 1). The head of the pancreas is in the C-loop of the duodenum and is surrounded by the renal vein and inferior vena cava. As shown in the figure, the common bile duct passes from the head into the duodenum and releases digestive enzymes. The neck is a short region and the point where the body and head meet. The anterior and posterior surfaces of the body have functionally different roles, as the latter has no peritoneum and is in contact with the aorta, left kidney

and renal vessels. The tail of the pancreas lies anterior to the left kidney, where it is closely associated with the splenic hilum and the left colic flexure.

The pancreas is a composite organ that has both endocrine and exocrine functions. The exocrine secretion of pancreatic juice, which contains bicarbonates and digestive enzymes, is released from the acinar cells, and enters the duodenum via the common bile duct. The endocrine secretions, on the other hand, are in the islets of Langerhans. These islets of Langerhans consist of different cell types, namely alpha, beta, delta, epsilon, and upsilon, and secrete hormones such as glucagon, insulin, somatostatin, ghrelin, and pancreatic polypeptide, which are then released into the blood. Therefore, the functions of the pancreas are to control blood sugar and assist in the digestive process.

Because of its intensive supply of enzymes and hormone regulation, the pancreas is susceptible to diseases that can affect throughout its life. The most important of these are diabetes (type 1, 2), hypoglycaemia, hyperkalaemia, pancreatitis, and eventually pancreatic cancer (PC). [2]

2. Pancreatic cancer

Pancreatic cancer can be classified as neuroendocrine or exocrine cancer. Neuroendocrine PC arise from cystic neoplasms such as intraductal papillary mucinous neoplasms (IPMN), while exocrine PC arise from precursor lesions known as pancreatic intraepithelial neoplasia (PanIN) that gradually acquire genetic alterations leading to pancreatic adenocarcinoma (PDAC) [3]. PDAC is the most common form, accounting for more than 90% of all cases of PC. Due to its frequent occurrence, PDAC is usually referred to as PC. It is predicted that PDAC will surpass breast cancer in mortality in Europe by 2025 [4]. In the United States, it is estimated to be the second leading cause of death in the next twenty to thirty years [4]. With a mortality rate of 95% and a 5-year survival rate after surgery of 7%, PC is described as an aggressive and rapidly metastatic cancer [5]. The main reason for these high-risk values is its poor prognosis due to late diagnosis, as early stages are often asymptomatic. Due to its aggressiveness, it is tolerant to various conventional treatments such as radiotherapy, chemotherapy, and molecular targeted therapy. Finally, PC exhibits numerous genetic and epigenetic alterations as well as a dense and complex tumour microenvironment [4].

2.1 Pancreatic ductal adenocarcinoma (PDAC)

2.1.1 Epidemiology

The number of patients with pancreatic ductal adenocarcinoma (PDAC) continues to increase worldwide. Mortality in patients with gastric, colorectal, and liver cancer has decreased due to advances in treatment, but there is no evidence that mortality has decreased in patients with PDAC. There is no specific method to improve the prognosis of patients with PDAC. Reducing the number of deaths from PDAC is an urgent global public health concern. According to a 2020 study by GLOBOCAN, there are 495,773 new cases of PDAC, which ranks 14th on the list of most common cancers. However, 466,003 people die from PDAC each year, making it the seventh leading cause of cancer death [5]. The 1-year overall survival rate (OS) for PDAC patients is very poor (24%) and its 5-year rate OS is even lower (9%) [5]. The incidence of PDAC varies by country, with the highest age-adjusted incidence in Europe and North America and the lowest in Africa and Central Asia [5]. The incidence of PDAC is slightly higher in men (5.7 per 100,000, 262,865 cases) than in women (4.1 per 100,000, 232,908 cases). Mortality rates associated with PDAC also vary by country. Europe has the highest PDAC mortality rate (7.2 per 100,000), followed by North America (6.5 per 100,000). East Africa has the lowest PDAC mortality rate (1.2 per 100,000 population). At least 90% of deaths from PDAC were reported in patients aged 55 years and older, suggesting that the disease becomes more common with age. [6] In Italy, 137,579 men and 137,208 women aged 35 years and older died from pancreatic cancer [standardised mortality ratios (SMRates): 26.43 and 23.78 per 100,000, respectively] [7] An increasing trend was observed in both men and women, but in women, rapid progression was mainly observed in the younger age group (up to 64 years). Although a geographical gradient in mortality was observed from northern to southern municipalities, there were significant differences among men, who lived mainly in southern and central Italy, and among women, as the number of municipalities scattered throughout the peninsula was increased. [7]

2.1.2 Risk factors

Risk factors for pancreatic cancer can be divided into modified and unmodified. Modified risk factors are primarily based on lifestyle and living conditions, while unmodified risk factors are genetic. Modified risk factors include smoking, alcohol consumption, obesity, and dietary

factors. A smoker has been shown to have twice the risk of developing PC even after quitting for 20 years. Alcohol in combination with smoking accelerates the onset of PC. Obesity is not only associated with PC, but also with premature mortality, and finally, eating red meat and processed foods increases the likelihood of PC, while eating fresh fruit and folic acid has been shown to be beneficial. Finally, occupational risks such as nickel workers are more prone to PC. Unchanged risk factors included African American ethnicity, gender, and age. 10% of PDAC are hereditary cases where the mutated gene is passed down in the family. These genes include ATM, APC, BRCA2, STK11, PALB2, CDKN2A, FANCC, FANCG and the Lynch syndrome genes. Although rare (1% of PDAC patients), therapeutically important inherited germline variants in the mismatch repair-deficient genes MLH1, MSH2, MSH6 and PMS2 also occur in PDAC as part of Lynch syndrome. In 2019, the National Comprehensive Cancer Network guidelines recommended that all newly diagnosed patients with PDAC undergo germline testing with a gene panel that includes the BRCA1/2, ATM, MLH1, MSH2, MSH6 and PMS2 genes. Helicobacter pylori infection and chronic diseases such as hepatitis A and B also increase the incidence of PDAC. Recent studies have shown that people with a blood group other than O are also susceptible to PDAC [8-16].

2.1.3 Progression of PDAC

PDAC is preceded by hyperplastic lesions known as pancreatic intraepithelial neoplasia (PanIN) and intraductal papillary mucinous neoplasia (IPMN). They are pre-malignant lesions and tend to develop into cancer (Figure 2). IPMNs look like papillae (finger-like structures) that protrude into the pancreatic duct. [17] Mucinous tumours are the second most common histological subtype of pancreatic cancer and account for less than 10% of cases. These tumours are usually much less invasive than adenocarcinomas at diagnosis and have a 0.88-fold lower risk of death. Mucinous tumours also arise from the ductal epithelium of the pancreas, but they secrete mucins that are found in and around the cells, giving them the appearance of 'floating' cells. There are many other subtypes of pancreatic cancer. B. arises from acinar cells, which are undifferentiated and resemble liver cancer. [18,19]

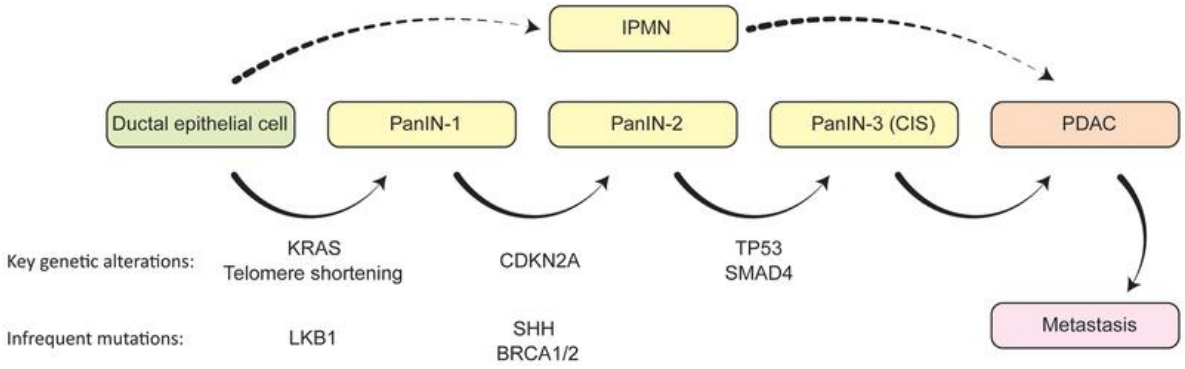

Figure 2. Model for Disease Progression in Pancreatic Cancer. Two histological subtypes of precursor lesions, PanINs and IPMNs, give rise to pancreatic cancer. As the pathogenesis progresses, molecular alterations take place that result in increasing levels of nuclear and cytoskeletal abnormalities. at relation to the stages at which they most frequently arise, genetic changes frequently seen in these lesions are represented in the figure. PDAC originates from ductal epithelial cells and progresses gradually, with *KRAS*, *CDKN2A*, *TP53* and *SMAD4* being the main genetic alterations. [19]

2.1.3 Subtyping of PDAC

Recently, several molecular subtypes and subtype-specific therapeutic responses have been recognised in pancreatic cancer. Two major transcriptome-based subtypes that have been validated in several studies are the classical/pancreatic progenitor and basal subtype [20], which are distinguished based on prognosis and response to therapy. The basal PDAC subtype is characterised by the expression of squamous and quasi-mesenchymal markers, whereas the classical subtypes are identified more with epithelial markers. Basal subtypes are poorly differentiated and inherently more aggressive, while classical subtypes have a more favourable prognosis. Classical subtypes have higher expression of SMAD4 and GATA6, while basal subtypes have a similar molecular profile to colorectal and breast cancers. [21] Another way of classifying PDAC based on genomic profile and RNA expression profile is to divide it into squamous cell carcinoma, immunogenic pancreatic, pancreatic precursor and aberrantly differentiated pancreatic endocrine exocrine carcinoma (ADEX). [22] These subtypes are based solely on gene expression profile. Pancreatic cancer is inherently desmoplastic, which makes it less neoplastic when sampled. Therefore, an in-depth study is still needed to classify the molecular subtypes. [23]

2.1.4 Molecular mechanism of PDAC

2.1.4.1 Proto oncogenes

KRAS

Although there is conflicting information in the literature about the actual prevalence of activating *KRAS* mutations in PDAC, studies of resected tumours suggest that this mutation is present in almost all cases. [24,25,26] In fact, the *KRAS* mutations are located on chromosome 12. The gene KRAS encodes a member of the Ras family of GTP-binding proteins involved in cell proliferation and differentiation as well as survival signalling. [26,27] Point mutations, which occur primarily at codon 12 of the gene KRAS, impair the intrinsic GTPase activity of the protein, thereby keeping it in its active (GTP-bound) form. [24,25,27] The consequences of downstream constitutively active KRAS signalling will be discussed later.

2.1.4.2 Tumor suppressor genes

***p16* (*CDKN2*, *p16INK4a*, *MTS1*)**

The tumour suppressor gene *p16* is inactivated in approximately 95% of pancreatic cancers. [29,26,30] This gene is located on chromosome 9 and inhibits cyclin-dependent kinase inhibition to induce entry into the S phase of the cell cycle. *p16* encodes a protein that inhibits CDK 4/6-dependent phosphorylation of retinoblastoma protein (RB). Inactivation of *p16* results in unregulated cell proliferation due to inappropriate progression through the cell cycle. [31,24,27,32] Mechanisms for *p16* inactivation include homozygous deletion, gene intramutations and loss of heterozygosity (LOH), and promoter hypermethylation.

p53

The tumour suppressor gene *p53* is inactivated in 50-75% of PDAC. [26,29,31] This gene is located on chromosome 17 and regulates the expression of many key genes involved in cell cycle progression. It encodes a regulatory transcription factor. Apoptosis and DNA repair. Among the important functions of p53 products is the inhibition of cell cycle progression in the face of DNA damage. Inactivation of *p53* leads to loss of cell cycle checkpoint function. [27,32] The mechanism of *p53* inactivation is an intragenic mutation resulting in a defective product that cannot bind to DNA.

Gene Deleted in Pancreatic Carcinoma, Locus 4 (*DPC4/SMAD4*)

In 55% of pancreatic tumours, the gene DPC4 - Deleted in Pancreatic Cancer - is inactive. [33] The gene is located on chromosome 18 and encodes a protein that is crucial for the signalling pathway of the growth inhibitory effect of transforming growth factor beta (TGF). [26] Cell cycle progression can be dysregulated by inactivation of *DPC4*. There are several intragenic mutations and homozygous deletions that can inactivate *DPC4* [32].

2.1.4.3 Growth factors and their receptors

PDACs overexpress many growth factors and their receptors compared to normal pancreatic tissue. Growth, invasion, and angiogenesis are just some of the phenotypic features of PDACs that are thought to be influenced by downstream signals mediated by interactions between growth factor ligands and receptors. The following cases are particularly noteworthy.

Epidermal Growth Factor

Membrane receptor tyrosine kinases, known as epidermal growth factor receptors (EGFR), mediate signals for cell survival and proliferation. [27] Overexpression of EGFR and/or one or more of its ligands appears to be a sign of poor prognosis in patients with PDAC, as EGFR is overexpressed in PDAC. [27] Antibodies targeting EGFR (such as cetuximab) and tyrosine kinase inhibitors (such as erlotinib) are currently being investigated for the treatment of PDAC. [34]

Transforming Growth Factor-β

TGF family proteins are involved in a variety of processes, particularly the control of cell growth. Pancreatic cancer cells may be able to bypass the growth inhibitory effects of TGF- when DPC4/SMAD4 is inactivated. [35] Promoted invasion and angiogenesis are two hypothetical promalignant consequences of TGF- signalling. [36]

Vascular Endothelial Growth Factor

Vascular endothelial growth factor (VEGF) promotes endothelial cell proliferation and survival, which in turn promotes angiogenesis. Both pancreatic cancer tissue and cancer cells overexpress VEGF. [27] Bevacizumab, a monoclonal antibody that targets the VEGF receptor, is now being tested in clinical trials in people with pancreatic cancer. [34,37]

2.1.4.4 Signalling pathways

WNT pathway

In many tissues, the WNT signalling system includes both a non-canonical and a canonical pathway that regulates somatic stem cell maintenance. Canonical (-catenin-dependent) and non-canonical (-catenin-independent) signalling pathways have each been linked to tumour development, pancreatic cancer spread and resistance to therapy. [38,39] WNT signalling is necessary for the development of PanIN lesions and pancreatic cancer caused by KRAS. [40] By controlling the WNT/catenin signalling pathway or by enhancing the link between -catenin and the cyclic AMP response element-binding protein, activation of KRAS may promote pancreatic cancer cell invasion and migration. [41] Pancreatic cancer exhibits a more stem cell-like phenotype when WNT/catenin signalling is more activated. [42] The canonical pathway can be activated to stop the degradation of -catenin and promote its nuclear translocation, which enhances the transcription of certain genes such as cyclin D1 and c-Myc. [43,44] Pancreatic cancer and other cancers typically have abnormal accumulation of -catenin in the nucleus, which has been linked to the onset of these diseases. In pancreatic cancer tissue, canonical WNT ligands such as WNT family member 2, WNT family member 5A and WNT family member 7A have been found to be increased. These canonical WNT ligands activate the WNT pathway that promotes the spread of pancreatic cancer. [45,46] In addition, non-canonical ligands that activate the WNT pathway, such as R-spondin and mucin (MUC) family members (MUC1 and MCU4), contribute to the progression of pancreatic cancer. [47,48,49] The hypoxic conditions in which pancreatic cancer suffers are distinctive. HIF-2 (hypoxia-inducible factor-2) regulates WNT signalling by keeping SMAD4 and -catenin levels constant during pancreatic cancer development. [47,48,49]

The NFκB Signaling

The NF-B signalling pathway is crucial for the control of many different physiological processes in cellular signalling, including cell proliferation, differentiation, apoptosis, inflammation, and stress response. The fact that most human pancreatic cancer tissues and cell lines have constitutively active NF-B, whereas normal pancreatic tissues and cells do not, suggests that NF-B activation plays a role in pancreatic cancer development. [50] According to Liptay et al.

(2003), inhibition of NF-B by a super inhibitor of NF-B results in decreased proliferation and induction of apoptosis, indicating a significant function of NF-B in the development of pancreatic tumours [51] Moreover, liver metastasis of the pancreatic cancer cell line ASPC1 is completely suppressed when constitutive NF-B activity is inhibited. [50] uPA, one of the crucial proteases involved in tumour invasion and metastasis, is overexpressed in pancreatic cancer cells and triggered by constitutive NF-B activity, according to an experimental study. 52] These results suggest a close link between constitutively active NF-B and the invasion and metastasis typically observed in pancreatic malignancies. Furthermore, as mentioned above, Notch signalling may also be responsible for the dysregulation of NF-B. Accordingly, crosstalk between Notch and NF-B appears to be an important signalling event controlling tumour invasion and angiogenesis in pancreatic cancer. [53]

KRAS Pathway

Discussed in the next section.

2.1.5 Therapeutics advances

The only possible cure for pancreatic patients is surgical resection of the pancreas. However, only 20% of cases with anatomically resectable disease can be treated with this approach, of which up to 50% have a positive surgical margin. [54] Therefore, the 5-year survival rate for these patients drops to 7%. Neoadjuvant therapy may be beneficial for patients with locally advanced or borderline pancreatic cancer and may improve overall survival. [54]

FOLFIRINOX (5-fluorouracil, leucovorin, irinotecan and oxaliplatin), mFOLFIRINOX, gemcitabine or gemcitabine plus nab-paclitaxel are the recommended drugs for the treatment of pancreatic cancer. [55,56] Immunotherapy with pembrolizumab is a recently approved therapy after failure of first-line treatment. [57] A combination of 5 FU and liposomal irinotecan is the only approved second-line treatment. Several novel therapeutics for patients with pancreatic cancer are in the clinical trial phase. These dual therapeutics target DNA repair, tumour metabolism, the tumour microenvironment, and immune checkpoints. [57,58,59]

As we already know more than 90% of pancreatic cancer patients have *KRAS* mutation, several therapeutic advances have considered *KRAS* targeted therapy. Fortunately, there have been some compounds developed that are in phase one clinical trial. These compounds are targeting $KRAS^{G12C}$ mutation which consists of a small amount of KRAS mutation until now only one strategy targeting $KRAS^{G12D}$ mutation has entered phase one clinical trials this strategy uses exosomes or small extracellular vesicles loaded with siRNA targeting KRAS. [60,61]

Therefore, targeting low prevalence aberrations such as NTRK1/2/3, BRCA1/2, MMR deficiencies has attracted much attention. Two receptor tyrosine kinase inhibitors, Larotrectinib and Entrectinib, received FDA approval in November 2018 and August 2019, respectively. Strategies based on BRCA- poly (ADP - ribosome) polymerase (PARP) synthetic lethality have shown success in patients with BRCA mutations. The inhibitor Olaparib is in phase 2 clinical trials and has achieved of an order of 21.7% in PDAC patients. [61,62] In summary, targeting single pathways or molecules is unlikely to benefit the treatment of PDAC, as the complexity of PDAC makes it inevitable to rely on combination therapies.

3. *KRAS*

KRAS is a member of the RAS superfamily, also known as RAS -like GTPases, a subgroup of small GTP-binding proteins. According to research, mammalian genomes contain more than 150 RAS -like genes [63]. Even though each member of the RAS superfamily possesses a catalytic G domain, they differ in their evolutionary specialisation on specific cellular processes [64]. The most commonly studied proteins belong to the RAS subfamily (RAS, RHO, RAB, ARF, RAC and RAN), including Harvey-Ras (H- RAS), Neuroblastoma-Ras (N- RAS) and two variants of Kristen- RAS (K- RAS)-one, known as KRAS4A, which is weakly expressed in human cells, and the dominant form, known as KRAS4B, which is much more highly expressed. [65]

3.1 *KRAS* gene

The human genome has two copies of the KRAS gene, *KRAS1* and *KRAS2*. Only six codons separate the 5.5 kb long mRNA transcribed from the main *KRAS2* from the transcripts of the transforming Kristen mouse virus gene [66]. With an intervening sequence, 900 base pairs of the *KRAS1* gene are homologous to the corresponding sequence of the Kristen Murine Sarcoma Virus2 homologue, and 300 base pairs of the *KRAS2* gene are fully homologous to the viral counterpart, as revealed by analysis of human placental and embryonic cDNA libraries. Through alternative mRNA splicing, the KRAS1 gene is a pseudogene that arose from the *KRAS2* gene. [67]

Sequencing revealed six exons in the *KRAS2* gene. Two, three and four of these are invariant coding exons. Alternative splicing of exon 4 results in mRNA types 4A and 4B. Alternative splicing can omit exon 5, resulting in the KRASA and KRASB isoforms. The 6th exon (the 3' untranslated region, 3'UTR) in KRASA encodes the C-terminal portion of KRASB but is not translated. KRASB, the most common splice form of KRAS2, is abbreviated as KRAS [68].

KRAS expression is controlled by microRNAs that alter the stability of the *KRAS* mRNA during transcription elongation and by proteins that bind to the KRAS promoter during transcription initiation. A polypurine-polypyrimidine element that is nuclease hypersensitive is present in the KRAS gene promoters of humans and mice (NHPPE). Using an intramolecular parallel G-quadruplex consisting of three G-tetrads and three loops, the G-rich strand of NHPPE located in the proximal promoter sequence can recognise and bind nuclear proteins involved in transcriptional repression of the expression of KRAS. [69]

It was found that sequestering nuclear proteins that bind to NHPP by an oligonucleotide that mimics the G-quadruplex in KRAS resulted in a 40% reduction in KRAS transcription compared to controls. MicroRNAs and a link between the *KRAS* promoter region and the 65 kDa ESXR1 protein both play a role in regulating *KRAS* transcription (miRNAs). A human protein called ESXR1 has a cytoplasmic proline-rich repeat region I at its C-terminus and an N-terminal homeodomain in the nucleus. The mRNA expression of the *KRAS* gene is inhibited by binding of the N-terminal segment of ESXR1 to the TAATGTTATTA consensus motif in exon 1. [65]

With 188 amino acid residues and a molecular weight of 21.6 kD, the *KRAS* gene product, the KRAS protein, has a function in intracellular signal transduction. KRAS is a quiescent protein until it binds to GTP. Signals within the cell control the transition from an inactive to an active state. KRAS undergoes conformational changes affecting two domains of the protein after GTP binds to it, activating the protein. [69]

There are four domains in KRAS. The N-terminus of the first domain, which comprises 85 amino acids, is identical in all three variants of RAS (KRAS, NRAS and HRAS). The second domain of the RAS protein has 80 amino acids and has less sequence identity (70-80%) than the other two. Together, these domains form the G-domain, which is crucial for the signalling function of the KRAS protein (amino acids 1-165, Figure 3). The P-loop phosphate binding loops (amino acids 10-16 and 56-59) interact with the b-phosphate and c-phosphate of GTP in the GTP-binding pocket in the G-domain of the KRAS protein. The guanine base interacts with residues 116-119 and 152-165. [65]

The interactions between the putative downstream effectors and the GAPs depend on the region between amino acids 32 and 40, termed the "core effector region" In addition, the third domain (amino acids 165-188/189) of the RAS protein has a hypervariable region (HVR) that directs post-translational modification and controls anchoring in the plasma membrane. This region is crucial for controlling the biological activity of the RAS protein. When regulators and effectors are bound, switch regions I and II are crucial. Temporary GTP binding to the RAS protein is facilitated by the phosphate-binding pocket P loop. In addition, the GTPase activity that negatively controls the RAS protein through the RAS-GTP hydrolysis process and guanosine diphosphate binding is located here. [65]

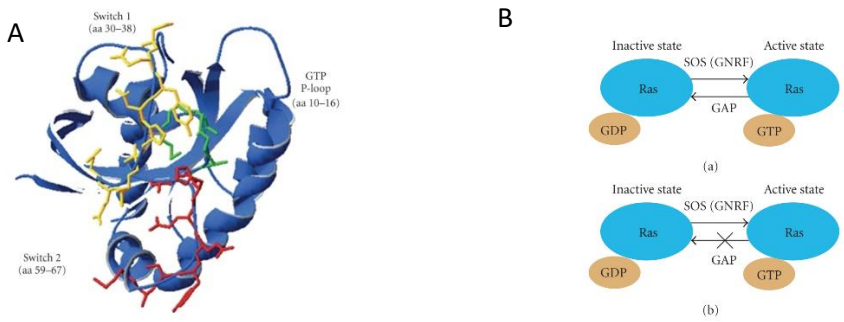

Figure 3. Structure and role of the protein KRAS. A) 3D structure of the protein KRAS, showing the location for switch 1, switch 2 and the GTP-P loop. Switch 1 (amino acids 30-38) and Switch 2(amino acids 59-67), two crucial sections, together constitute an effector loop that regulates the selectivity of the GTPase's binding to its effector molecules. The P-loop-phosphate binding loops (amino acids 10–16 and 56–59) interact with the b-phosphate and c-phosphate of GTP in the GTP-binding pocket found in the KRAS protein's G-domain. B) KRAS uses protein dynamics as a molecular on/off switch. When KRAS is activated, it binds to GTP. Additionally, it has an inherent enzyme activity that cleaves the nucleotide's terminal phosphate and converts it to GDP. KRAS is turned off when GTP is converted to GDP. The rate of conversion is typically modest, but an auxiliary GTPase-activating protein (GAP) protein, such RasGAP, can substantially speed it up. To force the release of the bound nucleotide (GDP), KRAS can attach to proteins of the SOS class of Guanine Nucleotide Exchange Factor (GEF) (such as GNRF). The GEF is subsequently liberated from ras-GTP when KRAS binds GTP that is present in the cytoplasm. [65]

3.1 KRAS signalling in Pancreas.

The oncogenic KRAS pathway in PDAC is very complex and is thought to involve three main pathways: Raf/MEK/ERK, PI3K/Pdk1/Akt and the Ral GTPase pathway (Figure 4, [70]).

1. The A, B and C Raf kinases are at the top of the Raf- MEK-ERK pathway, which makes up most of the mitogen-activated protein kinase (MAPK) system. The Raf kinases are attracted to the membrane after KRAS is turned on and they become phosphorylated. The serine-threonine kinases ERK1 and ERK2 are activated after MEK1 and MEK2 are phosphorylated by the active RAF. Interestingly, even though both PDAC and non-small cell lung cancer have the KRASG12D mutation, C-Raf is only required for tumour formation in the latter, whereas it has no effect in pancreatic cancer [71, 72]. Expression of the B-RafV600E oncogene in the pancreas of mice leads to rapid development of multifocal PanIN lesions. (Figure 4, dotted red). [73].

2. Another RAS effector pathway in pancreatic cancer that has been extensively studied is the PI3K/PTEN/AKT pathway. Phosphoinositides, negatively charged components of membrane

lipids important for intracellular signalling, are formed when the PI 3'- OH kinase phosphorylates hydroxyl groups at positions 3', 4' or 5' of the inositol rings of phosphatidyl inositol (PI) (PI3K). PI3Ks consist of different catalytic subunits from one of three classes (I, II and III). After GTP-KRAS stimulation in PDAC, class I PI3Ks become active. An active PI3K induces the synthesis of PIP3 from PIP2, which serves as a platform for the recruitment of AKT and phosphoinositide-dependent kinase 1 (PDK1). Phosphorylation is then used to activate AKT [70]. The MTOR and RAC pathways are part of the downstream phospho-AKT signalling. On the other hand, PTEN uses 3' dephosphorylation to hydrolyse PIP3 to PIP2 [74]. The class I oncogenic PI3KAH1047R drives ADM, PanIN formation and adenocarcinoma in a PDAC mouse model even in the absence of oncogenic RAS. In addition, these tumours showed activated AKT and GSK3B at levels indistinguishable from oncogenic KRAS -driven tumours. This is because the mutations in the PI3K/PTEN/AKT pathway are so strong. (Figure 4, dotted green). [70].

3. A third class of Ras effector molecules is represented by the ral GTPases. Similar to other small GTPases, Ral relies on RalGEFs to exchange GDP for GTP and on RalGAPs to hydrolyse GTP into GDP. In cells, Ral switches between the GDP-bound inactive state and the GTP-bound active state. The two proteins involved in this branch are RalA and RalB [75]. The importance of this pathway in pancreatic cancer was clarified by Lim, Counter, and colleagues: RalA was found to be essential for tumour initiation, while RalB was more involved in tumour spread in a group of pancreatic cancer cell lines and patient-derived tumours. Interestingly, the RalA-RalB pathway appeared to be more active in pancreatic cancer tissue compared to other Ras effector pathways. (Figure 4, dotted in blue). [76,77].

Numerous RAS -driven tumours have been shown to be highly dependent on the sustained expression of oncogenic KRAS [78]. Recent research demonstrates that KRAS alters cancer cell metabolism to generate the biomass required for rapid proliferation [79,80]. The notion of "oncogene addiction", whereby cancer cells often become dependent on a particular oncogene while also being dependent on several genetic abnormalities, was inspired by the dependence of metabolism on certain oncogenes. [81, 82]. According to recent research, the oncogene KRAS increases both the uptake and consumption of glucose, glutamine, and fatty acids to support biosynthesis and maintain cellular redox balance [83]. To generate ribose for nucleotide synthesis and reducing power (NADPH), KRASG12D directs some of the glycolytic

flux into the hexosamine/glycosylation pathways and the pentose phosphate pathways (PPP) [79]. In addition, glutamine and serine are particularly consumed by KRAS mutant pancreatic cancer cells. Gln is oxidatively deaminated in mitochondria to glutamate, which is subsequently transaminated by GOT2 with oxaloacetate to aspartate, while KRASG12D inhibits the enzyme glutamate dehydrogenase GLUD1, which introduces glutamate into the Krebs cycle by converting glutamate to alpha-ketoglutarate. The aspartate transaminase GOT1 transports aspartate into the cytoplasm, where it is converted by the NADP+-dependent malic enzyme into oxaloacetate and then into malate and pyruvate. The abnormal metabolic cycle caused by KRASG12D increases the NADPH level and thus the redox potential of the cell [80]. Besides glutamine, serine is also heavily used by PDAC cells. This is not unexpected, considering that serine is the amino acid that provides a one-carbon group to the folic acid pool, the vitamin required for the formation of purine and pyrimidine nucleotides. [84].

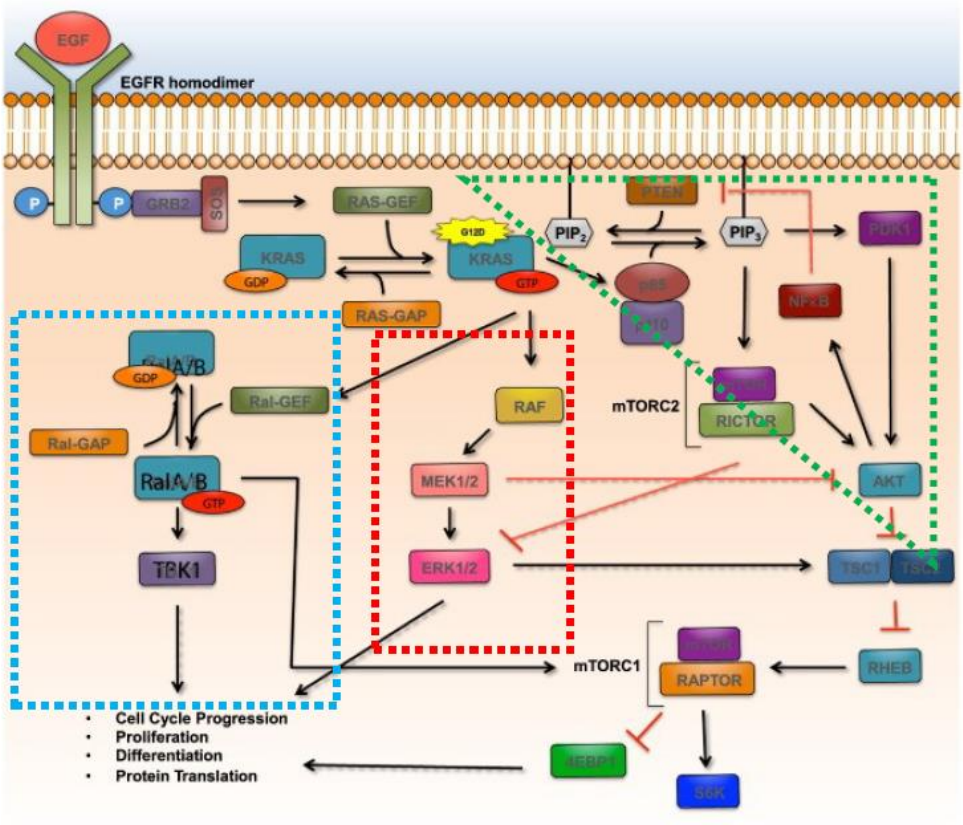

Figure4. Overview of KRAS signalling cascade in pancreatic cancer. RalA/B, RAF/MEK/ERK, and PI3K are the three signaling arms that are activated because of the small GTPase RAS being active. These three arms include several direct contacts between proteins, which are shown by solid black arrows. Solid red bars represent inhibitory

interactions, while dotted red lines represent established regulatory feedback loops. The activated RAS protein in pancreatic cancer is known as KRAS, and it can be activated by amino acid alterations brought on by acquired oncogenic point mutations, such as the missense mutation G12D shown here, which prevent GAPs (GTPase Activating Proteins) from hydrolyzing GTP (guanosine triphosphate) to GDP (guanosine diphosphate) and deactivating RAS. As an alternative, upstream activation involving receptor-linked tyrosine kinases like EGFR (Epidermal Growth Factor Receptor) can induce RAS. When extracellular growth factors like EGF (epidermal growth factor) bind to these receptors, they homodimerize and start a phosphorylation cascade that activates the adaptor protein GRB2 (growth factor receptor-bound) and the GEF SOS, which removes GDP from RAS and activates the molecule by allowing the binding of GTP. KRAS-GTP then attracts RAF serine/threonine kinases to the cellular membrane, where they are activated. The main RAF molecule involved in pancreatic cancer is BRAF, and once it is activated, it triggers a cascade of phosphorylation reactions that involve MEK (mitogen-activated protein kinase kinase) and ERK (extracellular signal-related kinases). TSC1 and TSC2, two genes that encode proteins that collectively function as a complex negative regulator of RHEB, are stimulated by ERK. KRASGTP stimulates PI3K signaling by activating the p110 subunit of PI3K (consisting of p85 and p110). Phosphatidylinositol 4,5-bisphosphate (PIP2) is converted to Phosphatidylinositol 4,5-triphosphate (PIP3) by active PI3K. PIP3 then induces PDK1 activation at the plasma membrane or mTORC2 complex activation, which promotes the activation of AKT (also known as protein kinase B). AKT suppresses PTEN, a negative regulator of AKT, while simultaneously activating NF-kB, which blocks the TSC1/TSC2 inhibitory co Last but not least, KRAS-GTP stimulates Ral-GEF, which in turn stimulates the Ral A/B small GTPases by allowing GTP to attach to it. One known downstream target of Ral A/B, which relieves NF-kB inhibition brought on by TANK, is TBK1 (TANK-binding kinase 1). Cell cycle progression, proliferation, differentiation, and protein translation are all impacted by all three signaling axes complex of mTORC1. [70]

3.2. KRAS targeted therapy in PDAC

As we already know, more than 90% of PDAC have a KRAS mutation and numerous efforts have been made to address KRAS either directly or indirectly. Despite the scientific input, targeted therapies have not provided sufficient benefits. Due to the high affinity of GTP and the lack of a deep hydrophobic pocket in the KRAS protein, the development of an effective therapy has been unsuccessful. [54]

Indirect methods have focused on inhibiting the activation of KRAS or downstream pathways. Farnesyl transferase (FTase) catalyses the post-translation modification of prenylation in KRAS. It is required for membrane localisation and signal transduction of the protein. The FTase inhibitors (FTIs) lonafarnib and tipifarnib were developed to target KRAS farnesylation and inhibit its membrane localisation. [85] Unfortunately, they were not successful in phase

III clinical trials. Alternatively, prenylation by Gernylgernayl transferase 1 (GGTase 1) and FTase have been validated for dual inhibitory action. Again, there is a limited therapeutic window as GGTase 1 has a broad spectrum of targets. [86, 87]

The RAF-MEK-ERK-MAPK pathway is the best characterised pathway downstream of the KRAS pathway. Several inhibitors targeting this pathway have been introduced clinically in PDAC. Vemurafenib and dabrafenib showed potential results in BRAF, but paradoxically led to progression and then suppression of cell signalling in the KRAS mutant PDAC. However, pan-RAF inhibitors targeting both monomers and diameters may be able to overcome upregulation of signalling pathways. [88]

Inhibitors targeting the PI3K-mTOR pathway have also been unsuccessful in targeting PDC. A possible explanation for this is the alternative activation of the MAPK-PI3K pathway, so targeting these two pathways is emerging as a potential therapeutic strategy. [54]

Protein-protein interactions are an important feature of KRAS signalling. Therefore, these indirect methods attempt to prevent KRAS from interacting with other protein molecules. Guanine nucleotide exchange factors are the most important proteins for ATP-ADP conversion in KRAS activation. SOS1 is one of the most important interacting proteins. Inhibitors targeting SOS1 have been developed to block the interactions between SOS1 and KRAS. These are pan- KRAS inhibitors that are already being tested in the first clinical phase. [89,90,91]

New advances in the development of drugs that directly target the KRAS mutant have accelerated in recent years. Small molecule inhibitors targeting a draggable switch to pocket in $KRAS^{G12C}$ have been developed. A new series of compounds have been discovered that can irreversibly bind to the switch one and switch to pockets of the KRAS in an inactive GDP-bound state and prevent binding to the raft. These molecules bind covalently to the one maintained in $KRAS^{G12C}$. Subsequently, several drugs have been developed based on this hypothesis. Sotorasib and adagrasib have reached phase III clinical trials. [92, 54]

Based on the principle of these direct $KRAS^{G12C}$ inhibitors, PROTAC (PROteolysis Targeting Chimaera) technology has been developed and is in preclinical testing. These molecules consist of two linked compounds, one targeting the protein of interest and the second being

an E3 ubiquitination ligase. LC-2 has been shown to be successful in degrading KRASG12C in PDAC cells. [93]

Direct targeting at KRAS has shown success with $KRAS^{G12C}$, but $KRAS^{G12D}$ is the most-known mutation form. Several research groups are working to target GTP-bound $KRAS^{G12D}$. A cyclic peptide KD-2 has been shown to bind successfully in the switch-to-groove of $KRAS^{G12D}$, but transport of these pounds within the cell is a problem that has been further improved by the cyclic compound KS- 58 Hash in terms of efficiency against $KRAS^{G12D}$ both in vitro and in vivo. Another class of molecules known as stem complex inhibitors, targeting the GTP-bound KRAS, bind in a novel pocket in the KRAS protein along with cyclophilin A- a chaperone protein. [54, 94]

3.3 Targeting either the promoter or the 5'-UTR/3'-UTR regions of KRAS gene.

In recent years, our group has offered several alternative methods to affect the expression of KRAS in PDAC. It has been shown that miR216b is abnormally downregulated in pancreatic tumours, providing a solid basis for the development of a miR-based approach to suppress the expression of *KRAS* and thus the survivability of PDAC [95]. Gene expression of *KRAS* is particularly suppressed in PDAC cells by double-stranded miR-26b mimics with unlocked nucleic acid (UNA) changes in the leading strand. In addition, single-stranded miRNAs mutated with UNA were found to be highly active. When Panc-1 and Mia PaCa2 cells were treated with engineered lipid-modified miR-216 administered with palmityl oleyl phosphatidylcholine liposomes, the technique was further confirmed. Clonogenic assays showed that these siRNAs significantly reduced cell proliferation. [95].

It was discovered that the 5'-UTR of *KRAS* adopted the G-quadruplex, a non-canonical nucleic acid structure. Stabilisation of this structure is essential to stop translation of KRAS [96, 97]. In our laboratory, small anthrafurandione (ATFD) and anthrathiophenedione (ATPD) molecules have been shown to significantly induce apoptosis in Panc-1 cells, as well as reduce their metabolic activity and colony formation [98]. The porphyrin TMpyP4 was recently used to test the effect of another typical G4 ligand on PDAC cells both in vitro and in vivo. Our team increased the lipophilicity of the compound by adding a C14 or C18 alkyl chain, which increased its permeability to cells [99]. When the mRNA is exposed to light, these alkylated porphyrins effectively attach to and break the 5'-UTR G4 structures of the KRAS and NRAS

transcripts. This resulted in a significant decrease in the metabolic activity of Panc-1, and C14 porphyrin also inhibits the growth of Panc-1 xenograft cells and induces apoptosis. [99].

In the late 1980s, Perucho and Jordano discovered that the promoter of the human KRAS gene contains a G-rich nuclease-hypersensitive element (NHE) that is required for transcription and is located upstream of the transcription start site (TSS) [100, 101]. The ability of NHEs to adopt a stable G4 structure under physiological conditions and to use this as a platform for the recruitment of various nuclear proteins was first demonstrated by our team in 2006 [102]. The production of oligonucleotides mimicking KRAS quadruplexes (G4 decoys) should capture these proteins and prevent transcription considering these findings. Our laboratory's experiments showed that the G4 decoys prevented pancreatic cancer cells from expressing KRAS, growing and forming colonies. [103].

4.G-quadruplex

Stacking nucleic acid structures known as G4 structures can develop inside repeating G-rich DNA or RNA sequences. Guanylic acid's ability to gel at large concentrations was discovered for the first time by Bang in 1910, raising the possibility that G-rich DNA sequences might create higher-order structures. [104, 105]

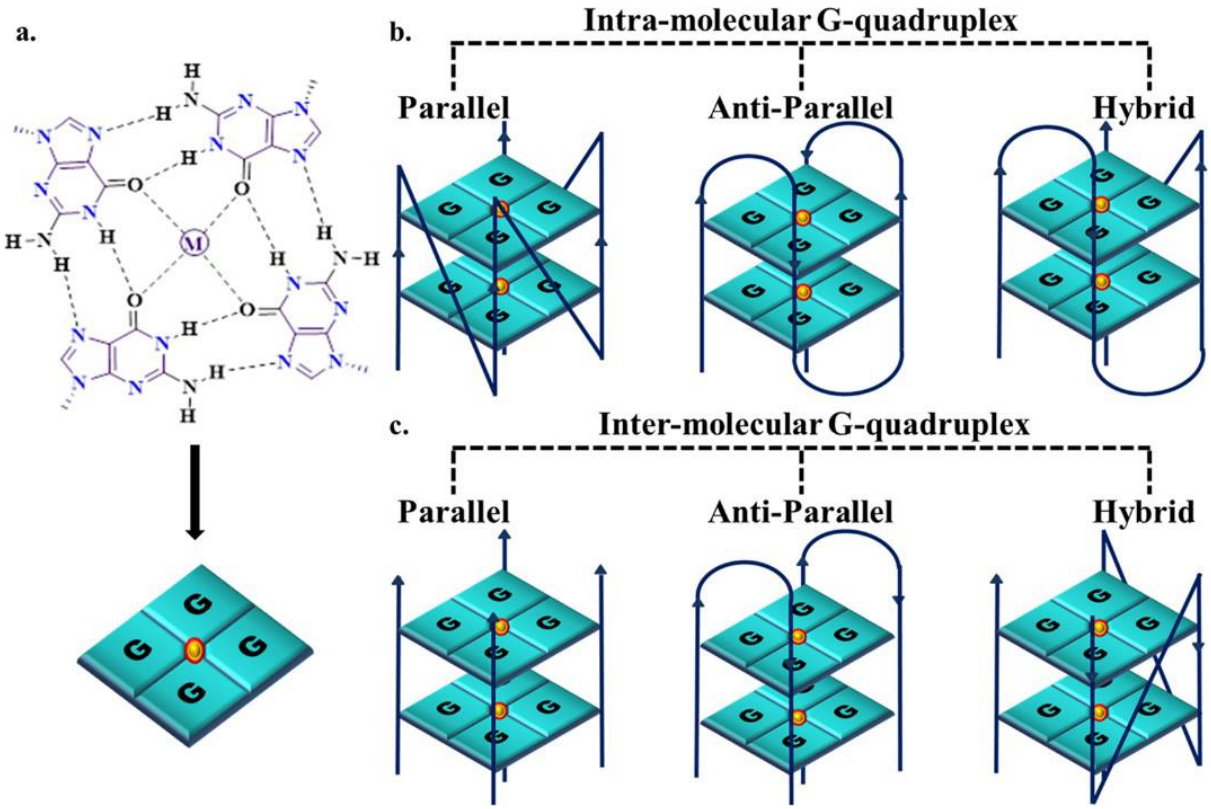

Figure 5. Structure of G-quadruplex; a) A G-tetrade seen from above, in which 4 guanines are held together by Hoogsteen bonds and coordinated by a monovalent cation (M) in the middle; b;c) Various topologies adopted by G-quadruplex [106]

Fifty years later, Gellert and colleagues used X-ray diffraction to demonstrate that guanylic acids can form tetrameric structures. These tetramers consist of four guanine molecules arranged in a G-quartet. This is a square, planar configuration in which each guanine is hydrogen bonded to the two neighbouring guanines. The G4 structure consists of stacked G-quartets, and the gaps between them are extruded as single-stranded loops (although tetramolecular G4 structures can also be without loops) (Figure 5). The size and arrangement of the loop regions is variable. However, loops are usually short (1-7 nucleotides (nt)), and shorter loops and longer G-tracts produce more stable G4 structures3. Monovalent cations located in the core cavities between the stacks support this structure by reducing the

electrostatic repulsion of the inwardly directed guanine oxygen atoms. Based on the orientation of the DNA strands, G4 structures can be divided into several groups and adopt a range of topologies. G4 structures can thus be parallel, anti-parallel or a combination of both. Furthermore, they can arise from a combination of strands (intermolecular) or within a single strand (intramolecular), and other loop topologies are also conceivable. The length and sequence structure of the entire G4 motif, the size of the loops between guanines, the stoichiometry and orientation of the strands, and the nature of the binding cations are just some of the variables that influence the topology and stability of the G4 structure. [106, 107, 108]

4.1. G4 in the Genome

Due to the growing interest in G4s and their function in biology, numerous bioinformatics methods have been developed to find potential G4 sequences in genomes. Sequences that could form a G4 include the following: G_m- X_n-G_m-X_o-G_m- X_p-G_m.

Where "m" refers to the number of G bases in each G run typically involved in tetrad construction; Xn, Xo, and Xp can be any mixture of residues involved in the loops, including G. [104] For example, the human genome has about 300,000 sequences with the ability to form G quadruplexes, corresponding to a G_3 - X_{1-7} - G_3 - X_{1-7} -G_3 consensus sequence input. G4s are not randomly distributed; they are found primarily on telomeres, ribosomal DNA, the untranslated region (UTR) of mRNA, micro- and minisatellite repeats, the boundaries between introns and exons, and the switch regions of the immunoglobulin heavy chain. Plants, bacteria, human DNA and RNA viruses have also been shown to contain putative G4 sequences (pG4s) [109]. In addition, topoisomerase I in yeast S. cerevisiae has been shown to play a critical role in preventing a variety of genomic rearrangements associated with the formation of G4 during transcription. [110]

Cellular transcription and translation were found to be affected by G4. During gene regulation, G4 remained mainly in promoters and near transcription start sites. The development of a G4-specific antibody (BG4) represents a significant advance, as it led to reports of the existence of G4 in cells and its dependence on the cell cycle. In addition, HeLa cells tested with BG4 provided evidence that G4 is present in telomeric regions as well as elsewhere on chromosomes. [111] Using G4-forming conditions and Illumina next-generation

sequencing, nearly 700,000 G4 structures were discovered, particularly in several oncogenes such as *BRCA1*, *BRCA2*, *MAP3K8*, *MYC*, *TERT*, *AKT1*, *FGFR3*, *BCL2L1, CUL7*, *FOXA1*, *TUSC2* and *HOXB13*. [112] Based on the previous strategy, Balasubramanian and colleagues performed this technique using a G4-specific ChIP-Seq and a BG4-specific antibody as probes. The number of G4 structures (10,000 G4 ChIP-seq peaks) is much lower than the calculations or G4-seq observations suggested. Interestingly, the immortalised HaCaT cell line showed G4 enrichment in cancer genes such as MYC, PTEN and KRAS compared to healthy NHEKs cells, suggesting a link between G4 occurrence and transcriptionally active chromatin status. Overall, there are two likely explanations for this: either heterochromatin has a suppressive effect in the development of G-quadruplexes, or G4 ChIP-seq has a higher sensitivity than BG4 immunostaining. [113]

In-vitro analyses have shown that numerous biological functions require G-quadruplexes. The 3 primary overhangs of telomeres form intramolecular g-forces to inhibit the activity of nucleases. They also found intermolecular G4 structures in the organisation of ciliate traffickers by providing a docking site for various G4-binding proteins and nuclear scaffolds. Finally, the length of the telomere bar influences binding to ligands and inhibition of telomerase activity. The putative function of G4 has also been investigated in DNA replication. An intramolecular G4 complex is formed in replicating DNA a few base pairs upstream of the replisome complex, while the replication fork has already been initiated. G-quadruplexes also play a role in epigenetic regulation, meiosis, and recombination. One of the most important roles of G4 is in the transcription process. They are found in high concentration near the promoter region, 1000 nucleotides upstream of the transcription start site in 50% of human genes. They have a dynamic role in the transcription start site as they can not only inhibit transcription by stalling the polymerase, but also facilitate transcription, stimulate transcription, and block transcription by recruiting repressor proteins. [105]

For the purposes of this paper, I will focus on the role of the G-quadruplex in the *KRAS* promoter site.

4.2. G4 structure in the *KRAS* promoter

Three G4 motifs, known as 91 32R (or G4-near), G4-mid and G4-far, are in the promoter of the proto-oncogene *KRAS* between 270 and 116 (3' to 5', non-coding strand) from the transcription start site (TSS). [103] Since this region serves as a platform for transcription factor recruitment, most of the studies published in the literature have focused on 32R. Primer extension studies in our lab originally showed that DNA polymerase I stopped at the 3' end of 32R inserted into a plasmid. [102] Our lab performed DMS foot printing experiments to gain insights into the G4 quadruplex. Typically, the bases in the nucleus are numbered from one to 32, starting with the adenine at the 5' end. Interestingly, it was found that the G_{18}-G_{19}-G_{20} triad of the G run IV was not involved in the formation of the G4 scaffold. Furthermore, G_6 and G_7 were fully protected, while G_9 was only partially protected. This shows that the "defective" trio is a component of the G4 scaffold, even if G_6-G_7-T_8-G_9 is broken by a thymine. The overall cleavage pattern is consistent with the development of a G4 structure supported by three G quartets of four G runs (I, II, III and V), one of which is interrupted by a thymine. In addition, 32R showed high ellipticity at 260 nm in a potassium-containing buffer, indicating a parallel G4 structure according to circular dichroism [Based on the Hoogsteen hydrogen bonds between the guanines, we concluded that 32R should form a parallel G-quadruplex with three stacked G-quartets. The G4 resulting from the central coordination of two K+ ions at the O6 of the guanine is characterised by two 1-n and one 11-n loops and a strand with a thymine bead (1/1/11 topology). [114, 115]

Furthermore, our group's research has shown that the 32R molecule folds into two G4 structures with different topologies (designated G25T and G9T) that coexist in an inertial equilibrium. The folding topology of the two 32R G4 conformers shows that the structures, including the prediction that G9 should be somewhat reactive towards DMS, are fully confirmed by the footprinting profile for DMS. The unusual structure of G9T (TM 14 61.2 C) is indeed defined by a refolded guanine in syn-conformation (G32) and a triad (G29, A30 and G31) terminating the 30-end (topology 1/3/11). According to the data from CD and DMS footprinting, the conformer G25T instead has a fold like that proposed for 32R. It is a parallel G4 with a large 11/12-nt loop and a thymine bulge in one strand. G9 is a member of the G quartet in this G4 structure and should not respond to DMS. However, G9 in the 3-nt loop of the G9T structure is reactive to DMS. G9 appears to be somewhat protected, as predicted,

because the DMS footprint of the sequence G-32R shows the folding of the two G4 structures in equilibrium with each other. [116]

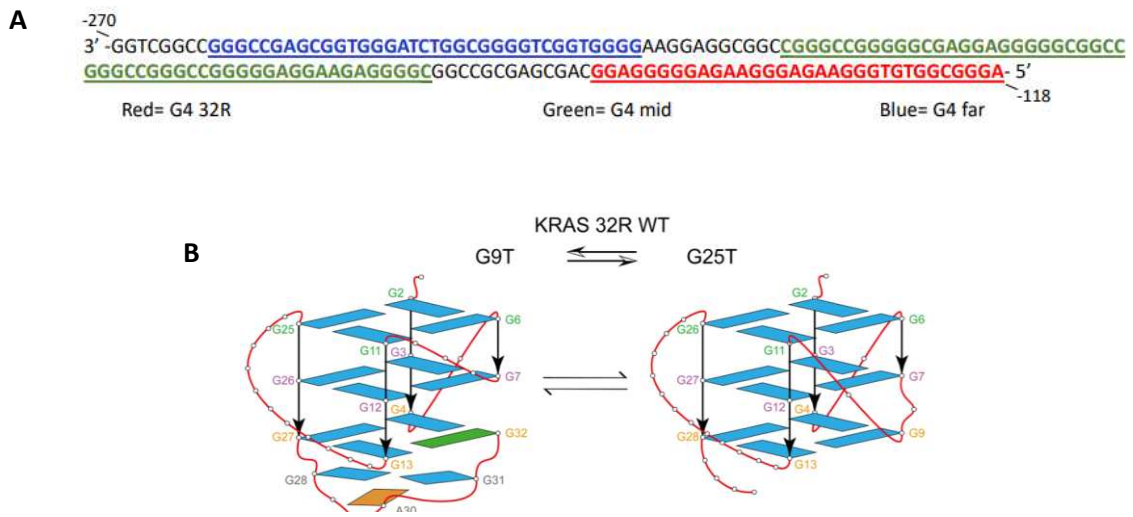

Figure 6. *KRAS* gene promoter site. A) The G4 motifs are located in the non-coding strand between -118 and -270 from TSS: G4 32R (sequence in red, -118/-149); G4-mid (sequence in green, -163/-217; G4-far (sequence in blue, -229-264) B) Two conformers of the KRAS 32R wild type are present in equilibrium and exhibit distinct structural characteristics, which are shown here by two families of mutations. A three-layered guanine tetrad core makes up the core of both mutants. G9T (left) is capped at the 3-end by a triad and has a fold-back guanine in syn glyosidic conformation (G32, green) (G28, A30 and G31). The conformer G25T (right) has three regular propeller loops, and all its guanines are in the anti-position.[116]

The parallel G4 with a T-bulge in one strand, two 1-nt and one 4-nt loops (AAGA) has an NMR structure identical to the G25T conformer of 32R. The substantial stacking between adenine residues seen in the crystal structure is a defining feature of the 4-nt loop. The 5'-UTR region is another KRAS -related sequence determinant that is critical for transcriptional control. It has a length of 192 nucleotides and a GC content of 77%. It consists of repeating GG blocks that are only a few nucleotides apart. Three non-overlapping RG4 motifs with a G-score of 21 were detected near the 5' end of the 5' UTR using the QGRS mapper and considering a G4 consensus motif with two G-tetrads and a loop length of up to 12 nt. The study yields > 300 possible RG4 sequences when the overlapping G4 motifs are considered. This shows that the KRAS mRNA 5'-UTR region has a high tendency to form RG4 structures. Each of the non-overlapping RG4 motifs has a CD spectrum with significant ellipticity at 265 nm and negative ellipticity at 240 nm, which is characteristic of parallel G-quadruplexes. The non-overlapping RG4 motifs are located within the first 80-nt of the 5'-UTR (s-80). In the presence of KCl, they

are thermally stable between 53°C and 62°C. An antibody that recognises G4 structures, BG4, also recognises the RG4 structures of the 5'-UTR. The RG4 structures were also recognised by BG4, an antibody specific for G4 structures. [8,102,103,113,116]

4.3 Role of G4 in KRAS promoter

14,769 putative G4-forming sequences (PQS) were discovered in gene promoters. This was revealed by a bioinformatic analysis of 19,268 human ENSEMBL genes (NCBI 34), covering about 193 Mb of the genome. PQS are enriched at gene promoters by a factor of 6.4 compared to their typical abundance throughout the genome. [110] It was later shown that the maximum abundance of RNA Pol II binding sites identified by chromatin immunoprecipitation sequencing correlates with the peak of G-richness near the transcription start site (TSS) (ChIP-Seq). [117] According to our data, G4 DNA underwent an evolutionary bias in favour of gene promoters. The PQS density steadily decreased to the genome average at a distance of > 20,000 bp from the TSS. [110] Furthermore, it showed that at least 42.7% of gene promoters have PQSs and that the density of these motifs in the first 100 bp upstream TSS is twelve times higher than the average PQS density of the genome. Bioinformatics research provided evidence for the idea that G4 DNA might control transcription. G4 DNA has been found to alter gene expression and the mobility of the RNA polymerase complex in in vitro studies of the transcription region of genes. [118] For example, a G4 that forms in the template or transcribed DNA strand could physically hinder RNA Pol II. In addition, a hybrid DNA:RNA G4 formed by the non-template strand and the developing RNA could possibly prevent the incoming RNA Pol II complex from being processed properly. [119] Another explanation is that an intramolecular G4 that occurs in the non-template strand promotes annealing of the developing RNA to the template strand and creates an R-loop that impedes the incoming RNA Pol II complex. [120] The role of G4 DNA in the upstream region TSS, where PQS density is highest, is likely to be more significant in the biological environment, although these methods of transcriptional repression have been identified. The G4 DNA serves as a surface for high-affinity binding of transcription factors, which is likely one of the functions of gene promoters. The G4 generated by the 32R region positioned upstream TSS in human and mouse KRAS promoters is one of the first examples to illustrate this idea. [117]

It was discovered that several proteins, including PARP-1, Ku70, and hnRNPA1, are able to bind to the folded conformation of KRAS. [115] It was later shown that the zinc finger protein MAZ, whose consensus binding sequence is GGGAGGG, binds to the KRAS G4 structure. [103] SP1, which identifies G4 structures in the c- KIT and HRAS promoters, is another example of a protein that binds to G4 DNA. [121, 122] About 36% of SP1 binding sites detected by ChIP-seq did not contain the typical *5'-GGGGCGG-3'*-Sp1 binding sequence, but most of these sites had one or more G4 motifs, according to a genome-wide study. This suggests that DNA conformation is also required for SP1 transactivation. [122] The idea that transcription factors might use G4 DNA as docking sites is supported by a recent study. Our laboratory has already demonstrated that various transcription factors are attracted to regions of human chromatin that contain endogenous G4s. Many transcription factors recognise the G4 promoters of highly expressed genes. [123] The functional aspect of the link between PARP-1 and certain G4 structures, which promotes the enzymatic activity of the protein, makes this interaction particularly interesting. The poly (ADP-ribosyl)ation (PARylation) of proteins, including its own, is catalysed by PARP-1 (auto-PARylation).[122, 123,124]

The results of a recent study by our laboratory on the function of PARP-1 in the activation of the gene KRAS in response to oxidative stress illustrate very well how the G4 DNA acts as a docking site for the assembly of a multiprotein complex. After interaction with the protein, the G4s generated by the 32R motif of KRAS caused extensive auto-PARylation synthesis of PARP-1, increasing the molecular weight of the protein from 113 to over 250 kDa. In vitro experiments with *KRAS* G4 and increasing PARP-1 concentrations in the presence of NAD+ allowed this process to be observed. During the interaction of PARP-1 with the KRAS promoter, only a small auto-PARylation takes place. The net charge of the protein is changed during this process, making it anionic. It also promotes the recruitment of cationic transcription factors such as MAZ and hnRNP A1 to the promoter, which are essential for the transcription of KRAS. Indeed, several papers have attributed a function to PARP-1 in the formation of regulatory complexes at the gene promoter. In summary, our research demonstrates that PARP-1 is a key mediator of the increase in KRAS transcription observed in the presence of increased oxidative stress (Figure 7). [124, 125]

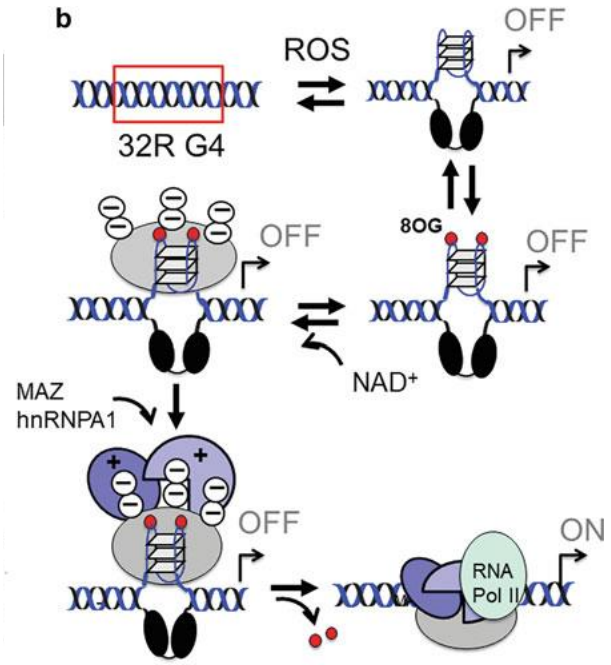

Figure 7. Mechanism for activating transcription triggered by oxidative stress. Under more severe oxidative stress, certain G4 32R-guanines can convert to 8-oxoguanine. The PARP-1 is brought to the promoter by the oxidised guanines when the G4 binds to it, where it becomes auto-PARylated. Since auto-PARylated PARP-1 is unfavourable, it electrostatically attracts cationic transcription factors such as MAZ and hnRNPA1 to its surface. [125]

4.4 Understanding the role of hnRNPA1 in KRAS promoter with respect to G4 site.

A large family of proteins known as heterogeneous nuclear ribonucleoproteins (hnRNPs) bind to developing pre-mRNAs and package them into hnRNP particles. This family includes about 20 major polypeptides, hnRNPs A1 to U, ranging in size from 34 to 120 kDa. There are other putative hnRNP genes that may encode smaller hnRNP proteins that remain to be investigated. [126] Each hnRNP protein contains at least one RNA-binding motif, such as an RNA recognition motif (RRM), an hnRNP K homology domain (KH), or an arginine/glycine-rich (RGG) box. Many show a strong preference for specific nucleic acid motifs. Auxiliary domains in several hnRNPs that promote protein-protein interactions have a particular amino acid composition. [127, 128] Numerous cellular functions, including roles in DNA maintenance and recombination, transcription and processing of primary transcripts, nuclear export,

subcellular localisation, translation, and stability of mature mRNA, have been attributed to hnRNP proteins in correlation with these various structural features. [129]

The hnRNP A1 gene contains two primary known isoforms, hnRNP A1-A and hnRNP A1-B, and is located on chromosome 12q13.13. Both hnRNP A1 isoforms, like other members of the hnRNP(A/B) subfamily, consist of two main structural parts: a prion-like domain (PrLD) at the C-terminus that mediates cellular compartmentalisation, protein-protein interaction, and RNA- binding; and an N-terminal part that contains two RNA recognition motifs (RRMs). [131] The RRMs, each about 90 amino acids long, serve as docking platforms to participate in both general and specialised RNA and messenger RNA (mRNA) binding. Although there is a high degree of similarity between the two RRMs (about 35% identical and 60% similar), they are not redundant and function as separate domains that can bind to different RNAs and mRNAs. The RRM domains at its N-terminus are followed by a highly flexible glycine-rich (Gly-rich) C-terminal region that serves as both an RNA-binding domain and a nuclear targeting sequence. The 195 amino acid N-terminal region known as UP1, which contains the RRM domains, has been thoroughly studied using X-ray crystallography and NMR spectroscopy. [132, 133]

While hnRNP A1 preferentially anneals to AU-rich elements (AREs) or UAGGGA(U) motifs in the 3'-untranslated regions (3'-UTR) of messenger RNA transcripts, their sequence-binding selectivity is identical. The arginine-glycine-glycine domain (RGG domain), the glycine-rich PrLD and the 38 amino acid long nuclear localisation/export sequence (NLS/NES), known as M9, are all located at the C-terminus of hnRNP A1 (Figure 8). The RGG domain of hnRNP A1 has been shown to affect the selectivity and strength of RNA binding, the binding and unfolding of G-quadruplex DNA, and the mediation of protein-protein interactions. [134]

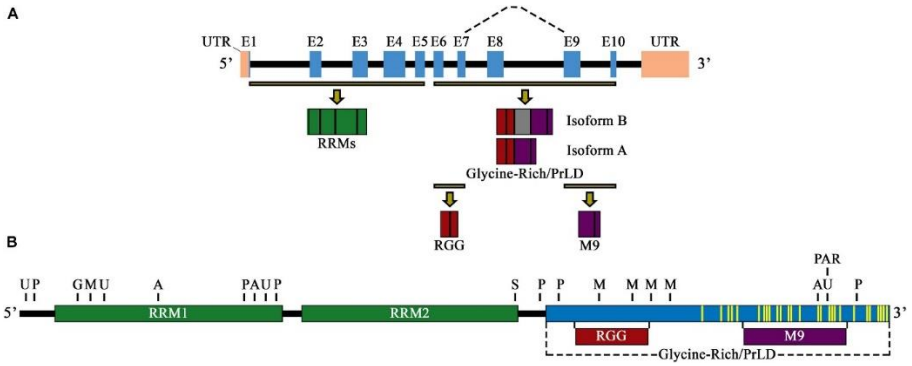

Figure 8. Schematic illustration of the primary pre-mRNA transcript and alternative mRNA splicing of hnRNP A1. (A) Exon numbers E1 through E10 are marked by blue boxes. Introns are denoted by black boxes, and

UTRs by pink boxes. The highlighted exon fractions (yellow-black lines) that make up the N- and C-terminal sections of hnRNP A1 are shown in green (RRM1 and RRM2), while the glycine-rich/PrLD domain is shown in a mix of red (RGG domain) and purple (M9 sequence). The primary spliced region of hnRNP A1 is represented by the dashed line, with E8 (gray box) included for isoform B and its exclusion for isoform A. (B) (B) Schematic representation of the hnRNP A1 isoform A's primary protein structure and functional domains. Green boxes stand in for RRM1 and RRM1, while blue boxes represent the glycine-rich/PrLD domain. The RGG domain (red box) and the M9 sequence (purple box) are highlighted protein fractions that, in relation to their position below, are in the glycine-rich/PrLD domain. Above the protein depiction are the PTM sites for ubiquitination (U), phosphorylation (P), O-GlcNAcylation (G), acetylation (A), sumoylation (S), methylation (M), and PARylation (PAR) (selectively representative; see Table 1 for a complete list of PTM locations). The mutation locations in hnRNP A1 that have been identified and linked to the neurodegenerative disorders ALS/FTLD and MS are shown by yellow lines. [134]

According to previous studies, hnRNP A1 is a DNA-binding protein that affects RNA transcription by binding to promoters. Depending on which gene is of interest, this interaction represses or activates transcription. There are mainly two lines of research that explain how hnRNP A1 affects transcriptional regulation. First, research has shown that hnRNP A1 controls promoter repression by modulating the activity of transcription factors through interactions with its PrLD domain on other proteins. [135] According to other studies, hnRNP A1 binds to and destabilises G-quadruplex structures in the promoters of genes, thereby modulating promoter activity. [136, 137] This latter effect depends on the loop nucleotides of the G-quadruplex DNA interlocking with the RGG domain during identification and subsequent binding. Through their interaction with single-stranded DNA, the RRMs of hnRNP A1 are able to disrupt the G-quadruplex structure and stabilise the unfolded form of the DNA. [136, 137]

Scientists have demonstrated that the protein hnRNPA1 can recognise and resolve DNA and RNA G4 structures. Fukuda et al. published the first study describing this property in 2002. They showed that UP1 unfolds the G4 structures of minisatellite repeats and telomeric DNA. A few years later, our team found that hnRNPA1 and UP1 recognise and unfold the G4 structure generated by 32R. In addition, studies with single molecules FRET have shown that hnRNPA1 partially unfolds the telomeric DNA overhang. Reportedly, the RGG box of hnRNPA1 identifies telomeric G4 DNA and facilitates UP1 G4 unfolding. The same scientists also found that TERRA G4 RNA is particularly recognised by the glycine-arginine-rich domain (RGG-box) of hnRNPA1, but not single-stranded RNA. All these studies suggest that hnRNPA1 is a nuclear

protein linked to odd DNA and RNA G4 structures. However, the exact nature of this connection and its function are still unclear. [125, 138, 139]

5. Photodynamic Therapy (PDT)

The dynamic interaction of a photosensitizer (PS), light of a certain wavelength and molecular oxygen underlies PDT and promotes the targeted death of the target tissue. [140] The PDT procedure involves the administration of a PS (topically or intravenously) that specifically accumulates in the tumour tissue (during a drug-light interval), followed by irradiation with an appropriate wavelength of light. The PS does not interact directly with biomolecules, but the illumination causes the production of reactive oxygen species (ROS), including singlet oxygen, superoxide radicals ($O2^-$), hydroxyl radicals (HO^-) and hydrogen peroxide (H_2O_2). These cytotoxic photoproducts initiate a series of metabolic processes that can damage and kill the target tissue. [141]

In clinical PDT, larger areas corresponding to healthy tissue with tiny malignant foci are often irradiated. It is in these situations that the tumour-trophic properties of the photosensitizers play a crucial role. The biodistribution of a photosensitizer, like that of other small molecules, is primarily influenced by its physicochemical properties, but unfortunately most compounds do not appear to have a strong selective attraction to tumour tissue. [142]

Liposomes have attracted attention as an effective carrier and delivery system due to their high loading capacity and adaptability to photosensitizers with a range of physicochemical properties. [143] It has been found that the use of liposomal formulations can significantly increase the PDT efficacy and safety of photosensitizers. However, the plasma half-life of these standard liposomes is too short to allow effective uptake into the tumour, so they have not proven to be the best tools for tumour-selective targeting of photosensitizers. On the other hand, liposomes with a carefully modified architecture, such as long circulating and particularly aggressively targeting liposomes, have a greater likelihood of becoming truly tumoritropic carriers of photosensitizers. [144, 145]

An important area of research in the treatment of cancer is the use of nanoparticles for drug delivery. Due to their ease of preparation and their natural composition of non-toxic phospholipids, liposomes have attracted the attention of several researchers among the nanostructures proposed for drug delivery. [146, 147] They are used as nanocarriers for drug delivery in the treatment of cancer and consist of a spherical phospholipid bilayer surrounding an aqueous central core space. [144, 145] Liposomes are used for the delivery of a wide range

of drugs into tissues due to their special ability to entrap both hydrophobic and hydrophilic molecules. Thus, hydrophilic chemicals can be entrapped in the aqueous central core, while lipophilic molecules can penetrate the bilayer of the membrane. In contrast to conventional chemotherapy, the side effects are less because the porphyrins are only active in the radiation-damaged tumour and not in the surrounding tissue. Drugs administered with nanoparticles can extravasate from leaky tumour vessels and accumulate in the tumour if their diameter exceeds the threshold for renal clearance. This leads to a property known as enhanced permeability retention (EPR) effect, which makes nanoparticle-associated drugs more tumour-specific than free drugs. In addition, free porphyrins may have a different cellular effect than liposomally bound porphyrins depending on their location in cells, as ROS and do not diffuse very far from the site of synthesis. [148, 149]

5.1. Reactive Oxygen Species

In aerobic organisms, metabolic activities constantly produce reactive oxygen species (ROS), such as the anion superoxide (O_2^-), hydrogen peroxide (H_2O_2) and the hydroxyl radical ($\cdot OH$). The main sources of reactive oxygen species (ROS) are: (i) mitochondria through electron loss from the ubiquinone/ubiquinol shuttle, (ii) peroxisomes in the oxidation of long-chain fatty acids, (iii) cytochrome P-450 enzymes and (iv) nicotinamide adenine dinucleotide phosphate (NADPH) oxidases of the family NOX. Cancer cells employ several defence mechanisms to maintain oxidative stress at non-toxic levels, as excessive amounts of ROS have a deleterious effect on proliferating cells. However, intracellular ROS are capable of oxidising lipids, proteins and nucleic acids and causing significant cellular damage. [150, 151, 152]

In PDAC, oxidative stress could be a double-edged sword. On the one hand, ROS -induced DNA damage promotes the onset of the carcinogenesis process and malignant transformation of cells. In addition, a small increase in ROS, which is common in cancer cells, promotes cancer cell survival and growth. On the other hand, too much ROS triggers apoptosis, which leads to cell death. Consequently, the degree of oxidative stress determines the involvement of ROS in the development of cancer. It is noteworthy that the promotion of cell proliferation depends on the control of redox homeostasis. [150, 151, 152]

As mentioned earlier, there are several ROS species, but the three most important are O_2^-, HO^- and OH. As electrons move across the mitochondrial electron transport chain, molecular

oxygen (O_2) is incompletely reduced, resulting in the anion superoxide. Superoxide dismutase converts O_2 to H_2O_2, and catalase subsequently reduces the H_2O_2 to water. [150, 151, 152]

5.2. ROS in cancer

Because of their faster metabolism than healthy cells, cancer cells produce greater amounts of ROS. ROS can promote the constitutive activation of growth factors that support cell growth and proliferation. Elevated levels of ROS have been found in several malignant tumours and are likely responsible for maintaining the aggressive phenotype. To maintain ROS at a level suitable for optimal cell growth, cancer cells develop the ability to establish a new redox balance. Thank you to these adaptations, cancer cells can grow despite a slight increase in oxidative stress. The balance between antioxidant and oxidative (ROS) molecules leads to oxidative stress. [153] Although several authors have suggested a link between ROS and cancer, in recent years there have been conflicting data on the involvement of ROS in carcinogenesis. Several studies have shown that in both human cells and mouse models, mild to moderate elevations of ROS promote the proliferation and spread of cancer cells. [154] In contrast, antioxidant therapies such as N-acetylcysteine (NAC) or vitamins A or E have not been very successful in reducing the incidence of cancer, including head and neck cancer and lung cancer. [155] However, increased metabolic rate alone cannot explain the higher ROS levels in cancer cells. ROS may either directly or indirectly affect genetic changes in certain genes (oncogenes). In fact, ROS can activate several genes and signalling pathways involved in tumour development and aggressiveness. ROS may support EMT (Epithelial to Mesenchymal Transition) leading to the development of metastases, (i) promote cellular proliferation through MAPK by activating the key transcription factors ERK1/2 and NF-B, (ii) escape apoptosis by controlling c-SRC, NF-B and PI3K/AKT, and (iii) promote angiogenesis by supporting the release of VEGF. However, increased metabolic rate alone cannot explain the higher ROS levels in cancer cells. ROS may either directly or indirectly influence genetic changes in specific genes (oncogenes). In fact, ROS can activate several metabolic pathways and genes that contribute to tumour development and aggressiveness [156]. ROS can (i) promote cellular proliferation through MAPK by activating the important transcription factors ERK1/2 and NF-B [155]; (ii) prevent apoptosis by controlling c-SRC, NF-B and PI3K/AKT [158]; (iii) support EMT, which can lead to the development of metastases [157]; and (iv) promote angiogenesis by stimulating the release of VEGF. [154]

5.3. ROS triggers PDAC proliferation via Nrf2

A slight increase in intracellular ROS in PDAC is thought to be a characteristic feature of the disease, acting as a pro-survival and anti-apoptotic agent. [154, 160]

In pancreatic cancer cells, the oncogenic KRAS can trigger the production of various antioxidant genes via nuclear factor erythroid 2-like 2 (*nfe2l2* or *Nrf2*), as excessive ROS levels are harmful to cells. The cap'n'collar (CNC) family of transcription factors belongs to the bZIP (basic region-leucine zipper) family, and Nrf2 is a member of this family. This transcription factor is thought to exert primary control over redox homeostasis. In the absence of stress, inactive Nrf2 is bound to the repressor protein Kelch-like ECH-associated protein1 and sequestered in the cytoplasm (KEAP1). The CUL3/RBX1 E3 ubiquitin ligase complex uses KEAP1, an adaptor protein, to ubiquitinate Nrf2 and then degrade it by proteolysis in the 26S proteasome. [161, 162, 163]

The half-life of Nrf2 is extremely short under unstressed conditions, ranging from 10 to 30 minutes, and the protein is constantly being directed to the proteasome to be destroyed. KEAP1 has several cysteine residues on its surface that serve as redox sensors. Under oxidative stress conditions, oxidation of the cysteines in the KEAP1 protein leads to a conformational shift that disrupts binding with Nrf2. The free protein migrates to the nucleus and forms a heterodimer with the regulatory protein small v-maf, an oncogene homolog (maf). [164] Several antioxidant enzymes, including phase II enzymes such as glutathione S-transferase and NAD (P)H-quinone oxidoreductase-1, are then transcriptionally activated by the subsequent binding of the complex to the antioxidant response element (ARE) on DNA (HNQO- 1). Some authors have hypothesised the dual function that Nrf2 may play in cancer. [165] Because of its ability to activate the cellular antioxidant response by inducing the transcription of many genes involved in the response to oxidative stress or xenobiotics, this major transcription factor has long been considered a tumour suppressor. The potential "evil side" of Nrf2 has come to light in recent years. A growing body of data suggests that Nrf2 activation promotes tumour growth and acts as a chemoresistant agent. [166, 167, 169, 169]

Since oncogenic KRAS and Nrf2 are correlated, $KRAS^{G12D}$ upregulates Nrf2 to maintain redox balance in cells and reduce intracellular ROS to support proliferation. Deregulation of the Nrf2/KEAP1 system leads to increased cell proliferation and promotes chemo- and

radioresistance in pancreatic cancer cells. Furthermore, using Nrf2 labelling of tumour and benign epithelium, researchers in the same study have shown that pancreatic tumours are associated with increased expression of Nrf2. [157, 167, 168, 169]

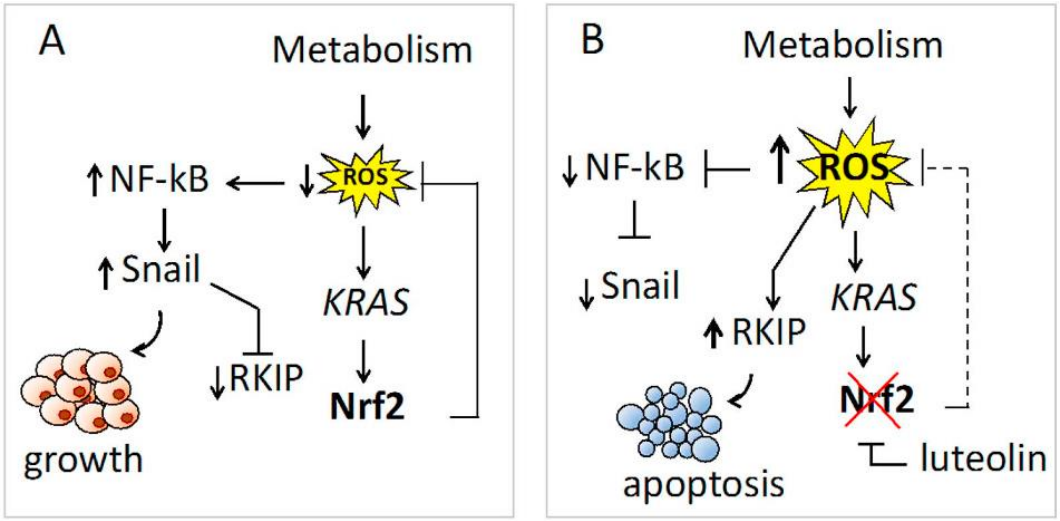

Figure 9. The NF-kB-Snail-RKIP junction and the ROS-KRAS-Nrf2 axis. (A) The ROS level is low, NF-kB and Snail are upregulated, and RKIP is downregulated when Nrf2 is elevated by KRAS. This expression pattern encourages cell development; (B) The ROS level rises when Nrf2 is blocked by luteolin. As a result, RKIP is upregulated while NF-kB and Snail are downregulated. Apoptosis is promoted by this expression profile. [170]

Our group aimed to identify the mechanism of action between Nrf2 and KRAS in PDAC cells, as KRAS reprograms metabolism in PDAC (Figure 9). We discovered that ectopic $KRAS^{G12D}$ or $KRAS^{G12V}$ expression increased Nrf2 two-fold in PDAC cells, suggesting a direct relationship between KRAS and Nrf2. Our results suggest that ROS, KRAS and Nrf2 work together to establish a molecular axis that prevents ROS from growing to dangerous levels that could impede proliferation. We also discovered that the survival and apoptosis pathways cross the ROS /KRAS/Nrf2 axis. The ROS /KRAS/Nrf2 axis controls the expression of pro-survival Snail and proapoptotic RKIP by regulating redox homeostasis. When NRF2 is active, low ROS levels result in upregulation of pro-survival Snail and proapoptotic RKIP, which means proliferation triumphs over apoptosis. In contrast, when Nrf2 is blocked, high ROS levels lead to overexpression of proapoptotic RKIP and downregulation of pro-survival Snail; in this situation, apoptosis triumphs over proliferation. These results indicate that PDT can be

enhanced by co-administering the photosensitizer with an Nrf2 inhibitor, which inhibits the cell's detoxifying response to therapy. It is expected that a combination of PDT (porphyrin P4+Nrf2 inhibitor) will be more successful than simple PDT (P4 only). We present experimental evidence to support this claim. The results show that combination therapy of P4/ and luteolin reduces colony formation and cell survival in Panc-1 and BxPC-3 cells more than treatment with P4/ alone. The same results were obtained with ochratoxin A, a non-flavonoid Nrf2 inhibitor, as an adjuvant to porphyrin P4. [170]

6. Nrf2

Nrf2 is a member of the Cap'n'Collar (CNC) subfamily of Basic Leucine Zipper (bZIP) transcription factors, along with Nuclear Factor Erythroid-derived 2 (NFE2), Nrf1, Nrf2 and Nrf3 [171]. Nrf2 is encoded by the gene nuclear factor, erythroid 2 like 2 (NFE2L2). Seven conserved Nrf2 ECH homology (Neh) domains in Nrf2 regulate different aspects of Nrf2 transcriptional activity (Figure 10). In contrast, the Neh2 domain contains ETGE and DLG motifs that specifically interact with the Kelch domain of Kelch-like ECH-associated protein 1 (KEAP1) to mediate Nrf2 ubiquitination and degradation (Figure 10). The bZip in the Neh1 domain heterodimers with the small musculoaponeurotic fibrosarcoma proteins (sMAF) K, G and F as well as other bZip proteins to recognise antioxidant response elements (ARE) to activate gene transcription [172].

By binding to various elements of the transcriptional machinery, the Neh3-5 domains serve as transcriptional activation domains [173]. Two redox-independent degrons, DSGIS and DSAPGS, found in the Neh6 domain, bind to the E3 ubiquitin ligase transducin repeat-containing protein (TrCP), which facilitates Nrf2 degradation in cells under oxidative stress (Figure 10) [174]. Retinoic X receptor alpha (RXR) and the Neh7 domain interact to suppress NRF2 activation [175]. The stability of Nrf2 and the transcriptional activation of its target genes are influenced by these domains at multiple levels, including transcriptional, post-transcriptional and post-translational regulation in response to various stressors. In addition to its redox-regulating abilities, recent studies have found Nrf2 to have several novel activities, including regulation of inflammation, autophagy, metabolism, proteostasis and unfolded protein response (UPR), particularly in the context of carcinogenesis. The activities of Nrf2 are broader than originally thought and are the focus of in-depth studies of inflammation, metabolism, cancer prevention and therapy. Understanding how Nrf2 activity is regulated and how its novel roles evolve brings new problems but also new perspectives for Nrf2 cancer therapy. [176]

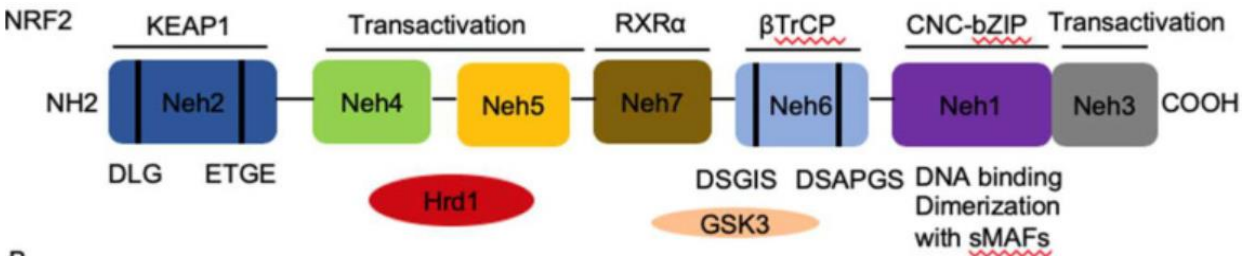

Figure 10. NRF2 Structure. There are seven preserved NRF2-ECH homologies in NRF2. Neh1–Neh7 are NRF2-ECH homology (Neh) domains. Neh1 has a basic leucine zipper (bZip) motif, in which the basic region binds DNA and the Zip dimerizes with additional binding partners, such as sMAFs. Neh2 has ETGE and DLG motifs, which are necessary for KEAP1 binding and the subsequent proteasomal degradation caused by KEAP1. The transactivation domains of NRF2 are Neh3, 4, and 5. NRF2 degradation is mediated by an interaction between HRD1 and the Neh4 and Neh5 domains. Two TrCP degrons, DSGIS and DSAPGS, found in Neh6, are in charge of the TrCP-mediated proteasomal degradation. [176]

Cysteine residues C151, C273 and C288 are shown to be particularly reactive and open to covalent modification by ROS, RNS, H2S and other electrophilic substances. In this context, it has been demonstrated that S-sulfenylation, S-nitrosylation and S-sulfhydration of these important residues cause Keap1 to adopt new conformations, which in turn promote the dissociation of Nrf2 and its stabilisation [182, 183, 184].

Two hypotheses have been put forward in the literature to explain how Nrf2 stability is regulated, although the exact mechanism of Nrf2-Keap1 interaction is still unclear. The first, sometimes referred to as the "hinge and lock" hypothesis, proposes that a stronger contact between Keap1 and the ETGE domain serves as a lock, while weaker interaction with the DLG motif serves as a hinge. The DLG motif separates from Keap1 when certain thiol residues are altered by electrophiles, leading to a disruption in the orientation of the lysine residues of Nrf2 that eventually prevents its ubiquitination. The DSGIS and DSAPGS motifs of -TrCP (beta-transducin repeats-containing protein), which serve as a substrate receptor for the Skp1-Cul1-Rbx1/Roc1 ubiquitin ligase complex that catalyses Nrf2 ubiquitination, are bound by the Neh6 domain in the normal state according to the second model, also known as Keap1-independent regulation [185, 186, 187, 188].

6.1. Functions of Nrf2

In addition to its redox-regulating abilities, several novel activities of Nrf2 have been discovered in recent studies, including the regulation of inflammation, autophagy, metabolism, proteostasis and unfolded protein response (UPR), particularly in the context of carcinogenesis. The activities of Nrf2 are broader than originally thought and are the focus of in-depth studies of inflammation, metabolism, cancer prevention and therapy. Understanding how Nrf2 activity is regulated and how its novel functions evolve brings new problems but also new perspectives for Nrf2 cancer therapy (Figure 11).

6.1.1 Role in Redox Stress and Drug Toxicity

Nrf2 plays an important role in the antioxidant stress response and in defence against drug toxicity. The downstream signalling genes of NRF2 work together to manage cell stress and drug detoxification to maintain cellular homeostasis. They are categorised as Phase I, II and III. [189] Phase I enzymes regulate oxidations, reductions, and xenobiotic hydrolytic reactions such as carbonyl reductase, aldoketo reductase, NQO1, cytochrome P450 oxidoreductases (CYPs). [190] Enzymes that catalyse conjugation reactions such as glutathione S-tranferase (GST), UDP-glucuronic acid synthesis enzymes, HO -1 belong to the phase II network. The enzymes of phase III are associated with the transport of the conjugated metabolites of phase II. Thus, they are mainly the drug efflux transporters such as Multidrug Resistance-Associated Proteins (MDR), Breast Cancer Associated Proteins (BCRP), ATP-Binding Cassette g5 and g8 (ABCG5, ABCG8). [189, 190]

Figure 11 shows in detail the external and internal causes of oxidative stress leading to ubiquitination of Keap 1. The free Nrf2 protein then binds to an actin and is transported into the nucleus where it activates the ARE /EpRE for transcription of genes belonging to 5 different types of effects. These include i) activation of phase I and phase II metabolising enzymes ii) activation of phase III transporters iii) antioxidant proteins iv) ubiquitination and proteasomal degradation proteins v) chaperones and stress response proteins. These 5 categories of genes/proteins play important roles in cell survival, tumourigenesis, transport of metabolites and xenobiotics, reduction of oxidative damage, and repair and removal of damaged proteins. [191]

6.1.2. Role in Unfolded Protein Response (UPR) and Proteostasis

The homeostatic control of the synthesis, folding, transport and degradation of the proteome is called proteostasis. The Unfolded Protein Response (UPR) is a conserved signalling pathway involved in the response to protein misfolding. The accumulation of misfolded proteins leads to stress in the endoplasmic reticulum (ER). This ER stress activates 3-armed signalling pathways coordinated by IRE1-XBP1, PERK -eIF 2a- ATF 4 and ATF 6, which ultimately trigger the UPR. [192]

NRF2 is activated by the excessive production of ROS by mitochondria, ER and other sources. In addition, stress triggered EPRK phosphorylates Nrf2, leading to dissociation of the Nrf2/KEAP1 complex and activation of Nrf2. Nrf2 is a centre for emergency signals generated by the accumulation of misfolding proteins to coordinate transcriptional responses in the cell. And Nrf2 acts directly to activate transcription of ATF 4, which is also linked to amino acid metabolism and resistance to oxidative stress. The heterocomplex formed by Nrf2 and ATF4 also helps cell survival against proteotoxic stress. [193, 194]

Nrf2 also regulates the expression of genes of several subunits of the 20S proteasome, including PSMA1, PSMA3, PSMA4, PSMA5 and PHSMA 6, and for the 19S proteasome subunit, it regulates the gene expression of PSMC1, PSMC 2 and PSMD 14. [195] Nrf2 also mediates and induces the expression of the proteasome maturation protein (POMP) by binding to the promoter of its gene. [196]

6.1.3. Role in Autophagy

Nrf2 induces expression of calcium binding and coiled coil domain containing protein 2 (CALCOCO2/NDP52), unc- 51- like kinase 1 (ULK1), autophagy genes encoding SQSTM1/p62, autophagy protein 5 and gamma amino butyric acid receptor associated protein- like 1 (GABARAPL1). A lack of autophagy leads to an accumulation of p62, which sequesters KAP1 and stabilises Nrf2, thereby activating it. Therefore, p62 and Nrf2 form a positive feedback loop to regulate cellular functions. [197, 198]

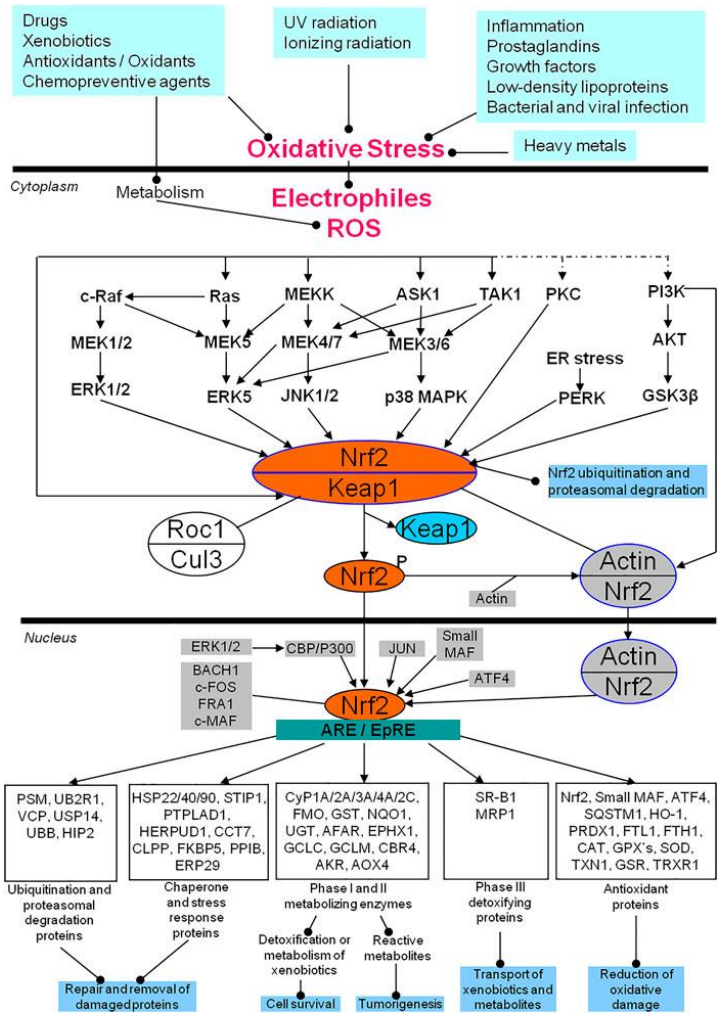

Figure 11. Nrf2 mediated pathways in humans. These pathways represent the complex network of signalling responsible for antioxidant stress reduction and other physiological roles performed by the cell. Multiple causative agents result in rise of ROS levels in the cells, either directly through metabolism or in-directly through oxidative stress and free electrophiles. This increased ROS activates different pathways which act on Nrf2 bound to keap, resulting in its phosphorylation and activating ARE/EpRE responses in the cell nucleus. The details are in the text. [191]

6.1.4 Role in Mitochondrial Physiology and Biogenesis

Nrf2 influences several aspects of antioxidant response, intermediate metabolism, and mitochondrial function by regulating some metabolic genes or by overlapping with transcription factors. Activation of NRF 2 enhances amino acid metabolism, glycolytic flux and PPP, leading to increased input of substrates and reducing equivalents into the TCA cycle and mitochondrial respiratory chain. Nfe2l2-deficient cells have shown lower oxygen

consumption rate, lower basal mitochondrial membrane potential and lower basal ATP levels, while nfe2l2-null cells have shown impaired mitochondrial fatty acid oxidation. [199, 200].

Nrf2 positively regulates NADPH levels by enhancing the expression of genes encoding pentose phosphate pathway (PPP) enzymes, glucose-6-phosphate dehydrogenase (G6PD), isocitrate dehydrogenase 1 (IDH1) and malic enzyme 1 (ME1). In addition, ME1 again produces pyruvate, which can be recycled into the mitochondria. GSH levels are also regulated by Nrf2 by increasing the expression of genes encoding enzymes involved in the biosynthesis of GSH and the regeneration of its oxidised form from GSSG, including the enzyme glutathione reductase (GR). Nrf2 negatively regulates acetyl-CoA carboxylase, ATP citrate lyase (ACL), stearoyl-CoA desaturase and fatty acid synthase. These are the four crucial enzymes involved in fatty acid synthesis (FAS). An increase in malonyl-CoA levels can decrease mitochondrial fatty acid oxidation (FAO) by enhancing its inhibitory function on carnitine palmitoyltransferase 1 (CPT1), which mediates the transport of long-chain fatty acids into mitochondria (Figure 12) [201].

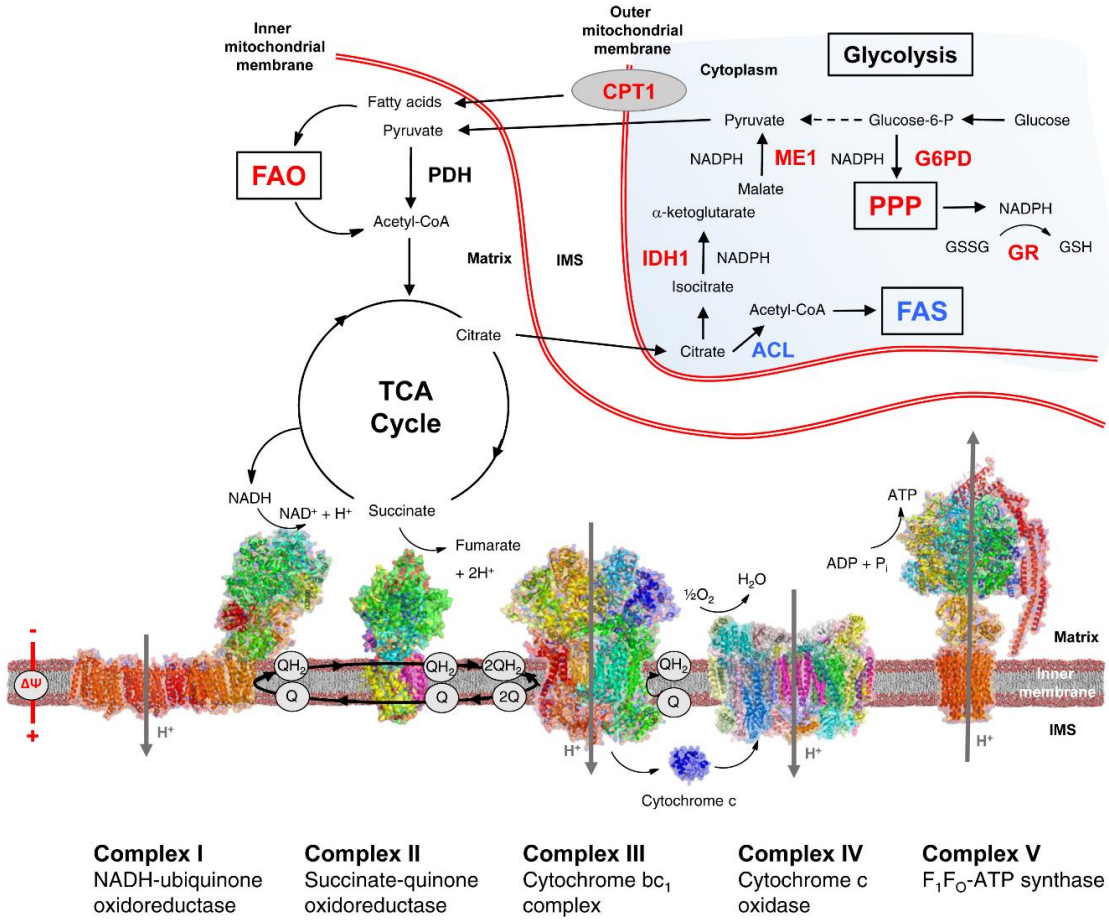

Complex I NADH-ubiquinone oxidoreductase

Complex II Succinate-quinone oxidoreductase

Complex III Cytochrome bc_1 complex

Complex IV Cytochrome c oxidase

Complex V F_1F_O-ATP synthase

Figure 12. Nrf2 regulates mitochondrial function at multiple stages. The potential of the mitochondrial membrane (), the availability of substrates for respiration, and ATP generation are all increased by Nrf2 activation. By promoting the expression of the genes for glucose-6-phosphate dehydrogenase (G6PD), the pentose phosphate pathway (PPP), malic enzyme 1 (ME1), and isocitrate dehydrogenase 1 (IDH1), Nrf2 positively regulates the levels of NADPH. ME1 creates pyruvate, which can return to the mitochondria, in addition to NADPH. By promoting the expression of genes for enzymes involved in GSH biosynthesis and regeneration from its oxidized form, GSSG, such as glutathione reductase (GR), Nrf2 also controls the levels of GSH. Four essential enzymes involved in fatty acid synthesis (FAS) are negatively regulated by Nrf2: ATP-citrate lyase (ACL), acetyl-CoA carboxylase, fatty acid synthase, and stearoyl CoA desaturase. Malonyl-CoA has an inhibitory role on the enzyme carnitine palmitoyltransferase 1 (CPT1), which facilitates the transport of long-chain fatty acids into the mitochondria, and its levels falling may promote mitochondrial fatty acid oxidation (FAO). The blue and the red colours indicate negative and positive regulation by Nrf2, respectively. IMS:mitochondrial intermembrane space. [201, 202]

Nrf2 triggers mitochondrial biogenesis by activating nuclear respiratory factor 1 (NRF1), which transcribes biogenesis transcription factor A, mitochondrial (TFAM) and transcription factor B2, mitochondrial (TFBM2). (Figure 13) [42]

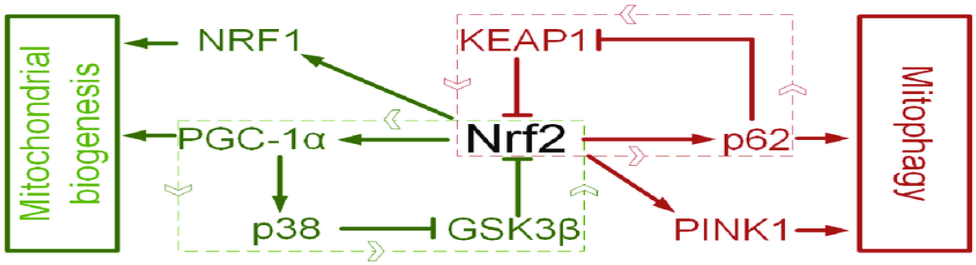

Figure13. Regulatory loops controlling mitochondrial turnover. Nrf2-PINK1 and Nrf2-p62-KEAP1-Nrf2 loop interaction regulate of mitochondrial biogenesis. Nrf2-NRF1 and Nrf2-PGC1α-p38-GSK3β-Nrf2 loop interaction regulate of mitochondrial biogenesis. [203]

7. Nrf2 and Metabolic reprograming in cancer

7.1 Gluconeogenesis

Nrf2 is constitutively activated in many human cancers and is thus the cause of poor prognosis.[205] Our RNA-seq data show that Nrf2 stimulates glycolysis to produce ATP and biomass, i.e., the precursors for supplying the anabolic pathways to maintain tumour growth.

Expression of the glucose transporter GLUT 1 is induced by Nrf2; this transporter allows large amounts of glucose to enter the glycolytic flux (Warburg effect). [206] Nrf2 induces the expression of several glycolytic enzymes, including hexokinase 1 and 2 (HK1/2), phosphofructo-2-kinase (PFK2), PFK4, aldolase A (ALDO A), fructose biphosphate, enolase 1 and 4 (ENO1/4), glucose phosphate isomerase 1 (GPI 1), and pyruvate kinase isoform 2 (PKM2). These enzymes increase glycolytic flux to maintain the pool size of intermediates for anabolic reactions. [206] The final step of glycolysis is catalysed by pyruvate kinase, which converts phosphoenolpyruvate to pyruvate and phosphorylates ADP to ATP. Since cancer cells require large amounts of energy and biomass to support their cell proliferation, they have a high expression level of PKM2. [207]. Pyruvate kinase activity promotes the build-up of glycolysis intermediates and their channelling into the synthesis of nucleic acids, amino acids and phospholipids [176]

Keap1-null, albumin-Cre: $Keap1^{(flox/-)}$ (CKO) mice are ideal models for studying genetic activation of Nrf2 signalling. [208] CKO mice crossed with diabetic db/db mice have shown that genetic activation of Nrf2 inhibits gluconeogenesis by inhibiting fructose-1,6-bisphosphatase 1 (FBP1), glucose-6-phosphatase (G6PC), peroxisome proliferator-activated receptor g-coactivator 1-a (PGC1a), phosphoenolpyruvate carboxykinase (PCK1) and nuclear receptor subfamily 4, group A, member 2 (NR4A2) in the liver, leading to the prevention of diabetes mellitus. [209]

The first product of glycolysis is glucose-6-phosphate, which can be converted by phosphoglucomutase (PGM) into glucose-1-phosphate for glycogen synthesis. Nrf2 regulates the expression of PGM along with other proteins required for glycogen synthesis, including 1,4-alpha-glucan branching enzyme 1 (GBE1), glucosidase alpha, acid (GAA) and phosphorylase kinase regulatory subunit alpha 1 (PHKA1). [206,211,212] Skeletal muscle and the liver are the two main organs responsible for the synthesis and storage of glycogen. Nrf2 regulates glycogen metabolism in these two locations in different ways. In the liver, Nrf2 activation causes an increase in glycogen accumulation to maintain blood glucose levels during fasting, while in skeletal muscle it reduces glycogen concentrations, leading to improved glucose tolerance. [210,212]

7.2 Pentose Phosphate Pathway (PPP)

Glucose-6-phosphate dehydrogenase (G6PD) and phosphogluconate dehydrogenase (PGD) enable the transfer of glucose-6-phosphate into the pentose phosphate pathway. These two enzymes are the key enzymes of the oxidative segment of PPP and are directly regulated by Nrf2. PGD and G6PD also mediate the formation of the reducing agent NAPDH, which is required for the biosynthesis of nucleotides, lipids, and other molecules important to the cell. [206, 211]. In tumors, Nrf2, PGD and G6PD are upregulated (REF), which also affects lipid and nucleotide metabolism (purines and pyrimidines). The other enzymes responsible for NADPH production are malic enzyme (ME1) and isocitrate dehydrogenase (IDH1). These are also upregulated by Nrf2. [205,206]

The non-oxidative part of PPP is also regulated by Nrf2, with the PGD, Transaldose1 (TALDO1), TKT and G6PD enzymes being directly activated by Nrf2 binding to the ARE in their promoter region. The expression of miR-1 and miR-206 is indirectly downregulated by Nrf2 via G6PD, PGD and TKT [211, 213].

7.3. Purine biosynthesis

The pentose phosphate pathway leads to two major products, ribose 5-phosphate and erythrose 4-phosphate, which are the precursor molecules for the biosynthesis of nucleotides and aromatic amino acids, respectively (REF). These metabolites provide a continuous flux through the pentose phosphate pathway. The conversion of ribose-5-phosphate to 5-phospho-ribosyl-a-1-pyrophosphate (PPRP) and the catalysis of the latter by phosphoribosyl pyrophosphate amidotransferase (PPAT) to form phosphoribosylamine (5PRE) is a rate-limiting step in purine biosynthesis. Methyltetrahydrofolate dehydrogenase 2 (MTHFD2) provides a carbon unit for purine synthesis. Both MTHDF2 and PPAT are directly regulated by NRF 2. Keap1 knockout showed an increase in purine metabolites such as ATP, AMP and inosine monophosphate (IMP), while these were downregulated in Nfe2l2 knockout counterparts. [205, 206, 211]

7.5 Lipid metabolism

Lipid metabolism mediated by Nrf2 is cell type and context dependent. It regulates the synthesis of fatty acid oxidation, triglycerides, and lipid transport. [206, 208, 214] CKO mice have reduced liver triglycerides and free fatty acids, while they have increased phospholipids and long-chain free fatty acids (FFA) in the oesophagus. [206] CHIP -Seq analyses have shown that genes encoding several key lipid metabolism enzymes, including acyl-CoA synthetase short-chain family member 2 (ACSS2), elongation of very long-chain fatty acids protein 7 (ELOVL7), acyl-CoA thioesterase 7 (ACOT7), acyl-coenzyme A dehydrogenase family member 10 (ACAD10), fatty acid desaturase 1 (FADS1) and acyl-coenzyme A dehydrogenase family member 12 (ACAD12) are activated by Nrf2. [206] In addition, Nrf2 also activates CD36, the transporter/receptor for lipid uptake in various cells, to regulate lipid metabolism [215]. Cancer cells are often more dependent on lipid metabolism. [216] Increased dependence on lipid metabolism is a characteristic feature of pancreatic malignancies [216,217,218] In a hypoxic environment, they rely on the import of fatty acids. However, in normoxic cells, oncogenic KRAS transformation leads to a shift to fatty acid import. [219] KRAS modulates lipid metabolism by downregulating a free fatty acid storing triglyceride, hormone sensitive lipase (HSL) and increasing the protein levels of the lipid droplet protein PLIN-2, which helps in lipid storage and used for oxidative metabolism [219,220]

Lipid metabolism in pancreatic cancer is also dependent on the cancer subtype [221,222]. The levels of low-density lipids supress the binding of Sterol regulatory element-binding protein 1 (SERBP1) to TGFB1 promoter which results in an increased TGF1 signalling which leads to a more aggressive tumour. [223,224,225,226]

7.6 Amino acids metabolism

Because they have less access to nutrients and oxygen, pancreatic cancer cells rearrange their amino acid metabolism to keep up with the rising demand. As a result, amino acid transporters that promote the development and multiplication of cancer cells, such as the L-type amino-acid transporter 1 (LAT1, SLC7A5) and SLC6A14, are substantially elevated in PDAC tumors. [227,228] Glutamine, the most prevalent amino acid in blood plasma, is an essential source of nitrogen and carbon for PDAC cells, as it is in many other malignancies.

[229,230] Glutamate dehydrogenase (GLUD1) in a healthy pancreas transforms glutamate into α-ketoglutarate, which is then used in the TCA cycle. The aspartate aminotransferase 1 (aspartate aminotransferase 1), glutamic-oxaloacetic transaminase 1 (GOT1), malate dehydrogenase 1 (MDH1), and numerous other components of the malate-aspartate shuttle are upregulated in response to KRAS, which alters glutamine consumption and encourages PDAC development.[229] PDAC cells rewire a non-canonical KRAS-mediated metabolic pathway in which another isoform, GOT2, in the mitochondria converts glutamine into aspartate. Aspartate is transferred to the cytoplasm where it is processed by GOT1 into oxaloacetate, malate, and finally pyruvate. [231,232] This maintains the cell's redox equilibrium and raises the NADPH/NADP+ ratio [233,234]. It's interesting to note that PDAC cells upregulate GOT1 to regulate reactive oxygen species (ROS) levels and support cancer cell survival when exposed to an acidic microenvironment [235]. The glutathione needed for redox equilibrium is maintained at relatively low levels by this PDAC-specific metabolic pathway [235]. Additionally, glutamine is used by pancreatic cancer cells to synthesize glutathione and produce NADPH for anabolic processes and redox equilibrium. [236]. It is also noteworthy that pancreatic cancer stem cells (CSCs) exhibit enhanced expression of the tetraspanin CD9, which boosts the glutamine transporter ASCT2's plasma membrane localization and promotes glutamine absorption [237].

In addition to glutamine, the metabolism of other amino acids is also modified in PDAC. According to several studies, branched-chain amino acids (BCAA; leucine, isoleucine, and valine) produced into the plasma because of tissue breakdown are metabolized by PDAC cells at an early stage of tumor formation [234,238,239]. Accordingly, PDAC cell proliferation, survival, and tumor development under nutrient/oxygen-deficient circumstances are promoted by collagen-derived proline and cysteine [240,241]. Finally, it was shown that arginase 2 (ARG2), a mitochondrial gene that catalyses the hydrolysis of arginine to ornithine and urea, was upregulated in PDAC tumors caused by obesity, reprogramming the urea cycle pathway to fuel mitochondrial metabolism [242,243].

8. Arginine metabolism

Diet, endogenous synthesis, and protein turnover provide the body with free arginine in the tissues. Although many different cell types can synthesize arginine from citrulline [244,245], a significant portion of endogenous synthesis is carried out by a partnership between the epithelial cells of the small intestine and proximal tubule cells of the kidney (the "intestinal-renal axis" of arginine synthesis") [246,247,248,249]. The degree of endogenous synthesis is so high in healthy people that arginine is normally not a necessary dietary amino acid. However, quantities of endogenous synthesis may not be sufficient to fulfil metabolic demands in situations of catabolic stress (such as inflammation or infection) or disorders involving kidney or small intestine failure. As a result, arginine is categorized as a conditionally essential or semi-essential amino acid. [250,251,252]

Citrulline serves as a precursor for the production of arginine, and endogenous arginine can be produced in the kidneys and liver thanks to the crucial role of ASS1.[253] However, there is no net production of arginine in the liver because there is an abundance of arginase (ARG), which can immediately catalyse arginine to produce urea and ornithine, which lowers blood ammonia, through a metabolic pathway called the ornithine cycle. The primary means of arginine transport from the extracellular environment is through cationic amino acid transporter (CAT) proteins. [254-259] The four different types of enzymes that break down arginine are arginine decarboxylase (ADC), nitric oxide synthetase (NOS), arginine: glycine amidinotransferase (AGAT) and arginase ARG1/2. The primary by-products of the degradation of arginine are ornithine, urea, NO, glutamate, polyamines, proline and creatine. ARG currently contains two isoforms: ARG 1 and 2. While the latter is found in the mitochondria and is very weakly expressed in extrahepatic cells, the former is found in the cytoplasm and is mostly expressed in liver cells, where it participates in the urea cycle. Neuronal NOS (nNOS), inducible NOS (iNOS), and endothelial NOS (eNOS) are the three isoforms of NOS, which catalyze the conversion of arginine into citrulline, create NO, and have distinct functions in various organs. [260, 261]

Notably, arginine feeds the metabolic pathways leading to the synthesis of polyamine, creatine, and NO: compounds that are critical for the development and progression of tumors. (Figure14) [16-18] As for arginine production, the primary enzyme is argininosuccinate synthetase 1 (ASS1). Certain cancer cell types, including human melanoma

and hepatocellular carcinoma (HCC) cells, can be susceptible to arginine deprivation therapy, such as arginine deiminase (ADI). [262]

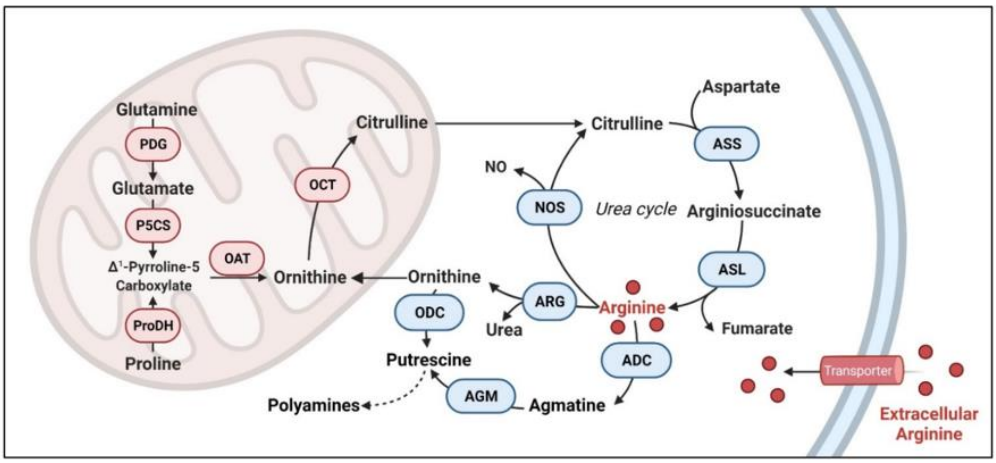

Figure14. Arginine Metabolism. Arginine can either be directly delivered into healthy cells or produced from citrulline and aspartate. Citrulline can be produced in the mitochondrion from proline, glutamine, and glutamate. Nitric oxide (NO), urea, and agmatine can all be produced from arginine. Putrescine and other polyamines are produced from agmatine or from ornithine. ASL: argininosuccinate lyase, ASS: argininosuccinate synthetase, AGM: agmatinase, ADC: arginine decarboxylase, ODC: ornithine decarboxylase, ARG: arginase, NOS: nitric oxide synthase, OCT: ornithine carbamoyl transferase, OAT: ornithine aminotransferase, PDG: phosphate-dependent glutaminase, P5CS: pyrroline-5-carboxylate synthase, ProDH: proline dehydrogenase. [263]

Moreover, arginine can feed the synthesis of creatine through GATM. From creatine via CKB, the cells produce phosphocreatine which constitutes an energy buffer for the cells, useful for proliferation.

8.1 Arginine Metabolism and cancer reprograming

Studies on arginine-deprivation in cancer cells have contributed significantly to our current understanding of the effects of arginine on cancer metabolism. Depending on the types of cells examined, the responses may often be divided into two groups. As a result of epigenetic remodelling, arginine deprivation in breast and prostate cancer cells results in the global transcriptional suppression of metabolic genes including those involved in oxidative phosphorylation (OXPHOS) and mitochondrial functions, glycolysis, purine and pyrimidine synthesis, and DNA repair genes. [264,265,266,267] As evidenced by OCR (oxygen

consumption rate) and membrane potential, removal of arginine fragments mitochondria and impairs mitochondrial functioning. The overall decrease of TCA cycle metabolites such ??KG, malate, fumarate, and succinate is shown by metabolomics research, which is indicative of the repressed transcription of genes involved in mitochondrial activities. [266,269]

The activation of ASNS (asparagine synthetase), which depletes aspartate and reduces the aspartate-malate shuttle and TCA, was hypothesized to be one cause of these depletions, at least in breast cancer cells.[270,271] The transcriptional inhibition of the nuclear-encoded OXPHOS genes, which occurs as a result of the disruption of the OXPHOS process caused by metabolite depletion, produces a large quantity of ROS, which causes DNA damage and ultimately results in cell death. Indeed, functional mitochondrial deletion reduced DNA damage and cell death in these cells [266]. The morphological alterations from hyperfusion at an early stage to fragmentation at a late state provide additional support for the hypothesis that arginine deficiency impairs mitochondria. This transition is brought on by the decreased expression of Mfn2 (mitofusin2), which is regulated by p38 activation and KAP-1 phosphorylation brought on by arginine deprivation. [269,272]

The glycolysis pathway is downregulated in ASS1-low melanoma and sarcoma cells, although glutamine anaplerosis and serine synthesis are enhanced to support the TCA cycle. [273, 274] According to the scientists, one reason cancer cells might adapt to a stressful environment and ultimately develop resistance to therapy is because the Warburg effect is inhibited. C-myc activation following arginine deprivation is a trait of these cells, which is not always the case in the prostate and breast malignancies described above and may account for the variations in their responses to arginine deprivation. [275,276, 277]

Cells are known to become glutamine-dependent when c-myc increases glutaminase regulation. As a result, these cancers are synthetically fatal when treated with glutaminase inhibitor. In either of the circumstances mentioned above, arginine deprivation targets mitochondria, and arginine is a key regulator of mitochondrial functions in cancer metabolism.[277]

8.2 The Role of Arginine Metabolism in PDAC Cells

Panc-1 cells lacking ASS1 experienced a dose- and time-dependent reduction in proliferation after receiving Arginine Deiminase therapy (ADI). [278] As previously discussed, arginine activates mTORC1, which causes the release of important amino acids from lysosomes, and controls PI3K/AKT and NF-kB signaling pathways, which promote proliferation of PDAC cells. [278,279,280] Asparagine synthetase (ASNS), which diverts aspartate from de novo nucleotide production and causes nucleotide insufficiency and cell cycle arrest in the S phase, may also be greatly upregulated by arginine deprivation.[281] Additionally, the formation of intracellular NO, which can control cancer cell proliferation and development, can only come from the catabolism of arginine.[281]

For instance, a low level of NO might promote the development of tumors, whereas a high level of NO causes cytotoxicity that is linked to the generation of DNA and apoptosis. [283] Furthermore, it was demonstrated that, in contrast to cancer cells with mutant p53, cancer cells with wild type p53 were more susceptible to cytotoxicity that was mediated by NO. [284]

Autophagy has been found to be activated by amino acid deficiency. In pancreatic cancer cells, it has been shown that arginine deprivation induced by a pegylated, cobalt-substituted, human recombinant Arginase I, (HuArgI (co)- PEG5000) induced arginine deprivation causes autophagy-dependent cell death rather than caspase-dependent apoptosis, which causes G0/G1 cell cycle arrest in the surviving cell fraction. Excess L-citrulline was added to PDAC Capan-1cells that express ASS1, and these cells were rescued, demonstrating partial arginine auxotrophy. However, other studies on cancer cells, including acute leukemia, discovered that arginine deficiency causes apoptotic cell death. Additionally, there is ongoing debate regarding how autophagy affects cell death caused by arginine deficiency. [284,285]

A number of studies conducted recently have shown how arginine contributes to the spread of cancer. According to Wang et al., arginine deprivation caused by ADI prevents pancreatic cancer cells from metastasizing via affecting the markers of the epithelial-mesenchymal transition. [279,281] Arginine is thought to encourage the invasion of pancreatic cancer cells via NO, including RhoA, PI3K/AKT, and ERK-FOXO3 signalling pathways. This because arginine is the sole precursor available to produce NO. [284] The link between NO and VEGF, which is elevated by NO through the activation of HIF-1a and encourages angiogenesis in a variety of

human malignancies, has been the subject of several research. [56] Regarding the NO synthetase, eNOS overexpression is linked to vascularization and neovascularization of pancreatic cancer and is seen in the vasculature and peritumoral tissue of PDAC. [284] In comparison to either medication used alone, NOS inhibition and VEGF receptor 2 blockage can greatly increase the anti-vascular therapeutic effectiveness. This results in a considerable suppression of pancreatic tumor development. [285] According to the findings of these research, arginine metabolism plays a significant role in the growth of PDAC, and medicines that specifically target this process may be an effective way to treat pancreatic cancer.

AIM of the PhD work

Previous work from our laboratory showed that an increase of oxidative stress (for instance by photoactivated porphyrin TMPyP4), results in the upregulation of KRAS and Nrf2. These results are in keeping with literature. We demonstrated by western blots band luciferase assays that the ectopic expression of $KRAS^{G12D}$, particularly, in the presence of high levels of ROS, stimulates Nrf2. This suggests that ROS, KRAS and NRF2 form a molecular axis which controls the redox homeostasis in cancer cells. In fact, when oxidative stress increases in the cells, KRAS stimulates the expression of Nrf2, the master regulator of the redox homeostasis, that in turn activates the expression of detoxification genes: The result is that ROS are brought down to levels compatible with cell proliferation. The transcriptional activation of the detoxification genes is mediated by a cis-acting element called the antioxidant responsive element (ARE), which is recognized by Nrf2. We also found that ROS-KRAS-Nrf2 axis also regulates the function of the NF-kB/Snail/RKIP circuit and hence apoptotic and survival pathways. [173] As explained in the introduction, despite the KRAS dependence of PDAC, the inhibition of the KRAS gene or protein as well as the inhibition of downstream pathways showed a limited therapeutic efficacy. Therefore, alternative strategies are required.

My PhD work focused on the role of the ROS-$KRAS^{G12D}$-Nrf2 axis in the pancreatic cancer cells. In particular, I have been involved in:

i) Studying the mechanism of expression of KRAS and the dependence of transcription and cell proliferation from the transcription factor hnRNP A1: This work has been carried out in collaboration with a research group from the University of Bordeaux, specialized in NMR experiments (Prof. Salgado group). For this part of the project, my contribution was in production of recombinant UP1 protein, understanding the CD and the UV melting profiles and performed the biological replicates for the interaction of the two G4 structures of KRAS with hnRNP A1 and UP1 using EMSA along with their interaction with different proteins of the pre-initiation complex using pull down assay. Finally, I demonstrated the metabolic and survival assay for the different hnRNP A1 knock out cells.

ii) How to inhibit KRAS in pancreatic cancer cells with small molecules. We used cationic porphyrins conjugated to an alkyl chain. We examined the capacity of these small molecules to internalize in pancreatic cancer cells and suppress KRAS. We tested two ways of delivery

the porphyrins: as free molecules or engrafted on the surface of 1-palmitoyl-2-oleoyl-sn-glycero-3-phosphocholine (POPC) liposomes. Also, this study has been carried out in collaboration with a group of Odense (DK) (prof. Stefan Vogel) and Moscow (Prof. Andrey Andrey Shchekotikhin) Universities. The first, develop a technique for preparing POPC liposomes, the second synthesized the alkyl porphyrins. For this, I contributed to experimental investigation of alkyl porphyrins activated ferroptosis and apoptosis.

iii) The third project addressed by using transcriptomic and metabolomic approaches the impact of the KRAS-Nrf2 axis in the control of the redox homeostasis and metabolism of PDAC cells. I have dedicated most of my efforts for the development of this part that due to its complexity involved besides myself also other researchers of the laboratory: Dr. Eros Di Giorgio and prof. Luigi E. Xodo. My major contribution has been in this final part of the thesis, where I have been involved in the wet lab investigation of the project, I started with the characterization of the Nrf2(-/-) and Nrf2(-/+) knock out cells. Then I proceeded with the proteomic and transcriptomic studies to understand the role of Nrf2 in deep metabolic reprogramming and in alternative pathways for energy supply. Furthermore, demonstrating the role of arginine metabolism and the role of amino acids with respect to glucose and studying the effect of combined therapies aimed towards KRAS-Nrf2 axis.

The results of the projects regarding the role of hnRNPA1 of KRAS expression and the potency of alkyl porphyrins in downregulating KRAS and arrest cell growth have been published in two peer-reviewed journals (ASC-Omega and I. Photechem Photobiol B), while the work focused on the impact of the KRAS-Nrf2 axis in the control of redox homeostasis and reprogramming the metabolism are under review in Cell Chemical Biology. The text of the paper can be drawn from SSRN.

For a detailed description of the results of the three projects, I have attached the texts of the three papers. In short, the main results can be summarized as follows:

i) The promoter of the oncogene KRAS contains a G4 motif that folds into a stable G4 structure that is in equilibrium between two G4 conformers. This G4 structure is located immediately upstream of the transcription start site (TSS). In this and other work of the lab, we demonstrated that KRAS G4 acts as a platform for the assembly of the transcription initiation complex. HnRNP A1 binds to KRAS G4 in a way that unfolds the structure. This is shown by the decrease in the imino proton peaks of the G4 when hnRNPA1 binds to G4 DNA. The KRAS G4 forms a structure elaborated by NMR and characterised by three G-tetrads. Imino proton analysis indicates that the protein binds to the upper and lower G-tetrads of G4. We also found that the G25T-G4 conformer provides a better platform for hnRNPA1. The data show that after binding to G4, hnRNPA1 unfolds the structure and the G-rich strand hybridises with the complementary C-rich strand, forming a canonical duplex which is bound by other transcription factors. The data suggest that hnRNP A1 may be a good target for repression of KRAS. To prove this, we used CRISPR-Cas9 to delete the hnRNP A1 gene in Panc-1 cells and observed that the expression of KRAS was significantly reduced in the knockout cells. The knockout cells had lower levels of the PI3K-AKT pathway and a lower ability to form colonies than normal Panc-1 cells, suggesting that hnRNP A1 is a good target for the treatment of PDAC.

ii) Since PDAC is addictive to KRAS, many researchers are pursuing the idea of treating PDAC with small compounds that suppress the KRAS gene or protein. Considering that the mRNA of KRAS contains a 5'-UTR region rich in guanine blocks (GG) and adopts G4 RNA structures that can serve as targets for cationic and alkyl porphyrins. We found that these molecules are efficiently internalised into cells due to the alkyl moiety, where they are mainly localised in the cytoplasm. Confocal microscopy data showed that the porphyrins, when delivered as free molecules, partly fuse in the cell membrane, and partly are transported into lysosomes, from where they gradually accumulate in the cytoplasm. When they reach a certain concentration in the cytoplasm, they bind to KRAS G4 RNA. Upon photoactivation, they produce strong oxidants such as ROS and singlet oxygen, which locally degrade the 5'-UTR of KRAS. The expression of the gene is stopped, and the cells die by apoptosis and ferroptosis. Interestingly, we tried to increase the delivery of alkyl porphyrins by grafting them into the surface of POC liposomes. We found that POPC liposomes are internalised by endocytosis. The grafted

porphyrins remained attached to the liposome surface and did not bind to the mRNA. The grafted porphyrins produced ROS upon irradiation without degrading the KRAS mRNA that activates apoptosis.

iii) In the third part of the thesis, we focused on the KRAS -Nrf2 axis. This is because the suppression of KRAS by small molecules also leads to the suppression of the KRAS -Nrf2 axis. So, we wondered what effect the inhibition of the KRAS -Nrf2 axis has on PDAC metabolism. To investigate this important point, we decided to inhibit the KRAS-Nrf2 axis by deleting Nrf2 into Panc-1 cells using CRISPR-Cas9. The clone obtained, called Nrf2(-/-), represents a good model for studying PDAC cells in which the KRASANrf2 axis has been deleted. Inhibiting the KRAS -Nrf2 axis by deleting KRAS was out of the question for us, as the cell cannot survive without the expression of the KRAS oncogene. We performed RNA-seq analysis on normal Panc-1 cells expressing the KRAS -Nrf2 axis and on Nrf2(-/-) Panc-1 cells not expressing the KRAS -Nrf2 axis and found, that 1888 genes were down-regulated and 666 up-regulated in Nrf2(-/-) cells compared to normal Panc-1 cells, assuming a threshold log2 FC ≥1, $P < 0.05$. The analysis clearly shows that Panc-1 cells are glycolytic and use glucose to produce ATP and biomass when KRAS -Nrf2 is active. PPP and glutathione cycle are also activated by KRAS -Nrf2. In contrast, if KRAS -Nrf2 is inhibited, the cells switch to aerobic metabolism, which then requires mainly arginine and short-chain fatty acids. Under metabolic stress caused by the loss of the KRAS -Nrf2 axis, the cells thus maintain their malignancy by changing their metabolism and becoming dependent on aerobic metabolism. Arginine becomes the main substrate of Panc-1 cells under metabolic stress. The amino acid is used to synthesise phosphocreatine, i.e., to generate an energy buffer to produce ATP. In addition, arginine is involved in the synthesis of polyamines and nitric oxide, which stimulate mitogenic signalling. The results of our study show that when PDAC is treated with small molecules that inhibit the expression of KRAS, the KRAS-Nrf2 axis is stopped, and the cells undergo a metabolic switch that then makes them dependent on the phosphocreatine and polyamine pathways. Efficient strategies for the treatment of PDAC.

RESULTS

Section 1

hnRNPA1/UP1 Unfolds KRAS G-Quadruplexes and Feeds a Regulatory Axis Controlling Gene Expression

Section 2

Photosensitization of pancreatic cancer cells by cationic alkyl-porphyrins in free form or engrafted into POPC liposomes: The relationship between delivery mode and mechanism of cell death.

Section 3

The Suppression of the KRAS G12D -Nrf2 Axis Shifts Arginine into the Phosphocreatine Energy System in Pancreatic Cancer Cells.

Section 4

Targeted Cancer Therapy: KRAS-Specific Treatments for Pancreatic Cancer

Section 1

hnRNPA1/UP1 Unfolds KRAS G-Quadruplexes and Feeds a Regulatory Axis Controlling Gene Expression.

ACS OMEGA

http://pubs.acs.org/journal/acsodf

Article

hnRNPA1/UP1 Unfolds *KRAS* G-Quadruplexes and Feeds a Regulatory Axis Controlling Gene Expression

Annalisa Ferino, Julien Marquevielle, Himanshi Choudhary, Giorgio Cinque, Coralie Robert, Anne Bourdoncle, Raffaella Picco, Jean-Louis Mergny, Gilmar F. Salgado,* and Luigi E. Xodo*

Cite This: *ACS Omega* 2021, 6, 34092−34106

Read Online

ACCESS | Metrics & More | Article Recommendations | Supporting Information

ABSTRACT: Recent studies have proven that the genetic landscape of pancreatic cancer is dominated by the *KRAS* oncogene. Its transcription is controlled by a G-rich motif (called 32R) located immediately upstream of the TSS. 32R may fold into a G-quadruplex (G4) in equilibrium between two G4 conformers: G9T (T_M = 61.2 °C) and G25T (T_M = 54.7 °C). We found that both G4s bind to hnRNPA1 and its proteolytic fragment UP1, promoting several contacts with the RRM protein domains. 1D NMR analysis of DNA imino protons shows that, upon binding to UP1, G25T is readily unfolded at both 5′ and 3′ tetrads, while G9T is only partially unfolded. The impact of hnRNPA1 on *KRAS* expression was determined by comparing Panc-1 cells with two Panc-1 knockout cell lines in which hnRNPA1 was deleted by the CRISPR/Cas9 technology. The results showed that the expression of *KRAS* is inhibited in the knockout cell lines, indicating that hnRNPA1 is essential for the transcription of *KRAS*. In addition, the knockout cell lines, compared to normal Panc-1 cells, show a dramatic decrease in cell growth and capacity of colony formation. Pull-down and Western blot experiments indicate that conformer G25T is a better platform than conformer G9T for the assembly of the transcription preinitiation complex with PARP1, Ku70, MAZ, and hnRNPA1. Together, our data prove that hnRNPA1, being a key transcription factor for the activation of *KRAS*, can be a new therapeutic target for the rational design of anticancer strategies.

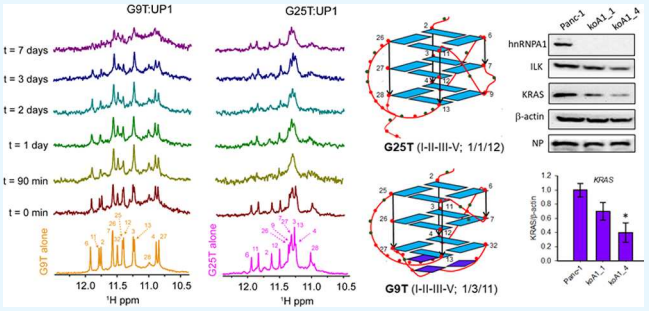

INTRODUCTION

The transcription of human *Kirsten ras* gene (*KRAS*) is regulated by a G-rich element (called 32R) located between −144 and −112 from the transcription start site (TSS).[1,2] Sequence 32R forms a stable G-quadruplex (G4) structure recognized by nuclear proteins including PARP-1, Ku70, and hnRNPA1. These proteins have been identified by biotin−streptavidin pull-down assays coupled to mass spectrometry.[3] In addition, a DNA-binding protein tool (Matinspector, Genomatix) predicted that the Myc-associated zinc-finger protein (MAZ) should also recognize 32R. This was indeed confirmed by EMSA and chromatin immunoprecipitation.[4,5] Further studies suggested that the 32R G4 should act as a platform for the recruitment of TFs to the promoter to form the transcription preinitiation complex.[6] Indeed, by silencing MAZ or PARP-1 with specific siRNA, we observed a downregulation of *KRAS* transcription.[5,6] Within this framework, a question still remains unanswered: what is the role of hnRNPA1 in the *KRAS* promoter?

HnRNPA1 is a multifunctional protein regulating several aspects of mRNA metabolism, nuclear export,[7−12] translation,[13,14] and telomerase activity.[15] Protein hnRNPA1 is composed of 322 amino acids, and its *N*-terminal contains two RNA recognition motif (RRM) domains followed by a highly flexible glycine-rich (Gly-rich) *C*-terminal region, which acts as an RNA-binding domain and as a nuclear targeting sequence.[16] Its *N*-terminal portion of 195 amino acids containing the RRM domains, called UP1, has been extensively studied by X-ray crystallography and NMR spectroscopy.[17] Some high-resolution crystal structures of the two tandem RRMs of hnRNPA1 have been obtained with the free protein or with the protein bound to telomeric DNA repeats at a resolution of 1 Å.[18−20] In addition to RNA, hnRNPA1 has been found to be associated with promoter sequences and to participate in the regulation of transcriptional events.[7−9] The association of hnRNPA1 with the promoters of thymidine kinase (TK)[7] and gamma-fibrinogen[8] was found to repress transcription, while hnRNPA1 acts as an activator in the promoters of the ApoE[9] and interferon-inducible RNA-dependent protein kinase genes.[21]

Received: October 5, 2021
Accepted: November 12, 2021
Published: November 30, 2021

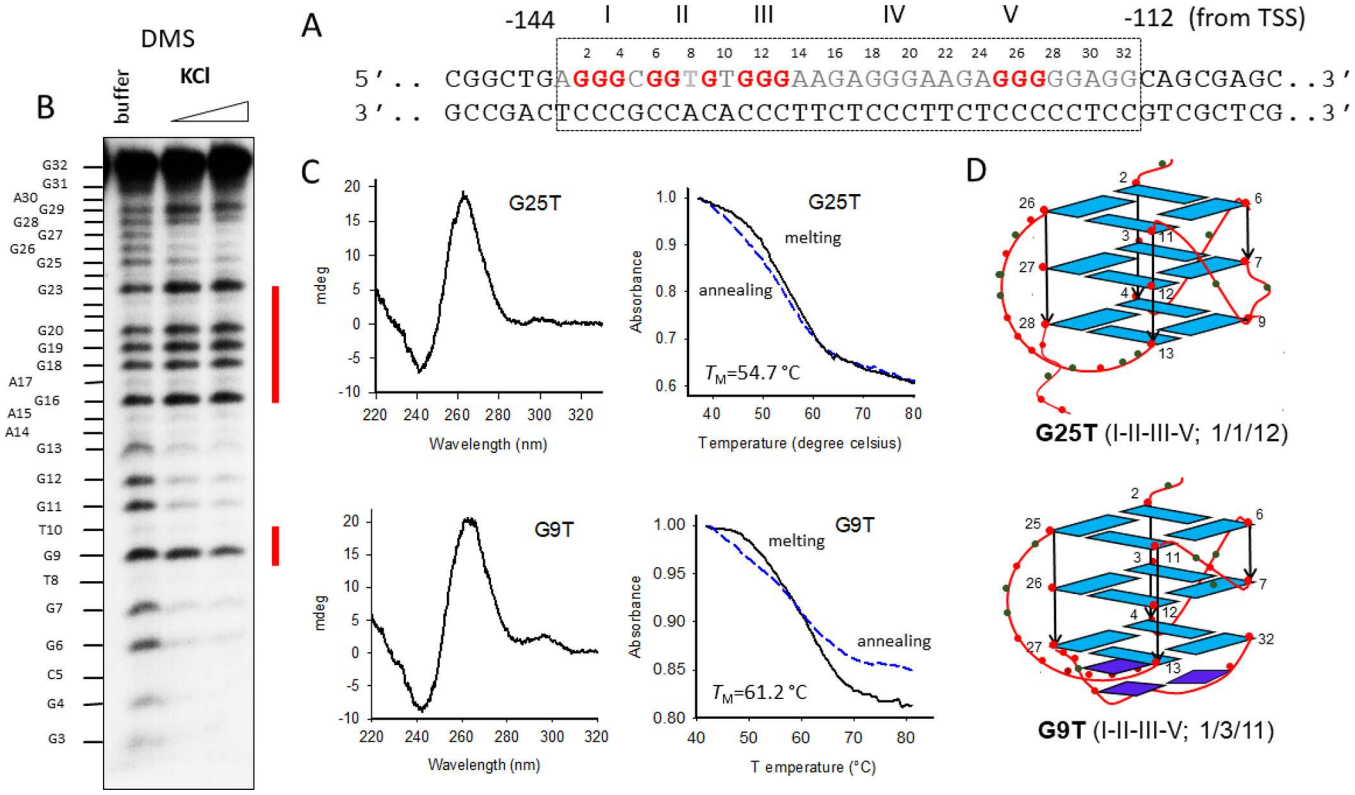

Figure 1. (A, B) 32R sequence and its typical DMS footprinting in 0, 50, and 100 mM KCl, (C) CD and UV-melting profiles in 50 mM Na-cacodylate (pH 7.4) and 100 mM KCl of 3 μM G25T and G9T. Guanines in red form the G-tetrads according to DMS-footprinting; (D) NMR structure of the two G4 conformers formed by 32R adapted from ref 29 (*Nucleic Acids Res.* **2020**, *48*, 9336−9345), Oxford University Press.

Some authors have reported that hnRNPA1 is able to recognize and unfold DNA and RNA G4 structures. The first paper reporting this feature was published in 2002 by Fukuda *et al.*,[22] who demonstrated that the G4 structures from the minisatellite repeat and telomeric DNA are unfolded by UP1. Some years later, our laboratory discovered that the G4 structure formed by 32R is recognized and unfolded by hnRNPA1 and UP1.[23] Moreover, single molecule FRET experiments showed that the telomeric DNA overhang is partially unfolded by hnRNPA1.[24] It has been reported that the RGG-box of hnRNPA1 recognizes telomeric G4 DNA and enhances the G4 unfolding of UP1.[25] The same authors also reported that the glycine−arginine-rich domain (RGG-box) of hnRNPA1 specifically recognizes TERRA G4 RNA but not single-stranded RNA.[26] All these studies suggest that hnRNPA1 is a nuclear protein associated with unusual DNA and RNA G4 structures, for which the association model and role are still unknown.

A recent NMR study from our laboratories showed that 32R folds into two co-existing conformers, called G25T and G9T, characterized by a different structure. Here, by EMSA and NMR, we explored the interaction between UP1 and the two *KRAS* G4 conformers. In addition, we tried to define the role of hnRNPA1 in the *KRAS* promoter. Previous work showed that hnRNPA1 is able to interact with the G4 formed by 32R[23,27] and that *KRAS* is controlled by the *KRAS*-ILK-hnRNPA1 regulatory loop.[28] To further address this issue, we employed CRISPR/Cas9 technology to obtain hnRNPA1 knockouts of Panc-1 cells (koA1). We compared the expression of the ras genes in the normal and knockout cells and the capacity of these cells to survive and grow. We concluded that hnRNPA1 is an essential TF for the transcription of *KRAS*. Our study opens a new therapeutic window for designing anticancer drugs to treat pancreatic ductal adenocarcinomas (PDACs).

RESULTS AND DISCUSSION

The *KRAS* 32R Sequence Forms Two G4 Structures. Although *KRAS* holds two G4 motifs (32R and G4-mid), the vast majority of the studies reported in the literature focused on 32R, as this G-rich motif overlaps with a nuclease hypersensitive site and is an important platform for the recruitment of TFs.[3] The first evidence that 32R spontaneously folds into a G4 structure was observed by running primer-extension experiments using two plasmids as DNA templates: one bearing the human 32R sequence and the other bearing its murine homolog.[2,3] The finding that DNA polymerase I paused at the 3′-end of both G-rich motifs suggested the formation of a folded G4 structure by both templates. To determine the guanines of the G4 motif involved in the formation of the G-tetrad core, DMS footprinting experiments were carried out.[2,3] In Figure 1A,B, we report a typical cleavage pattern of the human 32R motif. The expected folding involving G-runs I, III, IV, and V was not observed. The footprinting showed that G-run IV (G18-G19-G20) is strongly reactive to DMS, while guanines G6 and G7 are instead protected and G9 partially protected. This indicates that G-run II (GGTG) takes part in the formation of the G-tetrad core, while G-run IV does not. Combining footprinting and CD data for the critical 32R motif of the human *KRAS* promoter, we proposed a tri-stacked G-tetrad parallel G4 structure with two

https://doi.org/10.1021/acsomega.1c05538
ACS Omega 2021, 6, 34092−34106

1-nt and one 11-nt loops and a T-bulge in one strand (1/1/11 topology)[3] (Figure S1).

Recently, we carried out an NMR study to gain insight into the folding of 32R.[29] The results indicated that 32R assumes two major G4 conformations, which are reported in Figure 1C,D (Table 1). The one called G25T has a structure similar

Table 1. Oligonucleotides Used in this Study[a]

Name	*Sequence 5' → 3'*
32R	AGGGCGGTGTGGGAAGAGGGAAGAGGGGGAGG
92[(a)]	AGGGC^{ox}GGTGTGGGAAGAGGGAAGAGGGGGAGG
96[(a)]	AGGGCGGTGTGGGAA^{ox}GA^{ox}GGGAAGAGGGGGAGG
G9T	AGGGCGGTTTGGGAAGAGGGAAGAGGGGGAGG
G25T	AGGGCGGTGTGGGAAGAGGGAAGATGGGGAGG
32Rmut	AGTGCGTTTTGTGAAGAGGGAAGAGTTGGAGG
b-32R	Biotin -TTTTTAGGGCGGTGTGGGAAGAGGGAAGAGGGGGAGG
b-G9T	Biotin -TTTTTAGGGCGGTTTGGGAAGAGGGAAGAGGGGGAGG
b-G25T	Biotin -TTTTTAGGGCGGTGTGGGAAGAGGGAAGATGGGGAGG
Cy5-32R	Cy5.5 -TTTTTAGGGCGGTGTGGGAAGAGGGAAGAGGGGGAGG
Cy5-G9T	Cy5.5 -TTTTTAGGGCGGTTTGGGAAGAGGGAAGAGGGGGAGG
Cy5-G25T	Cy5.5 -TTTTTAGGGCGGTGTGGGAAGAGGGAAGATGGGGAGG

[a]^{ox}G = 8-oxoguanine; b = biotin; red T = G/T substitution in G9T and G25T compared to 32R.

to that proposed for 32R on the basis of CD and DMS footprinting: a tri-stacked G-tetrad G4 with a T-bulge in one strand, two 1-nt, a 12-nt loop, and all guanines in *anti*-conformation. G25T (T_M = 54.7 °C) is in equilibrium with G9T (T_M = 61.2 °C), which exhibits a structure characterized by a fold-back guanine in *syn* conformation (G32) and a triad (G29, A30, and G31) capping the 3′-end. In addition, in previous studies,[30,31] we observed by primer extension experiments that G-runs I, II, III, and IV may fold into an alternative G4 with a 1/1/4 topology in the presence of a G4-stabilizing phthalocyanine (DIGP). However, the fact that, in the absence of DIGP, Taq polymerase paused only at G32 clearly suggests that 32R folds spontaneously into the G9T/G25T G4 conformers, which can be considered the major G4 structures of sequence 32R.

The Two G4 Structures of *KRAS* Interact with hnRNPA1 and UP1. In 2008, we carried out pull-down and mass spectrometry experiments and found that the critical 32R G4 motif is recognized by several nuclear proteins including PARP-1, Ku70, and hnRNPA1.[3] Later on, we discovered that MAZ also binds to 32R.[4,5,32] As stated above, in this study, we focused on the role played by hnRNPA1 in the *KRAS* promoter. First, we investigated by EMSA if both 32R G4 conformers are recognized by hnRNPA1/UP1. Figure 2A shows that G9T and G25T with hnRNPA1 form two DNA−protein complexes, c1 and c2, of different electrophoretic mobility. The wild-type 32R sequence forms, in addition to c2, another complex of very low mobility. In contrast, the 32R duplex shows little affinity for hnRNPA1. We also examined the proteolytic fragment of 196 amino acids of hnRNPA1 called unfolding protein 1 (UP1), which maintains both the binding and G4-unfolding capacity of the entire protein.[22] It can be seen that UP1 also forms with the two G4 conformers DNA−protein complexes. The fact that these complexes do not run with sharp bands may be due to the complexity of the interaction involving the disruption of the G4 structures. Considering that the protein upon binding to G4 unfolds the structure, a 32R mutant unable to form a G4 (32Rmut) is also bound by UP1. The structure of the DNA−protein complexes observed by EMSA can be predicted from the crystal of UP1 bound to the telomeric d(TTAGGG)$_2$ oligonucleotide (TR2).[20] TR2 and UP1 form a dimeric complex consisting of two oligonucleotides and two protein molecules. The two TR2 strands are antiparallel to one another and completely unfolded. The complex is stabilized by multiple interactions occurring between the TTAGGG hexamers and the two RRM protein domains. In keeping with the TR2−UP1 crystal,[20] a structural model for the complexes formed by the G4 conformers G25T/G9T and hnRNPA1/UP1 is proposed: a U-shaped complex with (1:1, **c1**) and (1:2, **c2**) stoichiometry.[23,24]

Subsequently, we determined the K_D's of the interaction between the G4 structures and UP1 by isothermal titration calorimetry. Owing to low yields in expressing UP1 and hnRNPA1, titrations were conducted with UP1 in the sample cell and G4 in the injection syringe (reverse titration). Figure 2B shows the binding curves obtained by plotting the area of the peak *versus* the G4/protein molar ratios. The binding curve analysis gave dissociation constants (K_D's) between 0.49 and 1.1 μM and ΔG of complex formation between −8.5 and − 8.9 kcal/mol (Table 2). We also obtained a 1:2 stoichiometry for complex G9T−UP1, in keeping with EMSA. Instead, the binding curves of G25T−UP1 and 32R−UP1 suggested a more complex stoichiometry, >1:2, probably owing to the apparent extra degree of flexibility that these sequences seem to have from NMR spectra.

Interaction between hnRNPA1/UP1 and *KRAS* G4s by NMR. The interaction between G25T/G9T and UP1 was investigated by NMR. We performed titrations with uniformly {^{13}C and ^{15}N} isotopically labeled UP1 followed by the evolution of each protein residue upon the addition of either G9T or G25T by 2D ^{1}H-^{15}N HSQC NMR experiments. The analysis of the chemical shift deviations ($\Delta\delta$/ppm) of the amide group for the most affected amino acids is proportional to the change in the chemical environment caused by the interaction with G4. To better assess the chemical shift differences, we superimposed the spectra before and after each successive G4 addition and depicted the most important $\Delta\delta$ as a function of the residues (Figure 3A−C).

The spectrum of UP1 alone showed peaks that were separated and well resolved as described in the literature.[17] Upon the addition of G4, the UP1 spectrum became more complex and some peaks, especially in a central region around 8.5 ppm for the ^{1}H dimension and around 122.5 ppm for the ^{15}N dimension, faded in intensity, which are typical of peaks undergoing chemical exchange from local unfolding events and dynamics. Although these perturbations are complex to interpret, they were accurately examined to determine the binding with the G4s. Nevertheless, the vast majority of peaks were identifiable up to molar ratios of 1:1. Among the remaining peaks that could be analyzed, some peaks either did not shift or disappeared. While the former are probably not involved in the interaction, the latter ones may play a specific, yet undefined, role. We compared the global chemical shift peak pattern in the HSQC, and we identified unambiguously some residues, such as R7, K45, and R75 (purple arrows), that have relatively important shifts. The same residues are also involved through hydrogen bonding in the binding of UP1 with a telomeric repeat sequence.[33] These residues belong to a nucleic-acid binding region β-sheet platform and a short α-helical turn interdomain that connects both RRM domains. The global shifts, calculated from eq 1 described in the

https://doi.org/10.1021/acsomega.1c05538
ACS Omega 2021, 6, 34092−34106

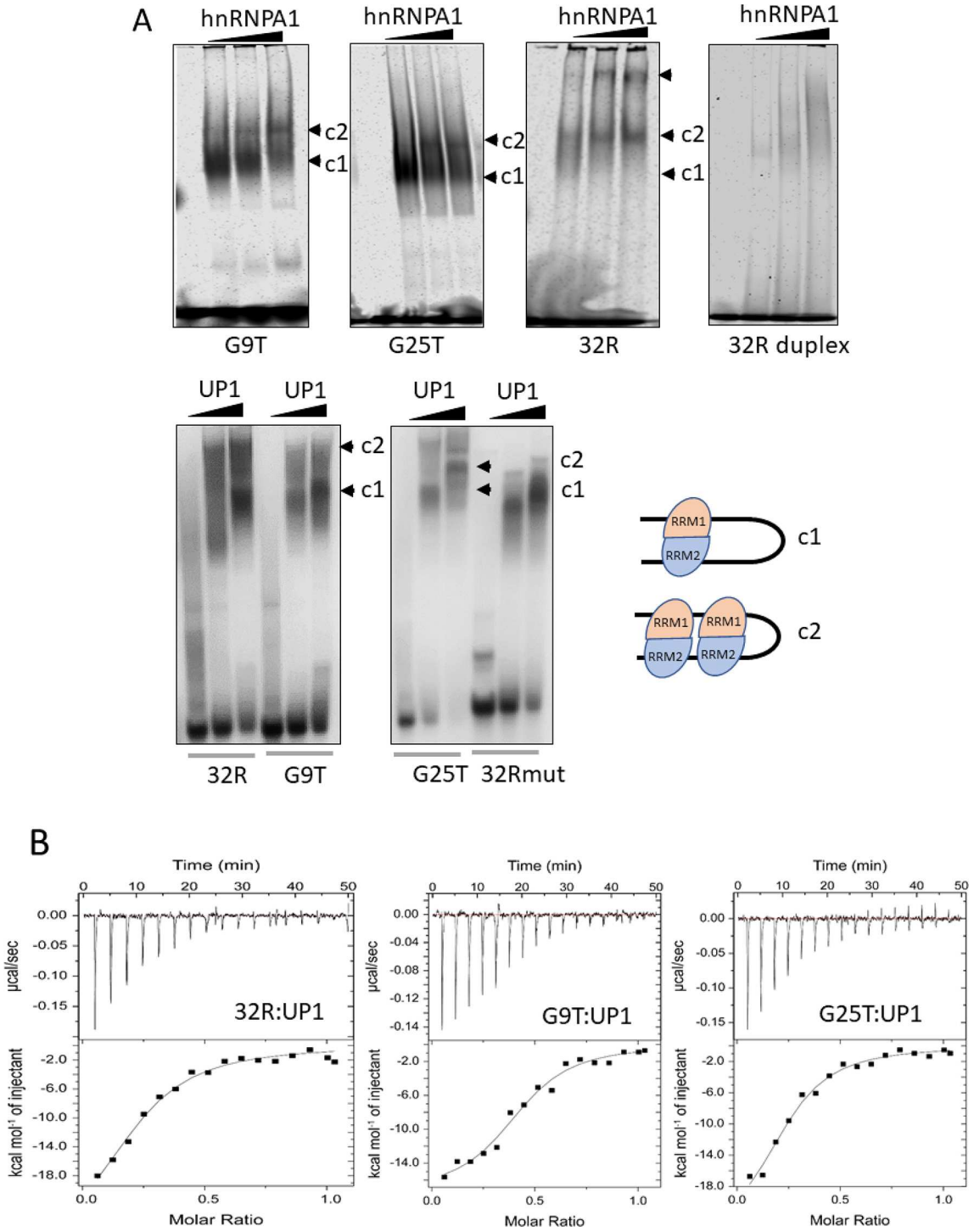

Figure 2. (A) EMSA showing the binding of hnRNPA1 and UP1 to G9T, G25T, and 32R G4 structures. Samples with hnRNPA1, containing 50 nM G4 labeled with Cy5.5 and 0, 2.5, 5, or 10 μg of protein, were incubated in 50 mM Tris−HCl (pH 7.4), 50 mM KCl, 2.5 ng/mL poly[dI-dC], 1 mM EDTA, 50 mM Zn-acetate, 1 mM NaV, 5 mM NaF, 0.01% phosphatase inhibitor, 1 mM DTT, and 8% glycerol for 30 min at 25 °C and then run in 5% PAGE in TBE. EMSA with UP1 were run in a 10% PAGE. 32Rmut is unable to assume a G4 structure (Table 1). Proposed models for the complexes c1 and c2 between hnRNPA1/UP1 and G9T/G25T are shown. (B) Isothermal calorimetry titrations relative to the binding of UP1 to 32R, G9T, and G25T G4 structures at 37 °C in a phosphate buffer and 50 mM KCl (pH 6.6). Binding isotherms from which the thermodynamic parameters of the interaction were obtained (Table 2).

experimental procedures, are plotted in Figure 3C. The plot shows that interactions with the G9T and G25T G4 conformers involve residues in both RRM domains of UP1, with some preference for domain 1. This observation is in agreement with the crystal structure between UP1 and TR2[20] and the results supported by other NMR and ITC experiments available in the literature.[25] The residues with the most intense $\Delta\delta$ have been plotted in red and orange within the UP1 structure (Figure 3C). To probe the effect of UP1 on the folding of both 32R G4 conformers, we performed 1D ^{1}H

https://doi.org/10.1021/acsomega.1c05538
ACS Omega 2021, 6, 34092−34106

Table 2. Thermodynamic Parameter Concerning the Interaction between UP1 and *KRAS* G4s

sequence	K_D (μM)	ΔG (kcal/mol)	ΔH (kcal/mol)	$T\Delta S$ (kcal/mol)
32R	1.1 ± 0.25	−8.5 ± 1.9	−29 ± 4.0	−20.5 ± 5.9
G9T	0.49 ± 0.12	−8.9 ± 2.2	−17 ± 1.0	−8.1 ± 3.2
G25T	0.79 ± 0.18	−8.6 ± 2.0	−25 ± 2.6	−16.4 ± 4.6

NMR experiments as a function of time, looking at the G-quadruplex imino signatures at a 1:1 molar ratio. The NMR spectra were acquired at different time periods, and the samples were kept at 37 °C for a week (Figure 4). Ninety minutes after the addition of UP1, we observed a significant decrease in the intensity of all imino peaks of G25T, suggesting that the sequence bound to UP1 was unfolded, although probably not completely. Instead, the G9T showed a far lower drop in the intensity of the imino peaks. It can be seen that the G9T most affected imino protons, showing broadening and decline in intensity after 90 min incubation with UP1, are those of the guanines corresponding to the 5′-end tetrad (G2, G6, G11, and G25) (Figure 1D). The imino protons of the guanines of the 3′-end tetrad (G4, G32, G13, and G27) instead show an initial broadening, but their intensity slowly decreases within a time scale of hours/days (after 1 day, the G4 should be partially unfolded in rapid refolding equilibrium when not bound to UP1). As for G25T, all imino peaks except those of the central G-tetrad (G3, G7, G12, and G27) disappeared after 90 min exposure to UP1, showing that the end-tetrads are disrupted. The data suggest that, under the experimental conditions of the experiments, UP1 binds to the G4-ends of the structures (Figure S2). It is noteworthy that, gradually over time, some peaks in both G4 conformers reappeared. This process is mostly due to the unfolding of UP1 itself, especially after more than 2 days at 37 °C, confirmed by an HSQC experiment (not shown). Taken together, both the 2D and 1D NMR experiments indicate that G25T in the presence of UP1 is practically unfolded, while conformer G9T is only partially unfolded. In agreement with the data of the TR2−UP1 complex,[20] chemical shift plots reported in Figure 3C show that there are many contacts between G25/G9T and the two RRM domains of the proteins. As the unfolding of both G4s appears to be not complete, we can hypothesize that UP1 without the glycine C-terminus domain (RGG-box) is not as efficient in unfolding as the entire hnRNPA1protein, as observed in the case of human telomeric G-quadruplex Tel22,[25] or that not all the G4 molecules are bound to UP1 at a 1:1 ratio. In fact, at G4/protein ratios of 1:5 and 1:10, FRET experiments suggest that G9T bound to hnRNPA1 or UP1 is unfolded (Figure S3).

HnRNPA1 Is Upregulated in PDAC Cells and Plays a Key Role in the *KRAS* Promoter. Previous studies suggested that hnRNPA1 should be involved in the mechanism regulating *KRAS* transcription.[23,27,28] We then asked what the real impact of hnRNPA1 in *KRAS* expression is. To address this issue, we compared *KRAS* expression in normal and knockout Panc-1 cells, in which hnRNPA1 was deleted by the CRISPR/Cas9 technology (Panc-1 cells are human PDAC cells bearing the *KRAS* mutation G12D). The genome editing of Panc-1 cells was carried out by Synthego (CA), which provided us with a pool of Panc-1 edited cells from which we managed to isolate three clones: koA1_1, koA1_4, and koA1_8, which were fully knocked out for hnRNPA1.

Figure 5A,B reports the guide and target sequences used to obtain the hnRNPA1 knockout cell lines as well as a typical Western blot showing that koA1_1, koA1_4, and koA1_8 do not express hnRNPA1, while they do express β-actin. To confirm the specificity of hnRNPA1 knockout, we detected the level of hnRNPA1 isoforms such as hnRNP M, hnRNP F/H, and hnRNP A2/B1 (Figure 5C). We observed that these isoforms are equally expressed in normal and knockout cells, as expected. Subsequently, we reasoned that if hnRNPA1 is a TF essential for *KRAS*, the knockout cell lines should express a lower level of *KRAS* compared to normal Panc-1 cells. To test this, we measured the levels of *KRAS* in koA1_1 and koA1_4 knockout cells (Figure 6A,B).

Compared to β-actin and nucleoporin, both koA1_1 and koA1_4 express a lower level of *KRAS* protein: residual KRAS is ∼70 and ∼40% in koA1_1 and koA1_4, respectively, compared to normal Panc-1 cells. As a control, we silenced hnRNPA1 in normal Panc-1 cells (residual hnRNPA1 ∼50%) by using a specific siRNA and observed that a transient suppression of hnRNPA1 resulted in the downregulation of *KRAS* by ∼50%, in agreement with the results obtained with koA1_1 and koA1_4 knockout cell lines (Figure 6C,D). Taken together, the data obtained with the knockout and normal Panc-1 cells treated with siRNA clearly suggest that hnRNPA1 is important for *KRAS* expression. We then asked ourselves whether in the knockout cell lines the downregulation of *KRAS* is compensated by an overexpression of *HRAS* and *NRAS*.

The levels of the HRAS and NRAS proteins in koA1_1 and normal Panc-1 cells were measured by specific monoclonal antibodies (Figure 6E). We found that the knockout and normal cells show roughly similar levels of the HRAS and NRAS proteins. In conjunction with literature data, the role played by hnRNPA1 in the mechanism controlling *KRAS* transcription in pancreatic cancer can be represented as in Figure 6F. When *KRAS* transcription is stimulated by oxidative stress, *i.e.*, by treating the cells with H_2O_2[6] or with ROS-generating porphyrins,[34] we observed by ChIP that (i) hnRNPA1, MAZ, and PARP-1 are recruited to the *KRAS* promoter in the region containing the 32R motif[32] and (ii) the level of 8OG increases in the 32R region more than in other genomic G-rich regions lacking G4 motifs.[32] Therefore, we hypothesized that 8OG-modified G4 in the *KRAS* promoter acts as a platform for the recruitment of PARP-1, MAZ, and hnRNPA1 and the assembly of the transcription preinitiation complex. This and previous studies provide evidence that the function of hnRNPA1 is to unfold the G4 and facilitate the reconstitution of the duplex before the formation of the preinitiation complex with the recruited proteins. Chu *et al.*[28] showed that *KRAS* expression depends not only on hnRNPA1 but also on ILK, which forms an axis, ROS-*KRAS*-ILK-hnRNPA1, that maintains the expression of *KRAS* in PDAC high, as illustrated in Figure 6F. The high metabolic rate of PDAC enhances the level of ROS that stimulate TF recruitment and *KRAS* expression via ILK and hnRNPA1. If hnRNPA1 is suppressed, the axis and thus *KRAS* activities fall, together with the *KRAS*-induced metabolic rewiring necessary to produce biomass for cell growth.[35]

KRAS promotes a complex downstream signaling involving the RAF/MEK/ERK and PI3K/PDK1/AKT pathways.[36] Recent findings have shown that the initiation, progression, and maintenance of PDAC heavily depend on the KRAS/PI3K/PDK1/AKT signaling, which stimulates cell growth and survival.[37] By Western blots, we investigated the activity of the

https://doi.org/10.1021/acsomega.1c05538
ACS Omega 2021, 6, 34092−34106

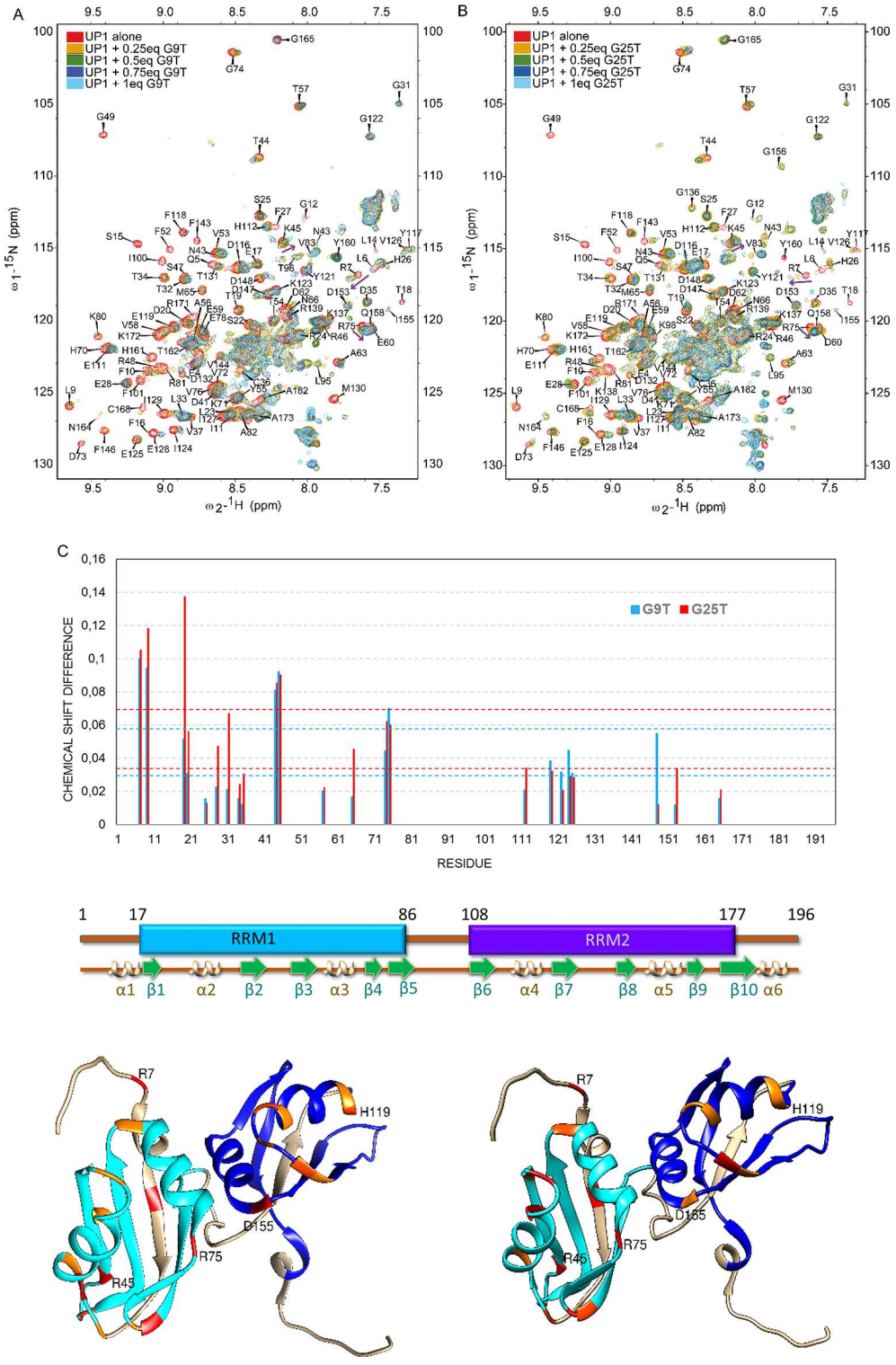

Figure 3. (A, B) Superimposition of ^{15}N-^{1}H NMR HSQC spectra of UP1 showing each residue with NH bond of the backbone, measured alone and with an increasing amount of *KRAS* G9T (*top*) and G25T (*bottom*) G4 structures. (C) Plotted chemical shifts calculated using eq 1. Dotted lines indicate values of one and two sigma above standard deviation (SD). The corresponding residue with a schematic view of the UP1 structure to identify regions implicated in the interaction with the G9T and G25T G4 conformers. Structures of the two UP1 RRM domains with the most shifted residues in the presence of G9T (*left*) or G25T (*right*) are colored in red for strong shifts and in orange for medium shifts, e.g., 2 and 1 SD, respectively.

two pathways in Panc-1 and koA1_1 cell lines (Figure 7A). It can be seen that in koA1_1, which is characterized by a lower expression of *KRAS* (*vide infra*), the MEK/ERK pathway is substantially active as in normal cells, while the more critical PI3K/PDK1/AKT pathway appeared inhibited, as indicated by the low level of phosphorylated AKT. As hnRNPA1 is a critical TF for *KRAS*, the knockout cell lines should exhibit a lower metabolic activity, proliferation, and colony formation

https://doi.org/10.1021/acsomega.1c05538
ACS Omega 2021, 6, 34092−34106

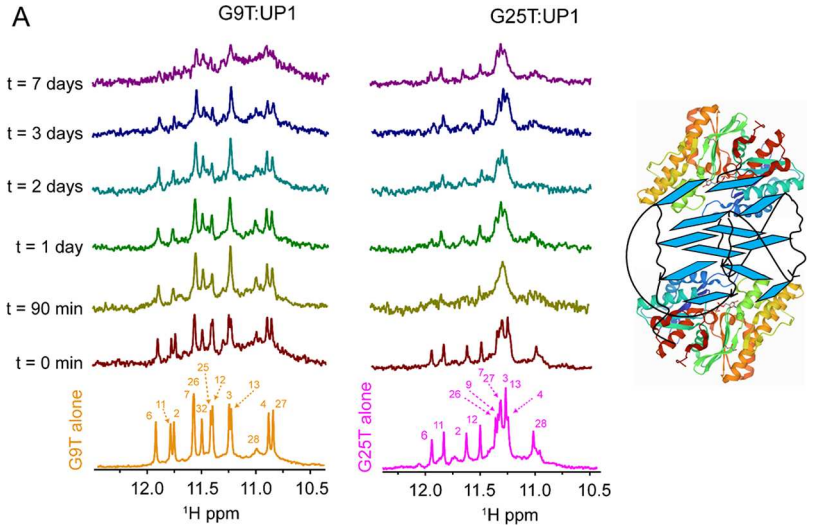

Figure 4. (A) G9T and G25T G4 imino proton region after the addition of 1 equiv of UP1 at different time periods. At a G4/UP1 ratio of 1:1, UP1 binds to the end-tetrads of the G4s and unfolds completely (G25T) or partially (G9T) the structures.

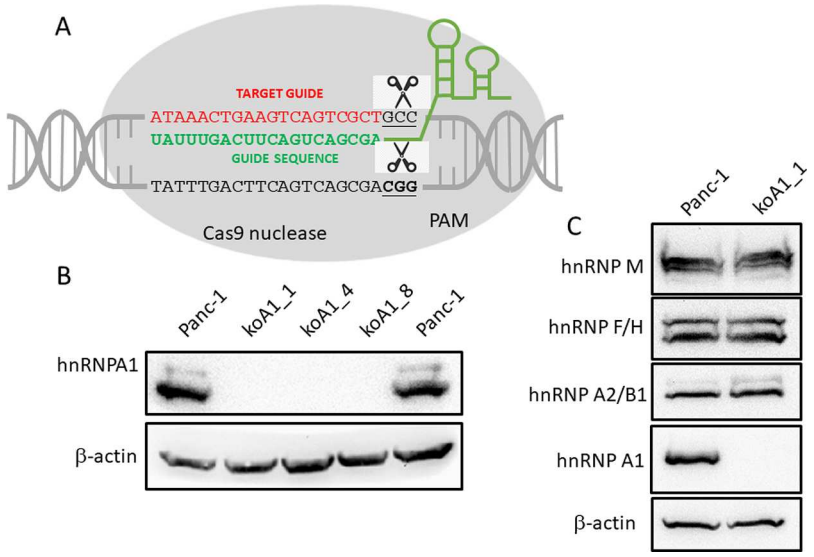

Figure 5. (A) Target and guide sequences used to suppress hnRNPA1 in Panc-1 cells. Two knockout clones for hnRNPA1 were isolated, koA1_1 and koA1_4, which show no expression of hnRNPA1. (B) Western blots showing that koA1_1 and koA1_4, but not the wild-type Panc-1 cells, do not express hnRNPA1, while they do express β-actin. (C) The DNA editing by the CRISPR Cas9 technology does not affect the expression of the hnRNP M, hnRNP F/H, and hnRNP A2/B1 isoforms of hnRNPA1.

compared to normal Panc-1 cells. To test this, we first carried out a resazurin assay that evaluates metabolic activity (resazurin in viable cells is enzymatically reduced to highly fluorescent resorufin). Figure 7B–D shows that three knockout cell lines (including koA1_8) have a lower metabolic activity than normal Panc-1 cells and a significantly lower proliferation over a period of 6 days from cell seeding. Moreover, a clonogenic assay showed that the suppression of hnRNPA1 in Panc-1 cells results in ~60% drop in colony formation. Together, these data provide strong evidence that hnRNPA1 plays a vital role in PDAC, as it stimulates the expression of *KRAS*, the oncogene to which pancreatic cancer cells are addicted.

The 32R G4 Motif Is a Platform for the Formation of the Preinitiation Complex. Previous studies support the notion that the *KRAS* G4 structures may function as a platform for the recruitment of TFs.[6,32] Recently, we reported that upon binding to the 32R G4, PARP-1 undergoes auto-PARylation, becomes negatively charged, and stimulates the recruitment of cationic TFs such as hnRNPA1 and MAZ (pI > 7.4). We therefore asked ourselves whether both G4 conformers of 32R are able to form a multiprotein complex when they are incubated with a nuclear extract from Panc-1 cells. To address this issue, we used a streptavidin–biotin pull-down approach. We synthesized G25T, G9T, and 32R linked to biotin and let them fold into G4 in a buffer containing 100 mM KCl. The biotinylated oligonucleotides in G4 conformation were used as G4 baits in the pull-down experiments (Figure 8A). Each biotinylated G4 was incubated with 80 μg of nuclear extract in the presence of poly[dI-dC] to suppress unspecific binding for 30 min, and the proteins bound to G4 were pulled down with streptavidin-coated magnetic beads. The captured proteins (bound to the beads) were eluted with Laemmli buffer and analyzed by immunoblotting with antibodies specific for MAZ,

https://doi.org/10.1021/acsomega.1c05538
ACS Omega 2021, 6, 34092–34106

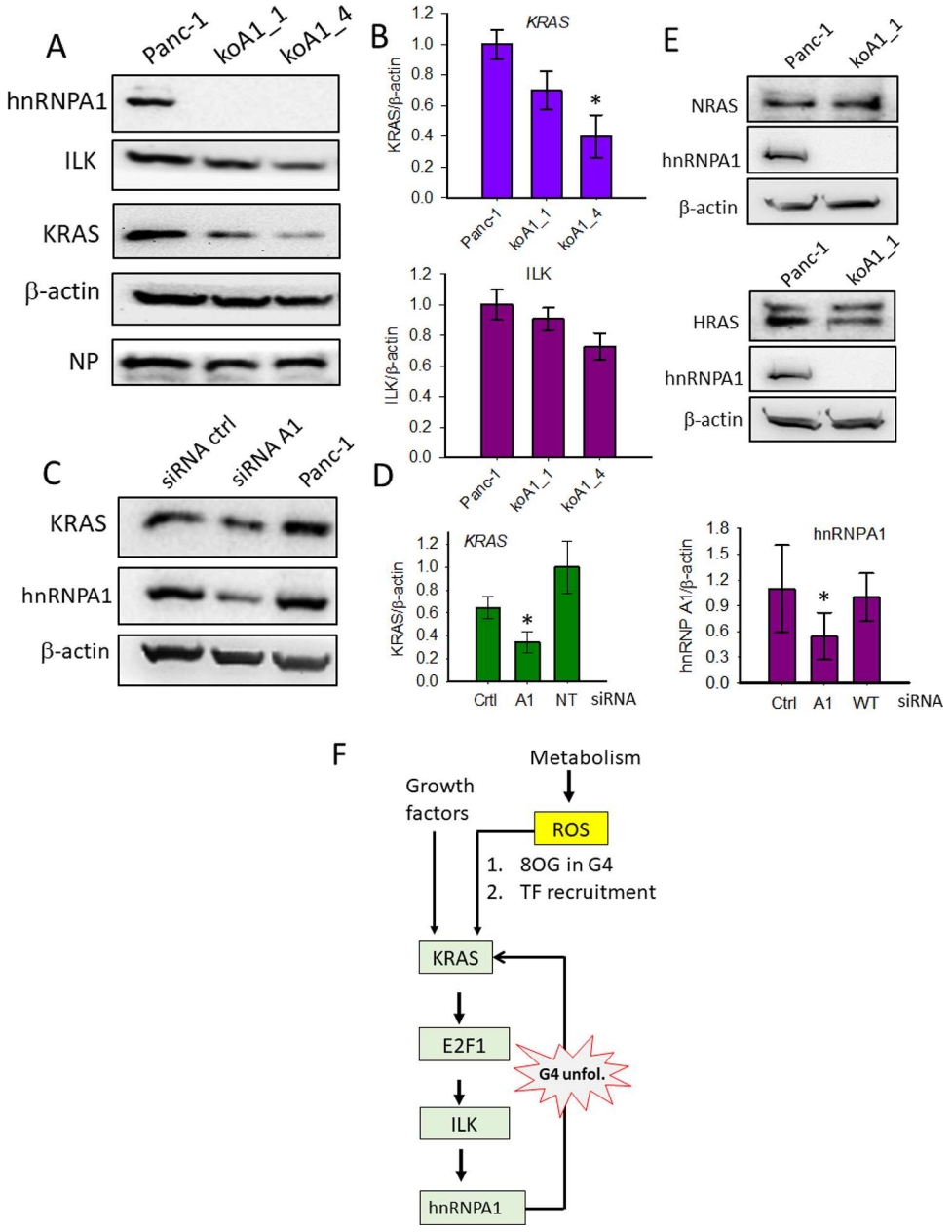

Figure 6. (A, B) Western blot showing the levels of hnRNPA1, ILK, KRAS, β-actin, and nucleoporin (NP) in the koA1_1 and koA1_4 knockouts and in wild-type Panc-1 cells. (C, D) Western blot showing the level of KRAS, hnRNPA1, and β-actin in Panc-1 cells untreated and treated with a specific siRNA for hnRNPA1and control siRNA. (E) Western blots showing the levels of HRAS and NRAS in normal Panc-1 cells and in koA1_1 knockout cells. (F) The *KRAS*-ILK-hnRNPA1 axis controlling the expression of *KRAS* in PDAC cells. (*) = $P < 0.05$.

hnRNPA1, Ku70, and PARP-1. It was observed that the G4s pulled down all four TFs, suggesting that they can indeed act as a platform for the formation upstream of the TSS of the transcription preinitiation complex (Figure 8B).

The eluates from the streptavidin-coated beads, incubated with the nuclear extract in the absence of the G4 bait, contained a small amount of proteins owing to unspecific interactions between the magnetic beads coated with streptavidin and the nuclear proteins (lane "beads"). The result obtained with G25T is quite similar to that observed with 32R, while conformer G9T appears less efficient in pulling down the proteins. The fact that G9T seems to be a less efficient platform than 32R and G25 correlates with its higher resistance to modifying its structure upon interacting with the hnRNPA1/UP1.

Another point that we considered is the following: as the distribution of the TFs in the promoter is dynamic and their recruitment is expected to be the result of the balance between protein−protein and DNA−protein interactions, we asked ourselves whether the proteins recruited to the *KRAS* promoter act independently or interact with one another. To investigate this point, we carried out an immunoprecipitation assay (Figure 8C). The nuclear extract from Panc-1 cells was incubated one by one with the monoclonal antibodies (Abs) specific for the TFs. The proteins bound directly or indirectly to the antibodies were pulled down by magnetic beads coated with protein A and analyzed by Western blots. It can be seen that anti-PARP1 Ab pulled down in addition to PARP-1 also Ku70, suggesting that these two proteins are associated with each other. Anti-Ku70 Ab gave a similar result: it pulled down

https://doi.org/10.1021/acsomega.1c05538
ACS Omega 2021, 6, 34092−34106

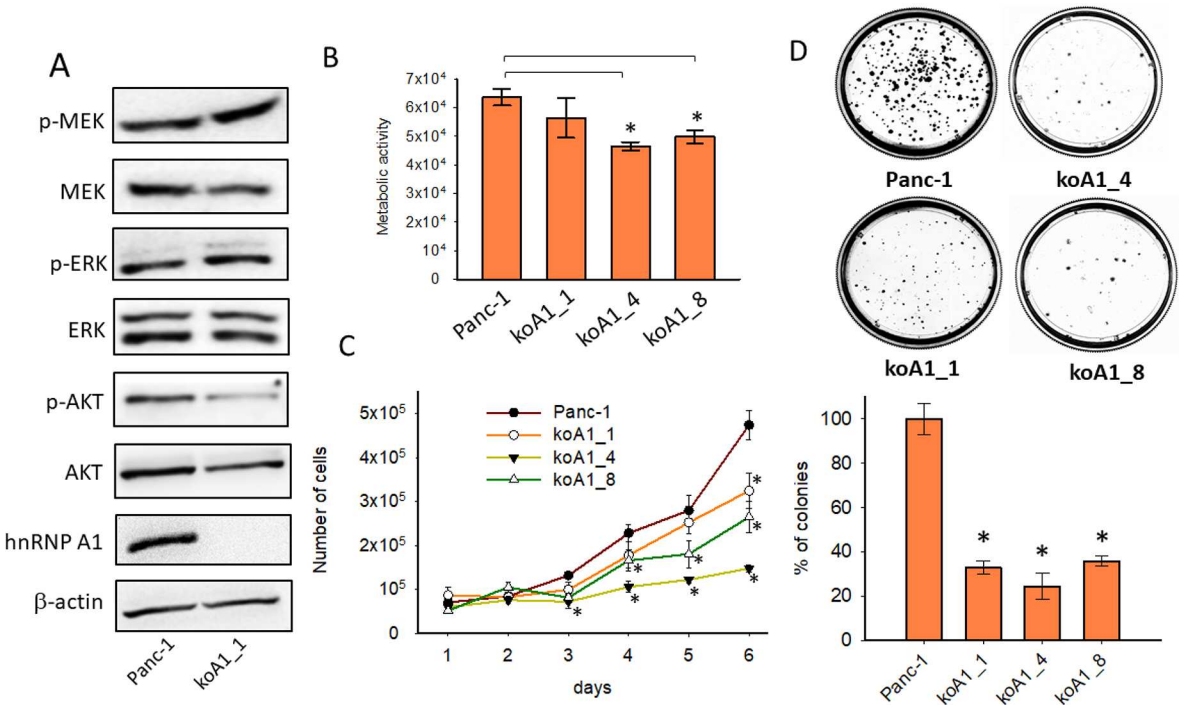

Figure 7. (A) Level of phosphorylation of KRAS downstream effector proteins. (B) Metabolic activity of normal and hnRNPA1-knockout Panc-1 cells measured 72 h after cell plating. (C) Cell growth assay reporting the number of normal and hnRNPA1-knockout Panc-1 cells up to 6 days from plating. (D) Clonogenic assay showing that normal Panc-1 cells form more colonies than the hnRNPA1-knockout clones. The bar plot shows a reduction of colony formation by the knockout clone of >60% compared to the wild-type cells. (*) = $P < 0.05$.

both Ku70 and PARP-1, confirming the contact between the two proteins. Anti-MAZ Ab only pulled down MAZ, while anti-hnRNPA1 Ab pulled down hnRNPA1 and MAZ in large amounts. The result suggests that MAZ and hnRNPA1 are strongly associated with each other. The fact that anti-MAZ Ab does not pull down hnRNPA1 indicates that the association between the two proteins overlaps the epitope recognized by anti-MAZ. In a second set of experiments, we used the 32R G4 containing 8-oxoguanine (8OG) as a bait to mimic a ROS-oxidized G4. We designed two oxidized G4 structures, called **92** and **96**, the former bearing 8OG in G-run I and the latter in the major groove (Figure S4 and Table 1).[32] When we incubated the wild-type and oxidized 32R sequences with a Panc-1 extract, we observed that the oxidized G4s pulled down the TFs as efficiently as wild-type 32R, indicating that the oxidized G4 acts as a platform for the recruitment of the TFs (Figure 8D). Interestingly, when we carried out a pull-down experiment with an extract obtained from the koA1_1 knockout cell line, we found that not only hnRNPA1 but also MAZ was not pulled down, in agreement with the fact that MAZ in the multiprotein complex is associated with hnRNPA1 (Figure 8E). In Figure 8F, we propose a mechanism for *KRAS* transcription activation. Under enhanced oxidative stress, typical of cancer cells, PARP-1 and its associated Ku70 protein are recruited to the *KRAS* promoter in the region containing the 32R G4 motif, most likely with 8OG modification. Upon binding to G4, PARP-1 undergoes autoparylation and becomes negatively charged.[6,38] Ku70, which is associated with PARP-1, having a pI = 6.23, is also anionic under physiological conditions. The resulting G4−PARP1−Ku70 complex forms a strongly anionic platform capable of recruiting cationic TFs such as hnRNPA1 (pI = 9.2). The electrostatic attraction of hnRNPA1 to the promoter should also recruit MAZ as it is associated with hnRNPA1.

The enrichment of the TFs in the neighboring G4 creates the conditions for the formation of the transcription preinitiation complex. Owing to the G4 unfolding property of hnRNPA1 and MAZ,[6,22,23] the G4 structures are unfolded and the transcription preinitiation complex is assembled on double-stranded DNA.

Finally, we compared the morphology of the knockout cell line koA1_1 with normal Panc-1 cells by performing confocal microscopy experiments (Figure S5). We obtained images of Panc-1 cells stained with phalloidin, syto-14, and Hoechst. Phalloidin binds to actin filaments and stains the cytoskeleton of the cells, syto-14 binds to cellular RNA, and Hoechst stains the nucleus. Compared to wild-type Panc-1 cells, the koA1_1 knockout appears more aggregated in keeping with the fact that the downregulation of *KRAS* affects cell adhesion.[39]

Correlation between the *KRAS*-ILK-hnRNPA1 Axis and PDAC Survival Probability. As the development, growth, and maintenance of PDAC heavily depend on *KRAS*,[40,41] we asked ourselves whether the oncogene and the TFs recognizing the *KRAS* G4 structures are overexpressed in PDAC patients. We consulted a publicly available microarray data set (GSE15471) to examine the differential expression of these genes between normal and tumor tissue samples. GSE15471 reports the global gene expression of 36 pairs of normal and PDAC samples obtained from resected pancreas of cancer patients. The results are reported in Figure 9A in the form of box plots. It can be seen that *KRAS* is almost twofold upregulated in PDAC compared to normal tissues ($P < 10^{-7}$). Remarkably, the genes encoding for PARP-1, hnRNPA1, and Ku70 that recognize the 32R G4 are also upregulated in PDAC tissues ($P < 0.007$). Only MAZ seems to be slightly

https://doi.org/10.1021/acsomega.1c05538
ACS Omega 2021, 6, 34092−34106

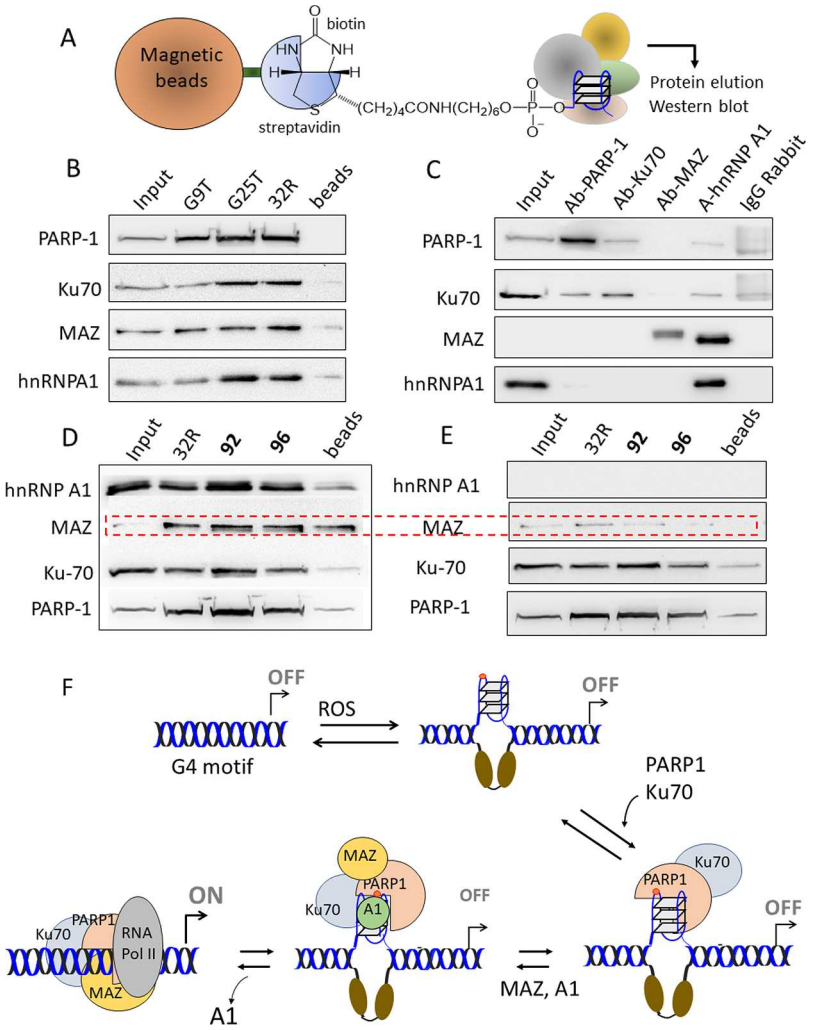

Figure 8. (A) Scheme of the pull-down experiments is illustrated. (B) Pull-down with biotinylated G9T, G25T, and 32R G4s. The biotinylated G4 (80 nM) was incubated with 80 μg of nuclear extract for 30 min at RT. The DNA bait−protein complexes formed were pulled down with streptavidin magnetic beads. The pull-down proteins were recovered and analyzed by Western blot with anti MAZ, anti PARP-1, and anti hnRNPA1 primary antibodies and a secondary antibody conjugated to horseradish peroxidase. (C) Pull-down with antibodies specific for PARP-1, Ku70, MAZ, and hnRNPA1. The recovered proteins from the pull-down were analyzed by Western blots. (D, E) Pull-down assays with biotinylated 32R and oxidized analogues 92 and 96, in the G4 structure, used as bait with the extract from normal Panc1 cells (left panel) and knockout koA1_1 cells (right panel). (F) Proposed mechanism for the activation of KRAS transcription. First, PARP-1 binds to the KRAS promoter at the G4 motif. After binding the protein, it undergoes auto-PARylation, becoming anionic. The G4−PARP-1 complex acts as a platform for the recruitment of the TFs. Protein hnRNPA1 should unfold the G4, thus promoting the G4 to duplex transformation at the promoter near TSS and the initiation of transcription.

downregulated ($P < 0.0012$). However, this finding is not in agreement with a recent study of Zhu *et al.*,[42] who reported that MAZ is also upregulated in PDAC (the discrepancy may be due to a different method of analysis).

As it is now established that *KRAS* is controlled by an axis involving hnRNPA1 and ILK,[28] we also focused on ILK and found that its expression in PDAC is higher than in normal tissues ($P = 0.0012$). So, the crucial *KRAS*-ILK-hnRNPA1 axis controlling *KRAS* expression is composed by effector proteins that are overexpressed in PDAC. To provide further support of the clinical relevance of the *KRAS*-ILK-hnRNPA1 axis, we investigated if its expression level correlates with the overall clinic outcomes of different tumors. We obtained Kaplan−Meier plots and found that PDAC patients with a highly expressed *KRAS*-ILK-hnRNPA1 axis showed a lower survival probability than patients with a lowly expressed axis (Figure 9B). We divided the data of 178 PDAC patients into two groups: one of 147 patients characterized by a high expression of KRAS-ILK-hnRNPA1 (group 1) and one of 31 patients with a low expression of the same genes (group 2). We then calculated the survival probability and found that group 2 had a survival probability significantly higher than that of group 1, $P = 0.038$. These data confirm the central role of the *KRAS*-ILK-hnRNPA1 axis in the maintenance of PDAC and suggest that hnRNPA1 is an interesting target for the rational design of anticancer drugs to treat PDAC.

CONCLUSIONS

The G4-motif located upstream of the transcription start site folds into a G-quadruplex in equilibrium between two G4 conformers: G9T (T_M = 61.2 °C) and G25T (T_M = 54.7 °C).[29] Here we have demonstrated that both G4s interact with hnRNPA1 and its proteolytic fragment UP1. 1D NMR analysis of G4 imino protons shows that, upon binding to UP1, G25T

https://doi.org/10.1021/acsomega.1c05538
ACS Omega 2021, 6, 34092−34106

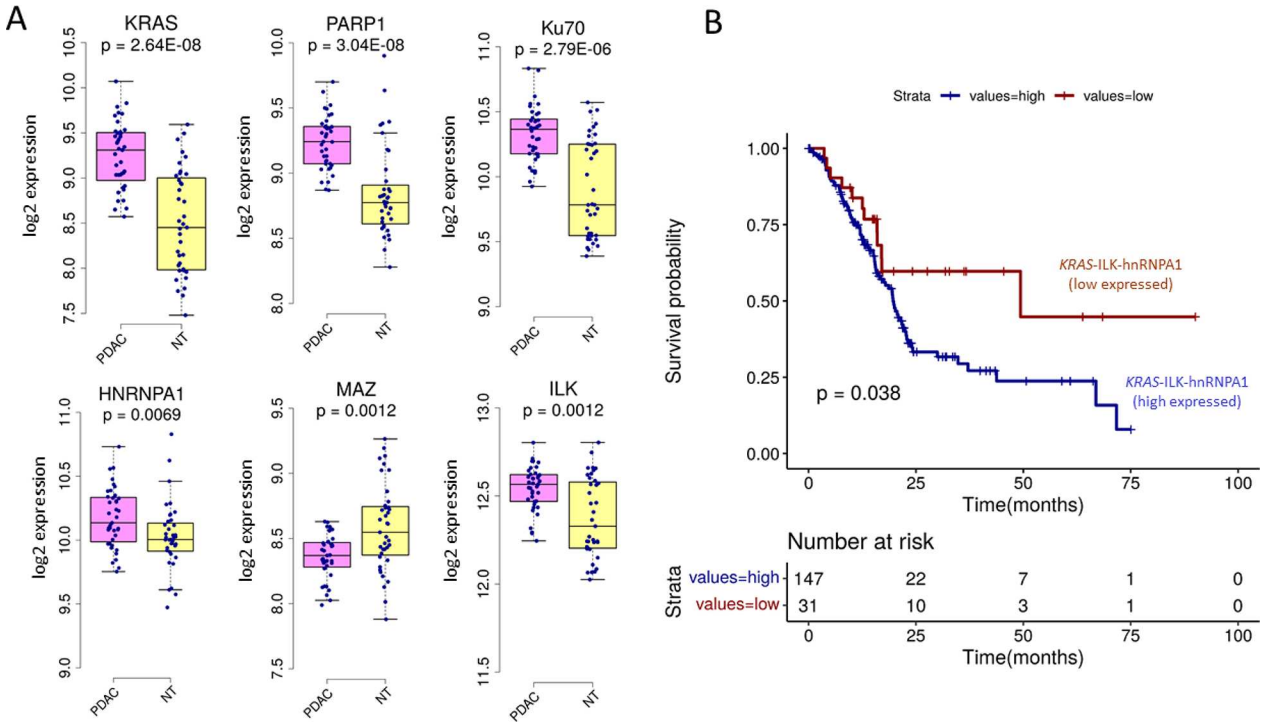

Figure 9. (A) Box plots showing the expression of genes related with KRAS in normal and PDAC pancreatic tissues (yellow and pink, respectively) obtained from the GSE15471 data set. (B) Survival probability of PDAC patients with the KRAS-ILK-hnRNPA1 axis upregulated or downregulated.

is practically unfolded, whereas G9T is only partly unfolded. As observed for the interaction between UP1 and telomeric G4, the UP1 residues showing important shifts upon binding to the *KRAS* G4 conformers are located in the two RRM domains.

The ability of hnRNPA1/UP1 to unfold G4 DNA suggests that this protein should play an important role in transcription regulation.[9,21,23,28,43] By using a Panc-1 knockout cell line in which hnRNPA1 was deleted by the CRISPR/Cas9 technology, we found that hnRNPA1 is essential for the transcription of *KRAS* and for cell growth. Pull-down/Western blot experiments indicate that conformer G25T is a better platform than conformer G9T for the assembly of the transcription preinitiation complex with PARP1, Ku70, MAZ, and hnRNPA1. A growing body of evidence indicates that PDAC cells are addicted to *KRAS*, which is regulated by the *KRAS*-ILK-hnRNPA1 axis.[28,44] Its expression correlates with the clinical outcome of PDAC patients. Kaplan−Meier plots show that the survival probability of PDAC patients with a high expression of the *KRAS*-ILK-hnRNPA1 axis is significantly lower than that of PDAC patients with a low expression of the axis. Together, the data confirm the central role of *KRAS*-ILK-hnRNPA1 in the maintenance of PDAC and suggest that hnRNPA1 can be an attractive target for the design of new anticancer drugs against PDAC.

MATERIALS AND METHODS

Oligonucleotides. The oligonucleotides have been purchased from Microsynth-AG, Balgach, Switzerland, or alternatively from Integrated DNA Technologies, Leuven, Belgium. Their sequences are reported in Table 1. DNA concentration was determined from the absorbance at 260 nm of the oligonucleotides diluted in milli Q water using as extinction coefficients 7500, 8500, 15,000, and 12,500 M^{-1} cm^{-1} for C, T, A, and G, respectively. The oligonucleotides, including those labeled to Cy-3, were HPLC purified.

Cell Culture, Metabolic Activity, and Proliferation Assay. Normal and hnRNPA1-deleted Panc-1 cells were maintained in exponential growth in Dulbecco's modified Eagle's medium (DMEM) containing 100 U/mL penicillin, 100 mg/mL streptomycin, 20 mM L-glutamine, and 10% fetal bovine serum (Euroclone, Italy). The metabolic activity assay was performed on a 96-well plate by seeding 9×10^3 cells per well. The cells were then treated with resazurin following a standard procedure. Cell growth assay was performed by seeding the cells in a 24-well plate and counting the cells on a cell counter every day for 6 days. Clonogenic assays were carried out with normal and hnRNPA1-deleted Panc-1 cells seeded in DMEM at a very low density and left for a period of 15 days. The colonies of at least 50 cells were counted, and the results were plotted in a histogram.

UV, CD, Fluorescence, and DMS Footprinting Experiments. UV melting was performed by using a Jasco V-750 UV−visible spectrophotometer equipped with a Peltier temperature control system (ETCS-761) (Jasco Europe, Cremella, Italy). The spectra were analyzed with Spectra Manager (Jasco Europe, Cremella, Italy). The oligonucleotides (3 μM) were annealed in 50 mM Na-cacodylate (pH 7.4) and 100 mM KCl (5 min at 95 °C, overnight at RT). The melting curves were recorded at 295 nm in a 0.5 cm path length quartz cuvette, heating (25−95 °C) at a rate of 0.5 °C/min.

CD spectra have been obtained with a JASCO J-600 spectropolarimeter equipped with a thermostated cell holder. CD experiments were carried out with 3 μM oligonucleotides in 50 mM Na-cacodylate (pH 7.4) and 100 mM KCl. Spectra were recorded in 0.5 cm quartz cuvettes. The spectra were calculated with the J-700 Standard Analysis software (Japan Spectroscopic Co., Ltd) and are reported as ellipticity (mdeg)

https://doi.org/10.1021/acsomega.1c05538
ACS Omega 2021, 6, 34092−34106

versus wavelength (nm). Each spectrum was recorded three times and subtracted to the baseline.

DMS footprinting was carried out as previously described.[3]

Production of Recombinant UP1. The recombinant protein comprising the RRM domains of UP1 (residues 17 to 196) was inserted into a modified pGEX vector containing a GST marker and then transformed on a Petri dish. The expression of UP1 in *E. coli* BL21 (DE3) bacteria was carried out in an LB medium (5 g/L yeast extract, 10 g/L peptone, and 10 g/L NaCl) at 37 °C overnight with ampicillin at 100 μg/mL. Bacteria were then transferred to a TB medium (24 g/L yeast extract, 12 g/L tryptone, 5 g glycerol, and 100 mM phosphate buffer (KH_2PO_4/K_2HPO_4)) supplemented with 100 μg/mL of Amp. For ^{15}N, ^{13}C labeled production, a minimal M9T medium (300 μM $CaCl_2$, 1 mM $MgSO_4$, 6 g Na_2HPO_4, 3 g KH_2PO_4, 0.5 g NaCl, 1 mg vitamin B1, 1 g NH_4Cl ^{15}N, and 2 g glucose ^{13}C) was used, always supplemented with 100 μg/mL of Amp. Expression was induced at an OD 600 nm between 1.5 and 2.0 with IPTG at 1 mM, overnight at 17 °C. The bacterial pellets were then recovered by centrifugation at 6500 rpm for 20 min at 4 °C, resuspended with PBS, and incubated under agitation for 30 min with 100 mM PMSF, lysozyme, and 1 M DTT. A lysis by sonication (40%: 45 s on, 45 s off for 4 min and 30 s) was then carried out, the lysate was then ultracentrifuged for 1 h at 4 °C at 42,000 RPM, and the supernatant was collected. Glutathione Sepharose 4B (GE Healthcare) (50% slurry in PBS) was added to the supernatant and incubated for 2 h at 4 °C with a slow shaking. The mix was centrifuged at 2000 rpm for 5 min, and the pellet was washed five times in PBS and eluted with an elution buffer containing 20 mM NaCl, 20 mM reduced glutathione, and 200 mM Tris−HCl (pH 7.5). GST tag was then cleaved from purified UP1 using PreScission protease (1.5 mg/mL) after exchange with a cleavage buffer (200 mM Tris HCl, 20 mM NaCl, 0.5 mM EDTA, and 1 mM DTT) overnight at 4 °C. GST and purified UP1 were then separated by size exclusion chromatography using GF S75 after equilibration in a buffer (50 mM KCl, 10 mM KPi (pH 6.66), and 0.5 mM DTT) overnight. Finally, purification was checked by SDS-PAGE and concentration was determined by measuring absorbance at 280 nm.

NMR Experiments. NMR spectra were recorded on a Bruker Advance III 700 MHz spectrometer equipped with a liquid TXI 1H/13C/15N/2H probe. All samples were prepared in 1X buffer (10 mM K2HPO4/KH2PO4; 50 mM KCl; pH 6.6) with the addition of 10% D2O for lock purposes and all spectra were acquired in 3 mm NMR tubes. For kinetics experiments containing UP1 and DNA, the G4 concentration (G9T and G25T) were 184 μM followed with the addition of one molar-equivalent of non-labelled UP1 in 1X buffer in presence of 1 mM DTT. Spectra of G4 mixed with UP1 were recorded at different time periods after addition of UP1 (0, 90 minutes, 1, 2, 3 and 7 days). In the 1D (1H) NMR experiments, the water signal was suppressed using excitation sculpting with gradients (zgesgppe; d1=2sec; 512 scans; time domain=64k). Samples were maintained at 37°C between each NMR experiment. Identification of UP1 residues implicated in the interaction with both KRAS32R conformers (G9T and G25T) have been done by using 2D NMR acquisitions with 15N, 13C isotopically enriched samples of UP1 in 1X buffer in presence of 1 mM DTT. We used SOFAST (Band-Selective Optimized-Flip-Angle Short-Transient) HMQC based on 2D H-1/X correlation via Heteronuclear zero and double quantum with decoupling during acquisition (sfhmqcf3gpph; d1=0.3sec; 256 scans, F2 (1H) time domain=2k; F1 (15N) time domain=160). Each residue has been identified by the −NH from its backbone connection and assigned using the deposited data from PDB structure 1L3K. Increasing amounts molar fractions of G4 (G9T or G25T) have been successively included (0.25, 0.5, 0.75, 1) and we followed UP1 chemical shift peak shifting after each oligo addition. Shifts have been determined for several peaks using the equation:

$$\delta = \sqrt{(\delta H2 + \left(\left(\frac{\delta N}{5}\right)2\right)} \quad (1)$$

with δH and δN being the chemical shifts in 1H and 15N dimensions respectively. Deviations of the chemical shifts were then plotted in function of the corresponding residue in Origin 8.6.

Isothermal Titration Calorimetry (ITC). ITC experiments were performed using a Microcal ITC200 instrument (Malvern). All experiments were performed at 37 °C. All samples were dialyzed in 1× buffer (10 mM K_2HPO_4/KH_2PO_4 and 50 mM KCl (pH 6.6)) with the addition of 1 mM DTT overnight and thoroughly degassed prior to use. Titrations were conducted with wild-type 32R and G4 conformers G9T and G25T. For the ITC titrations, the sample cell was filled to capacity with a dilute solution of UP1 at 10 μM and titrated with DNA at 50 μM in the same buffer. Titration has been done with 16 injections of 2.5 μL aliquots of the titrant with titrant injections made at 300 s intervals, with 600 rpm for stirring. The integrated heat data were corrected considering the heat of the dilution and blank effects. The corrected data were fit with a binding model by nonlinear regression. The binding isotherms were sigmoidal and well fit with the standard one-site binding model incorporated into the Microcal Origin ITC software.

CRISPR-Cas9 Suppression of hnRNPA1. HnRNPA1-deleted Panc-1 clones were generated by genome editing with the CRISPR/Cas9 system. The genome editing of Panc-1 cells has been carried out by Synthego (CA), which provided us a pool of Panc-1 edited cells. Individual clones were tested by Western blot to verify the deletion of the hnRNPA1 protein. Clones with extremely affected morphologic phenotype were excluded from further experiments.

Nuclear Extract and Biotin−Streptavidin Pull-Down Assay. To obtain nuclear extracts, six plates of 15 cm diameter of Panc-1 cells at a given confluence were washed with PBS and treated with 0.1 mM H_2O_2 in serum-free DMEM-high glucose for 30 min. The cells were collected in a PBS buffer and centrifuged at 800*g* for 10 min at 4 °C. Then, the cells were resuspended in a hypotonic buffer (10 mM HEPES-KOH (pH 7.9), 1.5 mM $MgCl_2$, 10 mM KCl, 0.2 mM PMSF, 0.5 mM DTT, 5 mM NaF, and 1 mM Na_3VO_4) and kept in ice for 10 min. Swollen cells were homogenized with a Dounce homogenizer and the nuclei, pelleted by centrifugation, and resuspended in a low-salt buffer (20 mM HEPES-KOH (pH 7.9), 25% glycerol, 1.5 mM $MgCl_2$, 20 mM KCl, 0.2 mM EDTA, 0.2 mM PMSF, and 0.5 mM DTT). The nuclear proteins were obtained by the addition of a high-salt buffer (low-salt buffer containing 1.2 M KCl). Protein concentration was determined according to the Bradford method. Biotinylated 32R, G9T, and G25T were folded in 50 mM Tris−HCl (pH 7.4) and 100 mM KCl by heating the solutions at 95 °C for 5 min and successive incubation overnight at RT. The

https://doi.org/10.1021/acsomega.1c05538
ACS Omega 2021, 6, 34092−34106

nuclear extract (80 μg) was incubated for 30 min at RT with 80 nM biotinylated 32R, G9T, or G25T in 20 mM Tris−HCl (pH 7.4), 150 mM KCl, 8% glycerol, 1 mM DTT, 0.1 mM ZnAc, 5 mM NaF, 1 mM Na_3VO_4, and 2.5 ng/μL poly[dI-dC]. Then Streptavidin MagneSphere Paramagnetic Particles (Promega Italia, Milano, Italy) were added and left to incubate for 30 min at RT. The beads were captured with a magnet and washed three times. The proteins were eluted with Laemmli buffer (4% SDS, 20% glycerol, 10% 2-mercaptoethanol, 0.004% bromophenol blue, and 0.125 M Tris−HCl).

Electrophoresis Mobility Shift Assays (EMSAs). Cy5.5-end labeled oligonucleotides 32R, G9T, and G25T were allowed to adopt their structure in 50 mM Tris−HCl (pH 7.4) and 100 mM KCl (heated at 95 °C for 5 min and annealed overnight at RT). Cy5.5-oligonucleotides (50 nM) were treated for 15 min at 25 °C with increasing amounts of hnRNPA1 in 50 mM Tris−HCl (pH 7.4), 50 mM KCl, 2.5 ng/mL poly[dI-dC], 1 mM EDTA, 1 mM Na_3VO_4, 5 mM NaF, 0.01% Phosphatase Inhibitor Cocktail I (Merck Life Science, Milano, Italy), 1 mM DTT, and 8% glycerol. The reaction mixtures were incubated for 10 min in ice, loaded in 5% TB (1×) polyacrylamide gel, and then run at 300 V, 50 mA, and 30 W for 3 h at 20 °C. After running, the gel was analyzed with the Odyssey CLx Imaging System (Li-COR Biosciences, Lincoln, NE, USA).

Immunoprecipitation Assay. Panc-1 cells were seeded onto 15 cm diameter plates. At 80% confluence, the cells were treated with 0.1 mM H_2O_2 in serum-free DMEM high-glucose medium for 30 min. Then the nuclear proteins were extracted and quantified as described in the Nuclear Extract and Biotin−Streptavidin Pull-Down Assay section. For immunoprecipitation, 1.5 mg of Protein A-Dynabeads (ThermoFisher Scientific-Invitrogen, Waltham, MA, USA) was incubated with 3 μg of anti-PAR (Poly/Mono-ADP Ribose (E6F6A) Rabbit mAb #83732, Cell Signaling Technology, Leiden, The Netherlands), anti-PARP-1 (46D11, Cell Signaling Technology, Leiden, The Netherlands), anti-Ku70 (D10A7, Cell Signaling Technology, Leiden, The Netherlands), anti-MAZ (clone 133.7, IgG mouse, Santa Cruz Biotechnology, Dallas, TX, USA), anti-hnRNPA1 (clone 9H10, IgG mouse, Merck Life Science, Milano, Italy), and IgG Rabbit (ThermoFisher Scientific-Invitrogen, Waltham, MA, USA) as negative control in 20 mM Tris−HCl (pH 7.4), 20 mM KCl, 8% glycerol, 1 mM DTT, and 0.1 mM ZnAc for 15 min at RT. After one wash with the same buffer, 80 μg was allowed to react with anti-PAR- and IgG rabbit-derivatized Dynabeads for 30 min at RT. The beads were captured with a magnet and washed three times with the same buffer. The proteins were denatured and eluted with Laemmli buffer (4% SDS, 20% glycerol, 10% 2-mercaptoethanol, 0.004% bromophenol blue, and 0.125 M Tris−HCl).

Western Blot Assays. Protein samples were separated in 10% SDS-PAGE and blotted onto the nitrocellulose membrane at 70 V for 2 h. The nitrocellulose membrane was blocked for 1 h with 5% nonfat dried milk in PBS and 0.1% Tween (Merck Life Science, Milano, Italy) at room temperature.

The primary antibodies used were as follows: anti-MAZ (clone 133.7, monoclonal antibody, IgG mouse, Santa Cruz Biotechnology, Dallas, TX, USA), anti-hnRNP A1 (clone 9H10, monoclonal antibody, IgG mouse, Merck Life Science, Milano, Italy), anti-PARP-1 (clone H-300, polyclonal antibody, IgG rabbit, Cell Signaling Technology, Leiden, The Netherlands), anti-PAR (Poly/Mono-ADP Ribose, clone E6F6A, monoclonal antibody, IgG Rabbit, Cell Signaling Technology, Leiden, The Netherlands), anti-Ku70 (clone 3C3.11, monoclonal antibody, IgG mouse, Cell Signaling Technology, Leiden, The Netherlands), anti-hnRNP M (clone A-12, monoclonal antibody, IgM mouse, Santa Cruz Biotechnology, Dallas, TX, USA), anti-hnRNP F/H (clone 1G11, monoclonal antibody, IgG Mouse, Santa Cruz Biotechnology, Dallas, TX, USA), anti-hnRNP A2/B1 (clone B-7, monoclonal antibody, IgG mouse, Santa Cruz Biotechnology, Dallas, TX, USA), anti-HRAS (clone C-20, polyclonal antibody, IgG rabbit, Santa Cruz Biotechnology, Dallas, TX, USA), anti-NRAS (clone F155-227, monoclonal antibody, IgG mouse, Calbiochem, San Diego, CA, USA), anti-KRAS (clone 3B10-2F2, mouse monoclonal, IgG mouse, Merk Life Science, Milano, Italy), anti-ILK (polyclonal antibody, IgG rabbit, Cusabio Technology LLC, Houston, TX, USA), anti-nucleoporin (polyclonal antibody, IgG Rabbit, Abcam, Cambridge, UK), and anti-β-actin (monoclonal antibody, IgG Mouse, Merk Life Science, Milano, Italy). The membranes were incubated overnight at 4 °C with the primary antibodies, washed with 0.1% Tween in PBS, and then incubated for 1 h with the secondary antibodies conjugated to horseradish peroxidase: anti-mouse IgG (diluted 1:5000), anti-rabbit IgG (diluted 1:5000), and anti-mouse IgM (diluted 1:5000) (Merck Life Science, Milano, Italy). The signal was developed with Super Signal West PICO and FEMTO (Thermo Fisher Scientific, Waltham, MA, USA) and detected with the ChemiDOC XRS, Quantity One 4.6.5 software (Bio-Rad Laboratories, Segrate, (Milano), Italy).

Gene Expression Analysis. Data set GSE15471 was downloaded from GEO.[45] CEL files were processed using standard tools available within the R affy package.[46] The normalization step was done with the standard RMA algorithm,[47] while the Jetset scoring was used to identify the optimal microarray probe set for each gene.[48] The impact of gene expression on patient survival in the PDAC data set from the Cancer Genome Atlas (TCGA-PAAD) was evaluated. mRNA expression data from 178 samples (normalized by the RNAseq by the Expectation−Maximization (RSEM) method) and patients' clinical data were retrieved from TCGA in May 2021 using the R package cgdsr.[49] The whole gene signature was taken into account: every patient's median expression value was determined, and all the patients were divided into "high" and "low" expression groups based on the optimal cutoff. This is the value that creates the largest survival separation between groups with the highest significance. For this purpose, we used the surv_cutpoint function in survminer package.[50] Overall survival (OS) of the two groups was compared by using the Kaplan−Meier plots, with p values calculated via log-rank test, using the R survival package in R.[51]

Statistics. Vertical bar graphs report mean values ± standard error (SE). Statistical analyses were carried out by using the Sigma Plot software. Group differences were analyzed by Student's t test or one-way analysis of variance (ANOVA). Groups are considered different when $P < 0.05$.

■ ASSOCIATED CONTENT

Supporting Information

The Supporting Information is available free of charge at https://pubs.acs.org/doi/10.1021/acsomega.1c05538.

Structures of 32R and oxidized 32R from DMS footprinting; FRET experiments with G25T/G9T and

https://doi.org/10.1021/acsomega.1c05538
ACS Omega 2021, 6, 34092−34106

hnRNPA1; and confocal microscopy of Panc-1 and Nrf2 knockout Panc-1 cells (koA1_1) (PDF)

AUTHOR INFORMATION

Corresponding Authors

Gilmar F. Salgado − *ARNA Laboratory, Université de Bordeaux, Pessac 33607, France;* orcid.org/0000-0002-0296-5979; Email: gilmar.salgado@u-bordeaux.fr

Luigi E. Xodo − *Department of Medicine, Laboratory of Biochemistry, Udine 33100, Italy;* orcid.org/0000-0003-3344-7207; Email: luigi.xodo@uniud

Authors

Annalisa Ferino − *Department of Medicine, Laboratory of Biochemistry, Udine 33100, Italy*

Julien Marquevielle − *ARNA Laboratory, Université de Bordeaux, Pessac 33607, France*

Himanshi Choudhary − *Department of Medicine, Laboratory of Biochemistry, Udine 33100, Italy*

Giorgio Cinque − *Department of Medicine, Laboratory of Biochemistry, Udine 33100, Italy*

Coralie Robert − *ARNA Laboratory, Université de Bordeaux, Pessac 33607, France*

Anne Bourdoncle − *ARNA Laboratory, Université de Bordeaux, Pessac 33607, France*

Raffaella Picco − *Department of Medicine, Laboratory of Biochemistry, Udine 33100, Italy*

Jean-Louis Mergny − *ARNA Laboratory, Université de Bordeaux, Pessac 33607, France; Laboratoire d'Optique et Biosciences, Ecole Polytechnique, CNRS, INSERM, Institut Polytechnique de Paris, Palaiseau 91128, France;* orcid.org/0000-0003-3043-8401

Complete contact information is available at: https://pubs.acs.org/10.1021/acsomega.1c05538

Funding

This work has been financed by AIRC (Associazione Italiana per la Ricerca sul Cancro, Project No. 19898) and La Ligue contre le Cancer, Comité de Gironde, France.

Notes

The authors declare no competing financial interest.

ACKNOWLEDGMENTS

The work on the 800 MHz NMR spectrometer (IECB) was possible thanks to support from TGIR-RMN-THC Fr3050 CNRS, CNRS UMS3033, Inserm US001, Univ. Bordeaux.

ABBREVIATIONS

KRAS Kirsten ras; hnRNPA1 heterogeneous nuclear ribonucleoprotein A1; UP1 unfolding protein 1; ILK integrin linked kinase; PARP1 poly(ADP-ribose) polymerase 1; MAZ Myc associated zinc finger protein; Ku70 ATP-dependent DNA helicase II, 70 kDa subunit; G4 G-quadruplex; TF transcription factor; EMSA electrophoresis mobility shift assay; FRET fluorescence resonance energy transfer; ITC isothermal titration calorimetry; DMS dimethyl sulfate; PDAC pancreatic ductal adenocarcinoma; 8OG 7,8-dihydro-8-oxoguanine

REFERENCES

(1) Cogoi, S.; Xodo, L. E. G4 DNA in ras genes and its potential in cancer therapy. *Biochim. Biophys. Acta* **2016**, *1859*, 663−674.

(2) Cogoi, S.; Xodo, L. E. G-quadruplex formation within the promoter of the KRAS proto-oncogene and its effect on transcription. *Nucleic Acids Res.* **2006**, *34*, 2536−2549.

(3) Cogoi, S.; Paramasivam, M.; Spolaore, B.; Xodo, L. E. Structural polymorphism within a regulatory element of the human KRAS promoter: Formation of G4-DNA recognized by nuclear proteins. *Nucleic Acids Res.* **2008**, *36*, 3765−3780.

(4) Cogoi, S.; Paramasivam, M.; Membrino, A.; Yokoyama, K. K.; Xodo, L. E. The KRAS promoter responds to Myc-associated zinc finger and poly(ADP-ribose) polymerase 1 proteins, which recognize a critical quadruplex-forming GA-element. *J. Biol. Chem.* **2010**, *285*, 22003−22016.

(5) Cogoi, S.; Zorzet, S.; Rapozzi, V.; Géci, I.; Pedersen, E. B.; Xodo, L. E. MAZ-binding G4-decoy with locked nucleic acid and twisted intercalating nucleic acid modifications suppresses KRAS in pancreatic cancer cells and delays tumor growth in mice. *Nucleic Acids Res.* **2013**, *41*, 4049−4064.

(6) Cinque, G.; Ferino, A.; Pedersen, E. B.; Xodo, L. E. Role of Poly [ADP-ribose] Polymerase 1 in Activating the Kirsten ras (KRAS) Gene in Response to Oxidative Stress. *Int. J. Mol. Sci.* **2020**, *21*, 6237−6259.

(7) Lau, J. S.; Baumeister, P.; Kim, E.; Roy, B.; Hsieh, T. Y.; Lai, M.; Lee, A. S. Heterogeneous nuclear ribonucleoproteins as regulators of gene expression through interactions with the human thymidine kinase promote. *J. Cell. Biochem.* **2000**, *79*, 395−406.

(8) Xia, H. Regulation of γ-fibrinogen chain expression by heterogeneous nuclear ribonucleoprotein A1. *J. Biol. Chem.* **2005**, *280*, 13171−13178.

(9) Campillos, M.; Lamas, J. R.; García, M. A.; Bullido, M. J.; Valdivieso, F.; Vázquez, J. Specific interaction of heterogeneous nuclear ribonucleoprotein A1 with the -219T allelic form modulates APOE promoter activity. *Nucleic Acids Res.* **2003**, *31*, 3063−3070.

(10) Tavanez, J. P.; Madl, T.; Kooshapur, H.; Sattler, M.; Valcárcel, J. hnRNP A1 proofreads 3′ splice site recognition by U2AF. *Mol. Cell* **2012**, *45*, 314−329.

(11) Mili, S.; Shu, H. J.; Zhao, Y.; Piñol-Roma, S. Distinct RNP complexes of shuttling hnRNP proteins with pre-mRNA and mRNA: candidate intermediates in formation and export of mRNA. *Mol. Cell. Biol.* **2001**, *21*, 7307−7319.

(12) Izaurralde, E.; Jarmolowski, A.; Beisel, C.; Mattaj, I. W.; Dreyfuss, G.; Fischer, U. A role for the M9 transport signal of hnRNP A1 in mRNA nuclear export. *J. Cell Biol.* **1997**, *137*, 27−35.

(13) Bonnal, S.; Pileur, F.; Orsini, C.; Parker, F.; Pujol, F.; Prats, A. C.; Vagner, S. Heterogeneous nuclear ribonucleoprotein A1 is a novel internal ribosome entry site trans-acting factor that modulates alternative initiation of translation of the fibroblast growth factor 2 mRNA. *J. Biol. Chem.* **2005**, *280*, 4144−4153.

(14) Cammas, A.; Pileur, A. F.; Bonnal, S.; Lewis, S. M.; Lévêque, N.; Holcik, M.; Vagner, S. Cytoplasmic relocalization of heterogeneous nuclear ribonucleoprotein A1 controls translation initiation of specific mRNAs. *Mol. Biol. Cell* **2007**, *18*, 5048−5059.

(15) Ford, L. P.; Wright, W. E.; Shay, J. W. A model for heterogeneous nuclear ribonucleoproteins in telomere and telomerase regulation. *Oncogene* **2002**, *21*, 580−583.

(16) He, Y.; Smith, R. Nuclear functions of heterogeneous nuclear ribonucleoproteins A/B. *Cell. Mol. Life Sci.* **2009**, *66*, 1239−1256.

(17) Barraud, P.; Allain, F. H.-T. Solution structure of the two RNA recognition motifs of hnRNP A1 using segmental isotope labeling: how the relative orientation between RRMs influences the nucleic acid binding topology. *J. Biomol. NMR* **2013**, *55*, 119−138.

(18) Xu, R. M.; Jokhan, L.; Cheng, X.; Mayeda, A.; Krainer, A. R. Crystal structure of human UP1, the domain of hnRNP A1 that contains two RNA-recognition motifs. *Structure* **1997**, *5*, 559−570.

(19) Shamoo, Y.; Krueger, U.; Rice, L. M.; Williams, K. R.; Steitz, T. A. Crystal structure of the two RNA binding domains of human hnRNP A1 at 1.75 A resolution. *Nat. Struct. Biol.* **1997**, *4*, 215−222.

(20) Ding, J.; Hayashi, M. K.; Zhang, Y.; Manche, L.; Krainer, A. R.; Xu, R. M. Crystal structure of the two-RRM domain of hnRNP A1

(UP1) complexed with single-stranded telomeric DNA. *Genes Dev.* **1999**, *13*, 1102−1115.
(21) Das, S.; Ward, S. V.; Markle, D.; Samuel, C. E. DNA damage-binding proteins and heterogeneous nuclear ribonucleoprotein A1 function as constitutive KCS element components of the interferon-inducible RNA-dependent protein kinase promoter. *J. Biol. Chem.* **2004**, *279*, 7313−7321.
(22) Fukuda, H.; Katahira, M.; Tsuchiya, N.; Enokizono, Y.; Sugimura, T.; Nagao, M.; Nakagama, H. Unfolding of quadruplex structure in the G-rich strand of the minisatellite repeat by the binding protein UP1. *Proc. Natl. Acad. Sci.* **2002**, *99*, 12685−12690.
(23) Paramasivam, M.; Membrino, A.; Cogoi, S.; Fukuda, H.; Nakagama, H.; Xodo, L. E. Protein hnRNP A1 and its derivative Up1 unfold quadruplex DNA in the human KRAS promoter: implications for transcription. *Nucleic Acids Res.* **2009**, *37*, 2841−2853.
(24) Krüger, A. C.; Raarup, M. K.; Nielsen, M. M.; Kristensen, M.; Besenbacher, F.; Kjems, J.; Birkedal, V. Interaction of hnRNP A1 with telomere DNA G-quadruplex structures studied at the single molecule level. *Eur. Biophys. J.* **2010**, *39*, 1343−1350.
(25) Ghosh, M.; Singh, M. RGG-box in hnRNPA1 specifically recognizes the telomere G-quadruplex DNA and enhances the G-quadruplex unfolding ability of UP1 domain. *Nucl. Acids Res.* **2018**, *46*, 10246−10261.
(26) Ghosh, M.; Singh, M. Structure specific recognition of telomeric repeats containing RNA by the RGG-box of hnRNPA1. *Nucl. Acids Res.* **2020**, *48*, 4492−4506.
(27) Cogoi, S.; Rapozzi, V.; Cauci, S.; Xodo, L. E. Critical role of hnRNP A1 in activating KRAS transcription in pancreatic cancer cells: A molecular mechanism involving G4 DNA. *Biochim. Biophys. Acta, Gen. Subj.* **1861**, *2017*, 1389−1398.
(28) Chu, P. C.; Yang, M. C.; Kulp, S. K.; Salunke, S. B.; Himmel, L. E.; Fang, C. S.; Jadhav, A. M.; Shan, Y. S.; Lee, C. T.; Lai, M. D.; Shirley, L. A.; Bekaii-Saab, T.; Chen, C.-S. Regulation of oncogenic KRAS signaling via a novel KRAS-integrin-linked kinase-hnRNPA1 regulatory loop in human pancreatic cancer cells. *Oncogene* **2016**, *35*, 3897−3908.
(29) Marquevielle, J.; Robert, C.; Lagrabette, O.; Wahid, M.; Bourdoncle, A.; Xodo, L. E.; Mergny, J. L.; Salgado, G. F. Structure of two G-quadruplexes in equilibrium in the KRAS promoter. *Nucleic Acids Res.* **2020**, *48*, 9336−9345.
(30) Paramasivam, M.; Cogoi, S.; Xodo, L. E. Primer extension reactions as a tool to uncover folding motifs within complex G-rich sequences: analysis of the human KRAS NHE. *Chem. Commun.* **2011**, *47*, 4965−4967.
(31) Kerkour, A.; Marquevielle, J.; Ivashchenko, S.; Yatsunyk, L. A.; Mergny, J. L.; Salgado, G. F. High-resolution three-dimensional NMR structure of the KRAS proto-oncogene promoter reveals key features of a G-quadruplex involved in transcriptional regulation. *J. Biol. Chem.* **2017**, *292*, 8082−8091.
(32) Cogoi, S.; Ferino, A.; Miglietta, G.; Pedersen, E. B.; Xodo, L. E. The regulatory G4 motif of the Kirsten ras (KRAS) gene is sensitive to guanine oxidation: implications on transcription. *Nucleic Acids Res.* **2018**, *46*, 661−676.
(33) Myers, J. C.; Shamoo, Y. Human UP1 as a model for understanding purine recognition in the family of proteins containing the RNA recognition motif (RRM). *J. Mol. Biol.* **2004**, *342*, 743−756.
(34) Ferino, A.; Rapozzi, V.; Xodo, L. E. The ROS-KRAS-Nrf2 axis in the control of the redox homeostasis and the intersection with survival-apoptosis pathways: Implications for photodynamic therapy. *J. Photochem. Photobiol. B.* **2020**, *202*, 111672.
(35) Camelo, F.; Le, A. (2021). The Intricate Metabolism of Pancreatic Cancers. In *Advances in Experimental Medicine and Biology;* (pp. 77−88). (Advances in Experimental Medicine and Biology; Vol. *1311*). Springer. DOI: 10.1007/978-3-030-65768-0_5.
(36) Eser, S.; Schnieke, A.; Schneider, G.; Saur, D. Oncogenic KRAS signalling in pancreatic. *Cancer. Br. J. Cancer.* **2014**, *111*, 817−822.
(37) Eser, S.; Reiff, N.; Messer, M.; Seidler, B.; Gottschalk, K.; Dobler, M.; Hieber, M.; Arbeiter, A.; Klein, S.; Kong, B.; et al. Selective requirement of PI3K/PDK1 signaling for Kras oncogene-driven pancreatic cell plasticity and cancer. *Cancer Cell* **2013**, *23*, 406−420.
(38) Soldatenkov, V. A.; Vetcher, A. A.; Duka, T.; Ladame, S. First evidence of a functional interaction between DNA quadruplexes and poly(ADP-ribose) polymerase-1. *ACS Chem. Biol.* **2008**, *3*, 214−219.
(39) Pollock, C. B.; Shirasawa, S.; Sasazuki, T.; Kolch, W.; Dhillon, A. S. Oncogenic *K-RAS* Is Required to Maintain Changes in Cytoskeletal Organization, Adhesion, and Motility in Colon Cancer Cells. *Cancer Res.* **2005**, *65*, 1251−1250.
(40) Collins, M. A.; Bednar, F.; Zhang, Y.; Brisset, J.-C.; Galbán, S.; Galbán, C. J.; Rakshit, S.; Flannagan, K. S.; Volkan Adsay, N.; Pasca di Magliano, M. Oncogenic Kras is required for both the initiation and maintenance of pancreatic cancer in mice. *J. Clin. Invest.* **2012**, *122*, 639−653.
(41) Ying, H.; Kimmelman, A. C.; Lyssiotis, C. A.; Hua, S.; Chu, G. C.; Fletcher-Sananikone, E.; Locasale, J. W.; Son, J.; Zhang, H.; Coloff, J. L.; et al. Oncogenic Kras maintains pancreatic tumors through regulation of anabolic glucose metabolism. *Cell* **2012**, *149*, 656−670.
(42) Zhu, X.; Luo, W.; Liang, W.; Tang, F.; Bei, C.; Ren, Y.; Qin, L.; Tan, C.; Zhang, Y.; Tan, S. Overexpression and clinical significance of MYC-associated zinc finger protein in pancreatic carcinoma. *Onco Targets Ther.* **2016**, *Volume 9*, 7493−7501. eCollection 2016
(43) Nishikawa, T.; Kuwano, Y.; Takahara, Y.; Nishida, K.; Rokutan, K. HnRNPA1 interacts with G-quadruplex in the TRA2B promoter and stimulates its transcription in human colon cancer cells. *Sci. Rep.* **2019**, *9*, 10276.
(44) Chu, P. C.; Kulp, S. K.; Bekaii-Saab, T.; Chen, C. S. Targeting integrin-linked kinase to suppress oncogenic KRAS signaling in pancreatic cancer. *Small GTPases* **2018**, *9*, 452−456.
(45) Barrett, T.; Troup, D. B.; Wilhite, S. E.; Ledoux, P.; Evangelista, C.; Kim, I. F.; Tomashevsky, M.; Marshall, K. A.; Phillippy, K. H.; Sherman, P. M.; et al. NCBI GEO: archive for functional genomics data sets—10 years on. *Nucleic Acids Res.* **2011**, *39*, D1005−D1010.
(46) Gautier, L.; Cope, L.; Bolstad, B. M.; Irizarry, R. A. affy–analysis of Affymetrix GeneChip data at the probe level. *Bioinformatics* **2004**, *20*, 307−315.
(47) Irizarry, R. A.; Hobbs, B.; Collin, F.; Beazer-Barclay, Y. D.; Antonellis, K. J.; Scherf, U.; Speed, T. P. Exploration, normalization, and summaries of high density oligonucleotide array probe level data. *Biostatistics* **2003**, *4*, 249−264.
(48) Li, Q.; Birkbak, N. J.; Gyorffy, B.; Szallasi, Z.; Eklund, A. C. Jetset: selecting the optimal microarray probe set to represent a gene. *BMC Bioinformatics* **2011**, *12*, 474.
(49) Jacobsen, A. *cgdsr: R-Based API for Accessing the MSKCC Cancer Genomics Data Server (CGDS)*; 2015. https://cran.r-project.org/web/packages/cgdsr/index.html (accessed 22 Apr2016).
(50) Kassambara, A., Kosinski, M., Biecek, P., Fabian, S. *survminer: Drawing Survival Curves using 'ggplot2' 0.4.9 ed2021;* (2021). Available online at: https://cran.r-project.org/web/packages/survminer/.
(51) Therneau, T., 2015, *A Package for Survival Analysis in S;* version 2.38, https://CRAN.R-project.org/package=survival;

https://doi.org/10.1021/acsomega.1c05538
ACS Omega 2021, 6, 34092−34106

Section 2

Photosensitization of pancreatic cancer cells by cationic alkyl-porphyrins in free form or engrafted into POPC liposomes: The relationship between delivery mode and mechanism of cell death.

Journal of Photochemistry & Photobiology, B: Biology 231 (2022) 112449

Contents lists available at ScienceDirect

Journal of Photochemistry & Photobiology, B: Biology

journal homepage: www.elsevier.com/locate/jphotobiol

Photosensitization of pancreatic cancer cells by cationic alkyl-porphyrins in free form or engrafted into POPC liposomes: The relationship between delivery mode and mechanism of cell death

Eros Di Giorgio [a,1], Annalisa Ferino [a,1], Himanshi Choudhary [a], Phillip M.G. Löffler [b], Francesca D'Este [a], Valentina Rapozzi [a], Alexander Tikhomirov [c], Andrey Shchekotikhin [c], Stefan Vogel [b], Luigi E. Xodo [a,*]

[a] Department of Medicine, Laboratory of Biochemistry, University of Udine, P.le Kolbe 4, 33100 Udine, Italy
[b] Department of Physics, Chemistry and Pharmacy, University of Southern Denmark, Odense, Denmark
[c] Gause Institute of New Antibiotics, B. Pirogovskaya 11, 119021 Moscow, Russia

ARTICLE INFO

Keywords:
Alkyl-porphyrins
POPC liposomes
Photodynamic therapy
KRAS
GXP4
Apoptosis
Ferroptosis

ABSTRACT

Cationic porphyrins bearing an alkyl side chain of 14 (**2b**) or 18 (**2d**) carbons dramatically inhibit proliferation of pancreatic cancer cells following treatment with light. We have compared two different ways of delivering porphyrin **2d**: either in free form or engrafted into palmitoyl-2-oleoyl-sn-glycero-3-phosphocholine liposomes (L-**2d**). Cell cytometry shows that while free **2d** is taken up by pancreatic cancer cells by active (endocytosis) and passive (membrane fusion) transports, L-**2d** is internalized solely by endocytosis. Confocal microscopy showed that free **2d** co-localizes with the cell membrane and lysosomes, whereas L-**2d** partly co-localizes with lysosomes and ER. It is found that free **2d** inhibits the *KRAS*-Nrf2-GPX4 axis and strongly triggers lipid peroxidation, resulting in cell death by ferroptosis. By contrast, L-**2d** does not affect the *KRAS*-Nrf2-GPX4 axis and activates cell death mainly through apoptosis. Overall, our study demonstrates for the first time that cationic alkyl porphyrins, which have a IC_{50} ~ 23 nM, activate a dual mechanism of cell death, ferroptosis and apoptosis, where the predominant form depends on the delivery mode.

1. Introduction

The use of nanoparticles for drug delivery is an important area of investigation in cancer therapy. Among the nanostructures proposed as drug-delivery vehicles, liposomes have drawn the attention of many researches as they are easily prepared and composed by non-toxic naturally occurring phospholipids [1–4]. They consist of a spherical phospholipid bilayer delimiting an aqueous central core space and are employed as nanocarrier for drug delivery in cancer. Due to their unique capacity to entrap both hydrophobic and hydrophilic compounds, liposomes are used to transport into the tissues a wide range of drugs [5]. In fact, lipophilic molecules can be engrafted into the membrane bilayer, whereas hydrophilic compounds can be entrapped in the aqueous central core [1–4]. Liposomes are attractive drug carriers because they are easily suspended in aqueous solution, they are non-immunogenic and biodegradable. They also have a good capacity of self-assembly, they possess a high drug loading [6,7] and the drugs loaded in liposomes exhibit, in general, a low systemic toxicity, and are also protected from degradation and inactivation [8–12].

In our study, as drugs to treat pancreatic cancer cells we used two cationic porphyrins: 5,10,15-tris(1-methylpyridinium-4-yl)-20-(1-tetradecylpyridinium-4-yl)porphyrin, **2b**; 5,10,15-tris(1-methylpyridinium-4-yl)-20-(1-octadecylpyridinium-4-yl)porphyrin, **2d**. These molecules possess four positive charges, making them soluble in water, as well as an alkyl chain of either 14 (**2b**) or 18 (**2d**) carbons (Fig. 1D). They have two interesting properties: they generate reactive oxygen species (ROS)

Abbreviations: PDAC, Pancreatic ductal adenocarcinoma; POPC, Palmitoyl-2-oleoyl-sn-glycero-3-phosphocholine; *KRAS*, Kirsten ras; **2b**, 5,10,15-Tris(1-methylpyridinium-4-yl)-20-(1-tetradecylpyridinium-4-yl)porphyrin; **2d**, 5,10,15-Tris(1-methylpyridinium-4-yl)-20-(1-octadecylpyridinium-4-yl)porphyrin; Nrf2, Nuclear factor erythroid 2-related factor 2; GPX4, Glutathione peroxidase 4; ROS, Reactive oxygene species; FACS, Fluorescence-activated Cell Sorter..

* Corresponding author.
E-mail address: luigi.xodo@uniud.it (L.E. Xodo).

[1] EDG and AF contributed equally to this work.

https://doi.org/10.1016/j.jphotobiol.2022.112449
Received 23 December 2021; Received in revised form 18 April 2022; Accepted 21 April 2022
Available online 25 April 2022

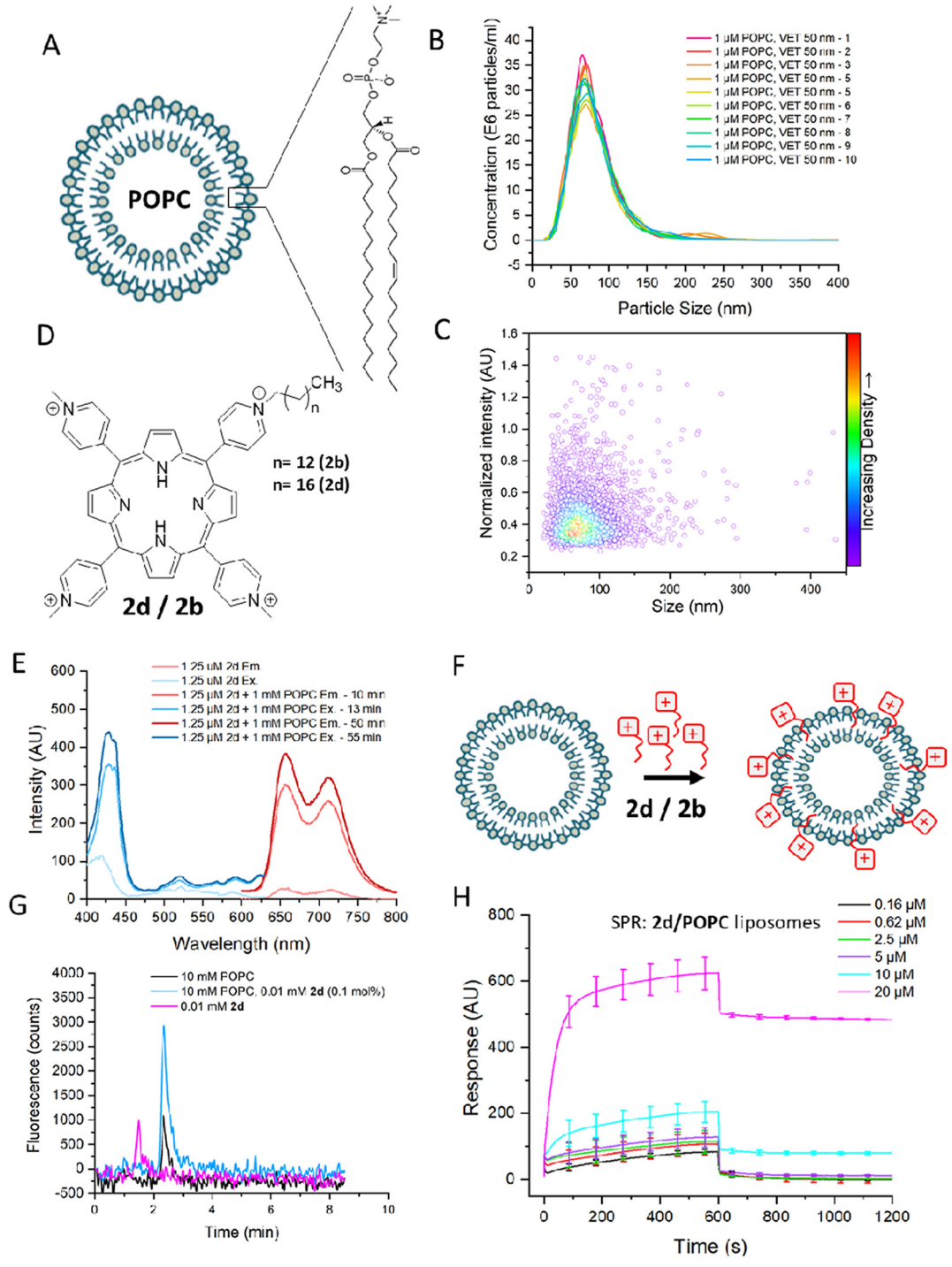

(caption on next page)

Fig. 1. (A) POPC liposomes; (B, C) Nanoparticle Tracking analysis of the liposomes; (D) Stuctures of the cationic porphyrins **2d** and **2b** free or engrafted into POPC liposomes, L-**2d**/L-**2b**; (E) Excitation and emission spectra of **2d** in PBS; (F) Liposome loading with alkyl-porphyrins **2b**/**2d**; (G) Size-exclusion HPLC chromatograms for **2d** and L-**2d**. Fluorescence signal of liposomes loaded with 0.1 mol% **2d** (light blue), native liposomes (visible due to light scattering, black), and porphyrin alone (10 μM, pink); (H) Surface plasmon resonance sensograms showing the binding of **2d** to POPC liposomes immobilized on the sensor chip surface; (I) ROS production in Panc-1 and BxPC-3 cancer cells by porphyrins **2b** and **2d** delivered as free molecules or engrafted into POPC liposomes. L = POPC liposomes. NT = nontreated, illuminated cells. Statistical significance respect to untreated cells (NT): $P \leq 0.05$ (*), 0.01 (**), 0.001 (***). Data relative to: Panc-1/**2d** are the average of 3 independent experiments in duplicate; BxPC3/**2d** and Panc-1/**2b** one experiment in duplicate. (For interpretation of the references to colour in this figure legend, the reader is referred to the web version of this article.)

and singlet oxygen ($^1O_2$) upon illumination with visible light; they tightly bind to G-quadruplex (G4) structures located in the promoter and 5′-untranslated mRNA region of the *KRAS* oncogene [13–16]. The *KRAS* gene is mutated in >90% pancreatic tumours where it reprograms the metabolism in order to produce the biomass necessary for proliferation [17,18]. It plays also the critical role of regulating the ROS homeostasis in PDAC cells by controlling Nrf2, a cellular ROS-sensor [19,20].

Contrarily to conventional chemotherapy, the porphyrins are activated only in the irradiated tumor and not in the surrounding tissues, thus giving limited side effects. Drugs delivered with nanoparticles with a diameter size exceeding the renal clearance threshold can extravasate from leaky tumor vessels and accumulate in the tumor [21]. This makes the drugs associated to nanoparticles more tumor specific than free drugs: a behavior called enhanced permeability retention (EPR) effect. Additionally, as ROS and $^1O_2$ do not diffuse very much from the production site [22], free porphyrins may trigger a different cellular effect than liposome-bound porphyrins, depending on their localization within the cells. In our study we have compared the anticancer activity of alkyl-porphyrins **2b** and **2d** delivered in two different ways: as free molecules or engrafted into POPC liposomes. The results show that both free and POPC-bound porphyrins (L-**2b** and L-**2d**) activate, upon illumination with visible light, a strong photodynamic process that dramatically reduces the cell viability in the nanomolar concentration range. Interestingly, the fraction of **2d** binding to the membrane produces lipid ROS, while the fraction of **2d** located in the cytoplasm inhibits the *KRAS*-Nrf2-GPX4 axis, thus activating cell death by ferroptosis. By contrast, L-**2d**, in which the porphyrin is engrafted into the liposomes, acts as a ROS-generating photosensitizer, promoting cell death mainly by apoptosis. In conclusion, our study demonstrates for the first time that cationic alkyl-porphyrins activate a dual mechanism of cell death: ferroptosis and apoptosis. The former mechanism prevails in cells treated with free alkyl porphyrins, while the latter is predominant when the porphyrins are delivered engrafted into POPC liposomes.

2. Materials and Methods

2.1. Cell Culture, Cell Viability and Proliferation Assay

Pancreatic cancer cells, Panc-1, BxPC-3, MIAPaCa-2 cells were mainained in exponential growth in Dulbecco's Modified Eagle's Medium (DMEM) containing 100 U/ml penicillin, 100 mg/ml streptomycin, 20 mM L-glutammine and 10% Fetal Bovine Serum (Euroclone, MI, Italy). Cell viability were measured by seeding 9×10^3 cells/well in 96-well plate and performing the resazurin assay, photoactivating the porphyrin with a metal halogen lamp (irradiance 8 mW/cm^2 for 15 min, light dose 7.2 J/cm^2). Clonogenic assays were carried out on Panc-1 or BxPC3 cells seeded in a medium after being diluted in a way that a single colony could be formed from each well. After 15 days of growth, the colonies of at least 50 cells were counted and the results reported in bar plots. The IC_{50} values, i.e. the concentration of the porphyrin necessary to reduce the metabolic activity by half, was calculated from dose-response curves.

2.2. Liposome Preparation

POPC (1-palmitoyl-2-oleoyl-sn-glycero-3-phosphocholine, ≥ 99%) was bought from Corden Pharma AG (Switzerland), **2b** and **2d** were synthesized as previously described[13] (**Supplementary S1**). The Phosphate Buffered Saline (PBS, pH 7.4, 10 mM $H_2PO_4^-/HPO_4^{2-}$, 137 mM NaCl, 2.7 mM KCl) for chromatography, spectroscopy and biophysical studies was prepared by dissolving a solid PBS mixture (Sigma-Aldrich) in ultrapure water (18.2 MΩcm^{-1}, MilliQ, MerckMillipore). 10 mM POPC was suspended in PBS and extruded 10 times through a 50 nm diameter polycarbonate membrane (Whatman Nucleopore®, GE Healthcare, Chicago, IL, USA), using a Lipex™ Extruder (Northern Lipids, Burnaby, Canada) and 35–40 bar N_2 pressure. Liposome stock solutions were stored at 4 °C. Liposomes were analyzed by Nanoparticle Tracking Analysis (NTA). Measurements were carried out on a NanoSight LM10-HS equipped with an Andor Lucas EMCCD camera, a LM14 temperature controller and a laser diode operated at 404 nm. The stock solution was diluted with a factor of 10^5 using filtered (to 0.1 μm) PBS. More than 9000 individual particle diffusion tracks were recorded (20 °C, 25 fps, camera gain 450, 10 videos of 15 s). The data was analyzed using the NanoSight NTA 2.3 software. Mode diameter 68 ± 1, Average diameter 85 ± 1 nm, SD of distribution 39 ± 1 nm, 1.95×10^{13} particles/ml for 10 mM POPC). To engraft the alkyl porphyrins to the liposome surface we mixed in phosphate buffer the liposome (16 mM POPC final) and the alkyl porphyrin (20 μM final), the mixture was breafly vortexed and incubated for 1 h at room temperature (phosphate buffer: 10 mM $NaH_2PO_4{\cdot}2H_20$, 5 mM $Na_2HPO_4{\cdot}2H_20$, 140 mM Na^+, pH 7.4). Stock solutions of liposomes functionalized with the porphyrins (L-**2b** and L-**2d**, 0.125 mol%) were stored at 4 °C.

2.3. Surface Plasmon Resonance, Size-Exclusion HPLC and Fluorescence Experiments

A Biacore sensor chip L1 (gold surface engrafted with hydrophobically modified dextran) was used in a Biacore X100 SPR instrument (both GE Healthcare Chicago, IL, USA). The instrument was equilibrated with filtered PBS at 37 °C for 2 h prior to beginning the measurement. During the measurement (37 °C), a suspension of POPC liposomes (0.5 mM lipid concentration,) in PBS was injected as the capture solution (300 s, 6 μl/min), immobilizing intact liposomes on the chip surface.[53,54] After rinsing with PBS at high flow (40 μl/min) and signal equilibration in a flow of PBS (1 μl/min), 0–100 μM solutions of **2b** or **2d** in PBS were injected (contact time 600 s, 1 μl/min) and afterwards their dissociation monitored under a continued slow flow. (600 s, 1 μl/min). The sensorgrams were aligned at the point of the sample injection (both on the time and response axes), and binding and stability values were extracted at 550 s after injection start and end, respectively.

Size-exclusion chromatography and fluorescence experiments are described in **Supplementary S1**.

2.4. FACS, ROS Detection and Annexin-PI Experiments

FACS was performed for uptake studies. Panc-1, BxPC-3 and MIA PaCa-2 cells, plated in a 12-well plate at density of 0.8×10^5 cells/well, were treated only with **2b**/**2d** or with L-**2b**/L-**2d** (1 μM) for 4 h or with 80 μM dynamin inhibitor I, Dynasore (Calbiochem, Merck Millipore, Germany), for 30 min and then with **2b**/**2d** or with L-2b/L-2d (1 μM for 4 h). After incubation, the cells were trypsinized and pelleted. The pellets were resuspended in 500 μl of PBS and immediately analyzed by BD FACSCalibur flow cytometer equipped with a 488 nm argon laser. A minimum of 10^4 cells for each sample were acquired in list mode and

analyzed using Cell Quest software. The cell population was analyzed by FSC and SSC light. The signal was detected by FL3 (680 nm) channel in log scale.

Annexin V–propidium iodide assays were carried out by using the Annexin-V-FLUOS Staining Kit (Roche Diagnostics GmbH, Germany) following the manufacturer instructions. Briefly, Panc-1 (0.9×10^5 cells/well) and BxPC-3 (1.2×10^5 cells/well) cells were seeded in 12-well plate and treated after 24 h with **2d** or L-**2d** in different concentrations (10, 20 or 30 nM). The day after the treatment, the plate was illuminated with visible light (light dose, 7.2 J/cm^2), and 24 h after irradiation, the cells were harvested by trypsinization and resuspended in incubation buffer containing annexin-V–fluorescein and propidium iodide. After 15 min of incubation in the dark, the cells were diluted by adding 200 μl of incubation buffer and analyzed on the BD FACSCalibur flow cytometer. A minimum of 10^4 cells for each sample were acquired in list mode and analyzed using Cell Quest software. The signal was detected by FL1 (530 nm) for annexin-V and FL2 (585 nm) for propidium iodide.

ROS were measured by cytofluorimetry. Panc-1 and BxPC-3 pancreatic cancer cells were treated with porphyrin **2b**/**2d** or L-**2b**/L-**2d** (10, 20 or 30 nM) for 24 h and then illuminated with visible light (light dose, 7.2 J/cm^2). After one day, the medium was removed, the cells were washed twice with PBS and incubated with 300 μl of 10 μM CM-H_2DCFDA (Invitrogen, USA) for 30 min in phenol red-free DMEM without serum. After two washings with PBS, the cells were trypsinized and transferred into FACS tubes containing 1 ml of PBS. The suspension was centrifuged at 1200 rpm for 3 min. The pellet was resuspended again in 300 μl of PBS, and the fluorescence was measured on the BD FACSCalibur flow cytometer.

2.5. Western Blot Assays

Protein samples were separated in 10% SDS-PAGE and blotted onto nitrocellulose membrane at 70 V for 2 h. The nitrocellulose membrane was blocked for 1 h with 5% non-fat dried milk in PBS and 0.1% Tween (Merck Life Science, MI, Italy) at room temperature. The primary antibodies used were: anti-*KRAS* (clone 3B10—2F2, mouse monoclonal, IgG mouse, Merk Life Science, Milano, Italy), anti-B-Raf (clone D9T6S, monoclonal antibody, IgG rabbit, Cell Signalling Technology, Leiden, The Netherlands), anti-pAKT (clone 193H12, monoclonal antibody, IgG rabbit, Cell Signalling Technology, Leiden, The Netherlands), anti-AKT (polyclonal antibody, IgG rabbit, Cell Signalling Technology, Leiden, The Netherlands), anti-pMEK (clone 41G9, monoclonal antibody, IgG rabbit, Cell Signalling Technology, Leiden, The Netherlands), anti-MEK (polyclonal antibody, IgG rabbit, Cell Signalling Technology, Leiden, The Netherlands), anti-pERK (polyclonal antibody, IgG rabbit, Cell Signalling Technology, Leiden, The Netherlands), anti-ERK (polyclonal antibody, IgG Rabbit, Cell Signalling Technology, Leiden, The Netherlands), anti-Nrf2 (clone D1Z9C, monoclonal antibody, IgG rabbit, Cell Signalling Technology, Leiden, The Netherlands), anti-β-actin (monoclonal antibody, IgG Mouse, Merk Life Science, Milano, Italy); anti-GAPDH (monoclonal antibody, IgG Mouse clone GAPDH-71.1, Merk Life Science, MI, Italy), anti-PARP (polyclonal antibody, IgG rabbit, Cell Signalling Technology, Leiden, The Netherlands), anti-Casp3 (polyclonal antibody, IgG rabbit, Cell Signalling Technology, Leiden, The Netherlands), anti-GPX4 (monoclonal antibody, IgG mouse, ab125066, Abcam, Cambridge, UK) . Apoptosis was triggered by using: 100 nM ADR and 1 μM AT-199 or TRAIL (2.5 ng/ml) and bortezomib (0.1 μM) (Merk Life Science, Milano, Italy) and inhibited by using Boc-D-FMK (Abcam, Cambridge, UK). The membranes were incubated overnight at 4 °C with the primary antibodies, then washed with 0.1% Tween in PBS and incubated for 1 h with the secondary antibodies conjugated to horseradish peroxidase: Anti-mouse IgG (diluted 1:5000) and anti-rabbit IgG (diluted 1:5000) (Merck Life Science, MI, Italy). The signal was developed with Super Signal® West PICO, and FEMTO (Thermo Fisher Scientific, Waltham, MA, USA) and detected with ChemiDOC XRS, Quantity One 4.6.5 software (Bio-Rad Laboratories, Segrate, MI, Italy).

2.6. Confocal Microscopy

To analyze the intracellular distribution of **2d**/L-**2d**, Panc-1 cells were seeded on 8-well polymer chambered coverslips (Ibidi GmbH, Germany, cat n° 80,826), grown for 24 h and incubated overnight with 5 μM **2d**/L-**2d** or L-Cy5 in complete DMEM in the dark. Cells were then loaded for 20 min with 2 μg/ml Hoechst and imaged in phenol red-free DMEM on a Leica TCS SP8 confocal microscope (Leica Microsystems, Germany) equipped with a stage-top environmental chamber (Okolab, Italy) and operated by Leica Application Suite X (LAS X) 3.5.5 software. Images were collected as z-stacks using a 63 x/1.4 oil immersion objective, a 405 nm diode laser (Hoechst excitation) and a tunable white-light laser (λ_{exc}: **2d**, 580 nm; Cy5, 650 nm), and are reported as maximum intensity projections.

The colocalization with organelle-specific markers was investigated on Panc-1 cells seeded on 8-well or 18-well polymer chambered coverslips (Ibidi GmbH, Germany, cat. n° 80,826 and 81,816) and incubated for 24 h with 3 μM **2d**/L-**2d** in the dark. Cells were then labeled for 30 min with 100 nM MitoTracker Green or 75 nM LysoTracker Green DND-26 (Invitrogen, Walthman, MA, USA) in the presence of 2 μg/ml Hoechst prior to in vivo confocal analysis on a Leica TCS SP8 microscope with environmental control. Alternatively, **2d**/L-**2d**-treated cells were fixed with 3% PFA and immunolabeled with anti-LAMP1 (clone D2D11, monoclonal antibody, IgG rabbit, monoclonal antibody, IgG Mouse, Merk Life Science, MI, Italy) or anti-KDEL (rabbit monoclonal, IgG rabbit, abcam, Cambridge, UK) primary antibodies followed by Goat Anti-Rabbit IgG AlexaFluor 488-conjugated secondary antibody (abcam, Cambridge, UK). Nuclei were counterstained with Hoechst. Single optical sections were acquired using 63×/1.4 (MitoTracker, LysoTracker) or 100×/1.4 (LAMP1, KDEL) oil objectives with excitation at 405 nm for Hoechst, 490 nm for MitroTracker and LysoTracker, 495 nm for AlexaFluor 488, and 580 nm for **2d**.

For in vivo lipid peroxidation assay, Panc-1 cells were seeded on glass dishes (WillCo Dishes 5040, WillCo Wells, Amsterdam, The Netherlands) and treated after 12 h with **2d**/L-**2d** (40 nM) in the dark. After 24 h, cells were irradiated or treated with Erastin (Sigma-Aldrich, MO USA) and loaded with 2 μM c-11 bodipy $^{581/591}$ (LifeTechnologies, CA, USA) and 10 μg Hoechst (Sigma-Aldrich, MO USA). The 591/510 emission shift was observed for 15 h by acquiring images every 10 min. Images were collected as z-stacks using a 63 x/1.4 oil immersion objective and a costant laser power was used for the four experimental conditions compared. ROI quantification tool (LASX) was used for the quantification, GraphPad prism for the analysis.

Images were deconvolved using Huygens Essential version 18.10 software (Scientific Volume Imaging, the Netherlands). Fluorescence intensity profiles were measured along a 25 μm-line using Leica Application Suite X (LAS X) 3.5.5. Each profile was normalized to its maximum peak intensity.

2.7. Statistics

Data are reported as mean values ± standard error (SE). Statistical analyses were carried out by using Sigma Plot software. Group differences were analyzed by Student's *t*-test. Groups are considered different when $P < 0.05$.

3. Results and Discussion

3.1. Preparation and Characterization of Porphyrin-Engrafted Liposomes

Palmitoyl-2-oleoyl-sn-glycero-3-phosphocholine (POPC) liposomes were obtained by extruding 10 times a 10 mM POPC solution in PBS through a 50 nm diameter polycarbonate membrane using N_2 at 35–40

bar [23]. The liposomes analyzed by Nanoparticle Tracking Analysis (NTA) gave an average diameter of 85 ± 1 nm (Fig. 1A-C), which did not practically change upon functionalization with the alkyl porphyrins (not shown). Porphyrins **2b** and **2d** have been synthesized as previously described [13] (Fig. 1D). Both have similar excitation/emission spectra in PBS. Typical excitation/emission spectra of porphyrin **2d** are shown in Fig. 1E. The emission spectra show that the fluorescence of 1.25 μM free **2d** is strongly quenched due to π-stacking interactions between the porphyrin planar macrocycles. The addition of POPC liposomes strongly increases the fluorescence intensity (spectrum after 10 min), which levels off with time (spectrum after 50 min). This is due to the fact that upon binding to the liposome, the porphyrins dissagregate and their quantum yield for fluorescence increases. The alkylated porphyrins efficiently bind to POPC liposomes (Fig. 1F), as determined independently by size-exclusion HPLC and Surface Plasmon Resonance (SPR) assays. The HPLC chromatograms in Fig. 1G showed that when 0.1 mM **2d** were injected alone on the size-exclusion column, the porphyrin fluorescence was not visible, as observed with **2b**, as a result of aggregation-related quenching. At a concentration of 10 μM a faint signal appeared. But when **2d** was mixed with POPC liposomes at 0.1 mol% (10 μM **2d**, 10 mM POPC), fluorescent liposomes were observed, eluting at the same time as the control empty liposomes, in nice agreement with fluorescence spectra. A similar behavior was obseserved with porphyrin **2b** at 1 mol% (100 μM **2b**, 10 mM POPC) (Fig. S2). These results are corroborated by the SPR data obtained with **2b** and **2d**, where an increase in detector response proportional to the concentration of the alkylated porphyrin was observed. Fig. 1H shows typical SPR curves obtained with **2d**. Upon binding, in the SPR flow-cell the liposome bilayers are expected to saturate in guest molecules (**2d**) to a steady state level, according to their concentration in the flow. At concentrations >5 μM, the response increased non-linearly for the data points at 10 and 20 μM, which again indicates the presence of aggregates. In fact, if **2d** forms aggregates, its interaction with POPC liposomes would fix on the liposome surface a higher amount of porphyrin so that the SPR response is expected to be higher. The binding was proportional to **2d** concentration but did not approach saturation, indicating that the liposomes have a very high loading capacity. The stability of **2d** engraftment during the dissociation phase on SPR was very high (approximately 80% of the maximal binding level after 550 s). We also performed experiments with **2b** and found that even higher amounts of porphyrin (50 μM) can efficiently bound to the liposomes without reaching saturation (Fig. S3).

Next, we measured the production of ROS by **2b**/L-**2b** and **2d**/L-**2d** in pancreatic Panc-1 and BxPC3 cancer cells, using CM-H_2DCFDA, which is non-fluorescent in the reduced state. When the probe is oxidized by cellular ROS and its acetate group removed by esterases, it becomes fluorescent. Fig. 1I shows that the fluorescence, measured by FACS, of Panc-1 and BxPC3 cells treated with **2d**, either in free form or engrafted into POPC liposomes (L-**2d**) increases in a dose-response manner. The experiment was performed also with **2b** and L-**2b**, which showed a lower ROS-generating capacity, probably because they enter into the cells less efficiently than **2d** and L-**2d**.

3.2. Uptake and Intracellular Distribution of Free and Liposome-Bound Alkyl Porphyrins

As the tetrapyrrole macrocycle of the porphyrins emits red fluorescence when excited at 488 nm, the uptake of porphyrins **2b** and **2d** was investigated by FACS (Fig. 2A). Both porphyrins, **2b**/**2d** and L-**2b**/L-**2d**, enter efficiently in pancreatic cancer cells. According to the fluorescence emitted by the porphyrins (Ex 488 nm, Em 660 nm), **2d**/L-**2d** with a C18 chain is taken up ~5-times more than **2b**/L-**2b** with a C14 chain. Due to its higher uptake, in this study we focused mostly on **2d**/L-**2d**. We found that **2d** and L-**2d** are taken up almost with the same efficiency by Panc-1 and MiaPaCa-2 cells, while in BxPC3 cells the uptake of L-**2d** is ~20% higher than that of free **2d** (Fig. S4**)**. An insight into the mechanism by which **2d** and L-**2d** penetrate the cell membrane was obtained by treating the cells with dynasore, a noncompetitive inhibitor of dynamin GTPase activity, which blocks clathrin-mediated endocytosis [24]. Fig. 2B-F shows that dynasore reduces the uptake of L-**2d** in Panc-1, BxPC3 and MIA-PaCa pancreatic cancer cells by ~45%, 20%, 50%, respectively, while free **2d** by ~55%, 30%, 70% (Fig. S4). We also tested cytochalasin, an inhibitor of micropinocytosis [25], finding that it did not have any impact on the uptake. Together, these experiments suggest that endocytosis is a mechanism through which **2d** and L-**2d** are internalized in Panc-1 cells.

We also performed confocal microscopy experiments to investigate how **2d** and L-**2d** distribute within the cell. Fig. 2G shows maximum intensity projections of living Panc-1 cells treated with free **2d** and L-**2d**. The nucleus of the cells was stained with Hoechst, while the porphyrin was visualized through its red fluorescence emitted upon excitation at 580 nm. The merge panel shows that free **2d** locates in the membrane lipid bilayer, owing to its lipophilic chain, and also in the cytoplasm, with a punctuated distribution. This suggests that **2d** is internalized by an active (endocytosis) and, to a lesser extent, also by passive a (membrane fusion) mechanism of transport. The fraction of **2d** following the endocytic pathway is trapped into endosomes, which account for the observed punctuated pattern. Most endosomes lay in the cytoplasm, but some seem to co-localize with the nucleus (pink dots). By contrast, L-**2d** seems to be taken up only by endocytosis, showing a robust punctuated cytoplasm distribution. The images did not show any location of L-**2d** in the membrane. Fig. 2H shows Panc-1 cells treated with POPC liposomes marked with Cy5.5, encapsulated in the central core of the nanoparticle. The merge image shows a punctuated distribution similar to that shown in Fig. 2G, where the liposomes where stained by the porphyrin**.** The two different staining methods gave the same distribution pattern according to which the liposomes are predominantely localized in the cytoplasm and slightly in the nucleus. The punctuated distribution of **2d** and L-**2d** suggested us to investigate if they target specific organelles (Fig. 3A-F). Micrographs of living Panc-1 cells treated with free **2d** or L-**2d** and stained with MitoTracker Green are presented in Fig. 3A, B. Individual channel images of porphyrin **2d** or L-**2d** and MitoTracker green are shown in grey scale, while the merge panel is reported in colour. The images show that the porphyrin, either free or engrafted into the liposomes, does not co-localize with the mitochondria, as demonstrated by the fact that the fluorescence intensity profiles of **2d**/L-**2d** and Mito Tracker green, along a fixed straight line, do not overlap. We then asked if there is co-localization between the porphyrins and lysosomes by using LysoTracker green. When we carried out the experiment with living cells, the LysoTracker green fluorescence was strongly quenched by **2d**/L-**2d**, suggesting that LisoTracker and the porphyrin co-localize and interact with each other (not shown). However, to directly demonstrate that **2d** and L-**2d** target the lysosomes, we treated living Panc-1 cells with the porphyrin, we then fixed the cells and immunolabeled them with LAMP-1 antibody, specific for the lysosomal-associated membrane protein 1 residing across the lysosomal membranes [26]. The merge panel and the fluorescence intensity plots of Fig. 3C show that free **2d** strongly co-localizes with the lysosomes: the yellow foci indicate co-localization between **2d** and lysosomes (Fig. S5 shows a magnified image). The fluorescence intensity plots show that L-**2d** co-localizes with lysosomes only partially, as most L-**2d** remains trapped into endosomes. Finally, we tested if **2d** and L-**2d** co-localize with the endoplasmic reticulum (ER) (Fig. 3E, F). We stained ER with KDEL antibody recognizing Lys-Asp-Glu-Leu (KDEL) at the carboxy-terminus of soluble endoplasmic reticulum (ER) resident proteins [27]. ER shows an intense staining spreading over the whole cytoplasm. The fluorescence intensity plots show that there is no overlapping between KDEL and **2d**. Indeed, free **2d** is accumulated in an area where the ER signal is more rarefied (most probably occupied by the lysosomes). Instead, L-**2d** shows a slight co-localization with ER. To sum up, we can state that: (i) free **2d** is transported into Panc-1 cells via endocytosis and passive diffusion; it localizes in the membrane as well as in the cytoplasm; in this latter case, it co-localizes with lysosomes but not with

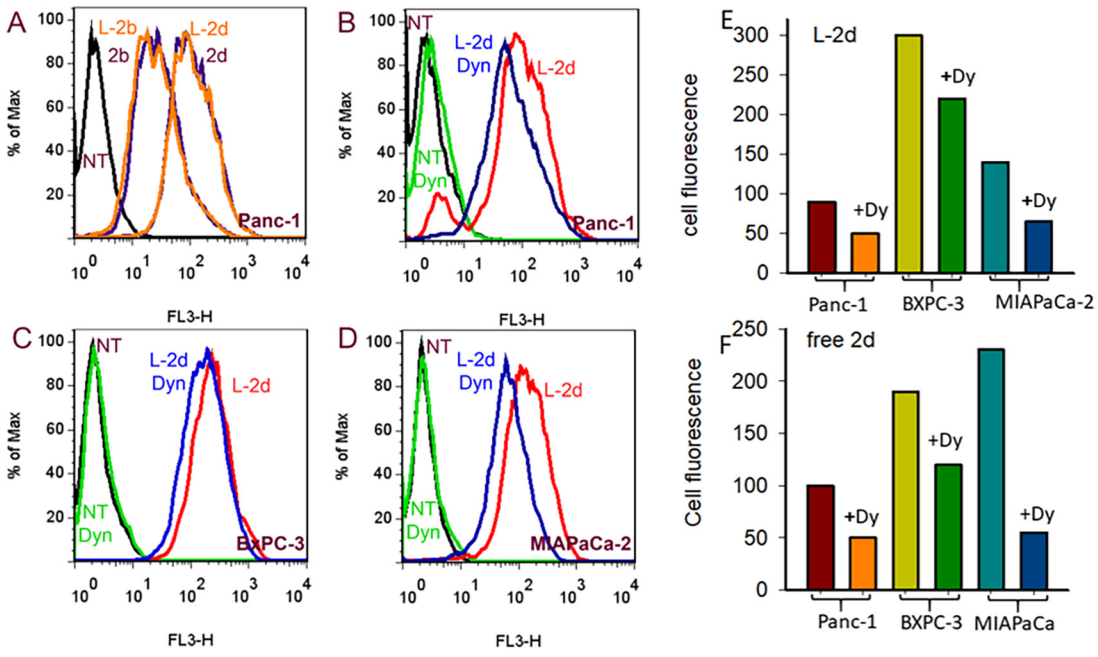

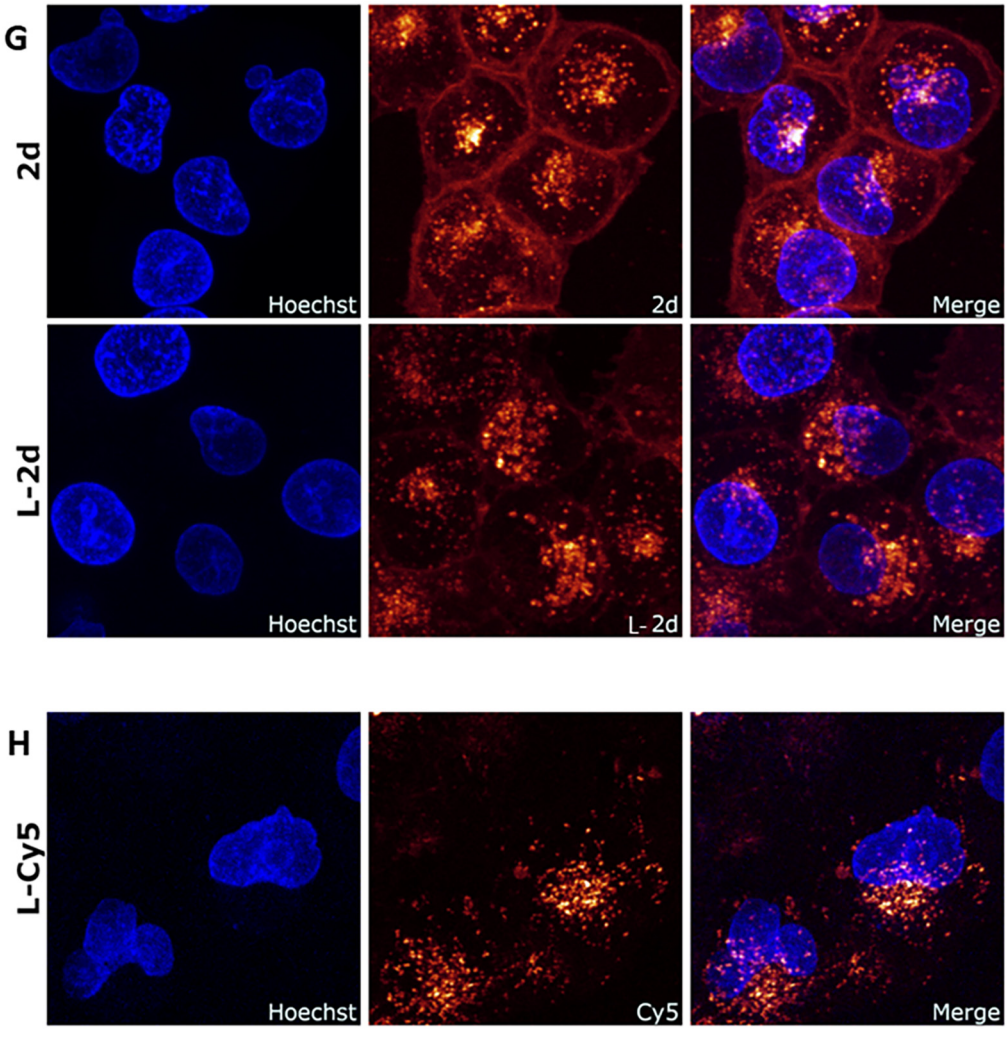

(caption on next page)

Fig. 2. (A) FACS analyses of Panc-1 cells treated with 1 μM free **2d**/**2b** or L-**2d**/L-**2b** for 6 h; (B–D) FACS of Panc-1, BxPC3 and MIA PaCa cancer cells treated with free **2d** or L-**2d** for 6 h in the presence and absence of dynasore; (E, F) Bar plots reporting the fluorescence of the cells terted with the L-**2d** in the absence and presence of dynasore; (G) Confocal microscopy images of living Panc-1 cells treated overnight with 5 μM **2d** and L-**2d**. The nuclei of the cells have been stained with Hoechst (blue), while porphyrins **2d** is visualized through its red emission. The merge images are also shown; (H) Living Panc-1 cells have been treated with POPC liposomes marked with Cy5 encapsulated in the central core of the liposomes (Hoechst, blue; Cy5, glow). The images show the distribution of Cy5-labeled liposomes in Panc1-cells. All the images are maximum intensity projections of confocal z-stacks spanning the entire cell. (For interpretation of the references to colour in this figure legend, the reader is referred to the web version of this article.)

mitochondria and ER; (ii) L-**2d** is instead taken up by endocytosis only, showing endosome particles in the cytoplasm, partly colocalizing with lysosomes and ER.

3.3. Free Porphyrin 2d Downregulates the KRAS-Nrf2 axis while Liposome-Bound Porphyrin L-2d Does Not

In general, cancer cells produce more ROS than normal cells, due to a higher metabolic rate and hypoxia conditions [28]. As high levels of ROS can cause oxidative damage to DNA, RNA and phospholipids, they are controlled through a sophisticated detoxifying system involving Nrf2 and enzymatic antioxidants [29–31]. As illustrated in Fig. 4A, the redox homeostasis in PDAC cells is controlled by the *KRAS*-Nrf2 axis. ROS stimulate *KRAS*, which in turn upregulates Nrf2: a ROS sensor gene that activates the cellular antioxidant response [29,30,32]. The *KRAS*-Nrf2 axis prevents the accumulation of ROS that could otherwise inhibit proliferation. When the cells are treated with porphyrin **2d** and light, intracellular ROS increase dramatically, via a type II photodynamic mechanism [33] (Fig. 4B). Although ROS stimulate the *KRAS*-Nrf2 axis, we observed a downregulation of *KRAS* and Nrf2 because free **2d** located in the cytopasm binds to *KRAS* mRNA, at G4 structures located in the 5′-untraslated region [13]. Upon irradiation, the porphyrin produces ROS and $^1O_2$ that degrade mRNA and thus suppress *KRAS* translation. The effect of **2d** in free form on *KRAS* is clearly seen in Fig. 4D–I, which shows that 48 h after irradiation, *KRAS* is reduced in a dose-response manner in Panc-1 and BxPC3 cells to ~30% of the control (non-treated cells). The suppression of *KRAS* results in the downregulation of Nrf2 (Fig. 4J, left), and thus in the loss of the control mediated by Nrf2 of the ROS homeostasis. Under these conditions, ROS increase dramatically and induce cell death. Interestingly, a different picture was observed when the cells were treated with L-**2d** and light. In this case, *KRAS* was upregulated in BxPC3 cells at both 24 and 48 h, while in Panc-1 cells only at 24 h. This suggests that the porphyrin engrafted into the liposomes is unable to bind to *KRAS* mRNA and suppress the gene. This correlates with the finding that L-**2d** only partly follows the endosome-lysosome pathway, differently from free **2d**. Most of L-**2d** is likely to remain engrafted into the liposomes, from where the porphyrin does not easily spread into the cytoplasm as molecule in free form capable to interact with G4 structures in *KRAS* mRNA. Upon illumination with visible light, L-**2d** generates ROS and $^1O_2$ that stimulate the *KRAS*-Nrf2 pathway (Fig. 4H–J), as occurs when the cells are treated with H_2O_2 [19,34]. As ROS generated by L-2d overcome the detoxification capacity of the cells, their accumulation induces apoptosis.

Next, it is known that in *KRAS*-driven pancreatic cancers, the signalling passes through the Mek/Erk and PI3K/Akt pathways [35]. Recent studies have demonstrated that the initiation, maintenance and progression of PDAC depend more on the PI3K/Akt pathway [36,37]. Given that cancer cells produce relatively high levels of oxidative stress, ROS play a critical role in cell growth and survival [38,39]. ROS affect *KRAS* signalling in a rather complex way. First, ROS act directly on Akt by promoting a conformational change through the formation of an intramolecular disulphide bond that causes dephosphorylation and inactivation of Akt [40,41]. This means that the large amount of ROS produced by the photoactivated porphyrin induces the dephosphorylation of Akt, the blockage of downstream pathway and inhibition of cell proliferation. By contrast, enhanced ROS generally leads to activation of the Mek/Erk pathway by a mechanism which is still unclear but probably going through the inactivation of MKPs and/or ROS-mediated modifications of Merk/Erk signalling proteins [42]. We examined by Western blots the status of the two signalling pathways in Panc-1 cells treated with the porphyrins (Fig. 4L). We found, indeed, that the ROS-generated by **2d** and L-**2d** have an opposing effect on the two pathways: the porphyrin strongly reduces P-Akt, and increases P-Mek and P-Erk in a dose-response manner. This behavior fits with the observation that the Raf/Mek/Erk pathway is activated by ROS, in a *KRAS*-independent manner [37,38]. A similar result was obtained with porphyrin **2b** (Fig. S6). As PI3K/Pdk1/Akt is the main proliferation pathway in PDAC, its inhibition by photoactivated **2d** and L-**2d** should result in a significant drop of cell proliferation.

3.4. Effect of Free and Liposome-Bound Alkyl Porphyrins on Cell Viability and Colony Formation

To evaluate the photosensitization of free or liposome-bound porphyrins **2d** and **2b**, we measured their potency to kill pancreatic cancer cells by performing cell viability assays with resazurin, a non-fluorescent phenoxazine that is reduced in fluorescent resofurin, in living and metabolically active cells.

The porphyrins were tested in Panc-1 and MIA PaCa cells, which are *KRAS* and *TP53* mutated, and in BxPC-3 cells which are only TP53 mutated. When the cells were treated in the dark with increasing amounts of L-**2d** (10, 20 and 30 nM) or free **2d**, no effect on viability was observed (typical behavior obtained with L-**2d** is shown in Fig. 5A). By contrast, upon treatment with visible light (7.2 J/cm^2) a dose-response decrease in viability was observed (Fig. 5B). By plotting the % viability at 48 h after illumination, as a function of porphyrin concentration, we found that the IC_{50} for **2d** and L-**2d** are 20.8 ± 0.6 and 19.1 ± 0.8 nM for Panc-1 cells; 25.8 ± 1.0 and 29.1 ± 1.4 nM for BxPC3 cells; 21.9 ± 1.1 and 23.5 ± 1.2 nM for MIA PaCa cells. The data show that there is little difference in phototoxicity between **2d** and L-**2d.** A similar behavior was detected with **2b** (Fig. S7).

To assess the effect of **2d** and L-**2d** on cell proliferation, we carried out a clonogenic assay with Panc-1 and BxPC3 cells (Fig. 5C, D). The cells were seeded at a dilution that a single colony could be formed by each cell. After 15 days of growth, the colonies of at least 50 cells were counted and the results reported in a bar plot. The number of colonies in the untreated and porphyrin-treated plates in the dark was the same, confirming that without photoactivation the porphyrins are not toxic. In contrast, after light treatment (7.2 J/cm^2), **2d** and L-**2d** strongly reduced the number of colonies in both types of cells. The bar plots show that 20 nM **2d**, reduced Panc-1 and BxPC3 colonies by ~50% and 70%, respectively, while L-**2d** by 70% in both types of cells. A similar result was obtained with Panc-1 cells treated with **2b** and L-**2b** (Fig. S8).

We then carried out annexin V–propidium iodide assays. In the early stage of apoptosis, the cell membrane loses its phospholipid asymmetry. Phosphatidylserine (PS) jumps into the outer leaflet of the membrane. Annexin V-FITC binding to PS can mark the cells in early apoptosis. In late apoptosis (LA), the plasma membrane is ruptured and PI can bind to intracellular DNA. The cells are stained by both PI and Annexin V. Fig. 6A, B shows a cell cytometry analysis performed on Panc-1 and BxPC3 cells treated with **2d**/L-**2d** and light. The results are reported in **Supplementary S9**. The percentage of apoptotic cells in the control (cells untreated with the porphyrin and illuminated with visible light) varies from 10 to 15%. The cells treated with empty liposome (L) and light did not induce apoptosis compared to control (nontreated cells). Instead, L-**2d** induced a strong apoptotic response, in a dose-response

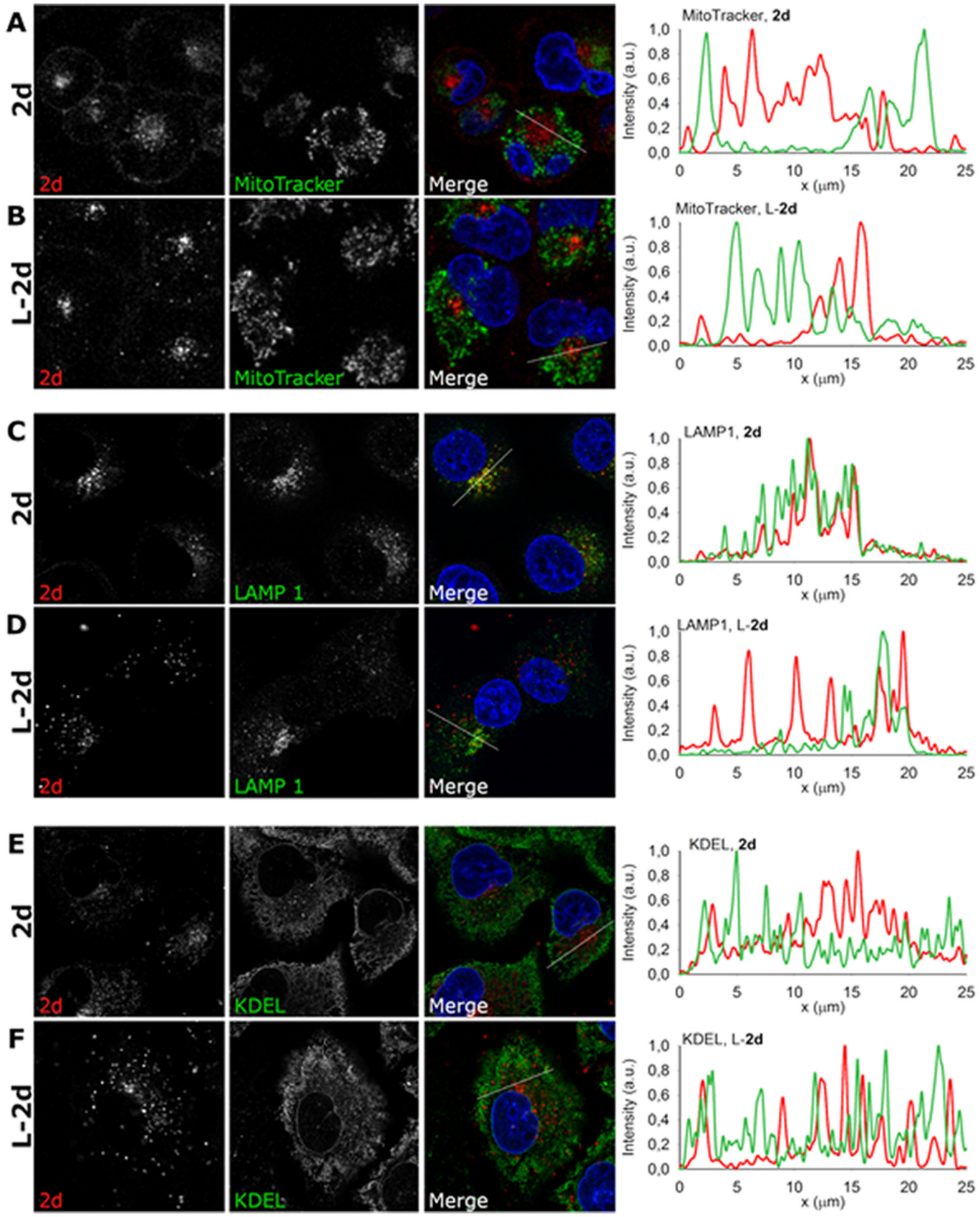

Fig. 3. (A) Confocal microscopy Fluorescence microscopic images of Panc-1 pancreatic cancer cells, co-treated with Hoechst, **2d**/L-**2d**, MitoTracker, LAMP 1, KDEL. The fluorescence intensity plots show **2d** or L-**2d** co-localization with the organelles.

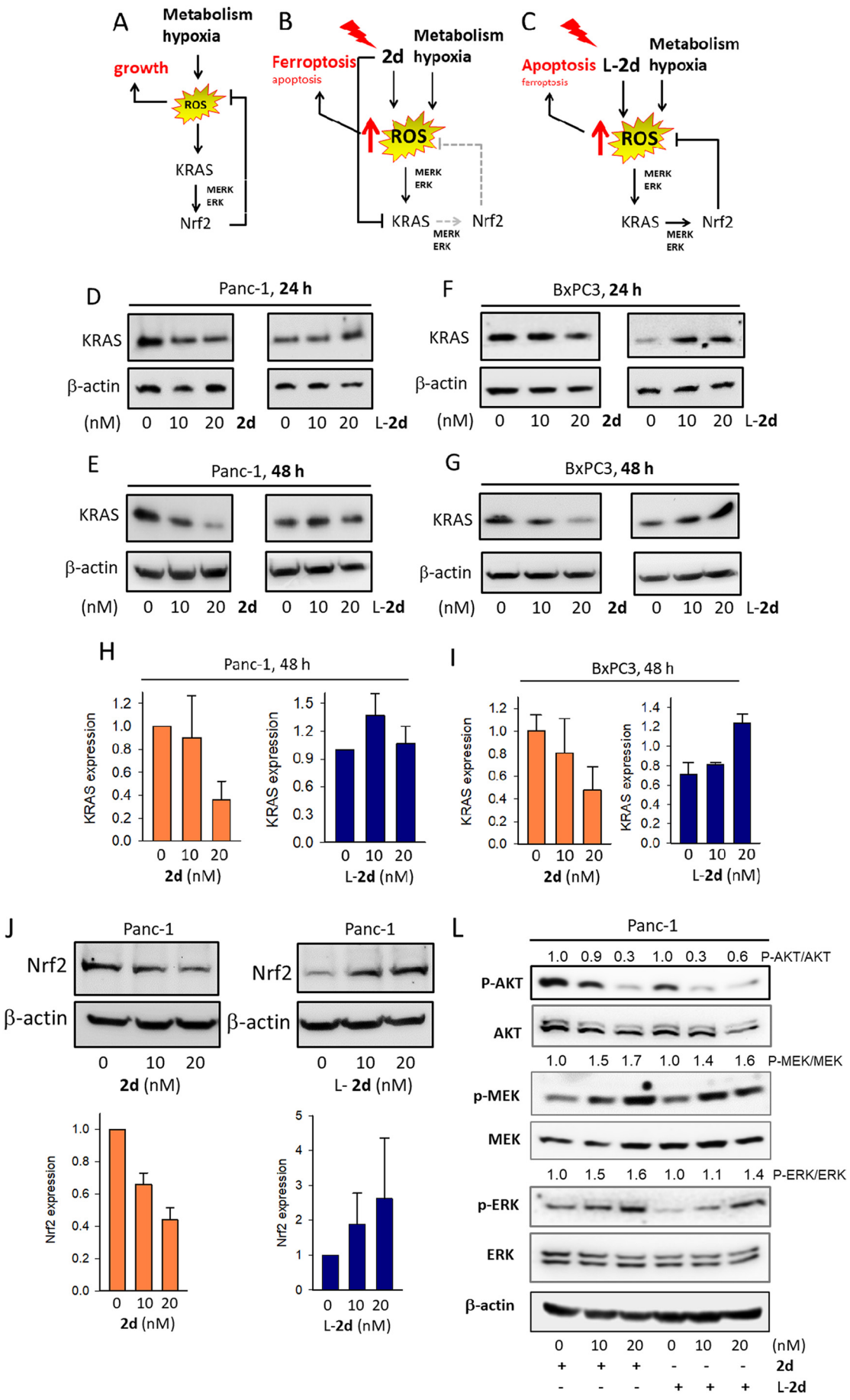

(caption on next page)

Fig. 4. (A-C) Schemes showing the *KRAS*-Nrf2 axis and the effect of porphyrin **2d** and L-**2d** on pancreatic cancer cells; (D—I) Western blots showing the expression of *KRAS* and β-actin in Panc-1 and BxPC3 cells 24 and 48 h after photo-treatment with porphyrin **2d** and L-**2d.** Panc-1 data are the average of two independent experiments. The data are the average of 2 independent experiments; (J) Expression of Nrf2 in Panc-1 cells treated with **2d**/L-**2d** and light. The data are the average of 2 independent experiments; (L) Activation of the Mek-Erk and PI3P-Akt pathways in Panc-1 cells treated with **2d** and L-**2d**.

manner, in both cell lines. The percentage of early and late apoptotic cells is 87% in Panc-1 and 75% (±10%) in BxPC3 cells, after treatment with 30 nM L-**2d**. By contrast, **2d** is less effective in promoting apoptosis: 30 nM **2d** induced apoptosis in 42% Panc-1 and 56% Bx PC3 cells (±10%). Collectively, the data show that L-**2d** is 2-fold stronger in inducing apoptosis than free **2d**.

3.5. The Alkyl-Porphyrins Activate a Complex Cell Death Involving Ferroptosis and Apoptosis

Recent studies have demonstrated that lipid peroxidation can trigger a new type of programmed cell death named ferroptosis. It was first proposed by Dixon [43] in 2012 as a new cell death caused by an iron-dependent accumulation of lethal lipid ROS. Morphologically, ferroptotic cells show a normal size nucleus in which DNA is not fragmented, a reduced mitochondrial volume and no rupture of the cell membrane. The process is inhibited by iron chelators but not by caspase inhibitors [44]. Confocal microscopy showed that only a fraction of porphyrin-treated cells exhibited the typical features of apoptosis: i.e. a rounding morphology and blebbing of the plasma membrane. Therefore we asked if our alkyl-porphyrins induce a mixed type of cell death, as observed with lung cancer cells treated with PdPT [45]. To provide evidence that the alkyl-porphyrins promote ferroptosis, we compared the behavior of **2d** and L-**2d** with erastin, a strong ferroptotic agent [46], in the presence and absence of ferrostatin 1 (Fer-1), an inhibitor of ferroptosis [47], or BocD-fmk, a broad range caspase inhibitor [48]. Fig. 7A, B shows that **2d** up to 40 nM strongly reduced the viability of Panc-1 cell in a dose response manner, after light treatment (7.2 J/cm^2). As expected, the treatment with erastin (15 μM) showed a dramatic drop in cell viability, attributed by us to ferroptosis. The cell viability was completely restored when the cells were co-treated with erastin (15 μM) and Fer-1 (15 μM). Analogously, Fer-1 strongly

rescue the viability also in Panc-1 cells treated with 20 or 40 nM **2d**, suggesting that the porphyrin too induced cell death by ferroptosis, as observed with porphyrin TPP loaded nanoparticles in B16 melanoma cells.[49] However, as Fer-1 did not fully recover the viability in the cells treated with 40 nM **2d**, in addition to ferroptosis the porphyrin activates apoptosis, in keeping with the FACS data. We then inhibited apopotosis with Bocd-fmk and found that the percentage of viable cells following a treatment with 20 and 40 nM **2d** was ~80% and ~ 50%, respectively, compared to control (untreated cells). This reduction in viability is due to ferroptosis. Together, the data indicate that free **2d** triggers a mixed mechanism of death: apoptosis and ferroptosis. We roughly estimated that 40 nM **2d** promotes ~50% ferroptosis and ~ 40% apoptosis. In Fig. 7B we report the results obtained with the liposome-bound porphyrin L-**2d**. The rescue in viability promoted by Fer-1 in Panc-1 cells treated with 40 nM L-**2d** was ~20%, suggesting that L-**2d** is a weaker ferroptotic activator than free **2d**. In this case we estimated that 40 nM L-**2d** promoted cell death by ferroptosis in 20% of the cells and apoptosis in 70% of the cells. A qualitatively similar result was observed with BxPC-3 cells (Fig. S10) and with **2b** (Fig. S11). Consistent with these data is the finding that **2d,** binding to the membranes, oxidizes the phospholipids, generating lipid ROS that trigger ferroptosis. To support this, we used C11-bodipy $^{581/591}$: a fluorescent ratio probe that allows to measure and visualize lipid peroxidation in living cells [50]. Its fluorescence shifts from red (maximum at 595 nm) to green (maximum at 520 nm) when the probe is challenged with oxidizing species [51]. Fig. 7C shows the fluorescence ratio as a function of time for a single cell loaded with C11-bodipy $^{581/591}$ and **2d** or L-**2d**. The analysis was extended to a number of cells varying from 11 to 27. It can be seen that **2d** (40 nM) increases the oxidized/reduced (510/591 nm) ratio of C11-bodipy $^{581/591}$ 2-fold more than L-**2d**, over a period of 15 h since light treatment, consistently with the finding that free **2d** binds to the membrane, while L-**2d** does not or does it in little amount. Note that erastin showed an oxidizing capacity similar to that of L-**2d** and about half of that induced by **2d.** In Fig. S12 we report Panc-1 cells treated for 15 min, 6 and 12 h with C11-bodipy $^{581/591}$ and porphyrins **2d** or L-**2d**. It can be seen that in the absence of porphyrin, the fluorescence of C11-bodipy $^{581/591}$ does not shift from red to green. In contrast, a fluorescence shift occurs in 6 h with **2d**, 12 h with L-**2d** or erastin.

Next, we investigated the extent of apoptosis triggered by the porphyrins. Fig. 7D, E shows that, compared to untreated cells, 40 nM **2d** and L-**2d** increase the fluorescence of *Z*-DEVD R110 by ~1.5- and 3-fold, respectively, suggesting that the porphyrin induces some caspase 3/7 activity. We then co-treated Panc-1 cells with **2d**/L-**2d** and Fer-1: under these conditions ferroptosis is inhibited and the cells die by apoptosis only. It can be observed that 40 nM **2d** + Fer-1 increase the Z-DEVD R110 fluorescence by 2.9-fold, while 40 nM L-**2d** + Fer-1 increase the fluorescence by 6-fold, suggesting that the inhibition of ferroptosis is compensated by an increase of apoptosis. Collectively, the data show that caspase 3/7 is more active in Panc-1 cells treated with L-**2d** than with **2d**, in agreement with FACS and cell viability assays. To confirm this behavior, we carried out Western blot experiments (Fig. 7F, G). It can be seen that L-**2d** induced more cleavage of PARP-1 and procaspase 3 than **2d** does, attesting that the porphyrin delivered with liposomes behaves more as a pro-apoptotic than ferroptotic compound.

Given the evidence that **2d** stimulates ferroptosis, we focused on GPX4, as previous studies have demonstrated that its depletion results in excessive lipid peroxidation and ferroptotic cell death [52,53]. Indeed, GPX4 is a phospholipid hydrogenperoxide glutathione peroxidase that catalyzes the reduction of lipid hydrogenperoxides in order to protect the cells against oxidative damage. Fig. 7H shows that photoactivated **2d** strongly suppresses GPX4 while L-**2d** does not. This is in keeping with the finding that **2d** induces mainly ferroptosis while L-**2d** induces mainly apoptosis. A similar behavior was observed with **2b** and L-**2b** (Fig. S13).

Finally, further support that free **2d** induces ferroptosis was obtained by a clonogenic assay (Fig. 7I, J). It can be seen that a 20 nM **2d** reduces the number of colonies to 25% of control (untreated cells). This strong inhibitory effect is nearly suppressed by Fer-1, consistently with the fact that **2d** significantly inhibits cell growth by ferroptosis.

4. Conclusion

The cationic alkyl-porphyrins **2b** and **2d** show an excellent photodynamic effect in PDAC cells, either as molecules in free form or engrafted into POPC liposomes. While the free alkyl- porphyrins penetrate the cell membrane by an active (endocytosis) and to a lesser extent by a passive (membrane fusion) transport, liposome-engrafted porphyrins are taken up by endocytosis only.

Confocal microscopy experiments showed that **2d** co-localizes with the lysosomes, from which it is released into the cytoplasm where it binds to and degrades upon illumination *KRAS* mRNA [13]. In contrast, when the porphyrin is delivered engrafted into liposomes (L-**2d**), it co-localizes only partially with the lysosomes, which presumably release into the cytoplasm a limited amount of porphyrin insufficient to suppress *KRAS*. Interestingly, this unexpected behavior affects the type of cell death mediated by the porphyrins. Indeed, the suppression of *KRAS* in Panc-1 cells results in the downregulation of Nrf2 and GPX4, which protects membrane lipids from peroxidation (GPX4 is among the targets

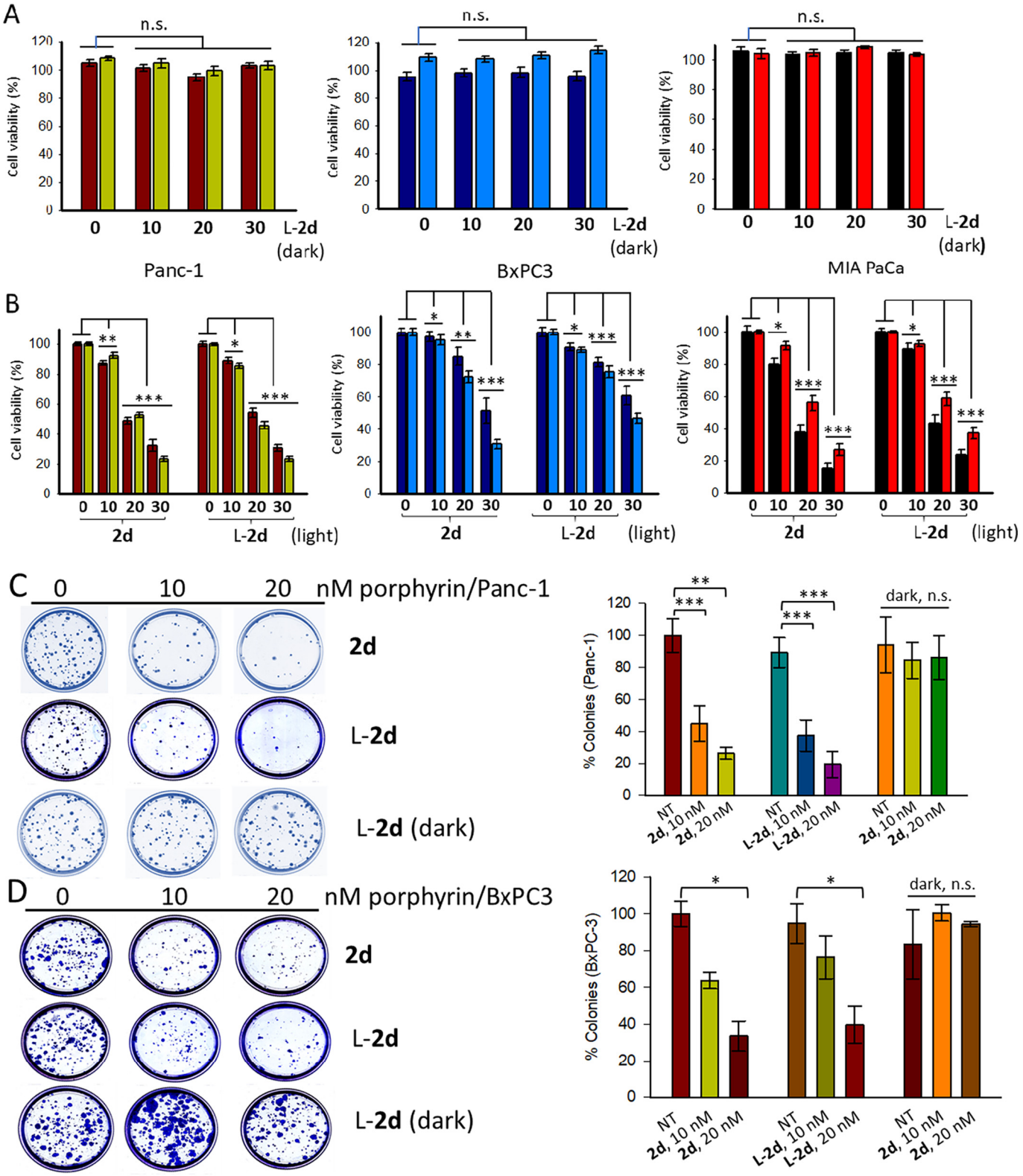

Fig. 5. (A, B) Cell viability (% values compared to cells treated only with light) of PDAC cells treated with 0, 10, 20, 30 nM L-**2d** in the dark or 0, 10, 20, 30 nM **2d** and L-**2d** after illumination with visible light (light dose, 7.2 J/cm^2). The assays were performed 24 (brown, blue and black bars) and 48 h (green, sky blue and red bars) after illumination. The data are the average of: 3 independent experiments, 7 replicates each with Panc-1; 2 experiments, 7 replicates with BxPC3; 1 experiments, 7 replicates with MIA PaCa-3. Statistical significance respect to untreated cells: $P \leq 0.05$ (*), 0.01 (**), 0.001 (***); (C, D) Clonogenic assays with Panc-1 and BxPC3 cells treated with **2d** or L-**2d** and visible light (light dose, 7.2 J/cm^2). Number of colonies was determined 15 days after illumination. Data are the average of one experiment in triplicate. Statistical significance respect to untreated cells: P $\leq$ 0.05 (*), 0.01 (**), 0.001 (***).

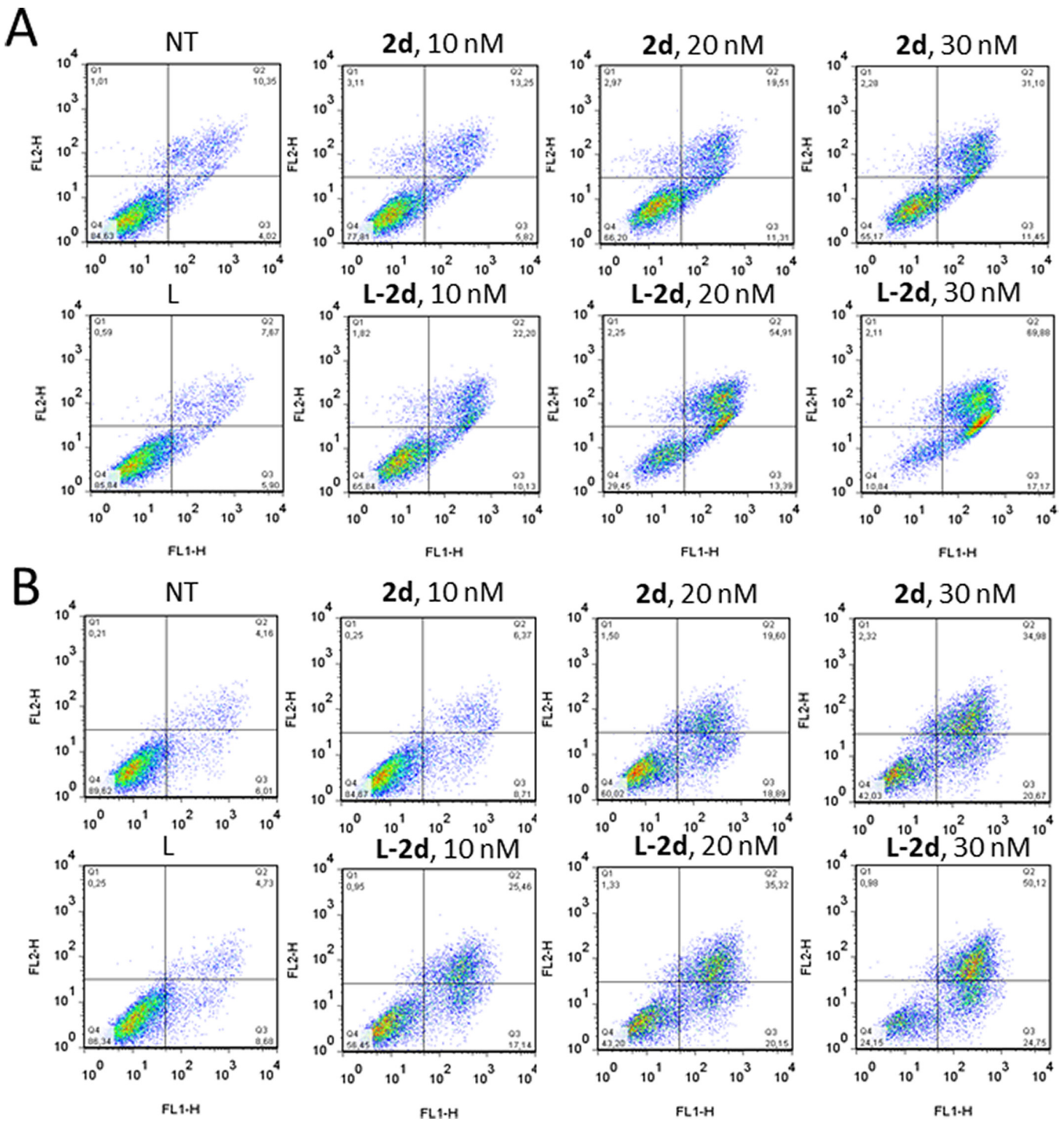

Fig. 6. Annexin-propidium iodide assay with Panc-1(top) and BxPC3 (bottom) cells treated with 0, 10, 20 and 30 nM **2d**/L-**2d** and light. Percentage of early and late apoptotic cells (Q2 + Q3) is reported in **Supplementary S9** (Table). FL1-H = annexin V, FL2-H = propidium iodide.

of Nrf2 [54]). Therefore, we think that the inhibition of the *KRAS*-Nrf2-GPX4 axis should dramatically lower the capacity of the cell to reduce lipid peroxidation and protect the membranes. Under these stress conditions, the oxidized membrane liberates lipid ROS that activate cell death by ferroptosis (Fig. 8A, B). By contrast, the porphyrin bound to the liposomes (L-**2d)** internalizes into cancer cells by endocytosis, without leaving enough porphyrin molecules in the lipid bilayer to generate lipid ROS. In the cytoplasm L-**2d** does not release sufficient porphyrin molecules to suppress *KRAS* [13] and its axis with Nrf2 and GPX4. L-**2d** is therefore a weak activator of ferroptosis. However, L-**2d** is found to efficiently generate ROS upon illumination, which strongly induce cell death by apoptosis.

To sum up, our results show that the mechanism of cell death induced by the cationic alkyl-modified porphyrins is complex, as it is based on ferroptosis and apoptosis. The two types of cell death co-exist in porphyrin treated cells and the prevalence of one over the other is in relationship with the delivery mode: liposome-engrafted alkyl-porphyrin promotes mainly apoptosis while free alkyl-porphyrin promotes mainly ferroptosis. Our study provides new insights into the type of cell death induced by alkyl porphyrins, which are useful for a rational

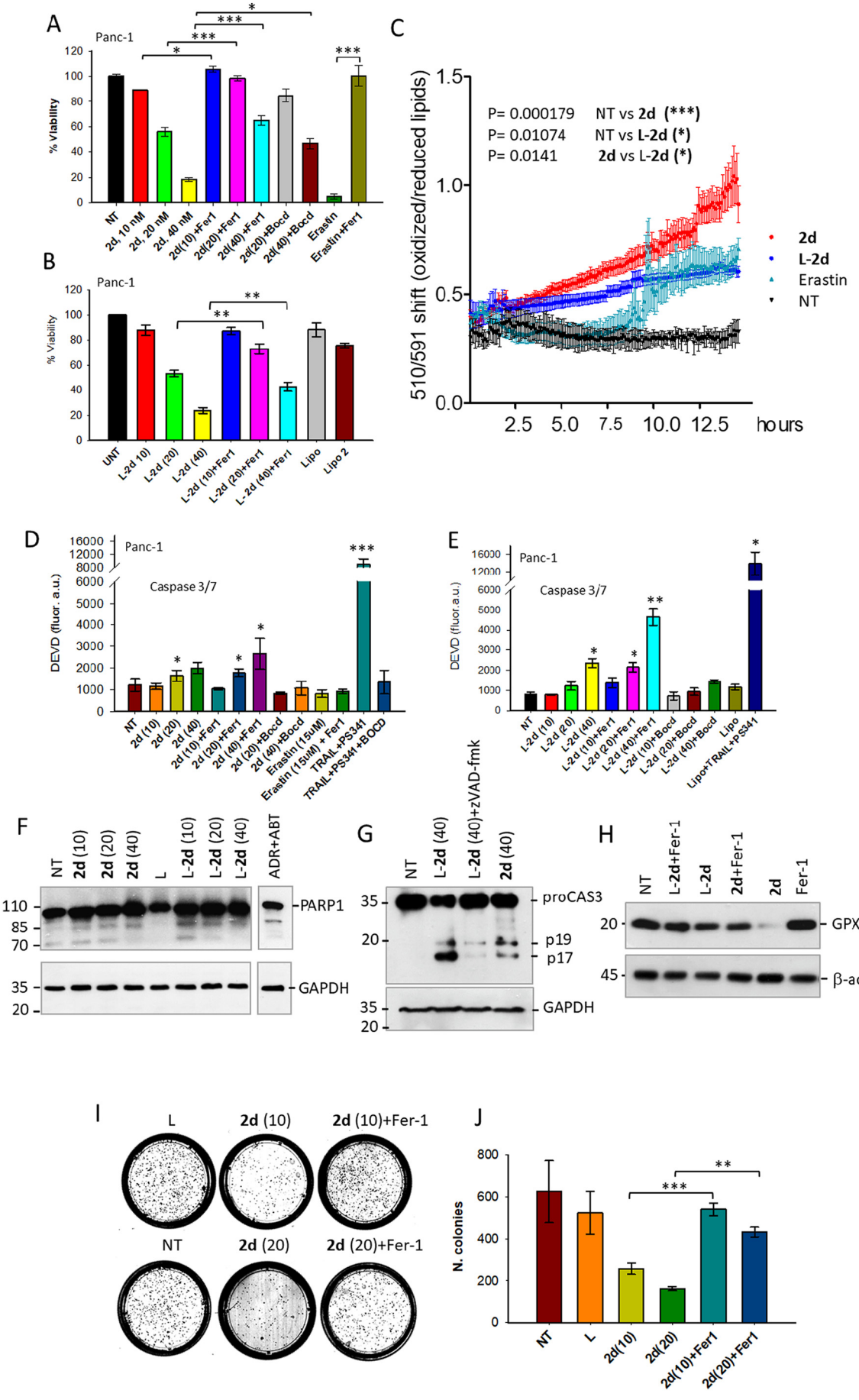

(caption on next page)

Fig. 7. (A) Cell viability assay (% compared to cells treated only with light). Panc-1 cells phototreated with **2d**, **2d** + Fer-1, **2d** + Bocd, erastin, erastin + Fer-1; (B) Viability assay of Panc-1 cells phototreated with L-**2d**, L-**2d** + Fer-1 and L (empty liposome); (C) Fluorescence ratio of C11-Bodipy $^{581/591}$ as a function of time for single cell loaded with the probe and **2d** or L-**2d**. The analysis was extended to a number of cells varying from 11 to 27 up to 15 h since illumination; (D, E) Caspase 3/7 activity assay. Panc-1 cells were phototreated with **2d**, **2d** + Fer-1, **2d** + Bocd, erastin, erastin + Fer-1, TRAIL+PS341, TRAIL+PS341 + bocd, L = liposome; (F, G) Western blots showing the expression of PARP-1, pro-caspase 3 and GAPDH in Panc-1 cells treated with **2d**, L-**2d**, ADR + ABT; (H) Expression of GPX4 and β-actin in Panc-1 cells treated with **2d**, Fer-1, **2d** + Fer-1, L-**2d**, L-**2d** + Fer-1. $P \leq 0.05$ (*), 0.01 (**), 0.001 (***); (I, J) Clonogenic assay of Panc-1 cells treated with liposome (L), **2d**, L-**2d**, **2d** + Fer-1. Bar plot reporting the number of colonies in untreated and treated Panc-1 cells 15 days after illumination. Each experiment has been performed in triplicate. P ≤ 0.05 (*), 0.01 (**), 0.001 (***).

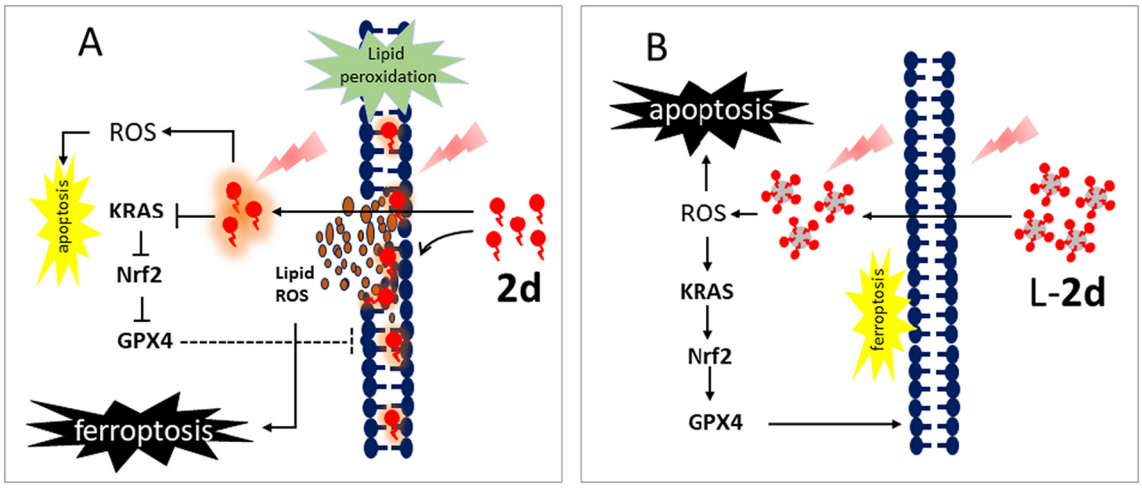

Fig. 8. (A, B) Putative mechanism of action of liposome-bound porphyrin (L-**2d**) and free porphyrin (**2d**). Free alkyl-porphyrin **2d** binds to the membrane and inhibits the *KRAS*-Nrf2-GPX4 axis. This results in lipid peroxidation and lipid ROS formation that trigger ferroptosis. In contrast, liposome-bound L-**2d** neither loads the membrane with **2d** molecules nor inhibits the *KRAS*-Nrf2-GPX4 axis. Upon illumination it generates ROS that promote a mechanism of cell death mainly based on apoptosis.

desigh of combination therapies.

Funding

This work was supported by AIRC (the Italian Association for Cancer Research). Grant number: IG 2017, Project Code 19898. Work at the Biomolecular Nanoscale Engineering Center (BioNEC), a Centre of Excellence has been funded by THE VILLUM FOUNDATION (grant no. VKR022710, S.V and P.M.G.L.). Funding for open access charge: AIRC (the Italian Association for Cancer Research).

CRediT authorship contribution statement

Eros Di: Giorgio Conceptualization, Investigation, Supervision. **Annalisa Ferino:** Investigation, Supervision. **Himanshi Choudhary:** Investigation. **Phillip M.G. Löffler:** Investigation, Resources. **Francesca D'Este:** Investigation. **Valentina Rapozzi:** Investigation. **Alexander Tikhomirov:** Resources, Formal analysis. **Andrey Shchekotikhin:** Resources, Formal analysis. **Stefan Vogel:** Resources, Formal analysis. **Luigi E. Xodo:** Conceptualization, Funding acquisition, Writing – original draft.

Declaration of Competing Interest

The authors declare that they have no known competing financial interests or personal relationships that could have appeared to influence the work reported in this paper.

Appendix A. Supplementary data

Supplementary data to this article can be found online at https://doi.org/10.1016/j.jphotobiol.2022.112449.

References

[1] G.A. Koning, G. Storm, Targeted drug delivery systems for the intracellular delivery of macromolecular drugs, Drug Discov. Today 8 (2003) 482–483, https://doi.org/10.1016/s1359-6446(03)02699-0.
[2] J.M. Metselaar, G. Storm, Liposomes in the treatment of inflammatory disorders, Expert. Opin. Drug Deliv. 2 (2005) 465–476, https://doi.org/10.1517/17425247.2. 3.465.
[3] B.S. Ding, T. Dziubla, V.V. Shuvaev, S. Muro, V.R. Muzykantov, Advanced drug delivery systems that target the vascular endothelium, Mol. Interv. 6 (2006) 98–112, https://doi.org/10.1124/mi.6.2.7.
[4] S. Hua, S.Y. Wu, The use of lipid-based nanocarriers for targeted pain therapies, Front. Pharmacol. 4 (2013) 143, https://doi.org/10.3389/fphar.2013.00143.
[5] D.R. Khan, E.M. Rezler, J. Lauer-Fields, G.B. Fields, Effects of drug hydrophobicity on liposomal stability, Chem. Biol. Drug Des. 71 (2008) 3–7, https://doi.org/10.1111/j.1747-0285.2007. 00610.x.
[6] T.M. Allen, P.R. Cullis, Liposomal drug delivery systems: from concept to clinical applications, Adv. Drug Deliv. Rev. 65 (2013) 36–48, https://doi.org/10.1016/j.addr.2012.09.037.
[7] B.S. Pattni, V.V. Chupin, V.P. Torchilin, New developments in liposomal drug delivery, Chem. Rev. 115 (2015) 10938–10966, https://doi.org/10.1021/acs.chemrev.5b00046.
[8] A. Akbarzadeh, et al., Liposome: classification, preparation, and applications, Nanoscale Res. Lett. 8 (2013) 102–111, https://doi.org/10.1186/1556-276X-8-102.
[9] N. Oku, K. Doi, Y. Namba, S. Okada, Herapeutic effect of adriamycin encapsulated in long-circulating liposomes on meth-A-sarcoma-bearing mice, Int. J. Cancer 58 (1994) 415–419, https://doi.org/10.1002/ijc.2910580318. 10.1002/ijc.2910580318.
[10] A.S. Ulrich, Biophysical aspects of using liposomes as delivery vehicles, Biosci. Rep. 22 (2002) 129–150, https://doi.org/10.1023/a:1020178304031.
[11] V.P. Torchilin, Liposomes as delivery agents for medical imaging, Mol Med Today. 2 (1996) 242–249, https://doi.org/10.1016/1357-4310(96)88805-8.
[12] Y. Liu, K.M. Castro Bravo, J. Liu, Targeted liposomal drug delivery: a nanoscience and biophysical perspective, J. Nanoscale Horiz. 6 (2021) 78–94, https://doi.org/10.1039/d0nh00605j.
[13] A. Ferino, G. Nicoletto, F. D'Este, S. Zorzet, S. Lago, S.N. Richter, A. Tikhomirov, A. Shchekotikhin, L.E. Xodo, Photodynamic therapy for *ras*-driven cancers: targeting G-Quadruplex RNA structures with bifunctional alkyl-modified porphyrins, J. Med. Chem. 63 (2020) 1245–1260, https://doi.org/10.1021/acs.jmedchem.9b01577.
[14] G. Miglietta, S. Cogoi, J. Marinello, G. Capranico, A.S. Tikhomirov, A. Shchekotikhin, L.E. Xodo, RNA G-Quadruplexes in Kirsten Ras (KRAS) oncogene

as targets for small molecules inhibiting translation, J. Med. Chem. 60 (2017) 9448–9461, https://doi.org/10.1021/acs.jmedchem.7b00622.
[15] S. Burge, G.N. Parkinson, P. Hazel, A.K. Todd, S. Neidle, Quadruplex DNA: sequence, topology and structure, Nucleic Acids Res. 34 (2006) 5402–5415, https://doi.org/10.1093/nar/gkl655.
[16] J. Spiegel, S. Adhikari, S. Balasubramanian, The structure and function of DNA G-Quadruplexes, Trends in Chemistry. 2 (2020) 123–136, https://doi.org/10.1016/j.trechm.2019.07.002.
[17] H. Ying, A.C. Kimmelman, C.A. Lyssiotis, S. Hua, G.C. Chu, E. Fletcher-Sananikone, J.W. Locasale, J. Son, H. Zhang, J.L. Coloff, et al., Oncogenic kras maintains pancreatic tumors through regulation of anabolic glucose metabolism, Cell 149 (2012) 656–670, https://doi.org/10.1016/j.cell.2012.01.058.
[18] J. Son, C.A. Lyssiotis, H. Ying, X. Wang, S. Hua, M. Ligorio, R.M. Perera, C. R. Ferrone, E. Mullarky, N. Shyh-Chang, et al., Glutamine supports pancreatic cancer growth through a KRAS-regulated metabolic pathway, Nature. 496 (2013) 101–105, https://doi.org/10.1038/nature12040.
[19] A. Ferino, V. Rapozzi, L.E. Xodo, The ROS-KRAS-Nrf2 axis in the control of the redox homeostasis and the intersection with survival-apoptosis pathways: implications for photodynamic therapy, J. Photochem. Photobiol. B 202 (2020), 111672, https://doi.org/10.1016/j.jphotobiol.2019.111672.
[20] S. Mukhopadhyay, D. Goswami, P.P. Adiseshaiah, W. Burgan, M. Yi, T.M. Guerin, S.V. Kozlov, D.V. Nissley, F. McCormick, Undermining Glutaminolysis bolsters chemotherapy while NRF2 promotes Chemoresistance in KRAS-driven pancreatic cancers, Cancer Res. 80 (2020) 1630–1643, https://doi.org/10.1158/0008-5472.CAN-19-1363.
[21] K. Susanne, Golombek, Jan-Niklas may, Benjamin Theek, Lia Appold, Natascha Drude, Fabian Kiessling, and Twan Lammers tumor targeting via EPR: strategies to enhance patient responses, Adv. Drug Deliv. Rev. 130 (2018) 17–38, https://doi.org/10.1016/j.addr.2018.07.007.
[22] M.K. Kuimova, G. Yahioglu, P.R. Ogilby, Singlet oxygen in a cell: spatially dependent lifetimes and quenching rate constants, J. Am. Chem. Soc. 14 (131) (2009) 332–340, https://doi.org/10.1021/ja807484b.
[23] U. Jakobsen, S. Vogel, Chapter 12 - DNA-controlled assembly of liposomes in diagnostics, Methods Enzymol. 464 (2009) 233–248, https://doi.org/10.1016/S0076-6879(09)64012-X.
[24] H.T. McMahon, E. Boucrot, Molecular mechanism and physiological functions of clathrin-mediated endocytosis, Nat Rev Mol Cell Biol. 12 (2011) 517–533, https://doi.org/10.1038/nrm3151.
[25] P. Davies, A.C. Allison, Effects of cytochalasin B on endocytosis and exocytosis, Front. Biol. 46 (1978) 143–160. 352738.
[26] E.L. Eskelinen, Roles of LAMP-1 and LAMP-2 in lysosome biogenesis and autophagy, Mol. Asp. Med. 27 (5–6) (2006) 495–502, https://doi.org/10.1016/j.mam.2006.08.005.
[27] Irina Raykhel, Heli Alanen, Kirsi Salo, Jaana Jurvansuu, Van Dat Nguyen, Maria Latva-Ranta, and Lloyd Ruddock. A molecular specificity code for the three mammalian KDEL receptors, J. Cell Biol. 179 (2007) 1193–1204, https://doi.org/10.1083/jcb.200705180.
[28] L. Castro, B.A. Freeman, Reactive oxygen species in human health and disease, Nutrition 2001 (161) (2001) 163–165, https://doi.org/10.1016/s0899-9007(00)00570-0.
[29] G.M. DeNicola, F.A. Karreth, T.J. Humpton, A. Gopinathan, C. Wei, et al., Oncogene-induced Nrf2 transcription promotes ROS detoxification and tumorigenesis, Nature 475 (2011) 106–109, https://doi.org/10.1038/nature10189.
[30] A. Lister, T. Nedjadi, N.R. Kitteringham, F. Campbell, E. Costello, et al., Nrf2 is overexpressed in pancreatic cancer: implications for cell proliferation and therapy, Mol. Cancer 10 (2011) 37, https://doi.org/10.1186/1476-4598-10-37.
[31] J.M. Matés, C. Pérez-Gòmez, I. Nùnez de Castro, Antioxidant enzymes and human diseases, Clin. Biochem. 32 (1999) 595–603, https://doi.org/10.1016/s0009-9120(99)00075-2.
[32] Q. Ma, Role of Nrf2 in oxidative stress and toxicity, Annu. Rev. Pharmacol. Toxicol. 53 (2013) 401–426, https://doi.org/10.1146/annurev-pharmtox-011112-140320.
[33] G. Cinque, A. Ferino, E.B. Pedersen, L.E. Xodo, Role of poly [ADP-ribose] polymerase 1 in activating the *Kirsten ras* (*KRAS*) gene in response to oxidative stress, Int. J. Mol. Sci. 21 (2020) 6237, https://doi.org/10.3390/ijms21176237.
[34] M. da Silva Baptista, J. Cadet, P. Paolo Di Mascio, A.A. Ghogare, A. Greer, et al., Type I and II photosensitized oxidation reactions: guidelines and mechanistic Pathways, Photochem. Photobiol. 93 (2017) 912–919, https://doi.org/10.1111/php.12716.
[35] S. Eser, A. Schnieke, G. Schneider, D. Saur, Oncogenic KRAS signalling in pancreatic cancer, Br. J. Cancer 111 (2014) 817–822, https://doi.org/10.1038/bjc.2014.215.
[36] S. Eser, N. Reiff, M. Messer, B. Seidler, K. Gottschalk, Selective requirement of PI3K/PDK1 signaling for Kras oncogene-driven pancreatic cell plasticity and cancer, Cancer Cell 23 (2013) 406–420, https://doi.org/10.1016/j.ccr.2013.01.023.
[37] R. Ferro, M. Falasca, Emerging role of the KRAS-PDK1 axis in pancreatic cancer, World J. Gastroenterol. 20 (2014) 10752–10757, https://doi.org/10.3748/wjg.v20.i31.10752.
[38] K.M. Holmstrom, T. Finkel, Cellular mechanisms and physiological consequencesof redox-dependent signalling, Nat. Rev. Mol. Cell Biol. 15 (2014) 411–421, https://doi.org/10.1038/nrm3801.
[39] B. D'Autreaux, M.B. Toledano, ROS as signalling molecules: mechanisms that generate specificity in ROS homeostasis, Nat. Rev. Mol. Cell Biol. 8 (2007) 813–824, https://doi.org/10.1038/nrm2256.
[40] C. Wen, H. Wang, X. Wu, et al., ROS-mediated inactivation of the PI3K/AKT pathway is involved in the antigastric cancer effects of thioredoxin reductase-1 inhibitor chaetocin, Cell Death Dis. 10 (2019) 809, https://doi.org/10.1038/s41419-019-2035-x.
[41] J. Cao, D. Xu, D. Wang, R. Wu, L. Zhang, ROS-driven Akt dephosphorylation at Ser-473 is involved in 4-HPR-mediated apoptosis in NB4 cells, Free Radic. Biol. Med. 47 (2009) 536–547, https://doi.org/10.1016/j.freeradbiomed.2009.05.024.
[42] Y. Son, Y.-K. Cheong, N.-K. Kim, H.-T. Chung, D.G. Kang, H.-O. Pae, Mitogen-Activated Protein Kinases and Reactive Oxygen Species: How Can ROS Activate MAPK Pathways? J. Signal. Trans. (2011), 792639 https://doi.org/10.1155/2011/792639.
[43] S.J. Dixon, K.M. Lemberg, M.R. Lamprecht, R. Skouta, E.M. Zaitsev, et al., Ferroptosis: an iron-dependent form of nonapoptotic cell death, Cell 149 (2012) 1060–1072, https://doi.org/10.1016/j.cell.2012.03.042.
[44] W.S. Yang, B.R. Stockwell, Synthetic lethal screening identifies compounds activating iron-dependent, nonapoptotic cell death in oncogenic-RAS-harboring cancer cells, Chem. Biol. 15 (2008) 234–245, https://doi.org/10.1016/j.chembiol.2008.02.010.
[45] L. Yang, X. Chen, Q. Yang, J. Chen, Q. Huang, Front. Oncol. 10 (2020) 949, https://doi.org/10.3389/fonc.2020.00949.
[46] S. Dolma, S.L. Lessnick, W.C. Hahn, B.R. Stockwell, Identification of genotype-selective antitumor agents using synthetic lethal chemical screening in engineered human tumor cells, Cancer Cell 3 (2003) 285–296, https://doi.org/10.1016/s1535-6108(03)00050-3.
[47] R. Skouta, S.J. Dixon, J. Wang, D.E. Dunn, M. Orman, et al., Ferrostatins inhibit oxidative lipid damage and cell death in diverse disease models, J. Am. Chem. Soc. 136 (2014) 4551–4556, https://doi.org/10.1021/ja411006a.
[48] L. Cao, Y. Liang, Y. Liu, Y. Xu, W. Wan, C. Zhu, Pseudo-phosphorylation at AT8 epitopes regulates the tau truncation AT aspartate 421, Exp. Cell Res. 370 (2018) 103, https://doi.org/10.1016/j.yexcr.2018.06.010.
[49] J. Li, J. Li, Y. Pu, S. Li, W. Gao, B. He, PDT-enhanced Ferroptosis by a polymer nanoparticle with pH-activated singlet Oxygen generation and superb biocompatibility for Cancer therapy, Biomacromolecules 22 (2021) 1167, https://doi.org/10.1021/acs.biomac. 0c01679.
[50] E.H. Pap, G.P.C. Drummen, V.J. Winter, T.W.A. Kooij, P.J. Rijken, Ratio-fluorescence microscopy of lipid peroxidation in living cells using C11-BODIPY581/591, FEBS Lett. 453 (1999) 278–282, https://doi.org/10.1016/s0014-5793(99)00696-1.
[51] G.P.C. Drummen, L.C. Mvan, L.C.M. van Liebergen, J. Op den Kamp, J.A. Post, C11-BODIPY$^{581/591}$, an oxidation-sensitive fluorescent lipid peroxidation probe: (micro)spectroscopic characterization and validation of methodology, Free Radic. Biol. Med. 33 (2002) 473–490, https://doi.org/10.1016/s0891-5849(02)00848-1.
[52] G.C. Forcina, S.J. Dixon, GPX4 at the crossroads of lipid homeostasis and Ferroptosis, Proteomics 19 (2019), e1800311, https://doi.org/10.1002/pmic.201800311.
[53] C. Xu, S. Sun, T. Johnson, R. Qi, S. Zhang, J. Zhang, K. Yang, The glutathione peroxidase Gpx4 prevents lipid peroxidation and ferroptosis to sustain Treg cell activation and suppression of antitumor immunity, Cell Rep. 35 (2021), 109235, https://doi.org/10.1016/j.celrep.2021.109235.
[54] W. Liu, Y. Zhou, W. Duan, J. Song, S. Wei, et al., Glutathione peroxidase 4-dependent glutathione high-consumption drives acquired platinum chemoresistance in lung cancer-derived brain metastasis, Clin. Transl. Med. 11 (2021), e517, https://doi.org/10.1002/ctm2.517.

Section 3

The Suppression of the KRAS G12D -Nrf2 Axis Shifts Arginine into the Phosphocreatine Energy System in Pancreatic Cancer Cells.

The suppression of the *KRAS* ^{G12D}-*Nrf2* axis shifts arginine into the phosphocreatine energy system in pancreatic cancer cells

Eros Di Giorgio[&*], Himanshi Choudhary[&], Annalisa Ferino, Ylenia Cortolezzis, Emiliano Dalla, Francesca D'Este, Marina Comelli, Valentina Rapozzi, Luigi E. Xodo*

Department of Medicine, Laboratory of Biochemistry, P.le Kolbe 4, 33100 Udine, Italy

Corresponding authors: Eros Di Giorgio, eros.digiorgio@uniud.it; Luigi E. Xodo, luigi.xodo@uniud.it

Lead contact: Luigi E. Xodo, luigi.xodo@uniud.it

[&] EDG and HC have equally contributed to this work

Highlights

- The *KRAS* ^{G12D}-*Nrf2* axis controls redox homeostasis and metabolism in PDAC cells;
- Suppression of *KRAS* ^{G12D}-*Nrf2* decreases glycolysis, PPP and glutathione cycle and promotes a metabolic shift of arginine into the synthesis of phosphocreatine;
- Combination therapies that can target simultaneously the phosphocreatine pathway and the *KRAS* ^{G12D}-*Nrf2* axis produce a stronger anticancer effect than monotherapies.

Summary

In pancreatic ductal adenocarcinomas, the *KRAS* ^{G12D}-*Nrf2* axis controls numerous cellular functions including redox homeostasis and metabolism. Its disruption by suppressing *Nrf2* leads to an increase in cellular ROS and profound reprogramming of metabolism. Unbiased transcriptome analyses show that genes encoding key enzymes of glycolysis, the pentose phosphate pathway and the glutathione cycle are downregulated, while genes encoding arginine and medium-chain fatty acid metabolism are upregulated. Pancreatic cancer cells lacking the *KRAS* ^{G12D}-*Nrf2* axis are highly dependent on arginine, which

feeds the synthesis of phosphocreatine and polyamines. This shift in metabolism produces an energy buffer that allows pancreatic cancer cells to cope with increased energy demands. Inhibition of the creatine pathway with cyclocreatine was found to reduce both ATP and rate of invasion in 3D spheroids of Nrf2-deficient pancreatic cancer cells. Combination therapies that simultaneously target the creatine pathway and the *KRAS* ^{G12D}-*Nrf2* axis are more effective than monotherapies.

Graphical Abstract

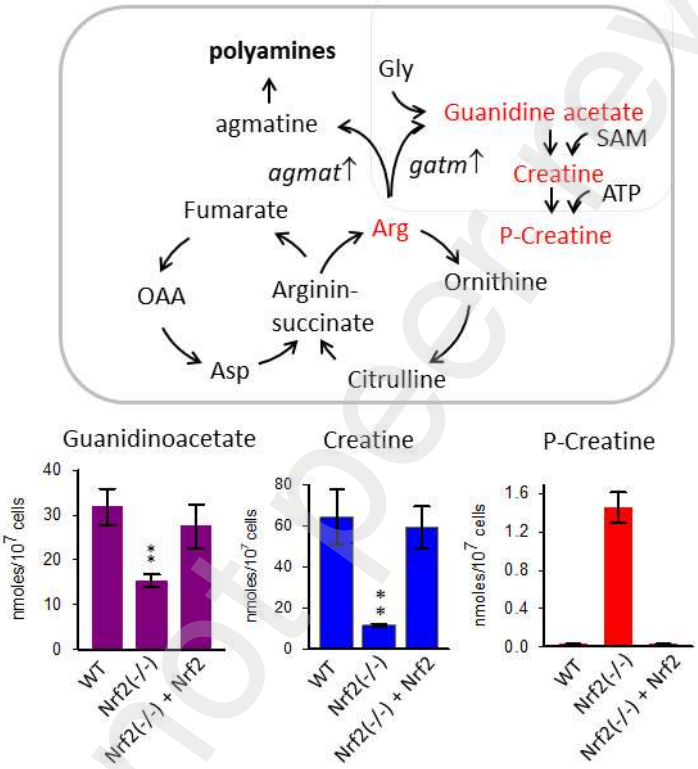

Keywords

KRAS ^{G12D}-*Nrf2* axis, RNA-seq, metabolomics, arginine, glutamine, creatine/phosphocreatine, polyamines, cyclocreatine, combination therapies

Introduction

Pancreatic ductal adenocarcinoma (PDAC) is estimated to become the second cause of cancer-related death in Western countries by 2030 (Rahib et al., 2014). The 5-year survival rate of PDAC patients is < 8 %, as the disease is often diagnosed at an advanced stage and develops resistance to conventional chemotherapy (Siegel et al., 2016). A wide

range of genetic alterations are present in PDAC including activating point mutations in the *KRAS* proto-oncogene and loss-of-function mutations in tumour suppressor genes, such as TP53, CDNK2A, DPC4/SMAD4 and BRCA2 (Jaffeeet al., 2002). Missense mutations in *KRAS* - exon 1, codon 12, 13 and 61- are present in > 95 % PDAC cases (Bos JL., 1989). These mutations lock the RAS protein in the active GTP-bound state which constitutively stimulates cancer growth. The role of oncogenic *KRAS* in pancreatic tumorigenesis has been the subject of investigation for many years. Hingorani et al (2003) reported that the endogenous expression of *KRAS* ^{G12D} in mouse pancreatic cells results in ductal lesions as occur in human pancreatic intraepithelial neoplasia giving rise to invasive pancreatic cancer. Recent studies demonstrated that *KRAS* ^{G12D} is required in all stages of the PDAC carcinogenesis, although progression to metastatic cancer requires the acquisition of additional genetic alterations, such as mutation of TP53 (diMagliano and Logsdon, 2013). That *KRAS* ^{G12D} plays a preeminent role in the development of PDAC is suggested by the fact that the inactivation of this oncogene by genetic tools results in the reversion of the carcinogenesis (Collins et al., 2012). Transcriptomic and metabolomic studies have demonstrated that KRAS ^{G12D} is a key regulator of the metabolic reprogramming occurring in PDAC cells to fuel an increased demand of nutrients by highly proliferating cells. Under the action of constitutively active *KRAS* ^{G12D}, pancreatic cancer cells acquire a glycolytic phenotype characterized by a high glycolytic flux: a metabolic condition known as the Warburg effect (Warburg O, 1956). This high glycolytic flux channels intermediates into anabolic pathways to satisfy the requirements of biomass and reducing power of cancer cells (Ying et al., 2012). Recent studies have reported that Nrf2, the master regulator of oxidative stress in the cell (Vomund et al., 2017), is upregulated by *KRAS* in PDAC cells, suggesting that *KRAS* is likely to be the prime regulator of the redox homeostasis in pancreatic cancer (DeNicola et al., 2011, Ferino et al., 2020). However, as *Nrf2* was reported to be essential for the growth of human tumor organoids and tumor xenografts in athymic nude mice, in the absence of any correlation between *Nfr2* and DNA damage (Chio IIC et al., 2016), suggests that *Nrf2* has also ROS-independent functions. In fact, evidence that *Nrf2* promotes pancreatic tumour maintenance by modulating translation and by redirecting glucose and glutamine into anabolic pathways has been provided (Mitsuishi et al., 2012). In a previous work we have reported the in Panc-1 cells (*KRAS* ^{G12D}, TP53 mutated) *KRAS* ^{G12D} and *Nrf2* form an axis that controls cell growth (Ferino et al., 2019). The mechanism by which oncogenic *KRAS* rewires the metabolism in PDAC and the role played by Nrf2 in the process is not yet defined. In this study, we have used a

transcriptomic and metabolomic approach to investigate the impact of the *KRAS* ^{G12D} -*Nrf2* axis on the metabolism of Panc-1 cells. We found that the repression of the *KRAS* ^{G12D} -*Nrf2* axis through the deletion of *Nrf2* produces a cellular phenotype strongly dependent on glutamine and arginine, which boosts the activity of creatine kinase (*ckb*) and the synthesis of phosphocreatine, generating a vital energetic reserve for the cell (Ellington, 2001). Phosphocreatine is a phosphagen energy-storing compound found mainly in muscle and nervous tissues, but recently, it has been reported that it plays a role also in cancer (Fenouille et al., 2017, Papalazarou et al., 2020). The therapeutic implications of the results of our study are discussed.

Results

Generation and characterization of Panc-1 Nrf2(-/-) cells deficient of the *KRAS-Nrf2* axis

To examine the differential expression of *Nrf2* between normal and tumor tissues in PDAC patients, we interrogated GSE15471, a publicly available microarray data set. The database shows that *Nrf2* is 3-fold more expressed in PDAC compared to tumor-surrounding normal tissues (P≤0.0002). Moreover, the Kaplan–Meier plots disclose that PDAC patients with high *Nrf2* expression exhibit a lower survival probability than patients with a low *Nrf2* expression (P=0.0016) (Figure S1), suggesting that a highly expressed *Nrf2* is associated with a poor prognosis. An elegant metabolomic work by DePihno and co-workers reported that advanced PDAC strictly depends on *KRAS* ^{G12D}, as the oncogene reprograms glucose and glutamine metabolism (Ying et al., 2012, Son et al., 2013). However, how *KRAS* ^{G12D} controls cancer metabolism is still a matter of investigation. The discovery that *KRAS* ^{G12D} is tightly connected with *Nrf2* (DeNicola et al., 2011; Ferino et al., 2019; Tao et al., 2014), with which it forms an axis controlling several cellular functions, suggests that the metabolic reprogramming induced by *KRAS* ^{G12D} could be mediated, in part or entirely, by *Nrf2*. To address this issue, we completely inactivated the *KRAS* ^{G12D}-

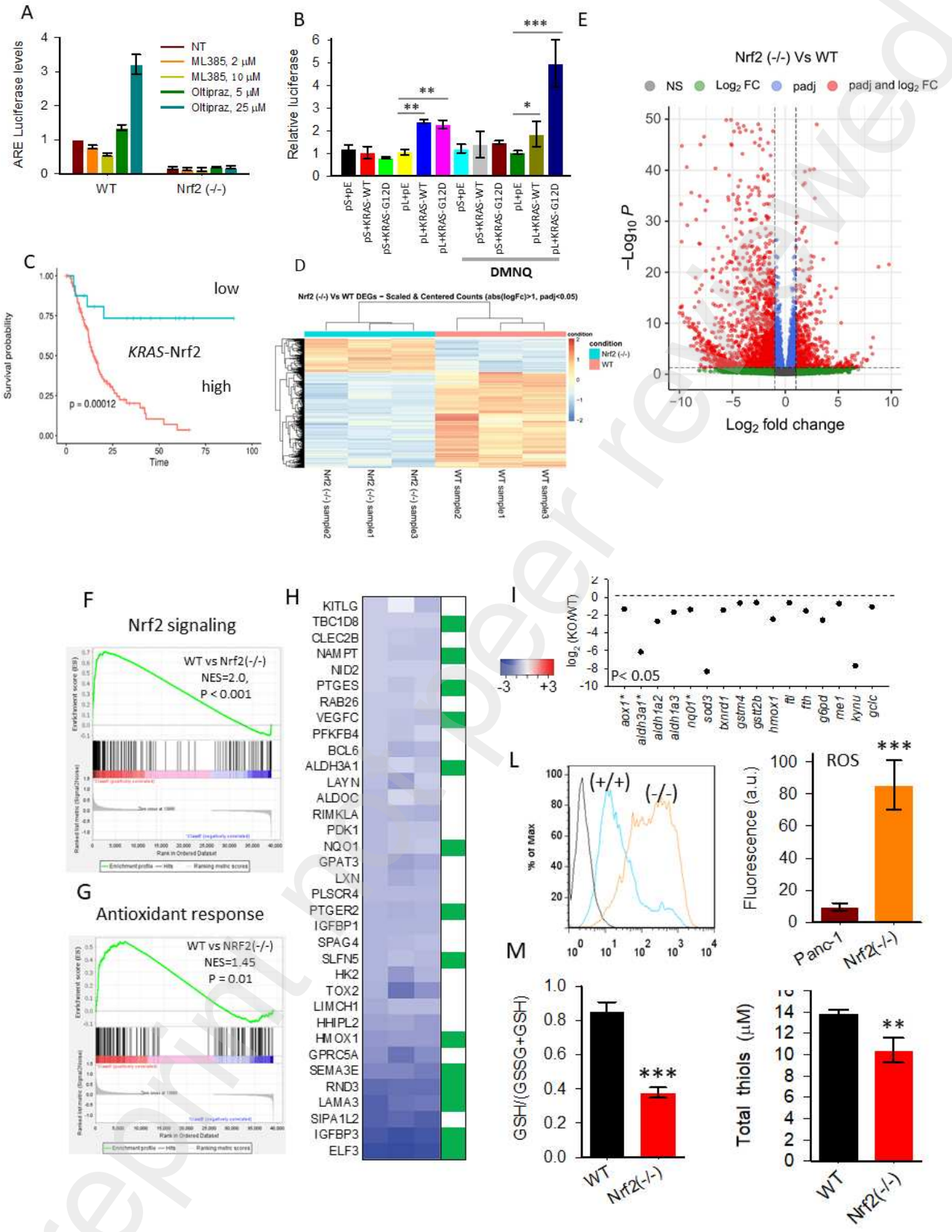

Figure 1: Characterization of Panc-1 Nrf2(-/-) cells. (A) Luciferase driven by the *NQO1* promoter bearing ARE recognized by Nrf2. Contrary to WT cells, Nrf2(-/-) cells do not express luciferase. Nrf2 activator oltipraz and repressor ML385 do not act on Nrf2(-/-) cells, as expected; (B) Luciferase driven by full (pL) or truncated (pS) *Nrf2* promoter after ectopic expression of *KRAS* ^{WT}

or *KRAS* ^{G12D}. DMNQ, 1,4 naphthoquione, is a molecule that produces ROS; (C) Survival probability of PDAC patients with high (above 3rd quartile) and low level of *KRAS* and *Nrf2*; (D) Heatmaps of the differentially expressed genes (DEGs) in three sample replicates of Nrf2(-/-) and WT Panc-1 cells; (E) Volcano plot of DEGs in Nrf2(-/-) versus WT Panc-1 cells; (F,G) Gene set enrichment analysis (GSEA) plots showing the enrichment of *Nrf2* signaling and antioxidant response genes in WT *versus* Nrf2(-/-) Panc-1 cells; (H) Heatmap showing the fold expression of Nrf2 signaling in Nrf2(-/-) Panc-1 cells with respect to WT cells; the genes directly regulated by Nrf2 through direct biding of proximal promoter are evidenced in green; (I) Log_2 (fold change) of important DEGs (P<0.05); (L) Level of basal ROS in Nrf2(-/-) and WT Panc-1 cells; (M) Levels of GSH/total glutathione and total thiol groups in Nrf2(-/-) and WT Panc-1 cells; Data represent the mean ± s.d. of at least 3 independent experiments: * P≤ 0.05; ** P≤ 0.01; ***P≤ 0.001 by Student's *t*-test.

Nrf2 axis in Panc-1 cells, carrying mutant *KRAS* ^{G12D} (Waters and Der, 2018), by deleting *Nrf2* using CRISPR-Cas9. Notably, we could not inactivate the axis by suppressing *KRAS* ^{G12D} because the cells are addicted to it and do not survive when the oncogene is inhibited. We isolated more than one knockout (KO) clone, in which both *Nrf2* alleles bear frameshift mutations causing the deletion of the gene. We found in clone KO-134 deletions of 2 and 10 nt in the *Nrf2* alleles, whereas in KO-16 deletions of 1 and 2 nt (not shown). We measured the level of Nrf2 protein by Western blot and found that it was indeed expressed in WT but not in the KO cells. From now on we called the latter cells Nrf2(-/-) (Figure S2). As a functional control, we tested the expression of luciferase driven by the NQO1 promoter bearing the antioxidant response element (ARE) recognized by Nrf2 (Figure 1A). Luciferase was not expressed in Nrf2(-/-) cells, whereas it was in WT cells, which expectedly responded to Oltipraz, an *Nrf2* activator (Yu et al., 2011), and ML385, an *Nrf2* inhibitor (Bollong et al., 2018). The direct link between oncogenic *KRAS* and *Nrf2* was proven by the fact that the ectopic expression of *KRAS* ^{G12D} in Panc-1 cells causes a clear increase of *Nrf2* (Ferino et al., 2019). To gain insight into the *KRAS-Nrf2* axis, we engineered two expression vectors, pL and pS (see Methods). Vector pL beared the full-length *Nrf2* promoter, with ARE-like elements at -754 and -492, upstream of *Firefly* luciferase. In contrast, vector pS beared *Nrf2* promoter lacking AREs. We found that the ectopic expression of mutant *KRAS* ^{G12D} or wild-type *KRAS* ^{WT} increased by 2-fold luciferase from pL but not from pS, showing that *KRAS* upregulates *Nrf2* and that the ARE-like elements are essential for the activation (Figure 1B). When the cells were transfected with *KRAS* ^{G12D} and treated with 1,4 naphthoquinone (DMNQ), a molecule that produces

ROS (Shit et al., 1994), luciferase driven by pL increased up to 5-fold. Together, ROS and *KRAS* induce a stronger upregulation of *Nrf2*. This effect on *Nrf2* could be mediated by the *PI3K/AKT* and *MAPK/ERK* signaling (Figure S3). Furthermore, we found that the suppression of *KRAS* with siRNA caused the simultaneous downregulation of *Nrf2*, confirming a close link between *KRAS* ^{G12D} and *Nrf2* (Figure S4). Finally, the GSE15471 data from PDAC patients support the notion that *KRAS* ^{G12D} and *Nrf2* are crucial for PDAC, as the Kaplan-Meier plot of patients with high expression of both *KRAS* ^{G12D} and Nrf2 showed a significantly lower probability of survival than patients with lower expression of the genes (P=0.00012) (Figure 1C, Figure S5). To evaluate the effects of the *KRAS* ^{G12D}-Nrf2 axis in PDAC, we performed transcriptomic and metabolomic analyses on WT (with *KRAS* ^{G12D}-Nrf2 active) and Nrf2(-/-) (with *KRAS* ^{G12D}-Nrf2 inactive) Panc-1 cells.

Transcriptome analysis of Panc-1 cells following the suppression of the *KRAS* ^{G12D}*-Nrf2* axis

The transcriptional changes induced by the suppression of the *KRAS* ^{G12D}*-Nrf2* axis in Panc-1 cells were determined by RNA-seq analysis on WT and Nrf2(-/-) cells. Differentially expressed genes (DEGs) between Nrf2 (-/-) and WT cells are shown by the principal component analysis (PCA) (Figure S6). PCA displays a high reproducibility of the sample replicates and significant variation between WT and Nrf2 (-/-) cells. Among the transcripts, a cluster of 1888 DEGs is downregulated and a cluster of 666 DEGs is upregulated in Nrf2 (-/-) cells compared to WT cells, according to a threshold $|\log_2 FC| \geq 1$, Padj.< 0.05. These data suggest that the blockage of the *KRAS* ^{G12D} *-Nrf2* axis has a strong impact on the transcriptome of Panc-1 cells. The data are summarized by a heatmap of DEGs (Figure 1D) and a volcano plot (Figure 1E). An unbiased gene set enrichment analysis (GSEA) revealed a striking impairment of KEGG-defined pathways relative to *Nrf2* signaling (GSE94393) (P<0.0001) and the antioxidant response to oxidative stress (M5968) (P<0.01) in Nrf2(-/-) cells (Figure 1F,G).

Downregulated DEGs associated to *Nrf2* are shown in the heatmap of Figure 1H. Notably, the key genes involved in the maintenance of the redox homeostasis are downregulated in Nrf2 (-/-) cells: *aox1*, *aldh3a1*, *nq01*, *hmox1*, *txnrd1, gst, gclc* and *sod3* (Figure 1I). The genes that are directly targeted by *Nrf2* are marked in green in the right column of the heatmap. As the antioxidant response coordinated by *Nrf2* in response to an increase of

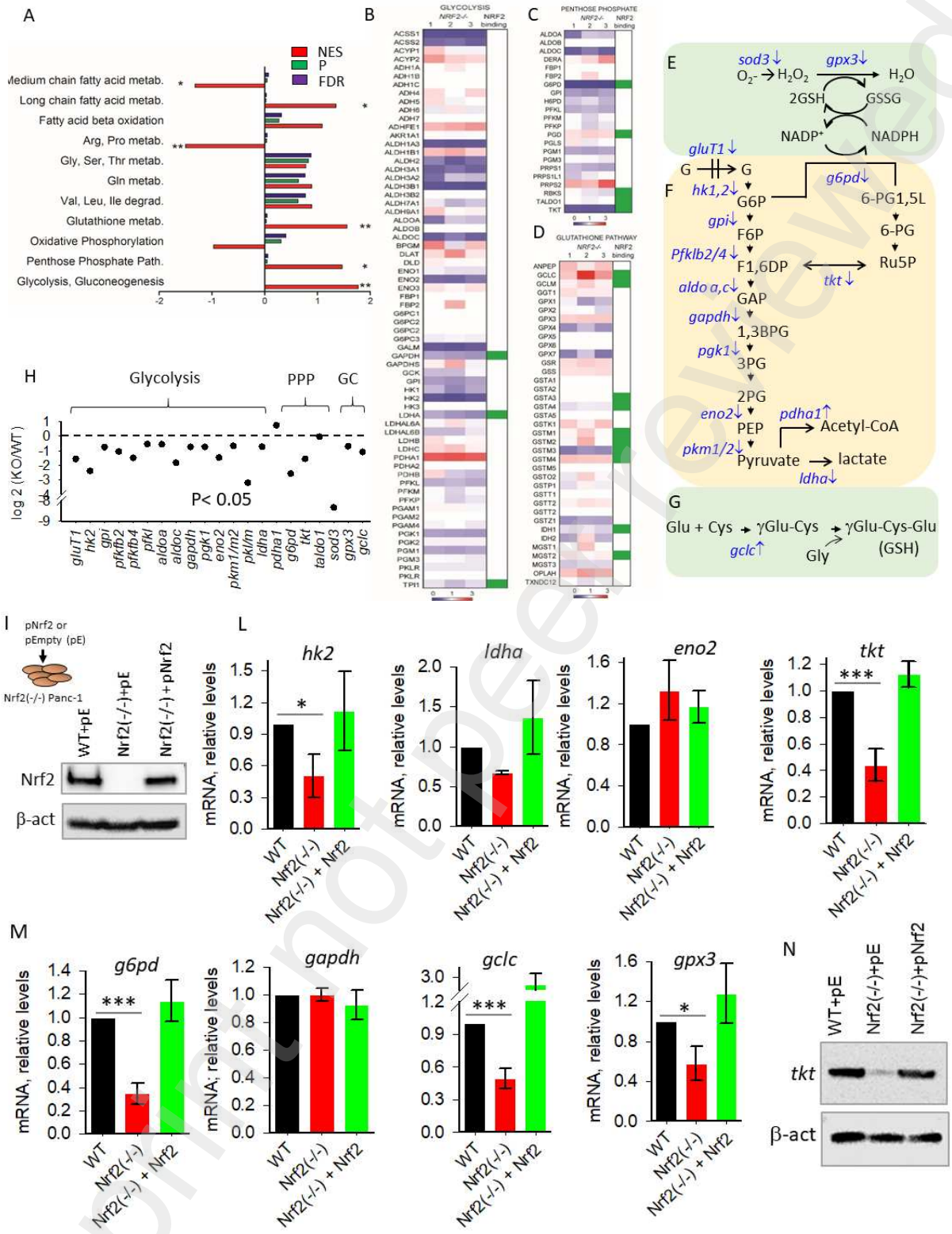

Figure 2: Nrf2 depletion affects Panc-1 transcriptome and promotes a deep metabolic reprogramming: (A) Functional enrichment analysis of WT cells compared to Nrf2(-/-) cells; (B-D) Heatmaps of DEGs relative to glycolysis, PPP and glutathione pathways; (E-G) Glycolysis, PPP and glutathione cycle pathways. DEGs of enzymes involved in the pathways are shown, ↓= downregulated, ↑= upregulated; (H) Log_2 (fold change) of key DEGs (P<0.05) involved in the glycosysis, PPP and glutathione cycle pathways; (I, L,M) Expression level of some key enzymes

involved in the pathways determined by qRT-PCR. To demonstrate that the enzymes are controlled by the *KRAS*^{G12D}*-Nrf2* axis, we re-expressed Nrf2 in Nrf2(-/-) cells and obtained an expression profile similar to that of WT cells; (M) Western blot showing the level of *tkt* in WT, Nrf2(-/-) and Nrf2(-/-) cells in which Nrf2 was re-expressed. Data represent the mean ± s.d. of at least 3 independent experiments: * P≤ 0.05; ** P≤ 0.01; ***P≤ 0.001 by Student's *t*-test.

oxidative stress is lost in Nrf2(-/-) cells, the basal level of ROS, measured by cell cytometry, was indeed found ~ 8-fold higher than in WT cells (Figure 1L). We also found that the ratio between reduced and total glutathione was 0.88 in WT and 0.4 in Nrf2(-/-) cells, and the total amount of reduced thiols was ~ 25 % lower in Nrf2(-/-) compared to WT cells (Figure 1M). Collectively, our data show that the suppression of the *KRAS* ^{G12D}*-Nrf2* axis strongly affects the redox homeostasis in pancreatic cancer cells. Finally, we observed that *Nrf2*-deficient cells showed a proliferation rate ~ 25 % lower than that of WT cells, over incubation of 11 days (Figure S7).

The *KRAS* ^{G12D}*-Nrf2* axis controls the metabolic reprogramming of PDAC cells

We interrogated clusterProfiler to carry out a functional enrichment analysis of DEGs to reveal enrichment of specific metabolic pathways (Figure 2A). The analysis evidenced a strong and statistically significant decline of glycolysis, pentose phosphate pathway (PPP), glutathione cycle and long-chain fatty acid metabolism and a simultaneous deep reactivation of arginine/proline and medium-chain fatty acid metabolism in Nrf2(-/-) cells. The heatmaps relative to glycolysis, PPP and glutathione cycle are reported in Figure 2B-D. Consistent with gene microarray data of two GEO datasets which showed that glycolysis, PPP and GSH are upregulated in *Nrf2*-active esophagus cells (Fu et al., 2019), we found that the suppression of the *KRAS* ^{G12D}*-Nrf2* axis in Panc-1 cells results in the downregulation (P<0.05) of glycolytic (*hk2*, *gpi*, *pfkl*, *aldoa/c*, *tpi1*, *pgk1*, *eno2*, *pkm1/2* and *ldha*), PPP (*g6pd*, *taldo1* and *tkt*), glutathione cycle (*gclc* and *gpx4*) and *gluT1* genes. In contrast, *pyruvate dehydrogenase A1 (pdha1)*, encoding for the E1 subunit alpha 1 component of the pyruvate dehydrogenase complex was upregulated in Nrf2(-/-) cells (Figure 2E-H). This suggests that a reduced glycolysis flux is compensated by the activation of the *pdh* complex conveying aminoacids yielding pyruvate for oxidative metabolism. Since *KRAS* ^{G12D} controls *Nrf2*, our data are consistent with those of DePinho

and co-workers who reported that *KRAS* ^{G12D} regulates glucose metabolism in PDAC (Ying et al., 2012). Moreover, knockdown of *Nrf2* by siRNA in A549 lung cancer cells resulted in a decrease in key PPP enzymes (*g6pd* and *tkt*) (Mitsuishi et al., 2012) and glutathione synthesis (*gclc*) (Lu, 2009), which agrees well with our data. However, despite the low glycolytic flux, Nrf2(-/-) cells show a proliferation rate only ~25% lower than that of WT cells, suggesting that they use substrates other than glucose for their growth, such as aminoacids, especially arginine, and medium-chain fatty acids.

To confirm the RNA-seq data, we measured by qRT-PCR the expression level of genes encoding for key glycolytic, PPP and glutathione enzymes. Moreover, to unambiguously prove that the metabolic rewiring occurring in PDAC cells is strictly linked with *Nrf2*, we carried out also rescue experiments. We reasoned that the constitutive re-expression of *Nrf2* in Nrf2(-/-) cells (with plasmid pWZL-Neo Nrf2, indicated as pNrf2 in Figure 2I) should reconstitute the *KRAS* ^{G12D}*-Nrf2* axis and thus the metabolic features typical of WT cells. In agreement with RNA-seq data, qRT-PCR showed that glycolytic *hk2, ldha* were indeed ~ 50 % downregulated in Nrf2(-/-) ($P< 0.05$) (Figure 2L,M). Notably, their level was completely rescued when *Nrf2* was re-expressed in Nrf2(-/-) cells. In contrast, *eno2* and *gapdh* show little dependence on *Nrf2*. Also the two genes encoding for key enzymes of PPP, *tkt* and *g6pd,* were found strongly downregulated in Nrf2(-/-) cells ($P< 0.05$), in agreement with RNA-seq. The downregulation of *tkt* in Nrf2(-/-) cells was also confirmed at protein level (Figure 2N). Notably, the level of the PPP genes (*tkt*, *g6pd*) were completely restored when the *KRAS* ^{G12D}*-Nrf2* axis was re-established in Nrf2(-/-) cells (Figure 2L,M). A similar result was observed with the genes involved in the glutathione cycle (*gclc* and *gpx3*) (Figure 2M). In general, the qRT-PCR data were in excellent agreement with those obtained with RNA-seq.

Panc-1 Nrf2(-/-) cells show higher mitochondrial function and a change in oncogenic program

We performed Seahorse XF Cell Mito Stress Test to examine the metabolic adjustment occurring in Nrf2(-/-) cells and performed *Nrf2*-rescue experiments as a control. The results are summarized in Table S1. Figure 3A-C reports a typical real-time oxygen

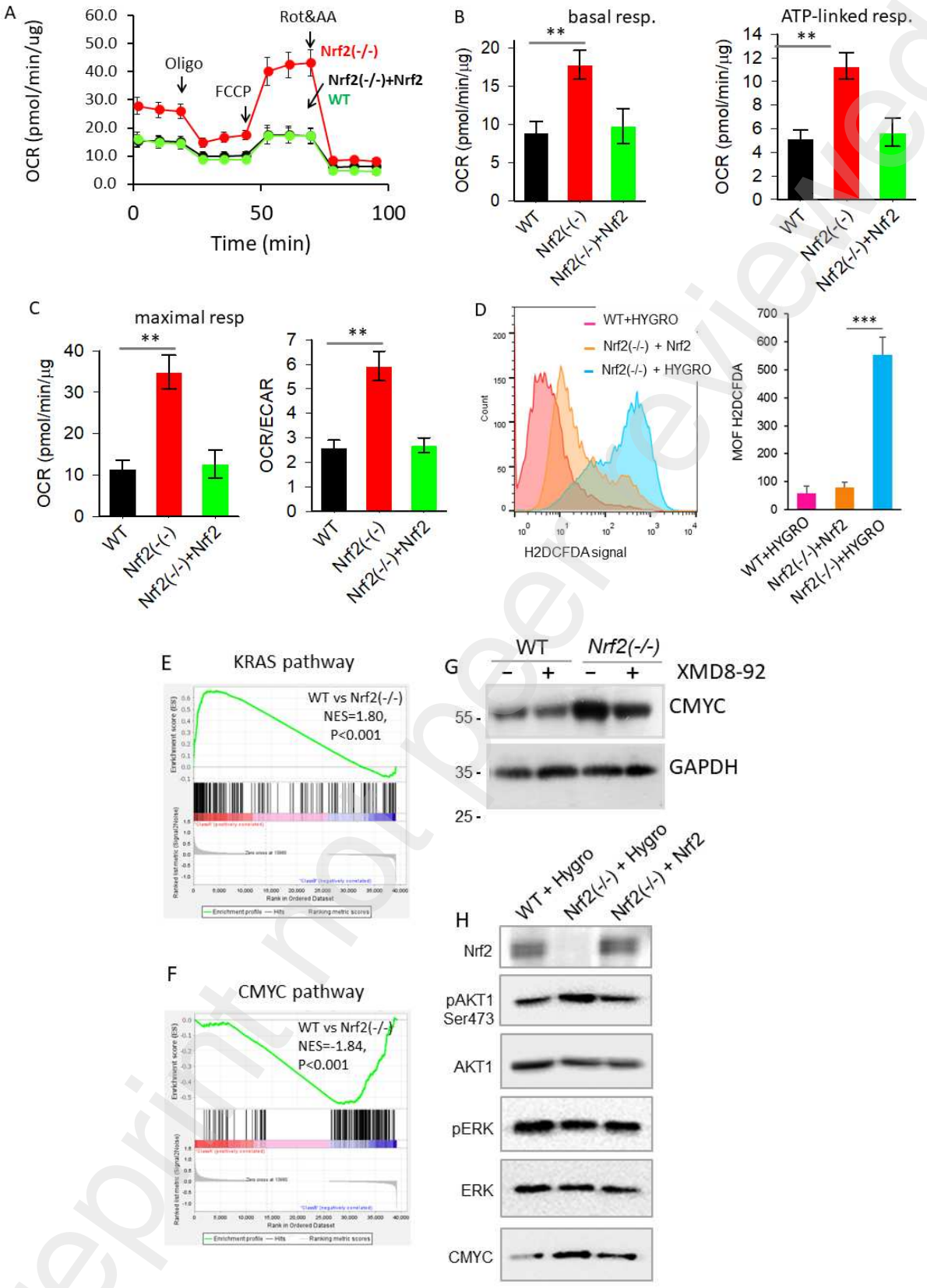

Figure 3: Panc-1 Nrf2(-/-) cells show higher mitochondrial function and a change in oncogenic program. (A) Real-time Oxygen Consumption Rate (OCR) was determined during sequential treatments with oligomycin (ATP-synthase inhibitor), FCCP (uncoupler of oxidative

phosphorylation), rotenone (complex I inhibitor) and antimycin-A (complex III inhibitor) in WT, Nrf2(-/-) and Nrf2(-/-)+Nrf2 cells; (B,C) The rates of basal respiration, ATP-coupled respiration, maximal respiration and the OCR/ECAR ratio in Nrf2(-/-) and Nrf2(-/-)+Nrf2 cells were normalized to total protein content and quantified; D) Nrf2(-/-) cells show a ROS level 10-fold higher than that of WT cells. When Nrf2 is re-expressed in the cells, ROS dropped to levels observed in WT cells; (E,F) GSEA plots showing the enrichment of *KRAS* in WT and *CMYC* in Nrf2(-/-) Panc-1 cells; (G) Expression of MYC in WT and Nrf2(-/-) cells; XMD8-92 (5 μM) was used for 24h to inhibit ERK5 (H) phosphorylation levels of AKT1 and ERK1/2 in WT, Nrf2(-/-) and Nrf2(-/-) + Nrf2 cells; Data represent the mean ± s.d. (or s.e.) of at least 3 independent experiments: * P≤ 0.05; ** P≤ 0.01; ***P≤ 0.001 by Student's *t*-test.

consumption rate (OCR) profile obtained with the classical protocol of three different injections: oligomicyn, FCCP and rotenone&antimycin A. The basal respiration of Nrf2(-/-) cells was 2-fold higher compared to WT cells, in keeping with RNA-seq data suggesting that the former cells are less glycolytic and more dependent on aerobic metabolism. By using the ATP-synthase inhibitor oligomycin, the ATP-linked respiration was 5.2 ± 0.7 and 11.3 ± 1.1 pmol/min·μg in WT and Nrf2(-/-) cells, respectively. When Nrf2 was re-expressed in Nrf2(-/-) cells, the ATP-linked respiration fell to 5.7 ± 1.2 pmol/min·μg, suggesting that the cells restored the glycolytic phenotype typical of WT cells. The successive addition of uncoupler FCCP showed that the maximal respiratory rate of Nrf2(-/-) cells was 3-fold higher than that of WT cells. The addition of rotenone/antimycin A showed that basal respiration over non-mitochondrial oxygen consumption is 1.5 in WT cells and ~2.1 in Nrf2(-/-) cells, confirming that the former are more glycolytic than the latter. The OCR-ECAR (bioenergetic profine) plot shows, indeed, that Nrf2(-/-) cells display less glycolysis and more oxidative phosphorylation than WT cells (Figure S8). The OCR/ECAR ratio is lower in WT cells (1.5) compared to Nrf2(-/-) cells (3.7), as expected (Figure 3C). Notably, the respiratory parameters fall to normal levels when *Nrf2* is rescued in Nrf2(-/-) cells, clearly demonstrating that the mitochondrial metabolism is controlled by the *KRAS* ^{G12D}-*Nrf2* axis. Furthermore, it also controls the redox homeostasis as the ROS level in Nrf2(-/-) cells drops to levels as in WT cells when *Nrf2* is re-expressed in Nrf2(-/-) cells

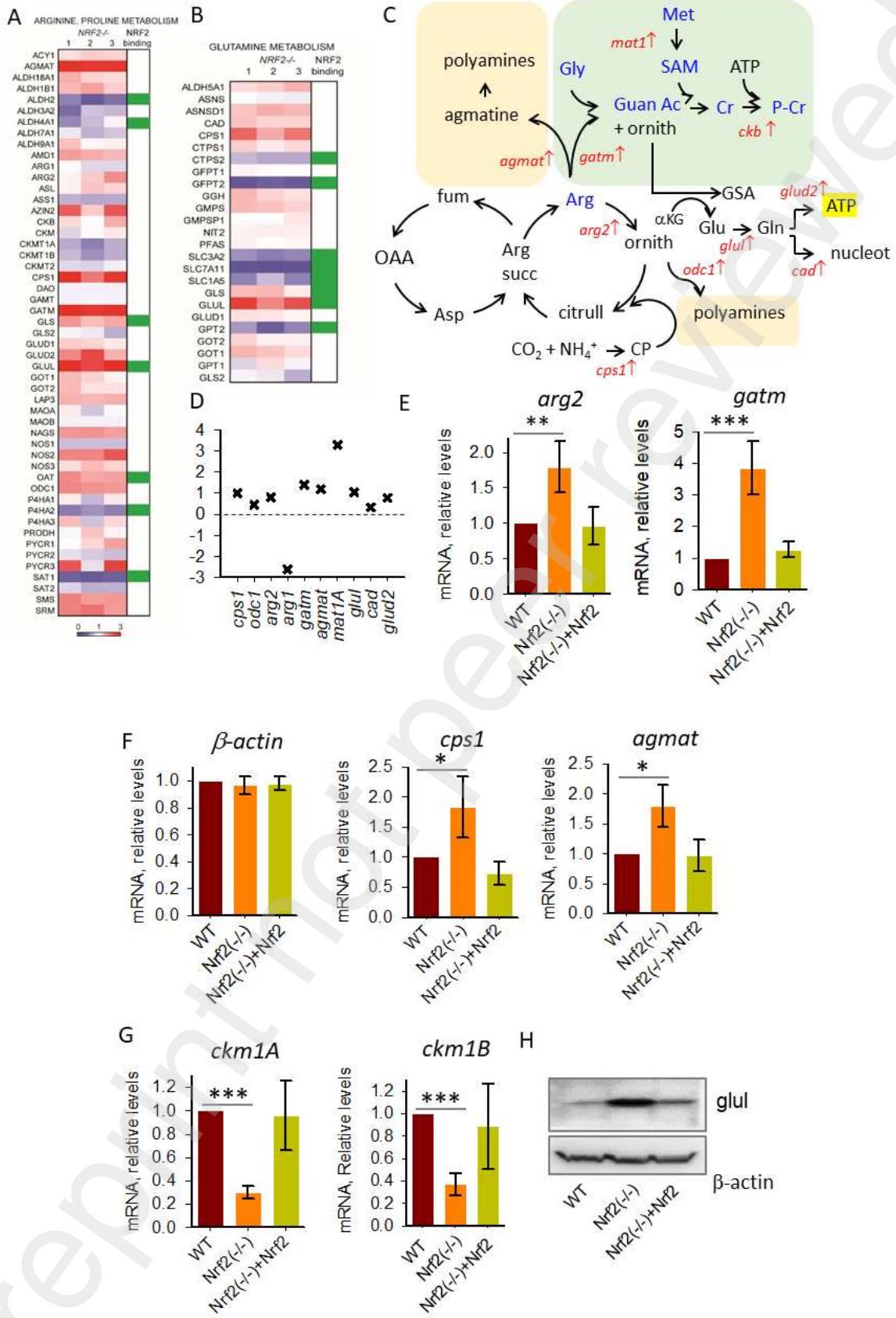

Figure 4: **NRF2 depletion leads to the activation of alternative pathways for energy supply.** (A,B) Heatmaps showing DEG clusters involved in arginine/proline and glutamine metabolism; (C) Metabolic network showing the fate of arginine in Panc-1 cells lacking the *KRAS* ^{G12D}-*Nrf2*(-/-) axis.

The cells respond to Nrf2 deletion by channelling arginine towards the creatine and polyamines pathways. Enzymes involved in the metabolic routes are shown, ↓= downregulated, ↑= upregulated; (D) Log_2 (fold change) of some key DEGs (P<0.05) involved in arginine metabolism; (E,F,G) Expression level of some key enzymes determined by qRT-PCR. As a control, we re-expressed *Nrf2* in Nrf2(-/-) cells. Enzymes *ckm1A* and *ckm1B* are mitochondria located *ckb* isozymes; (H) Expression of *glul* was measured by western blot. Data represent the mean ± s.d. (or s.e.) of at least 3 independent experiments: * P≤ 0.05; ** P≤ 0.01; ***P≤ 0.001 by Student's *t*-test.

(Figure 3D). Another interesting finding was obtained with GSEA which showed that in Nrf2(-/-) cells *KRAS* signaling is switched off, while *CMYC* signaling is switched on (Figure 3E,F). This means that the malignancy of Nrf2(-/-) cells is maintained by a change in the oncogenic program. According to ClueGO, the RAS-GEF pathway promoting the RAS nucleotide exchange for RAS activation is dramatically downregulated in Nrf2(-/-) cells, consistent with an impairment of the *KRAS* signaling in Nrf2(-/-) cells. We found a higher level of CMYC protein in Nrf2(-/-) cells compared to WT cells. The inhibition of ERK5 by XMD8-92 decreased CMYC protein in Nrf2(-/-) cells (Figure 3G), suggesting that the collateral activation of ERK5 may be responsible for the stabilization of CMYC, as previously observed in PDAC (Vaseva et al., 2018). Western blots confirmed the shift in oncogenic program as *KRAS* ^{G12D} activates the MAPK/ERK signaling in WT cells, while *CMYC* activates the PI3K/AKT in Nrf2(-/-) cells (Figure 3H). The switch from ERK to AKT signaling is *Nrf2* dependent, as the rescue of *Nrf2* in Nrf2-depleted cells results in a decrease of pAKT and an increase of pERK, as observed in WT cells. This analysis suggests that *Nrf2* acts at the crossroads of signaling pathways that are essential not only for important aspects of cellular homeostasis but also for oncogenesis. Indeed, Nrf2(-/-) cells showed only a small reduction of proliferation rate and malignancy compared to WT cells (Figure S6).

Panc-1 cells respond to the suppression of the *KRAS-Nrf2* axis by activating anabolic pathways fed by arginine

Pathway enrichment analyses showed that Nrf2(-/-) cells respond to their limited capacity to use glucose by up-regulating key enzymes of arginine/proline and medium-chain fatty acid metabolism (Figure 2A). We now focus on arginine metabolism. Figure 4A-D suggests that arginine goes through a metabolic shift when the *KRAS* ^{G12D}*-Nfr2* axis is

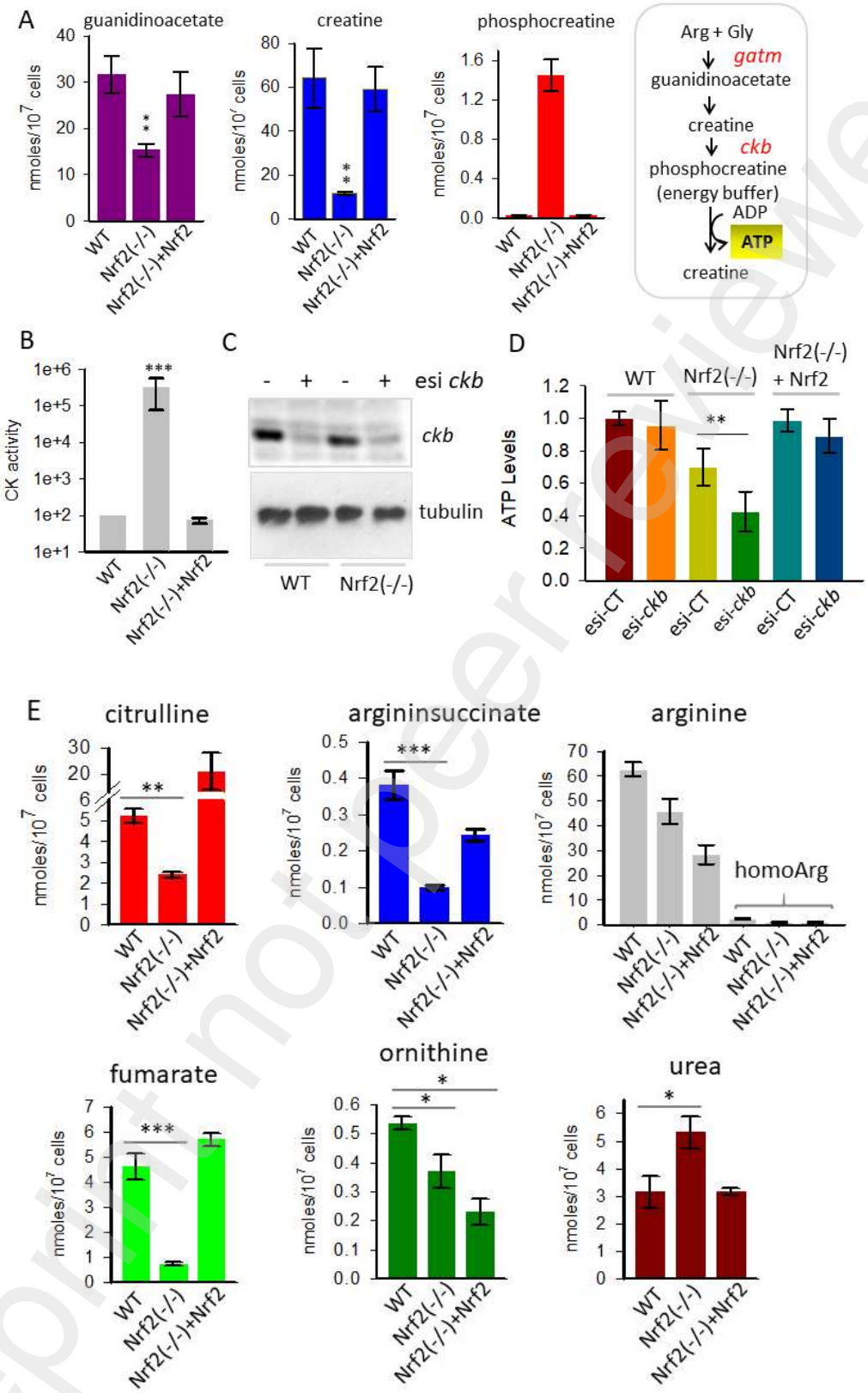

Figure 5: Arginine catabolism feeds the energy needs of Nrf2(-/-) cells. (A) Creatine biosynthesis metabolic intermediates in WT, Nrf2(-/-) and Nrf2(-/-) added with Nrf2 cells; (B) Activity of *ckb* enzyme in WT, Nrf2(-/-) and Nrf2(-/-) added with *Nrf2* cells; (C) Westen blot showing the silencing of *ckb* with esiRNAs against *ckb*; (D) Levels of ATP in WT, Nrf2(-/-) and Nrf2(-/-) cells

re-expressing Nrf2. Suppression of *ckb* results in a strong decrease in ATP level; (E) Urea-cycle metabolic intermediates in WT, Nrf2(-/-) and Nrf2(-/-) re-expressing Nrf2. Data represent the mean ± s.d. (or s.e.) of at least 3 independent experiments: * P≤ 0.05; ** P≤ 0.01; ***P≤ 0.001 by Student's *t*-test.

suppressed. Besides being a key component of the urea cycle (UC), arginine feeds the creatine energy pathway and the biosynthesis of polyamines. Arginine is channelled into the synthesis of creatine by *arginine-glycine amidinotransferase (gatm)*, which catalyses the transfer of the guanidino group from arginine to glycine, yielding guanidinoacetate: a metabolite that gives creatine through S-adenosyl-methionine (SAM) methylation. SAM is formed via *mat1*, which catalyses the transfer of the adenosyl moiety of ATP to methionine. Creatine is then phosphorylated to phosphocreatine by *creatine kinase* (*ckb*), forming an energy buffer, which transfers energy through a reversible reaction, called creatine phosphagen system (Zhang and Bu, 2022; Papalzarou et al., 2020). The *carbamoyl phosphate synthase 1* (*cps1*) gene, which encodes for an enzyme driving the synthesis of carbamoyl phosphate from ammonia and bicarbonate, conveys ammonia into UC. As *cps1* is upregulated in Nrf2(-/-) cells, UC is expected to be active not only as nitrogen disposal, but also as a supplier of nitrogen for the synthesis of arginine to be successively directed towards anabolic routes to sustain cancer growth (Keshet et al., 2018, Apiz-Saab et al., 2022). Interestingly, *arginase 1 (arg1)*, whose function in UC is to transform arginine into ornithine and urea, is downregulated in Nrf2(-/-) cells, consistent with a decreased utilization of arginine in UC and increased utilization in the phosphocreatine and polyamine pathways. In contrast, *arg2,* the isozyme expressed in non-hepatic tissues including cancer (Ino et al., 2013), is significantly upregulated. These data suggest that arginine is a key substrate for Nrf2(-/-) cells, having both anabolic and nitrogen disposal functions. RNA-seq data show that the genes of polyamines and phosphocreatine pathways are upregulated in Nrf2(-/-) cells (Figure 4D). To prove that key enzymes of arginine metabolism leading to the synthesis of polyamines and phosphocreatine are upregulated and dependent on the *KRAS* ^{G12D}*-Nrf2* axis, we carried out qRT-PCR and *Nrf2*-rescue experiments. Figure 4E-G shows that *arg2*, *gatm*, *cps1* and *agmat* are significantly upregulated in Nrf2(-/-) cells, in excellent agreement with RNA-seq data. Their expression drops to levels as observed in WT cells when *Nrf2* is re-expressed. It is of note that while cytosolic *ckb* is unchanged (Figure S9), the mitochondrial isozymes

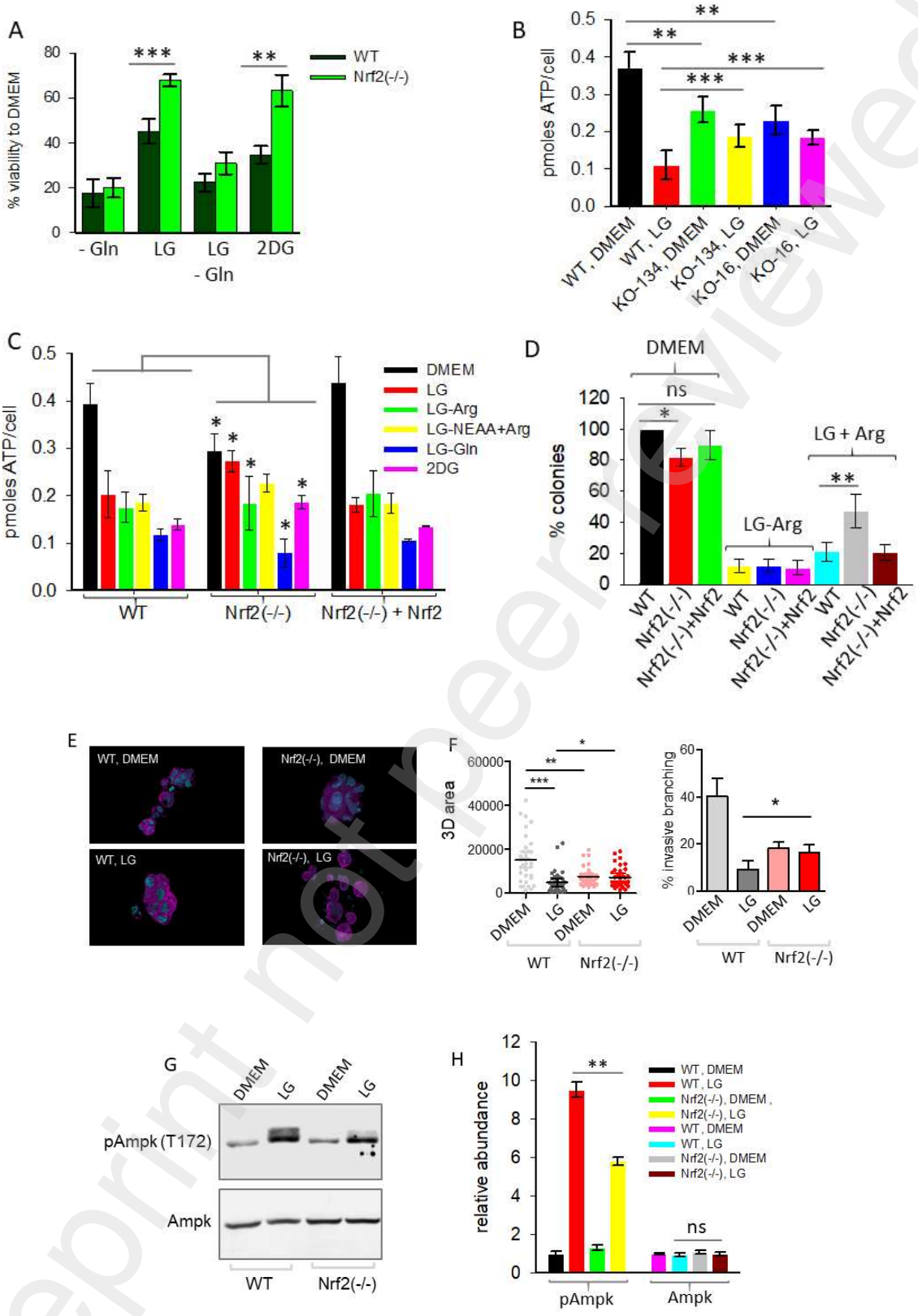

Figure 6: Nrf2 depletion makes Panc-1 cells addicted to aminoacids, in particular to arginine, but insensitive to glucose restriction. (A) % Cell viability relative to DMEM of WT, Nrf2(-/-) and Nrf2(-/-)+Nrf2 Panc-1 cells in medium without glutamine (-Gln), low glucose (LG), LG without glutamine and 2-deoxyglucose (2DG); (B) Amount of ATP (pmoles ATP/cell) in WT and

Nrf2(-/-) cells clone KO-134 and KO-16 cells in DMEM (high glucose) and LG; (C) Amount of ATP (pmoles ATP/cell) in WT, Nrf2(-/-) and Nrf2(-/-) re-expressing Nrf2 cells grown in DMEM, LG, LG without arginine, LG without NEAA but with arginine, LG without glutamine and 2DG; (D) % Colonies in WT, Nrf2(-/-) and Nrf2(-/-) re-expressing Nrf2 cells grown in DMEM, LG without arginine, LG added with arginine; (E) Confocal microscopy images of WT and Nrf2(-/-) spheroids embedded in Matrigel and cultured for 4 days in DMEM (high glucose) or LG; (F) Growth of WT, Nrf2(-/-) and Nrf2(-/-)+Nrf2 spheroids in DMEM or LG. The % of WT and Nrf2(-/-) speroids displaying invading/branching out structures when grown for 4 days in DMEM and LG; (G,H) Expression level of pAmpk and Ampk in WT and Nrf2(-/-) spheroids grown for 4 days in DMEM or LG. Data represent the mean ± s.d. (or s.e.) of at least 3 independent experiments: * P≤ 0.05; ** P≤ 0.01; ***P≤ 0.001 by Student's *t*-test.

ckm1A and *ckm1B* are strongly downregulated in Nrf2(-/-) cells. As a final point, *glul* is highly expressed in Nrf2(-/-) cells because it allows to recover a key aminoacid as glutamine from excess glutamate. Glutamine is substrate for the production of ATP (*glud2* is upregulated) and the synthesis of nucleotides (*cad* is upregulated). The accumulation of phosphocreatine creates a temporal reserve of energy in the form of high-energy phosphate bonds that can be rapidly mobilized when the cells encounter an increased energy demand (Wallimann et al, 2011). To gain insight into this metabolic route we performed metabolomic experiments which showed a dramatic accumulation of phosphocreatine in *Nrf2*-deficient cells (from ~ 0.05 to ~ 1.5 nmoles ATP/cell) (Figure 5A) In contrast, the levels of guanidinoacetate and creatine in Nrf2(-/-) cells were found markedly lower than those observed in WT cells, consistent with their rapid transformation into phosphocreatine. This step is catalysed by *creatine kinase* b (*ckb*) (Papalazarou et lal. 2020), whose activity was found 3-order of magnitude higher in Nrf2(-/-) compared to WT cells (Figure 5B). Cytoplasmatic *ckb* plays a key role in cell energy homeostasis, as it reversibly catalyses the transfer of phosphate between ATP and creatine. The energetic role of *ckb* in Nrf2(-/-) cells was proved by silencing *ckb* with *esi* siRNAs and measuring ATP production (Figure 5C,D). Expectedly, this treatment did not produce any effect on WT cells, whereas it reduced by 40 % ATP in Nrf2(-/-) cells, in keeping with a critical role played by the creatine pathway in these non-glycolytic cells but not in glycolytic WT cells. The metabolomic data show that Nfr2(-/-) cells produce an almost 2-fold higher amount of urea than WT cells, consistent with the fact that Nrf2-deficient cells oxidise aminoacids for energy (Figure 5E). Considering that urea comes mainly from arginine, we roughly estimated that ~10% of arginine follows UC in Nrf2(-/-) cells, while the amount drops to

~5% in WT cells. The fact that Nrf2(-/-) cells have a lower accumulation of fumarate is also consistent with a higher rate of aspartic recycling to maintain UC compared to WT cells. The other pathway fed by arginine involves its transformation into polyamines either via *agmatinase* (*agmat*) or via *arg2* and *ornithine decarboxylase* (*odc1*). Metabolomic data showed that the level of spermidine is 2.5-fold higher in Nrf2(-/-) compared to WT cells (not shown). Polyamines have important cellular functions and support cancer progression (Casero et al., 2018; Kahana, 2018; Novita Sari et al., 2021). Increased levels of polyamines and *odc1* have been reported to contribute to pancreatic carcinogenesis (Black and Chang, 1982, Subhi et al., 2004). Moreover, a recent study showed that *agmat* increases cell proliferation and metastasis in colorectal and pancreatic cancers (Zhang et al., 2022). qRT-PCR and RNA-seq showed that *agmat* in Nrf2(-/-) cells is 2-fold more expressed than in WT cells. Overall, transcriptomic, qRT-PCR and Nrf2-rescue experiments show that the inhibition of *KRAS* ^{G12D}*-Nrf2* axis in Panc-1 cells leads to a profound metabolic rewiring disactivating glycolysis and promoting the use of aminoacids, in particular arginine and glutamine to maintain survival and stimulate proliferation.

Aminoacids provide the substrates for the proliferation of Panc-1 Nrf2 (-/-) cells

To further investigate the metabolic reprogramming resulting from the inactivation of the *KRAS* ^{G12D}*-Nrf2* axis, we tested how WT and Nrf2(-/-) cells respond to glucose and glutamine restrictions. In both cell lines, glutamine starvation dramatically drops cell viability to ~ 20 % of the value observed in DMEM (Figure 6A), consistent with a strong glutamine dependence of PDAC cells as previously observed (Son et al., 2013). The exposure of WT and Nrf2(-/-) cells to low glucose (LG) (5.5 mM) or 2-deoxyglucose (2DG, 25 mM), a molecule that inhibits glycolysis, induced a stronger reduction of cell viability of WT cells (~45 % of DMEM) compared to Nrf2(-/-) cells (~30 % of DMEM), indicating that the latter are less glucose-dependent than the former. When glutamine was removed from LG medium, cell viability further dropped, as glutamine is critical for both WT and Nrf2(-/-) cells. We then measured ATP production (pmoles ATP/cell) under DMEM (i.e. high glucose) and LG conditions (Figure 6B). Expectedly, WT cells show a

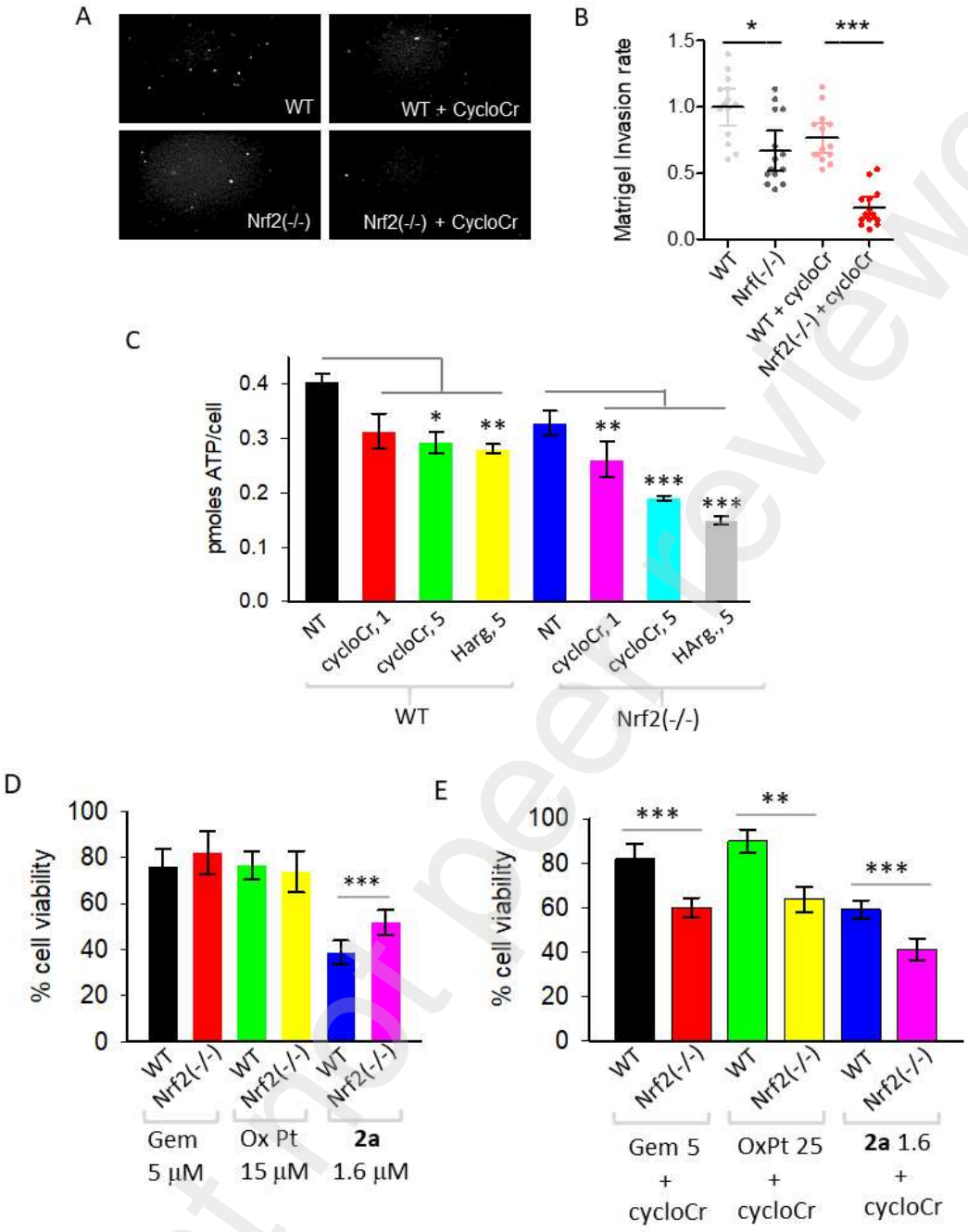

Figure 7 Successful adoption of combined therapies aimed at blocking KRAS/Nrf2 axis, increasing genomic instability and blocking the creatine phosphogen system. (A) Epifluorescent microscopy images of Hoechst + WT and Nrf2(-/-) cells invading 3D matrix after the exposure for 16h to 20% FBS as chemoattractant in the presence or absence of cyclocreatine, as indicated. (B) Matrigel invasion rate of WT and Nrf2(-/-) cells in the absence and presence of cyclocreatine; (C) ATP production (pmoles ATP/cell) in WT and Nrf2(-/-) cells treated with 1 and 5 μM cyclocreatine or 5 μM homoarginine; (D) % Cell viability plots of WT and Nrf2(-/-) cells treated with 5 μM gemcitabine, 15 μM oxaliplatin or 1.6 anthrafuranedione **2a**; (E) % Cell viability plots of WT and Nrf2(-/-) cells treated with 5 μM gemcitabine, 15 μM oxaliplatin or 1.6 anthrafuranedione **2a** in the presence of 5 μM cyclocreatine. Data represent the mean ± s.d. (or s.e.) of at least 3 independent experiments: * P≤ 0.05; ** P≤ 0.01; ***P≤ 0.001 by Student's *t*-test.

dramatic difference in ATP level (>70 %) between the two glucose conditions, due to their glycolytic nature. In contrast, Nrf2(-/-) cells show a minimal perturbation in ATP production between DMEM and LG conditions. This was observed with two Nrf2(-/-) clones: KO-134 and KO-16. Together, the data demonstrate that Nrf2(-/-) cells are less dependent on glucose than WT cells, while both types of cells show a strong dependence on glutamine. This is in keeping with the observed increase of ECAR and sensitivity to sodium oxamate, a *ldha* inhibitor, in WT and Nrf2(-/-) + Nrf2 cells comparted to Nrf2(-/-) cells (Figure S10).

Next, we explored the contribution of aminoacids (Gln, Arg and NEAA) to ATP production under LG conditions (Figure 6C). WT cells exposed to DMEM produce ~ 0.4 pmoles ATP/cell (mainly due to glycolysis). In LG, the level of ATP in WT cells drops by half (from 0.4 to 0.2 pmoles ATP/cell). Removal of arginine or non-essential aminoacids (NEAA) from LG medium did not affect ATP production, while glutamine starvation further reduced ATP by 20 %. The data show that arginine and NEAA are not essential for ATP production in WT cells, while glutamine is. In contrast, Nrf2(-/-) cells show a robust ATP level, ~ 0.3 pmoles ATP/cell, in both DMEM and LG media, confirming that glucose is not a critical substract for Panc-1 cells lacking the *KRAS* ^{G12D}*-Nrf2* axis. A drop of ATP in LG medium deprived of arginine or glutamine is observed. Notably, Nrf2-rescue experiments show that the re-expression of Nrf2 in Nrf2(-/-) cells regained the energetic profile of WT cells. Together, the data suggest that WT cells are glycolytic, while Nrf2(-/-) cells are not and show dependence on glutamine and arginine. To test the impact of arginine on growth of Nrf2(-/-) cells, we measured the capacity of colony formation under DMEM and LG conditions, with and without arginine (Figure 6D). In DMEM, Nrf2(-/-) cells showed a clonogenic growth ~20 % lower than that of WT cells. As a control, a Nrf2-rescue experiment was performed. In contrast, the number of colonies dropped dramatically to < 20% in LG medium without arginine, in all three cell lines. Remarkably, when arginine was supplemented, colony formation of Nrf2(-/-) cells significantly increased up to 50% compared to colony formation in DMEM. On the contrary, in WT or Nrf2(-/-) cells added with Nrf2, the number of colonies did not increase. Taken together, the data demonstrate that a metabolic circuit is activated in Nrf2(-/-) cells that is highly dependent on arginine to ensure malignancy, survival and growth. The independence of Nrf2 (-/-) cells from glucose for growth is even more evident by growing them as 3D spheroids in matrigel (Figure 6E). Nrf2 (-/-) cells formed smaller spheroids with respect to WT cells, but their growth was not

impaired in LG medium (Figure 6F). Similarly, while in DMEM the rate of Nrf2 (-/-) spheroids displaying invasive properties was half that of WT, in LG conditions it was doubled (Figure 6F). An important sensor of cellular energy is AMPK, which is activated by phosphorylation at threonine 172 when intracellular ATP is low. The net effect of pAMPK is stimulation of glucose uptake/β-oxidation and inhibition of anabolism (Garcia and Show, 2017). We measured the levels of AMPK and pAMPK in WT and Nrf2(-/-) 3D spheroids under DMEM or low-glucose conditions (Figure 6G,H). In LG, glycolytic WT cells showed a 5-fold increase of pAMPK, attesting that the primary source of ATP in these cells is glucose. In contrast, Nrf2(-/-) cells showed only a moderate increase of pAMPK (1.5-fold) in LG, consistent with the fact they depend on aminoacids as energy source. Taken together, these results demonstrate that the malignant and invasive properties retained by Nrf2 deficient cells are independent from glucose metabolism, but relay on arginine catabolism.

Effect of cyclocreatine on PDAC growth and design of combination therapies

To evaluate the impact of the phosphocreatine pathway on cell growth, we used cyclocreatine as a competitive inhibitor of *ckb* and homoarginine as an inhibitor of *gatm*. Figure 7A,B shows the ability to form 3D spheroids of WT and Nrf2(-/-) cells in the presence and absence of cyclocreatine. The results show that: (i) the 3D spheroid invasion rate of Nrf2(-/-) cells is ~30% lower than that of WT cells, consistent with the growth observed in 2D cell culture shown in Figure S7; (ii) the 3D spheroid invasion rate of Nrf2(-/-) cells decreases by ~70% in the presence of cyclocreatine, while the invasion rate of WT cells decreases by ~25%. These data suggest that the phosphocreatine pathway is energetically crucial for the growth of Nrf2(-/-) cells, while it is not for the growth of WT cells. Indeed, cyclocreatine (5 mM) and homoarginine (5 mM) reduce ATP levels in Nrf2(-/-) cells by ~50 and 65 %, respectively. In contrast, the two inhibitors only decreased ATP by 25% in WT cells, consistent with the fact that phosphocreatine is not critical for WT cells (Figure 7C).

Next, we tested whether the use of cyclocreatine in combination therapies sensitised PDAC cells to anticancer drugs. We first used 4,11-bis(2-aminoethylamino) anthra[2,3-b]furan-5,10-dione (**2a**), which strongly inhibits the expression of *KRAS* (Miglietta et al., 2017), as anticancer drug. In addition, we also used gemcitabine (Moycan et al, 2013) and

oxaliplatin (Bullock et al, 2017) as drugs against PDAC. Figure 7D shows that 5 μM gemcitabine and 15 μM oxaliplatin cause a weak decrease in cell viability (~20%) in both WT and Nrf2(-/-) cells, while 1.6 μM **2a** reduces cell viability by ~60% in WT cells and by ~50% in Nrf2(-/-) cells. However, when cells are treated simultaneously with 1.6 μM **2a** and 5 μM cyclocreatine, a greater inhibition of cell viability (~60%) is observed in Nrf2(-/-) cells (Figure 7E). This because Nrf2(-/-) cells depend for growth on the phosphocreatine energy buffer. It is noteworthy that cyclocreatine also sensitises pancreatic cancer cells to treatment with gemcitabine and oxaliplatin.

Discussion

In pancreatic cancer cells, redox homeostasis and metabolic reprogramming are under the control of the *KRAS* ^{G12D}-*Nrf2* axis. We proved that *KRAS* ^{G12D} controls *Nrf2* as: (i) the ectopic expression of *KRAS* ^{G12D} in the presence of ROS strongly increases luciferase driven by the Nrf2 promoter; (ii) the extinction of *KRAS* ^{G12D} by siRNA leads to simultaneous downregulation of Nrf2; (iii) the extinction of *Nrf2* promotes the downregulation of glycolytic and PPP enzymes as occurs when *Kras* ^{G12D} is downregulated in a PDAC mouse model (Ying et al, 2012).To investigate the effects of the *KRAS* ^{G12D}-*Nrf2* axis on pancreatic cancer cell metabolism, we knocked down Nrf2 in Panc-1 cells using CRISPR-Cas9. RNA-seq analysis showed that knocking down the axis down-regulated 666 genes and up-regulated 1888 genes. Functional enrichment analysis of DEGs showed strong impairment of sugar catabolism (glycolysis and PPP) and glutathione biosynthesis. Our results are in agreement with those of Fu et al. (2019) who grouped gene microarray data from 53 cases of human ESCC (GEO23400) into Nrf2-high (n=17) and Nrf2-low (n=36). When comparing gene expression between the two groups, they found that metabolic genes involved in glycolysis, PPP and GSH were overexpressed in Nrf2-high ESCC. Moreover, De Pihno and co-workers (Ying et al. 2012) reported that *KRAS* ^{G12D} in PDAC exerts strong control over glycolysis and PPP at the transcriptional level. Since *KRAS* ^{G12D} controls Nrf2 expression, the metabolic reprogramming in PDAC is likely controlled by the *KRAS* ^{G12D}-*Nrf2* axis. It has been suggested that a promising therapeutic approach for PDAC is based on suppression of *KRAS* ^{G12D} or inhibition of its encoded protein (Waters and Der, 2018; Miglietta et al., 2017; Ferino et al., 2020). By targeting either the protein with inhibitors or the gene with small molecules, the *KRAS* ^{G12D}-

Nrf2 axis should be off and arginine displaced from UC towards the creatine phosphagen system and the biosynthesis of polyamines. Therefore, the key enzymes in the de novo synthesis of creatine and polyamine, *agmat* and *gatm*, respectively, are likely to be attractive therapeutic targets for PDAC. Indeed, genetic silencing of *gatm* with shRNA leads to a significant decrease in cell proliferation and an increase in apoptosis in FLT3-ITD -mutated cell lines (Zhang et al., 2022b).

A recent study has shown that the phosphocreatine energy shuttle can metabolically support the migration and invasion of pancreatic cancer cells (Papalazarou et al. 2020). The authors found that although cancer cells rely on glucose consumption and aerobic glycolysis, they exhibit efficient metabolic plasticity that is controlled by the mechanical properties of the microenvironment, such as the stiffness of the extracellular matrix (ECM). In particular, the ECM mechanics were found to control arginine metabolism by diverting arginine from UC to creatine synthesis. This system supplies the cells with energy when their demand is increased. A key gene of the phosphocreatine pathway is *ckb*, whose protein catalyses the reversible phosphorylation of creatine to phosphocreatine: a phosphogenic compound that generates cellular energy by converting ADP to ATP.
Our results show that the phosphocreatine energy system supports pancreatic cancer cells when they are under metabolic stress due to loss of the *KRAS* ^{G12D}*-Nrf2* axis, which restricts the use of glucose. GSEA shows that in *Nrf2*-deficient cells, *KRAS* ^{G12D} signaling is lost while CMYC signaling is upregulated to maintain malignancy. When aerobic glycolysis is inhibited, PDAC cells shift their metabolism from glucose to amino acids and medium-chain fatty acids. Unbiased functional enrichment analyses showed that arginine metabolism adapts to metabolic stress. The levels of urea and phosphocreatine in Nrf2(-/-) cells are 2-fold and 30-fold higher, respectively, than in WT cells, consistent with the fact that Nrf2(-/-) cells become less glycolytic and use aminoacids for energy when the *KRAS* ^{G12D}*-Nrf2* axis is suppressed. Metabolomic data show that the creatine level in WT cells is high (60 nmol/10^7 cells) because it is virtually not converted to phosphocreatine. This is because the activity of *ckb* in WT cells is lower than in Nrf2(-/-) cells. Phosphocreatine forms an efficient energy buffer for proliferation and survival in Nrf2(-/-) cells. When the creatine-phosphagen system is inhibited by cyclocreatine or homoarginine, both Nrf2(-/-) and WT Panc-1 cells show a reduced ability to form 3D spheroids in Matrigel matrix 3D plates. Therefore, combination therapies targeting the *KRAS* ^{G12D}*-Nrf2* axis and the creatine pathway should be more effective than monotherapies. Anthrathiophenedione 2a, which disrupts the *KRAS* ^{G12D}*-Nrf2* axis by suppressing *KRAS*, is indeed more effective

than when used in combination with cyclocreatine. This is because PDAC cells respond to treatment with **2a** by redirecting arginine towards the synthesis of phosphocreatine. Interestingly, cyclocreatine was also found to sensitise PDAC cells to gemcitabine or oxaliplatin-based treatments.

Significance

The 5-year survival rate of PDAC patients is < 8% as the disease develops resistance to conventional chemotherapy. Due to these poor therapeutic outcomes, new therapeutic strategies are urgently needed. Recent studies have highlighted the crucial role of the genes *KRAS* ^{G12D} and *Nrf2* in PDAC cells, which form an axis that regulates not only redox homeostasis but also metabolism. Our work shows that inactivation of the *KRAS* ^{G12D}*-Nrf2* axis leads to a decrease in glycolysis, PPP and glutathione cycling and a simultaneous activation of arginine metabolism, which feeds the synthesis of phosphocreatine. This high-energy storage compound constitutes a critical energy buffer to support proliferation. This means that targeting the *KRAS* ^{G12D}*-Nrf2* axis with anti-cancer drugs leads to a shift in arginine metabolism, which reduces the effectiveness of treatment. Indeed, pancreatic cancer cells become more sensitive to anthrafenodione **2a**, gemcitabine or oxaliplatin when these drugs are used in combination therapy with cyclocreatine, which suppresses the creatine pathway. Our work provides metabolic insights for the rational design of combined strategies for PDAC.

Star Methods

Cell culture and reagents.

Panc-1, HEK293T and Ampho cells were previously characterized (Ferino et al., 2020) and cultured in 10 % FBS DMEM (Euroclone, Milan, Italy). Media were supplemented with 10 % FBS, L-glutamine (2 mM), penicillin (100 $U \cdot ml^{-1}$), and streptomycin (100 $\mu g \cdot ml^{-1}$) (Lonza, Basel, Switzerland). Nrf2 knock-out was achieved by means of CRISPR/Cas9. Monoclonal cultures were grown in 96-well plate and validated by western-blotting and Sanger sequencing. Growth curves were obtained by seeding Panc-1 cells (30000 cells per well) in 12-well plate and allowed them to adhere overnight. Trypan Blue negative cells were counted every 2 days and medium culture was changed every 48 h. For the resazurin reduction assays, the cells were grown in 96-well plate for 120 min. at 37 °C with resazurin solution (0.15 mg/ml) (Sigma-Aldrich, Milan, Italy). The fluorescence of the

reduced product (resorufin) was quantified on a Perkin Elmer EnSpire 2300 Multilabel Reader (ex 550 nm/em 590 nm). The following chemicals were used: 20 μM DMNQ (Enzo Biochem, Farmingdale, New York), 5 mM homoarginine (Merck, Milan, Italy), 5 mM cyclocreatine (Merck, Milan, Italy), 15 μM oxaliplatin (OxPt) (Tocris, UK), 5 μM gemcitabine (Tocris, UK), 1.6 μM anthrathiophenedione **2a** (Miglietta et al., 2017). The antobodies used in the study are reported in Table S3.

Plasmid construction, transfection, retroviral infection, silencing

Plasmid pWZL-Hygro Nrf2 was obtained by subcloning through a restriction-ligation based approach the ORF of Nrf2 (BamHI/SalI) from pBABE hygro mRFP1 NRF2 (Addgene plasmid #136579). Are-luc was obtained by cloning the promotor region of NQO1 (-587 to -379) in pGL3 Basic plasmid (BglII/HindIII). pL Nrf2 (-1810/+151) and pS Nrf2 (-112/+151) were obtaining through a PCR-restriction based approach (NheI/BglII-BamHI). The plasmids encoding *KRAS* were previously described (Ferino et al., 2019).
Transfections of 293 cells were carried out with polyethylenimine (PEI, 1μg/ml) using a 2:1 rate of PEI (μl): DNA (μg). Panc-1 cells were transfected with Lipofectamine 2000 (Thermo Fisher, Waltman, USA). siRNAs (74pmoles) were delivered by using Lipofectamine 3000 (Thermo Fisher, Waltman, USA). The following siRNAs were used: Ckb (esiRNA EHU153971, Merck); KRAS (esiRNA EHU114431, Merck). Retroviral infection was performed with M.O.I of 0.1-0.3 at 32°C by using Ampho cells as packaging cells.

Matrigel plug assay and spheroids culture

A total of 1600 cells were suspended in a Matrigel solution (20 μL 0.1% FBS-DMEM, 60 μL Matrigel, Corning) and plated on coverslips in 35-mm tissue culture plates. After 30 min of incubation at 37 °C, the cells were fed with DMEM–20% FBS or DMEM low glucose 20 % FBS. Following 4-day incubation, coverslips were fixed and stained with Phalloidin AF546 (Molecular Probes, Waltham USA) and Hoechst 33456 (Merck, Milan, Italy).

Invasion assays

Each well of the invasion chamber (CLS3428, Corning, New York, NY, USA) was coated with 200 μL of Matrigel matrix coating solution (Cultrex, Trevigen, Gaithersburg, MD USA). Next, a cell suspension of 3 x10^4 cells in 0.1 % FBS- DMEM or DMEM low glucose was added. As chemoattractant, 20 % FBS-DMEM was added in each lower chamber. As a control, 0.1 % FBS-DMEM was used to evaluate random invasion.

Cytofluorimetric analysis

ROS were quantified as follows: Panc-1 cells grown in adhesion for 2 days in 12-well plate were washed twice with PBS and incubated with 300 µl of 10 µM CM-H2DCFDA (Invitrogen, USA) for 30 min in phenol red-free DMEM without serum. For mitochondrial membrane potential (ΔΨm) quantification, $1x10^6$ cells were loaded with 20 nM TMRM reagent solution (Life Technologies, UK) and incubated for 30 minutes at 37 °C, 5 % CO_2. In both cases, after two washings with PBS, the cells were harvested, resuspended in 200 µl PBS and single cell-suspensions were acquired in FL1 channel (ROS) and in FL2 channel (TMRM) at BD FACSCalibur flow cytometer equipped with a 488 nm argon laser.

ATP, glutathione and total thiols quantification assay

To measure ATP, the cells grown in 35 mm plate and treated as reported in the text were lysed with 100 µl lysis buffer and processed accordingly to manufacturer (ab113849-Abcam). Luminescence was detected at GloMax 20/20 Luminometer (Promega, Madison, USA). Absolute quantification was achieved by comparison to ATP standard curve.
Reduced glutathione (GSH) was measured in cells grown in 96-well plate, lysed in 70 µl lysis buffer, deproteinized with 5-sulfosalicylic acid and processed accordingly to manufacturer (ab239709 Abcam). Absorbance was measured at O.D. 405 nm (EnSpire Multimode Plate Reader, PerkinElmer, Waltham USA). Total GSH was quantified as follows: GSH = (Slope sample -Slope blank)/Slope STD Curve.
For total thiols quantification, the cells grown in 96-well plate were incubated for 30 minutes with 50 µL of GSH reaction mixture at room temperature. Fluorescence intensity was recorded at Ex/Em = 490/520 nm (EnSpire Multimode Plate Reader, PerkinElmer, Waltham USA) and total thiols quantification was obtained through standard curve interpolation.

Immunofluorescence and immunoblotting

Spheroids were fixed with 3 % paraformaldehyde and permeabilized with 0.3 % Triton X-100. Actin was labelled with phalloidin-AF546 (Molecular Probes, USA). Cells were imaged with a confocal microscope Leica TCS SP8X. Nuclei were stained with Hoechst 33342 (10 µg/ml, Merck). Images represent maximum intensity projections of 3D image stacks and were adjusted for brightness and contrast for optimal visualization.

Cell lysates after SDS-PAGE and immunoblotting on nitrocellulose (Whatman, UK) were incubated with primary antibodies that are listed in Table S3. HRP-conjugated secondary antibodies were obtained from Sigma-Aldrich (Milan, Italy) and blots were developed with Super Signal West Dura (Pierce, USA). For fluorescence-based detection, AF660 or AF760 secondary antibodies were used (Merck, Milan, Italy) and images were acquired at Odyssey M Imaging System (LI-COR Biosciences, USA).

Cell Mito Stress test

The experiments have been carried out on XFe Extracellular Flux Analyzer (Seahorse, Agilent Technologies, Santa Clara, CA, USA). Briefly, $4x10^4$ Panc-1 cells were seeded (5 replicates for each experiment) and cultured in XF Cell Culture Microplates (Agilent Technologies) in 500 µl complete DMEM medium and incubated for 24 h at 37 °C in 5% CO_2 atmosphere. Before the measurements, the culture medium was removed from each well and replaced with 500 µl of Seahorse XF Base Medium (Agilent Technologies), pre-warmed at 37 °C and supplemented with 10 mM glucose (Sigma-Aldrich, Heidelberg, Germany), 1 mM pyruvate (EuroClone, Milan, Italy), 2 mM glutamine (Sigma-Aldrich, Heidelberg, Germany), at pH 7.4. Cells were incubated in a CO_2-free incubator at 37 °C for 1 h and OCR (oxygen consumption rate) and ECAR (extracellular acidicication rate) were detected under basal conditions. The following compounds were prepared for each injection port to reach the final concentration of 1 µM oligomycin A, 0.5 µM FCCP, 0.5 µM rotenone and 0.5 µM antimycin A (Merck, Milan, Italy). Volumes of respectively 56, 62, 69 µl of compounds were added to each injection port. OCR values were normalized to the protein content (µg) quantified by spectrophotometry (Bradford assay, Euroclone, Milan, Italy).

Metabolite extraction and Liquid chromatography–mass spectrometry of label-free metabolites.

Cells were plated in 10 cm plates and cultured in DMEM for 48 h. $1x10^7$ cells of each condition were harvested, and cell pellets were washed twice with physiological solution and resuspended into 1 ml of 80 % methanol. Four biological replicates of WT, Nrf2(-/-) and Nrf2 (-/-) cells re-expressing Nrf2 were analyzed. All samples were lysed on a MM 400 mill mixer for 1 min three times, at a shaking frequency of 30 Hz and with the aid of two metal balls, followed by sonication in ice water bath for 2 min. The samples were centrifuged at 21000 g, 5 ºC for 10 min. The clear supernatants were used for the following

LC-MS analyses and the protein pellets were used to measure protein content using a standardized Bradford assay procedure. For the analysis of fumaric acid, phosphocreatine and carbamoyl-P, metabolites were extracted with ice cold extraction buffer consisting of methanol, acetonitrile and water. A stock solution of the three targeted compounds was prepared in an internal standard solution of fumaric-d4 acid in 80 % acetonitrile. This solution was serially diluted with the same solution to have 8-point calibration solutions, in a range of 0.0001 to 10 nmol/ml for each compound. The clear supernatant of each sample solution was diluted 10 times with the internal standard solution. 10 µl aliquots of the calibration solutions and the sample solutions were injected into a HILIC column (2.1 x 100 mm, 1.8 µm) to run UPLC-MRM/MS with negative ion detection on a Waters Acquity UPLC coupled to a Sciex QTRAP 6500 Plus MS instrument, with the use of 5 mM ammonium acetate buffer and acetonitrile as the mobile phase for gradient elution (80% to 20% B in 10 min) at 30°C and 0.3 ml/min. A stock solution of the other compounds was prepared in internal standard solution in 80 % acetonitrile. This solution was serially diluted with the same internal standard solution to make 8-point calibration solutions, in a range of 0.0005 to 100 nmol/ml for each compound. The clear supernatant of each sample solution was diluted 10 times with the same internal standard solution. 10 µl aliquots of the calibration solutions and the sample solutions were injected into an Amide UPLC column (2.1 x 100 mm, 1.7 µm) to run UPLC-MRM/MS with positive ion detection on a Waters Acquity UPLC coupled to a Sciex QTRAP 6500 Plus MS instrument, with the use of 0.1 % formic acid and acetonitrile as the mobile phase for gradient elution (90 % to 30 % B in 12 min) at 30 °C and 0.35 ml/min. LC–MS analysis was performed at Creative Proteomics (Shirley, USA). For the analysis of the results, concentrations of the detected analytes were calculated with internal standard calibration by interpolating the constructed linear-regression curves of individual compounds, with the analyte-to-internal standard peak ratios measured from sample solutions, in an appropriate concentration range for each metabolite.

RNA extraction and quantitative qRT-PCR

Cells were lysed using Trizol (Invitrogen, USA). 1.0µg of total RNA was DNAse I treated (Ambion, USA) and retro-transcribed by using 100 units of M-MLV Reverse transcriptase (Life Technologies, USA) in the presence of 1.6 µM oligo(dT) and 4 µM Random hexamers (Euroclone, Milan, Italy). qRT-PCRs were performed using SYBR green technology (KAPA Biosystems). Data were analyzed by comparative threshold cycle (delta delta Ct ΔΔCt)

using *hprt* and *actb* as normalizer. The list of the primers used for qRT-PCR are reported in Table S2.

RNA-seq analysis and Gene-set enrichment analysis (GSEA)

Panc-1 cells were lysed using Tri Reagent (Molecular Research Center, USA). Total RNA was treated with DNAse I (NEB, USA) and purified with RNA Clean & Concentrator (Zymo Research, USA). RNA-seq poly A enriched transcripts library preparation and sequencing were performed at BMR-Genomics (Padua, Italy) following Illumina specifications. Quality control for raw sequencing reads was performed with FastQC (v0.11.9) (www.bioinformatics.babraham.ac.uk/projects/fastqc/) and MultiQC (v1.09). Alignment of reads was conducted with STAR (v2.5.3a) (Dobin et al. 2013), using the human genome assembly GRCh38 with reference annotation; reads were assigned to a gene based on EnsEMBL annotations and via the STAR function "quantMode GeneCounts". Differential expression (DE) analysis was performed using gene raw counts, within the R/Bioconductor DESeq2 package (Love et al., 2014): we estimated the dispersion parameter for each library using the biological group dispersion. Principal component analysis was carried out with the plotPCA function from the DESeq2 package (v1.28.1). Genes with raw counts mean < 64 between each condition replicates were removed from the analysis. Differential expression analysis was performed using DESeq2 with Wald test for significance. We adjusted for multiple hypothesis testing by employing Benjamini-Hochberg correction at a false discovery rate (FDR) of 0.05. Genes with an absolute fold change ≥1 were considered as differentially expressed. Genes were annotated with package AnnotationHub (v2.20.2) utilizing Ensembl annotation 100 data. Functional annotation was performed on KEGG, Reactome slimGO and Gene Ontology databases with ClusterProfiler (v3.16.1) and ReactomePA (v1.32.0). Gene set enrichment analysis (GSEA) and the MSigDB database were used to investigate statistically relevant biological associations. Heatmaps were generated for each gene set and the expression of each gene was expressed as $\log_2$ (fold change) of Nrf2(-/-) vs WT cell samples. The direct binding of Nrf2 in proximity (± 5 kb) to the TSS of the identified genes were retrieved from Harmonizome dataset (https://maayanlab.cloud/Harmonizome/).

Statistics

For experimental data, Student *t*-test was employed. Mann–Whitney test was applied when normality could not be assumed. P< 0.05 was chosen as statistical limit of

significance. For comparisons between more than two samples, tAnova test was applied coupled to Kruskal–Wallis and Dunn's Multiple Comparison Test. For correlation between two variables, Pearson correlation or Spearman correlation were calculated for normal or non-normal distributions, respectively. Excel and GraphPad Prism were used for routineer analysis, R/Bioconductor packages for large data analysis and heatmap generation. We marked with *P< 0.05, **P< 0.01, ***P< 0.001. Unless otherwise indicated, all the data in the figures were represented as arithmetic means ± the standard deviations from at least three independent experiments.

Data and code availability

RNA-seq data were deposited in GEO database: GSE217965.

For reviewers, enter token: sfutgqwkrhspbkz

Acknowledgment

This work was supported by AIRC (Associazione Italiana per la Ricerca sul Cancro): project number 19898 (LEX) and MFAG2020 ID 25000 (EDG). We thank Prof. Andrey Shchekotikhin for compound **2a**.

Author Contributions

Conceptualization, L.E.X and E.DG; Methodology, E.DG; Investigation, E.DG, H.C., Y.C., F.A., M.C. and V.R.; Confocal microscopy, FD; Writing – Original Draft, L.E.X and E.DG; Funding Acquisition, L.E.X and E.DG.; Bioinformatic analyses, E.D. and E.DG; Supervision, E.DG and L.E.X

Declaration of interest

The authors declare no competing interests.

Supplemental information

Table S1-S3, Figures S1–S10.

References

1. Apiz-Saab JJ, Dzierozynski LN, Jonker PB, Zhu Z, Chen RN, Oh M, Sheehan C, Macleod KF, Weber CR, Muir A. Pancreatic tumors activate arginine biosynthesis to adapt to myeloid-driven amino acid stress. *bioRxiv* 2022, **06**, 21.497008.

2. Black Jr O, Chang BK. Ornithine decarboxylase enzyme activity in human and hamster pancreatic tumor cell lines. *Canc. Lett*.1982, **17**, 87-93.

3. Bollong, MJ., Lee, G., Coukos, JS, Yun H, Zambaldo C, Chang JW, Chin EN, Ahmad I, Chatterjee AK, Lairson LL, Schultz PG. A metabolite-derived protein modification integrates glycolysis with KEAP1–NRF2 signaling. *Nature* 2018, **562**, 600–604.

4. Bos JL. Ras oncogenes in human cancer: a review. *Cancer Res* 1989, **49**, 4682-4689.

5. Bullock A, Stuart K, Jacobus S, Abrams T, Wadlow R, Goldstein M, Miksad R. Capecitabine and oxaliplatin as first and second line treatment for locally advanced and metastatic pancreatic ductal adenocarcinoma. *J Gastrointest Oncol.* 2017, **8**, 945-952.

6. Burris HA, Moore MJ, Andersen J, Green MR, Rothenberg ML, Modiano MR, Cripps MC, Portenoy RK, Storniolo AM, Tarassoff P. et al. Improvements in survival and clinical benefit with gemcitabine as first-line therapy for patients with advanced pancreas cancer: A randomized trial. *J. Clin. Oncol.* 1997, **15**, 2403–2413.

7. Casero RA, Murray Stewart T, Pegg AE. Polyamine metabolism and cancer: treatments, challenges and opportunities. *Nat Rev Cancer* 2018, **18**, 681–695.

8. Chio IIC, Jafarnejad SM, Ponz-Sarvise M, Park Y, Rivera K, Palm W, Wilson J, Sangar V, Hao Y, Öhlund D, Wright K, Filippini D, Lee EJ, Da Silva B, Schoepfer C, Wilkinson JE, Buscaglia JM, DeNicola GM, Tiriac H, Hammell M, Crawford HC, Schmidt EE, Thompson CB, Pappin DJ, Sonenberg N, Tuveson DA. NRF2 Promotes Tumor Maintenance by Modulating mRNA Translation in Pancreatic *Cancer. Cell*. 2016,**166**, 963-976.

9. Collins MA, Brisset JC, Zhang Y, et al. Metastatic pancreatic cancer is dependent on oncogenic Kras in mice. *PLoS One.* 2012;**7**:e49707.

10. DeNicola GM, Karreth FA, Humpton TJ, Gopinathan A, Wei C, Frese K, Mangal D, Yu KH, Yeo CJ, Calhoun ES, Scrimieri F, Winter JM, Hruban RH, Iacobuzio-Donahue C, Kern SE, Blair IA, Tuveson DA. Oncogene-induced Nrf2 transcription promotes ROS detoxification and tumorigenesis. *Nature*. 2011, **475**, 106-109.

11. di Magliano MP, Logsdon CD. Roles for KRAS in pancreatic tumor development and progression. *Gastroenterology*. 2013;**144**,1220-1229.

12. Dobin A, Davis CA, Schlesinger F, Drenkow J, Zalenski C, Sonali J, Batut P, Chaisson M, Gingeras TR (2013) STAR: ultrafast universal RNA-seq aligner. *Bioinformatics* 2013, **29**, 15–21.

13. Ellington WR. Evolution and physiological role of phosphagen systems. *Annu Rev. Physiol.* 2001, **63**, 289-325.

14. Fenouille N et al. The creatine kinase pathway is a metabolic vulnerability in EVI1-positive acute myeloid leukemia. *Nat Med*. 2017, **23**, 301-313.

15. Ferino A, Rapozzi V, Xodo LE. The ROS-KRAS-Nrf2 axis in the control of the redox homeostasis and the intersection with survival-apoptosis pathways: Implications for photodynamic therapy. *J Photochem Photobiol B*. 2020, **202**,111672.

16. Ferino A, Nicoletto G, D'Este F, Zorzet S, Lago S, Richter SN, Tikhomirov A, Shchekotikhin A, Xodo LE. Photodynamic Therapy for *ras*-Driven Cancers: Targeting G-Quadruplex RNA Structures with Bifunctional Alkyl-Modified Porphyrins. *J Med Chem*. 2020, **63**, 1245-1260.

17. Fu J, Xiong Z, Huang C, Li J, Yang W, Han Y, Paiboonrungruan C, Major MB, Chen KN, Kang X, Chen X. Hyperactivity of the transcription factor Nrf2 causes metabolic reprogramming in mouse esophagus. *J Biol Chem*. 2019, **294**, 327-340.

18. Garcia D, Shaw RJ. AMPK: Mechanisms of Cellular Energy Sensing and Restoration of Metabolic Balance. *Mol Cell*. 2017, **66**, 789-800.

19. Hingorani SR, Petricoin EF, Maitra A, Rajapakse V, King C, Jacobetz MA, Ross S, Conrads TP, Veenstra TD, Hitt BA, Kawaguchi Y, Johann D, Liotta LA, Crawford HC, Putt ME, Jacks T, Wright CVE, Hruban RH, Lowy AM, Tuveson DA.

Preinvasive and invasive ductal pancreatic cancer and its early detection in the mouse, *Cancer Cell*, 2003, **4**, 437-450.

20. Jaffee EM, Hruban RH, Canto M, Kern SE. Focus on pancreas cancer. *Cancer Cell* 2002**, 2**, 25-28.

21. Kahana C. The antizyme family for regulating polyamines. *J Biol Chem*. 2018, **293**, 18730-18735.

22. Keshet R, Szlosarek P, Carracedo A, Erez A. Rewiring urea cycle metabolism in cancer to support anabolism. *Nat Rev Cancer*. 2018, **18**, 634-645.

23. Koorstra JB, Hustinx SR, Offerhaus GJ, Maitra A. Pancreatic carcinogenesis. *Pancreatology* 2008, **8**,110-125.

24. Love MI, Huber W, Anders S (2014) Moderated estimation of fold change and dispersion for RNA-seq data with DESeq2. *Genome Biol* 2013,**15**, 550.

25. Miglietta G, Cogoi S, Marinello J, Capranico G, Tikhomirov AS, Shchekotikhin A, Xodo LE. RNA G-Quadruplexes in Kirsten Ras (KRAS) Oncogene as Targets for Small Molecules Inhibiting Translation. *J Med Chem*. 2017, **60**, 9448-9461.

26. Mitsuishi Y, Taguchi K, Kawatani Y, Shibata T, Nukiwa T, Aburatani H, Yamamoto M, Motohashi H. Nrf2 redirects glucose and glutamine into anabolic pathways in metabolic reprogramming. *Cancer Cell*. 2012, **22**, 66-79.

27. Ino Y, Yamazaki-Itoh R, Oguro S, Shimada K, Kosuge T, Zavada J, Kanai Y, Hiraoka N. Arginase II expressed in cancer-associated fibroblasts indicates tissue hypoxia and predicts poor outcome in patients with pancreatic cancer. *PLoS One* 2013, **8**, e55146.

28. Novita Sari I, Setiawan T, Seock Kim K, Toni Wijaya Y, Won Cho K, Young Kwon H. Metabolism and function of polyamines in cancer progression. *Cancer Lett.* 2021 **519**, 91-104.

29. Papalazarou V, Zhang T, Paul NR, Juin A, Cantini M, Maddocks ODK, Salmeron-Sanchez M, Machesky LM. The creatine-phosphagen system is

mechanoresponsive in pancreatic adenocarcinoma and fuels invasion and metastasis. *Nat Metab*. 2020, **2**, 62-80.

30. Rahib L, Smith BD, Aizenberg R, et al. Projecting cancer incidence and deaths to 2030: the unexpected burden of thyroid, liver, and pancreas cancers in the United States. *Cancer Res*. 2014, **74**, 2913-2921.

31. Shit MM, Kugelmant A, Iwamoto T, Tiant L, Formane JH. Quinone-induced oxidative stress elevates glutathione and induces y-glutamylcysteine synthetase activity in rat lung epithelial L2 cells. *J. Biol. Chem*. 1994, **269**, 26512-26517.

32. Siegel RL, Miller KD, Jemal A. Cancer statistics, 2016. *CA Cancer J Clin*. 2016, **66**, 7–30.

33. Son J, Lyssiotis CA, Ying H, et al. Glutamine supports pancreatic cancer growth through a KRAS-regulated metabolic pathway [published correction appears in Nature. 2013 Jul 25;499(7459):504]. *Nature*. 2013;**496**, 101-105.

34. Subhi AL, Tang B, Balsara BL, Altomare DA, Testa JR, Cooper HS, Hoffman JP, Meropol NJ, Kuger WD. Loss of methylthioadenosine phosphorylase and elevated ornithine decarboxylase is common in pancreatic cancer. *Clin. Canc. Res.* 2004, **10**, 7290-7296

35. Sunil R. Hingorani, Emanuel F. Petricoin, Anirban Maitra, Vinodh Rajapakse, Catrina King, Michael A. Jacobetz, Sally Ross, Thomas P. Conrads, Timothy D. Veenstra, Ben A. Hitt, Yoshiya Kawaguchi, Don Johann, Lance A. Liotta, Howard C. Crawford, Mary E. Putt, Tyler Jacks, Christopher V.E. Wright, Ralph H. Hruban, Andrew M. Lowy, David A. Tuveson, Preinvasive and invasive ductal pancreatic cancer and its early detection in the mouse, 2003, *Cancer Cell* 2003**, 4**, 437-450.

36. Tao S, Wang S, Moghaddam SJ, Ooi A, Chapman E, Wong PK, Zhang DD. Oncogenic KRAS confers chemoresistance by upregulating NRF2. *Cancer Res.* 2014, **74**, 7430-7441.

37. Vaseva AV, Blake DR, Gilbert TSK, Ng S, Hostetter G, Azam SH, Ozkan-Dagliyan I, Gautam P, Bryant KL, Pearce KH, et al. KRAS Suppression-Induced Degradation of MYC Is Antagonized by a MEK5-ERK5 Compensatory Mechanism. *Cancer Cell*. 2018, **34**, 807-822.e7.

38. Vomund S, Schäfer A, Parnham MJ, Brüne B, von Knethen A. Nrf2, the Master Regulator of Anti-Oxidative Responses. *Int J Mol Sci*. 2017, **18**, 2772.

39. Wallimann, T., Tokarska-Schlattner, M. & Schlattner, U. The creatine kinase system and pleiotropic effects of creatine. *Amino Acids* 2011, **40**, 1271–1296.

40. Warburg, O. On the origin of cancer cells, *Science 1956,* **123**, 309–314.

41. Waters AM, Der CJ. KRAS: The Critical Driver and Therapeutic Target for Pancreatic Cancer. *Cold Spring Harb Perspect Med*. 2018, **8,** a031435.

42. Yu Z, Shao W, Chiang Y, Foltz W, Zhang Z, Ling W, Fantus IG, Jin T. Oltipraz upregulates the nuclear factor (erythroid-derived 2)-like 2 [corrected](NRF2) antioxidant system and prevents insulin resistance and obesity induced by a high-fat diet in C57BL/6J mice. *Diabetologia*. 2011, **54**, 922-934.

43. Ying H, Kimmelman AC, Lyssiotis CA, et al. Oncogenic Kras maintains pancreatic tumors through regulation of anabolic glucose metabolism. *Cell*. 2012;**149**, 656-670.

44. Zhang L, Bu P. The two sides of creatine in cancer. *Trends Cell Biol*. 2022, **32**, 380-390.

45. Zhang Y, Newsom KJ, Zhang M, Kelley JS, Starostik P. GATM-Mediated Creatine Biosynthesis Enables Maintenance of FLT3-ITD-Mutant Acute Myeloid Leukemia. *Mol Cancer Res*. 2022, **20**, 293-304.

Supporting Information

The suppression of the *KRAS* ^{G12D}-*Nrf2* axis shifts arginine into the phosphocreatine energy system in pancreatic cancer cells

Eros Di Giorgio[&*], Himanshi Choudhary[&], Annalisa Ferino, Ylenia Cortolezzis, Emiliano Dalla, Francesca D'Este, Marina Comelli, Valentina Rapozzi and Luigi E. Xodo*

Table S1: Flux respiratory analysis of WT, Nrf2(-/-) and Nrf2(-/-) added with Nrf2 Panc-1 cells

	WT	Nrf2(-/-)	Nrf2(-/-) + *Nrf2*
Parameter			
Basal	9.0±1.4	17.8±1.9	9.8±2.3
Proton leak	3.8±0.7	6.5±0.9	4.0±1.1
Maximal respiration	11.6±2.0	34.9±4.1	12.7±3.4
Spare Res Capacity	2.6±1.0	17.2±2.3	2.9±1.1
Non-Mit OCR	6.0±1.7	8.2±0.9	4.6±1.2
ATP production	5.2±0.7	11.3±1.1	5.7±1.2

Table S2: qPCR primers used for this study.

OLIGO NAME	**SEQUENCE 5'->3'**
HK2_FW	TGCCACCAGACTAAACTAGACG
HK2_RV	CCCGTGCCCACAATGAGAC
GCLC_FW	AGGACAAACCCAAACCATCCT
GCLC_RV	TGTTAAGGTACTGGGAAATGAAGT
GPX3_FW	CCTTCCTACCCTCAAGTATGTCC
GPX3_RV	AGGCGGTCAGATGTACCCA
LDHA_FW	TTGACCTACGTGGCTTGGAAG
LDHA_RV	GGTAACGGAATCGGGCTGAAT
ENO2_FV	AGCCTCTACGGGCATCTATGA
ENO2_RV	TTCTCAGTCCCATCCAACTCC
TKT_FW	TCCACACCATGCGCTACAAG
TKT_RV	CAAGTCGGAGCTGATCTTCCT
G6PD_FW	ACCGCATCGACCACTACCT
G6PD_RV	TGGGGCCGAAGATCCTGTT
ARG2_FW	CGCGAGTGCATTCCATCCT
ARG2_RV	TCCAAAGTCTTTTAGGTGGCAG
GATM_FW	CACTACATCGGATCTCGGCTT
GATM_RV	CTAAGGGGTCCCATTCGTTGT
HPRT_RT_FW	AGACTTTGCTTTCCTTGGTCAGG
HPRT_RT_RV	GTCTGGCTTATATCCAACACTTCG
GAPDH RT_FW	CCCTTCATTGACCTCAACTACATG
GAPDH RT_RV	TGGGATTTCCATTGATGACAAGC
CPS1_RT_FW	AATGAGGTGGGCTTAAAGCAAG
CPS1_RT_RV	AGTTCCACTCCACAGTTCAGA
AGMAT_RT_FW	GTGTGGTGCAGATTGGCATC
AGMAT_RT_RV	GACCAGCAATTTCAGGTGTCC
CKMT1B_RT_FW	ATATGACCCCCGGACAATGAA
CKMT1B_RT_RV	CTTCGGCCAGTTCTGACTCT
CKMT1A_RT_FW	AGGCAAATCAGAGGTGGAGC
CKMT1A_RT_RV	GGATGACAGGTGTGGGGATG

Table S3: Antibodies used for this study

Antibody target	**Company**	**Code**	**RRID**
NRF2	Santa Cruz Biotechnology	sc-518033	AB_2892633
TKT	Santa Cruz Biotechnology	sc-390179	AB_2091939
GLUL	Santa Cruz Biotechnology	sc-74430	AB_1127501
CKB	Santa Cruz Biotechnology	sc-373686	AB_2291855
TUBULIN	Santa Cruz Biotechnology	sc-166729	AB_2288090
c-MYC	Cell Signalling	D84C12	AB_2798045
pAKT1 (Ser473)	Cell Signalling	D7F10	AB_2629283
AKT1	Cell Signalling	C73H10	AB_915788
p44/42 MAPK (Thr202/Tyr204)	Cell Signalling	D13.14.4E	AB_2728835
p44/42 MAPK	Cell Signalling	137F5	AB_10695739
AMPKα	Cell Signalling	2532	AB_490795
pAMPKα (Thr172)	Cell Signalling	40H9	AB_10697491
GAPDH	Merck	71.1	AB_11211543
ACTIN	Merck	A2066	AB_11212552
E-CADHERIN	Merck	5085	AB_10752268
VIMENTIN	Merck	VIM-13.2	AB_2315587
Cells and plasmids	**RRID**		
Panc-1	CVCL_0480		
Phoenix-Ampho	CVCL_H716		
pBABE hygro mRFP1 NRF2	Addgene_136579		
Pgl3	Addgene_48743		

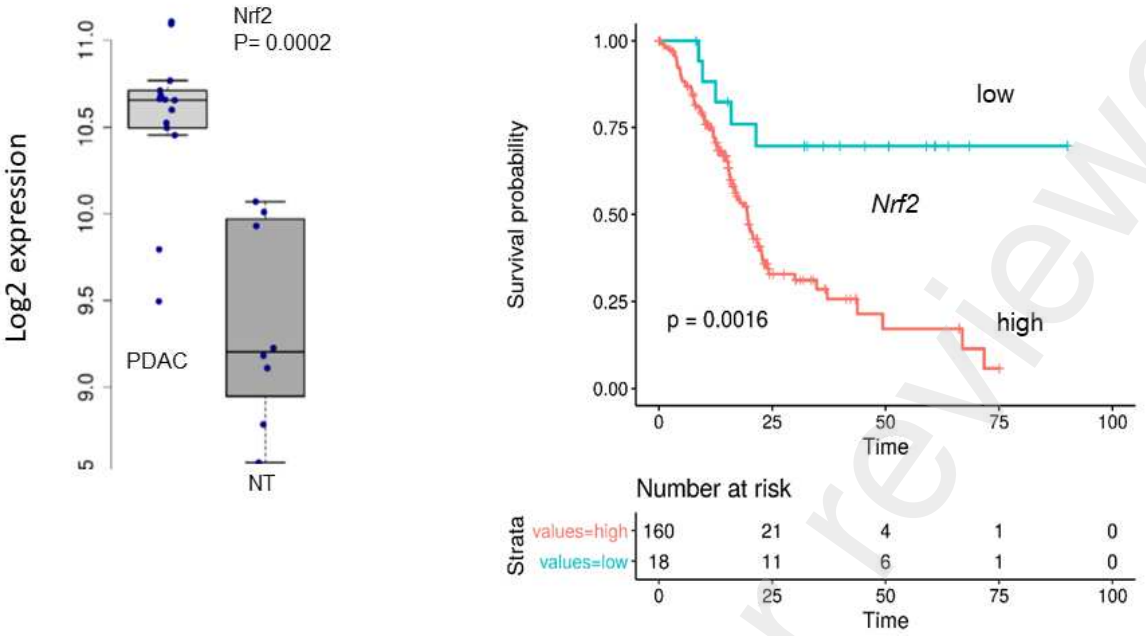

Figure S1: (left) Differential expression of Nrf2 between normal and tumor tissues in PDAC patients. Data obtained from GSE15471; (right) Kaplan-Meir plots show that patients with high Nrf2 expression exhibit a lower survival probability than patients with low Nrf2 expression.

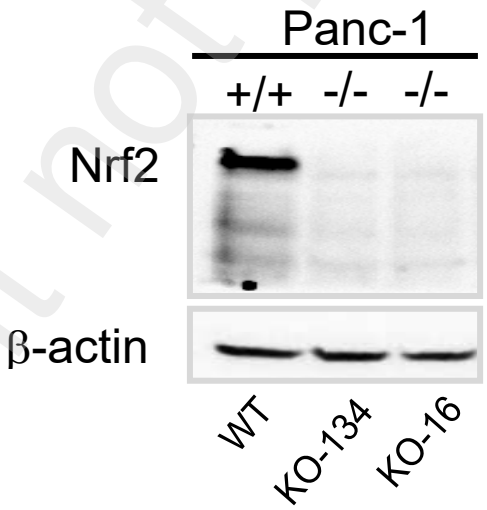

Figure S2: Wild-type Panc-1 cells express Nrf2, while the KO-134 and KO-16 clones in which Nrf2 was knockout with CRISPR-Cas9 do not express Nrf2, as expected.

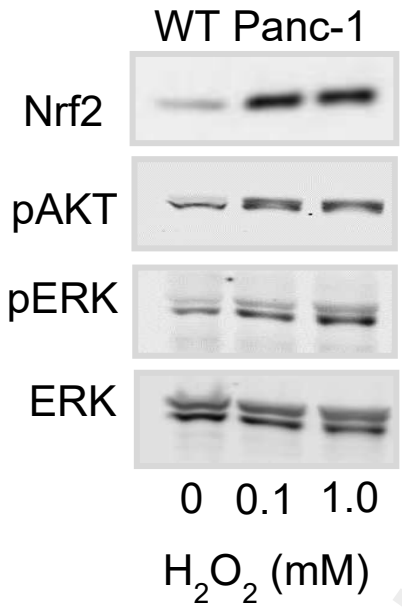

Figure S3: Panc-1 cells under oxidative stress (due to treatment with H_2O_2) the Nrf2 gene is upregulated and the AKT and ERK pathways are activated.

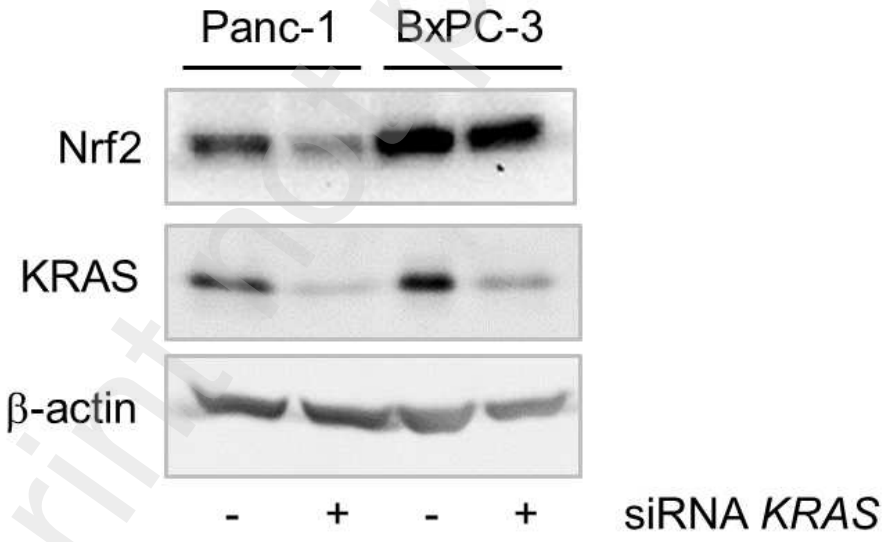

Figure S4: *KRAS*-specific siRNA downregulates KRAS expression in Panc-1 and BxPC-3 pancreatic cancer cells. In parallel, the siRNA also downregulates Nrf2 in Panc-1 cells bearing mutant *KRAS* ^{G12D} and slightly downregulates Nrf2 in BxPC-3 bearing only wild-type *KRAS*.

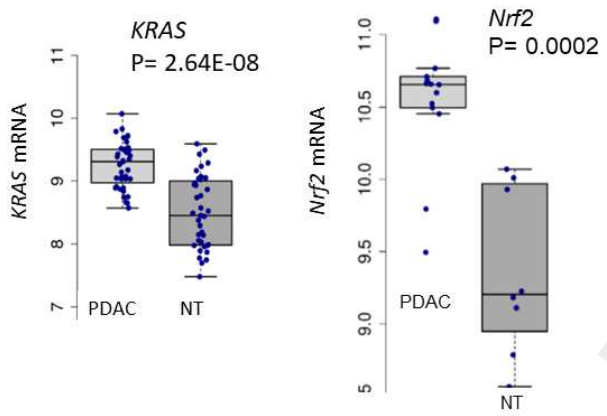

Figure S5: Differential expression of *Nrf2* and *KRAS* between normal and tumor tissues in PDAC patients. Data obtained from GSE15471.

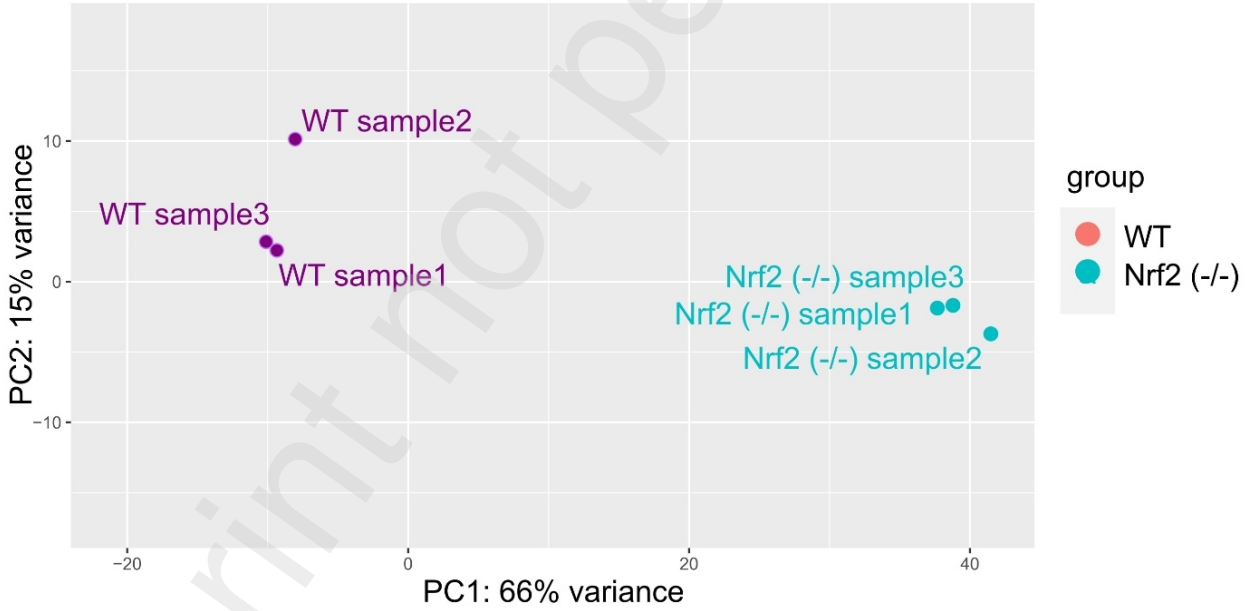

Figure S6: Differentially expressed genes (DEGs) between Nrf2 (-/-) and WT cells are shown by principal component analysis (PCA). PCA displays a high reproducibility of the sample replicates and significant variation between WT and Nrf2 (-/-) cells.

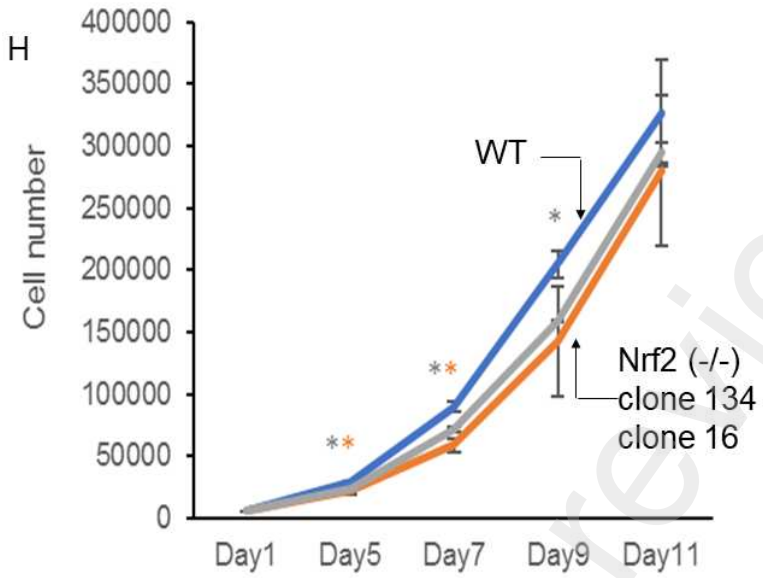

Figure S7: Proliferation of Nrf2(-/-) cells (clones KO-134 and KO-16) in DMEM over a period of 11 days. Wild-type Panc-1 cells grow at a higher rate compared to Panc-1 Nrf2(-/-) cells

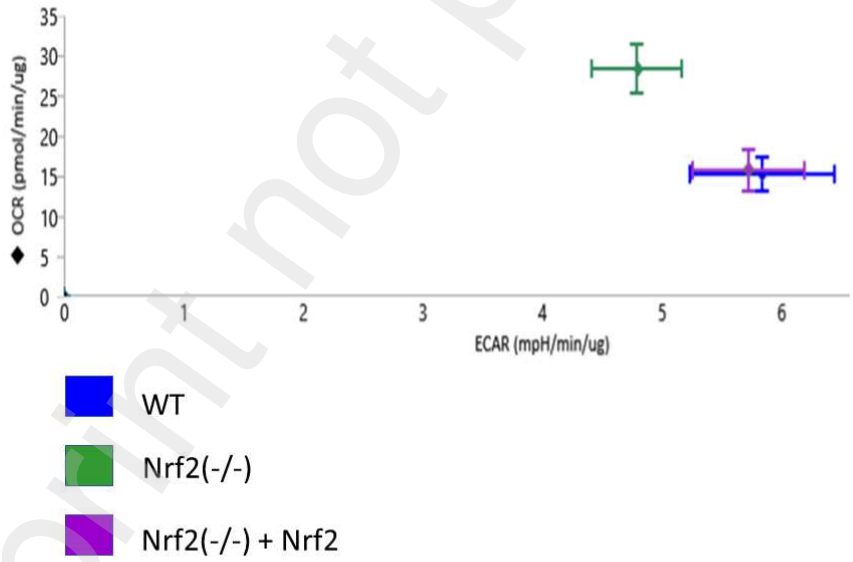

Figure S8: OCR (oxygen consumption rate) versus ECAR (extracellular acidification rate) plot provides a snapshot of the bioenergetics profiles of WT, Nrf2(-/-) and Nrf2(-/-) + Nrf2 cells. The Nrf2(-/-) cells display less glycolysis and more oxidative phosphorylation with respect to WT cells or Nrf2(-/-) cells re-expressing Nrf2.

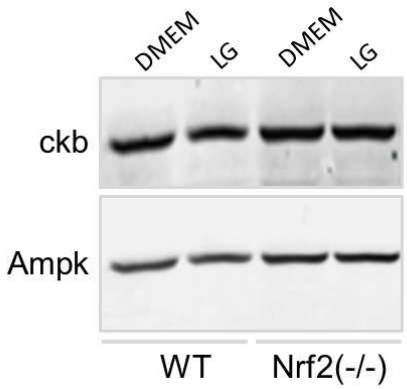

Figure S9: Level of *ckb* in DMEM (high glucose) and low glucose in WT and Nrf2(-/-) Panc-1 cells

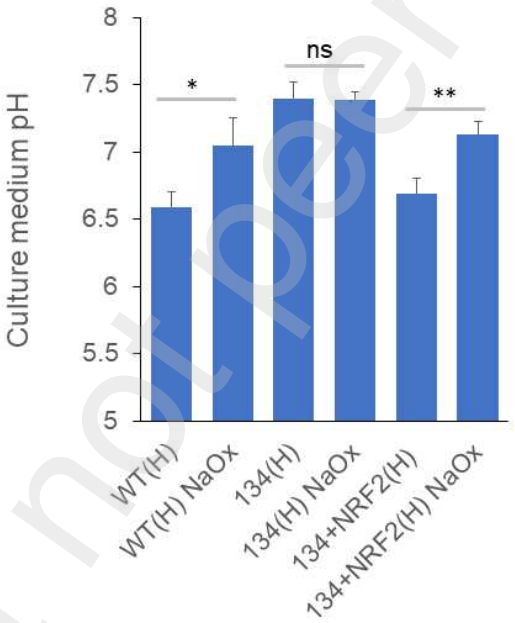

Figure S10: WT Panc-1 cells and Nrf2(-/-) cells expressing Nrf2 show sensitivity to sodium oxamate, an inhibitor of *ldha* because the cells are glycolytic and depend on glucose. In contrast, Nrf2(-/-) cells are not sensitive to sodium oxamate because they are not glycolytic and basically do not depend on glucose.

Section 4

Targeted Cancer Therapy: KRAS-Specific Treatments for Pancreatic Cancer

Targeted Cancer Therapy: KRAS-Specific Treatments for Pancreatic Cancer

Himanshi Choudhary and Luigi E. Xodo

Contents

Abstract

Pancreatic cancer is highly dependent on the activity of the *KRAS* oncogene, which controls the redox homeostasis and induces metabolic reprogramming. Since *KRAS* is critical for the growth of ~30% of human tumors, targeting this oncogene is a high priority in cancer therapy. Despite its proven importance in cancer, the numerous efforts over the last three decades to develop inhibitors for protein KRAS or for downstream signaling pathways have not reached the clinic. For this reason, the *KRAS* oncogene has been for a long time considered undruggable. Two sequence elements of *KRAS*, located in the promoter and 5′-untranslated region (UTR), have high guanine content that allows folding into G-quadruplex (G4) structures. The G4 motif near the transcription initiation site called 32R acts as a hub for transcription factors, making it an attractive target for small molecules capable of competing DNA-protein interactions. In addition, the 5′-UTR of mRNA folds into a complex tertiary structure in which three

H. Choudhary · L. E. Xodo (✉)
Department of Medicine, Laboratory of Biochemistry, University of Udine, Udine, Italy
e-mail: luigi.xodo@uniud.it

N. Sugimoto (ed.), *Handbook of Chemical Biology of Nucleic Acids*,
https://doi.org/10.1007/978-981-16-1313-5_69-1

nonoverlapping G4 motifs near the 5′-cap form RNA G-quadruplexes that are recognized by cationic porphyrins: photosensitizers that, when irradiated, can generate the strong oxidant singlet oxygen $^1O_2$, which degrades mRNA and inhibits translation. In addition, other *KRAS* targeting mechanisms based on the use of decoy oligonucleotides mimicking the critical promoter G4 structure and miRNA 216b targeting the 3′-UTR sequence are discussed.

Introduction

It is estimated that pancreatic ductal adenocarcinoma (PDAC) will be the second leading cause of cancer-related death by 2040 (Rahib et al. 2021). Despite numerous scientific advances, the 5 year survival rate for PDAC is still only 9% (Rawla et al. 2019). This poor prognosis is due to the fact that pancreatic cancer is often diagnosed at advanced stages that do not allow for surgical intervention and is resistant to conventional chemotherapy and radiotherapy. Pancreatic cancer can arise from endocrine (neuroendocrine tumors) or exocrine (PDAC and acinar carcinomas) cells. While endocrine tumors have a frequency of less than 5%, exocrine tumors, especially PDAC, account for more than 90% of pancreatic malignancies (Siegel et al. 2018). Tumorigenesis of PDAC begins with the formation of preneoplastic lesions in the ducts. Lesions in the small ducts, termed pancreatic intraepithelial neoplasia (PanIN), and lesions in the large ducts, intraductal papillary mucinous neoplasia, are associated with mutations in the *KRAS* proto-oncogene (Kanda et al. 2012). Genetically engineered mouse models demonstrate that PDAC is triggered by mutant *KRAS*, with the cooperative support of mutations in tumor suppressor genes. Surgical resection is the only effective cure whenever possible, but the 5 year survival rate is very low. Adjuvant chemotherapy with gemcitabine, nanoparticle albumin-bound paclitaxel (Von Hoff et al. 2013) or folfirinox, a toxic cocktail of 5-fluorouracil, leucovorin, irinotecan, and oxaliplatin (Conroy et al. 2018), has significantly improved the outcome. As PDAC patients develop chemoresistance, these treatments are not so effective and the life expectancy of PDAC patients is low.

The key driver of pancreatic cancer is mutant *KRAS*, which plays a crucial role in the initiation and maintenance of the disease. PDAC cells are highly dependent on *KRAS*, which switches the metabolism to produce biomass for proliferation and survival in a nutrient-deficient microenvironment (Ying et al. 2012). These findings suggest that inactivation or suppression of the oncogenic *KRAS* in PDAC cells may offer new therapeutic opportunities. This hypothesis is supported by the findings that: (i) suppression of *KRAS* mRNA by small interference RNA results in loss of tumorigenicity (Brummelkamp et al. 2002); (ii) decoy oligonucleotides down-regulating *KRAS* induce apoptosis and arrest growth of Panc-1 xenografts in SCID mice (Cogoi et al. 2013); and (iii) inactivation of $KRAS^{G12D}$ in the presence of Tp53 deficiency shows rapid regression of primary and metastatic (Collins et al. 2012) tumor growth. In the last 20 years, some strategies have been proposed to inhibit mutant *KRAS* or its downstream signaling in PDAC. They are based on the use of

inhibitors against: (i) the association of the protein KRAS with the membrane (Cox et al. 2015); (ii) the Mek-Erk and PI3K-Akt signaling pathways (Vallejo et al. 2017); (iii) the *KRAS*-dependent metabolic switching (Ostrem et al. 2013); and (iv) the activity of RAS protein (Son et al. 2013). Despite the efforts made, none of these strategies proved successful for PDAC. *KRAS* Inhibitors have shown promise in tumors with the *KRAS* G12C variant, which is most common in non-small cell lung cancer (11%) and colorectal cancer (2.9%) (Lindsay and Blackhall 2019), but not in PDAC, where G12C is a limited subtype (approximately 1%) (Dunnett-Kane et al. 2020). An alternative strategy is to target the gene *KRAS* directly. The authors focused on three functional elements of *KRAS*: a promoter sequence with guanine blocks which is able to adapt an unusual G-quadruplex (or G4) conformation that is recognized by nuclear factors as a unique target for small molecules; a 5′-untranslated region (5′-UTR) of 183 nt, characterized by a sequence motif rich in GG blocks that folds into a cluster of RNA G4 (RG4) structures that may also be potential targets for small molecules; and the 3′-UTR, which is the target for miRNAs. This chapter summarizes some therapeutic strategies aimed at down-regulating the *KRAS* oncogene in PDAC.

Sequence Determinants That Control *KRAS* Gene Expression

The promoter of the *KRAS* proto-oncogene contains three G4 motifs between −270 and −116 (3′➔5′, noncoding strand) from the transcription start site (TSS), called 32R (or G4-near), G4-mid and G4-far (Fig. 1a; Cogoi and Xodo 2016). Most studies reported in the literature have focused on 32R, as this sequence acts as a platform for transcription factor recruitment. In 2006, primer extension experiments demonstrated for the first time that DNA polymerase I paused at the 3′ end of 32R inserted into a plasmid (Cogoi and Xodo 2006).

Similarly, its murine analog also forms a G4 that blocks DNA polymerase I (Cogoi and Xodo 2006). This suggested the formation of a folded G4 by both the promoter sequences. Insight into the G4 structures was gained from DMS footprinting experiments (Cogoi and Xodo 2006; Cogoi et al. 2008). A typical DMS piperidine cleavage pattern of the human 32R motif is shown in Fig. 1b. The nucleobases were numbered from 1 to 32, starting with the adenine at the 5′ end (Fig. 1b). Surprisingly, DMS footprinting showed that the expected G4 was not formed from G-runs I, III, IV, and V. The triad G18-G19-G20 of G-run IV showed strong reactivity to DMS, suggesting that its guanines are not involved in the formation of the G4 scaffold.

Strikingly, G6 and G7 are fully protected, while G9 is partially protected. This suggests that despite the interruption of G6-G7-T8-G9 by a thymine, the “defective” triad is part of the G4 scaffold.

Overall, the cleavage pattern is in alignment with the formation of a G4 structure stabilized by three G-quartets of four G-runs (I, II, III, and V), one of which is interrupted by a thymine. Moreover, circular dichroism showed that 32R in a potassium-containing buffer exhibited strong ellipticity at 260 nm, which is typical

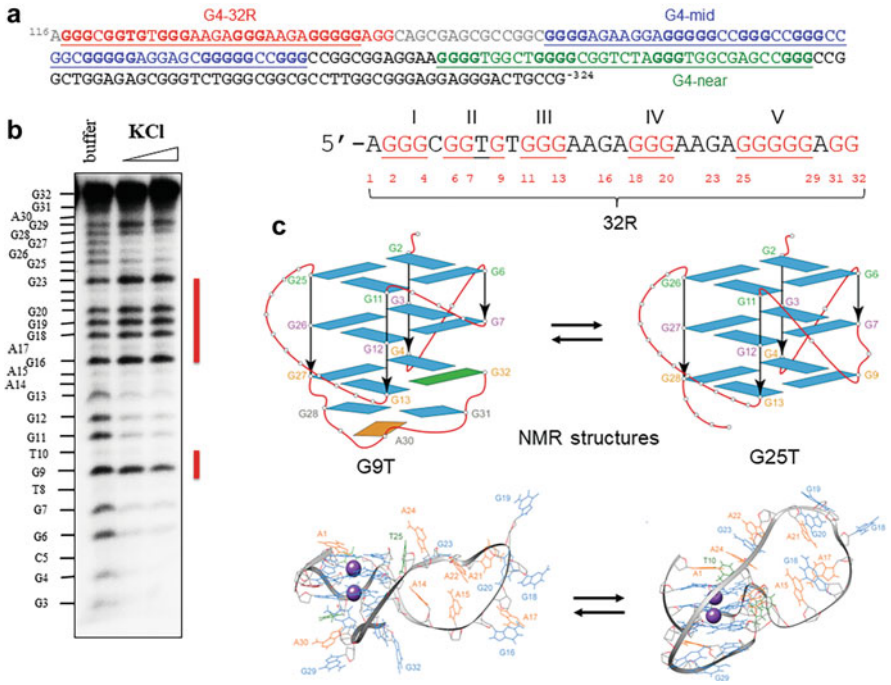

Fig. 1 (**a**) Sequence of the human *KRAS* promoter upstream TSS; (**b**) 32R sequence and a typical DMS footprinting in 0, 50, and 100 mM KCl (from left to right); and (**c**) Structure of the two G4 conformers (G9T and G25T) formed by 32R, obtained by NMR (Figure adapted from Marquevielle et al. (2020), Oxford University Press, and from Ferino et al. (2021))

of a parallel G4 structure. From this, it was concluded that 32R should form a parallel G-quadruplex with three stacked G-quartets stabilized by Hoogsteen hydrogen bonds between the guanines. Two K^+ ions are centrally coordinated at O6 of the guanines, and the resulting G4 is characterized by two 1-nt and one 11-nt loops and a strand with a thymine bulge (1/1/11 topology) (Cogoi et al. 2008). This putative structure is consistent with the DMS footprinting profile, with an exception of G9 reactivity to DMS, which should not be observed if the guanine is part of the scaffold. To investigate this unexpected behaviour, NMR experiments were performed NMR experiments (Marquevielle et al. 2020). The study showed that 32R folds into two G4 structures of different topologies (called G25T and G9T) that coexist in slow equilibrium with each other. The folding topology of the two G4 conformers of 32R is shown in Fig. 1c. Both structures are fully supported by the DMS footprinting profile, including the fact that G9 should be partially reactive to DMS, as observed. Indeed, G9T (T_M = 61.2 °C) exhibits a unique structure (topology 1/3/11) characterized by a refolded guanine in syn conformation (G32) and a triad (G29, A30 and G31) capping the 3′- end. Instead, the conformer G25T exhibits a fold similar to that proposed for 32R, based on DMS footprinting and CD data. It is a parallel G4 with a thymine bulge in one strand and a large 11/12-nt loop.

In this G4 structure, G9 is involved in a G-quartet and should be nonreactive to DMS. In contrast, in G9T structure, G9, falling into the 3-nt loop, is reactive to DMS. As the DMS footprint of sequence G-32R reflects the folding of the two G4 structures in equilibrium with each other, G9 appears partially protected, as expected.

In 2011, the authors used primer extension experiments to investigate whether 32R, which consists of 5 G runs, can fold into alternative G4 structures. It was discovered that a 21-nt stretch embedded in 32R can fold into a parallel G-quadruplex. However, this structure was only observed in the presence of DIGP, a G4-stabilizing phthalocyanine [tetrakis-(diisopropyl-guanidine) phthalocyanine] (Paramasivam et al. 2011). In the absence of DIGP, Taq polymerase paused only at the 3′ end of 32R, suggesting that the major G4 formed by 32R comprises the entire sequence and not the 21-nt segment. The structure of 21-nt G4 was also studied by NMR (Kerkour et al. 2017) and crystallography (Ou et al. 2020). The NMR structure of 21-nt G4 is shown in Fig. 2a. It is similar to that of the G25T conformer of 32R and is a parallel G4 characterized by a T-bulge in one strand, two 1-nt and one 4-nt (AAGA) loops. An important aspect of the 4-nt loop highlighted in the crystal structure is the extensive stacking between the adenine residues (Ou et al. 2020). Another sequence determinant associated with *KRAS*, which is important for transcriptional regulation, is the 5′-UTR sequence. It consists of 192 nt with a GC content of 77%, organized in repeating GG blocks separated by few nucleotides (Fig. 2b, c). Using the QGRS mapper and considering a G4 consensus motif with two G-tetrads and a loop length of up to 12 nt, three nonoverlapping RG4 motifs with a G-score of 21 were identified near the 5′ end of the 5′-UTR. If the overlapping G4 motifs are included in the analysis, the result is >300 potential RG4 sequences, indicating that the 5′-UTR sequence of *KRAS* mRNA has a high propensity to form RG4 structures. The nonoverlapping RG4 motifs are located within the first 80-nt of the 5′-UTR (s-80) and each shows a CD spectrum characterized by strong ellipticity at 265 nm and negative ellipticity at 240 nm, which is typical of parallel G-quadruplexes (Miglietta et al. 2017). Their thermal stability is in the range between 53 and 62 °C in the presence of KCl. The RG4 structures of 5′-UTR are recognized by BG4: an antibody specific for G4 structures (Miglietta et al. 2017). EMSA showed that s-80 forms a delayed band with BG4 in keeping with the formation of RG4 structures. To detect the formation of RG4s in the 5′-UTR sequence, the reactivity of the guanines of s-80 towards RNase T1 was tested by footprinting. Considering that the guanines forming Watson-Crick or Hoogsteen hydrogen bonds do not react with RNase T1, s-80 in the RG4 conformation would expose guanines G30 and G33 to cleavage by RNase T1, as they lie between the G4 structures utr-1 and utr-z (Miglietta et al. 2017). This was indeed observed in the presence of K^+, which stabilizes G4, but not in Li^+ (Miglietta et al. 2017). Furthermore, s-80 was found to interact with thioflavin T (ThT), a fluorescent sensor specific for G4. ThT showed a strong increase in fluorescence emission upon binding to s-80, which is consistent with the presence of a RG4 structures in s-80 (Miglietta et al. 2017).

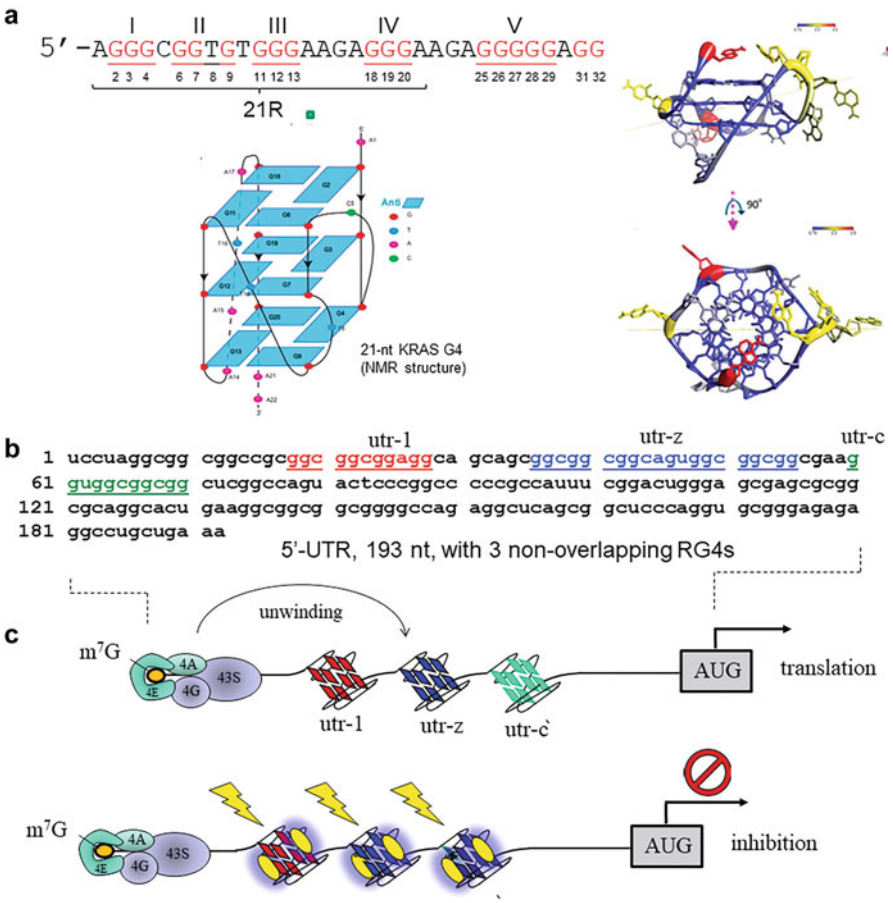

Fig. 2 (**a**) NMR structure of the 21-nt *KRAS* sequence called 21R. (This figure was originally published in Kerkour et al. (2017)); (**b** and **c**) Sequence of the 5′-UTR of KRAS gene. The G4 motifs shown in red, blue, and green form stable G4 RNA structures

The Biological Function of the *KRAS* Oncogene

There is growing evidence that pancreatic cancer develops through a series of PanIN precursor lesions. The most important genetic alteration found in PanIN is mutations in the KRAS gene, the most common of which is G12D (Fan et al. 2018). This point mutation in codon 12 reduces the ability of protein KRAS to hydrolyze GTP to GDP, keeping the protein in the active GTP-bound state (Di Magliano and Logsdon 2013) that stimulates constitutively proliferation. Despite its crucial role in cancer, the oncogenic *KRAS* alone is not sufficient to cause the conversion of PanIN to PDAC. Other genetic or epigenetic factors are required to drive the progression of initial lesions to metastatic pancreatic cancer, such as loss of the tumor suppressor genes

p16 or TP53 (Waters and Der 2018; Eser et al. 2014). Activated GTP-bound protein KRAS stimulates several signaling pathways, including mitogen-activated kinase (MAPK), phosphoinositide 3-kinase (PI3K), Ral-guanine exchange factor (RalGEF), nuclear factor kappa B (NF-Kb), and Nrf2 (Awasthi et al. 2017). In general, the RAF/MAPK/ ERK pathway activates survival and proliferation in KRAS-driven cancer; in PDAC, it promotes migration, invasion, and chemoresistance (Awasthi et al. 2017). Eser et al. (2013) demonstrated that PI3K and 3-phosphoinositide-dependent protein kinase 1 (PDK1) are the key effectors of *KRAS*-dependent cancer. Most therapies targeting the Ras effectors that are currently under clinical investigation focus on the Raf and PI3K pathways (Chen et al. 2021). Evidence that mutant *KRAS* is associated with a switch in metabolism to meet the increased nutrient requirements for a high proliferation rate has been provided. The oncogene increases glucose uptake for aerobic glycolysis (Warburg effect) and induces the diversion of glucose intermediates into the hexosamine biosynthesis and pentose phosphate pathways (Ying et al. 2012). In addition, *KRAS* increases the uptake of glutamine, which is used as fuel for the tricarboxylic acid cycle, and for the stimulation of fatty acid biosynthesis (Son et al. 2013). By controlling Nrf2 expression, *KRAS* regulates the redox state of cells by activating the synthesis of glutathione and detoxification enzymes. In addition, a recent study has shown that *KRAS* supports the maintenance of a transformed cell state by controlling the nucleotide pool (Santana-Codina et al. 2018). These data suggest that targeting oncogenic *KRAS* is an attractive therapeutic strategy.

The Role of G4 in the *KRAS* Promoter

A bioinformatic study performed on 19,268 ENSEMBL human genes (NCBI 34) covering ~193 Mb of the genome revealed the presence of 14,769 putative G4-forming sequences (PQS) in gene promoters. In gene promoters, PQS are enriched by a factor of 6.4 compared to their average occurrence in the whole genome (Huppert and Balasubramanian 2007). It was later shown that the peak of G-richness near the transcription start site (TSS) overlaps with the maximum abundance of RNA Pol II binding sites determined by chromatin immunoprecipitation sequencing (ChIP-Seq) (Eddy et al. 2011). This analysis suggests that there has been an evolutionary selection in favor of G4 DNA within gene promoters. The bioinformatic analysis showed that PQS density gradually decreased to the genome average at a distance >20,000 bp from TSS. It also showed that 42.7% of gene promoters contained at least one PQS and that the density of these motifs in the first 100 bp upstream TSS is 12-fold higher than the average PQS density of the genome (Huppert and Balasubramanian 2007). The bioinformatic studies supported the hypothesis that G4 DNA may play a regulatory role in transcription. In fact, the biological role of G4 DNA in the cell is still hotly debated. In vitro studies have shown that G4 DNA in the transcription region of a gene can interfere with the movement of the RNA polymerase complex and affects gene expression (Nayun 2019). For example, a G4 formed in the template or transcribed DNA strand can act

as a physical blockade for RNA Pol II (Belotserkovskii et al. 2010). Moreover, a hybrid DNA:RNA G4 formed by the non-template strand and the nascent RNA could also impede the processivity of the incoming RNA Pol II complex (Zheng et al. 2013). Another mechanism would be that an intramolecular G4 formed in the non-template strand promotes annealing of the nascent RNA to the template strand and forms an R-loop that impedes the incoming RNA Pol II complex (Belotserkovskii et al. 2017). Although these mechanisms of transcriptional inhibition have been characterized, the function of G4 DNA in the upstream TSS region, where PQS density is at its peak, is probably more important in the cellular context. One probable function in gene promoter is that G4 DNA provides a platform for high-affinity binding of transcription factors (Spiegel et al. 2021). One of the first examples supporting this hypothesis is the G4 formed by the 32R sequence located upstream TSS in human and mouse *KRAS* promoters (Cogoi and Xodo 2006). Combining pull-down experiments, performed with biotinylated 32R and Panc-1 extract, with mass spectrometry, it has been found that the folded structure of *KRAS* is bound by several proteins including PARP-1, Ku70, and hnRNPA1 (Cogoi and Xodo 2006). Subsequently, it was discovered that the zinc finger protein MAZ, whose consensus binding sequence is GGGAGGG, also binds to the *KRAS* G4 structure (Cogoi et al. 2013). Another example of a protein that binds to G4 DNA is SP1, which has been reported to recognize G4 structures in the c-*KIT* and *HRAS* promoters (Cogoi et al. 2014; Todd and Neidle 2008). A genome-wide analysis showed that approximately 36% of SP1 binding sites detected by ChIP-seq did not contain the 5′-GGGCGG-3′-Sp1 consensus binding sequence, but that the majority of these sites contained one or more G4 motifs (Todd and Neidle 2008). This suggests that the transactivation of SP1 is also dependent on DNA conformation. A recent study supports the hypothesis that G4 DNA may serve as docking sites for transcription factors. The authors reported that several transcription factors are recruited to sites containing endogenous G4s in human chromatin. In particular, the G4 promoters of highly expressed genes are recognized by a large number of transcription factors (Spiegel et al. 2021). Furthermore, a recent study using G4 ChIP-seq/RNA-seq analysis in liposarcoma cells showed that G4s in promoters are associated with high levels of transcription in open chromatin (Lago et al. 2021). The authors compared the transcription levels in liposarcoma cells with available data on keratinocytes and discovered that the promoter sequences of the same genes in the two cell lines had a different G4 folding state, with high transcription levels consistently associated with G4 folding. The transcription factors AP-1 and SP1, whose binding sites were most abundant in the G4-folded sequences, were coimmunoprecipitated with their G4-folded promoters.

Of particular interest is the interaction between PARP-1 and certain G4 structures, which is functional in nature, in the sense that the interaction stimulates the enzymatic activity of the protein. PARP-1 catalyzes poly(ADP-ribosyl)ation (PARylation) of proteins including itself (auto-PARylation) (Alemasova and Lavrik 2019). PARP-1 consists of six domains connected by a flexible linker (Alemasova and Lavrik 2019). When PARP-1 binds via its two zinc-finger domains to DNA bearing a lesion, it undergoes a structural change that triggers the synthesis of

ADP-ribose units using NAD^+ as a source of ADP-ribose (up to 200 ADP-ribose units at the target protein). PARP-1 can also transfer few ADP-ribose units or even only a single [mono(ADP-ribosyl)ation] (Eustermann et al. 2011; Gupte et al. 2017). In the PARylation process, dsDNA and G4-DNA behave like a positive allosteric effector by upregulating the basal catalytic activity of PARP-1. The allosteric function of G4 DNA towards PARP-1 was first documented by Soldatenkov et al. (2008), who discovered that PARP-1 undergoes auto-PARylation upon binding to the c-*KIT* quadruplex. A recent study showed that although PARP-1 binds to multiple G4 structures, only certain G4s promote PARP-1 activity (Edwards et al. 2021). This study supports the notion that the sequence and size of the G4 loops regulate PARP-1 activity. For example, c-KIT forms a G4 characterized by two 1-nt loops, a 5-nt loop, and three cytosines at the 5′-end, which may mediate the formation of an alternative stem-loop structure. This G4 binding to PARP-1 activates auto-PARylation of the protein, albeit to a fourfold lesser extent than with an 18-bp dsDNA. In contrast, PARP-1 is only weakly stimulated by T15, hTEL, or c-MYC. Shortening the cytosine tail at the 5′ end or the pentanucleotide loop, or both, reduced PARP-1 activation ~twofold, suggesting that both stem-loop and G4-DNA loop features are required for PARP-1 activation by c-*KIT*. Recently, the role of PARP-1 in the activation of the *KRAS* gene in response to oxidative stress was investigated, and the results provide a detailed example of how G4 DNA serves as a docking site for the assembly of a multiprotein complex (Cinque et al. 2020). The G4s formed by the 32R motif of *KRAS* induced auto-PARylation of PARP-1 after binding to the protein, increasing the molecular weight from 113 to approximately 250 kDa, indicating extensive auto-PARylation synthesis. This was observed in vitro by incubating *KRAS* G4 with increasing amounts of PARP-1 in the presence of NAD^+. After incubation, the mixture was run in a gel, blotted, and analyzed with an anti-poly/mono ADP-ribose antibody. The G4s from the promoter sequences 32R and G4-mid of *KRAS* as well as the oxidized G4s from 32R activated the auto-parylation of PARP-1 (Cinque et al. 2020; Cogoi et al. 2018). As expected, auto-PARylation was not observed when veliparib, an inhibitor of PARP-1, was added to the reaction mixture. To observe PARylation in a cellular context, Panc-1 cells were treated with H_2O_2 to induce guanine oxidation and recruitment of PARP-1, MAZ, and hnRNP A1 to the *KRAS* promoter (Cogoi et al. 2018). The nuclear extract obtained from H_2O_2 treated cells were used to perform pull-down assays with biotinylated 32R G4 (b-32R) as well as its oxidized form b-92 (containing one 8-oxoguanine) or b-96 (containing two 8-oxoguanines). The pull-down samples analyzed by Western blot with a poly/mono ADP-ribose antibody showed that all three G4 baits pulled down PARylated proteins. Compared to untreated cells, PARylation was found to increase with cell exposure to H_2O_2, resulting in PARylated proteins in the input (extract) ranging between ~130 and 250 kDa, while PARylated protein captured from the G4 baits yielded only a sharp band corresponding to a protein the size of PARP-1. This suggests that PARP-1 captured by G4 is characterized by limited auto-PARylation, if not mono (ADP-ribosyl)ation. To confirm that PARP-1 is PARylated in Panc-1 cells treated with H_2O_2, nuclear extracts from untreated or H_2O_2-treated Panc-1 cells were used for pull-down assays

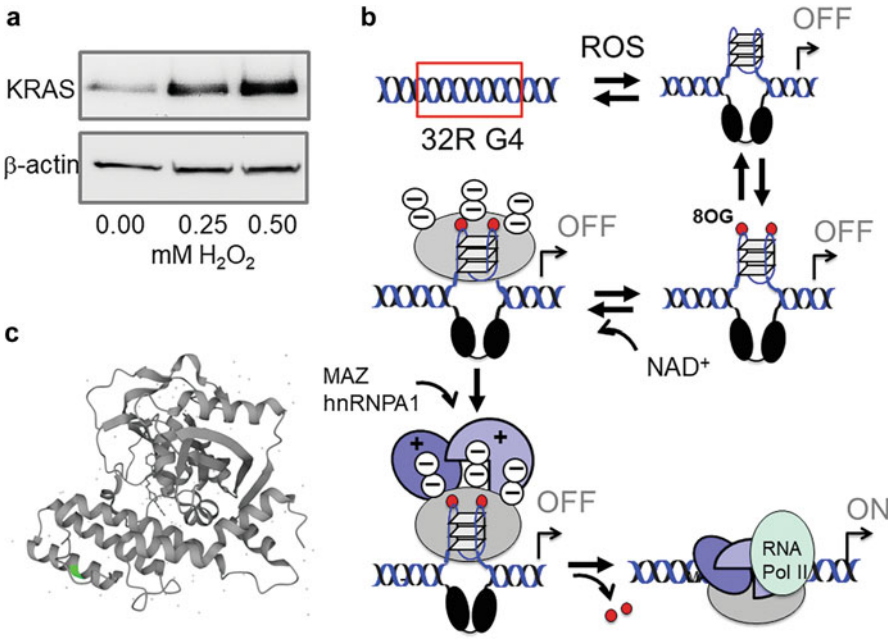

Fig. 3 (**a**) The expression of *KRAS* in Panc-1 cells is stimulated by ROS (6 h of treatment with H_2O_2) (Adapted from Cinque et al. (2020)). (**b**) Mechanism of transcription activation promoted by oxidative stress. Under enhanced oxidative stress, certain guanines of G4 32R can undergo oxidation to 8-oxoguanine. The oxidized guanines recruit PARP-1 to the promoter where upon interaction with the G4 undergoes auto-PARylation. Auto-PARylated PARP-1 is negative and attracts by electrostatic interaction cationic transcription factors as MAZ and hnRNPA1. (**c**) Structure of PARP-1 from Swiss Prot

with an anti-poly/mono-ADP ribose antibody. The recovered PARylated proteins were assayed in SDS gel and blotted in nitrocellulose. The blotted membrane was tested with antibodies specific for PARP-1, MAZ, and hnRNPA1. Only PARP-1 was found PARylated, whereas MAZ and hnRNPA1 were not. Taken together, the data show that PARP-1 undergoes PARylation after binding to the *KRAS* G4s. As suggested by the genome-wide analysis, the G4s of highly transcribed genes may be the platform for transcription factor recruitment (Spiegel et al. 2021). The *KRAS* G4 is a well-documented example of a protein-docking G4 structure. The mechanism illustrated in Fig. 3 is supported by the observation that the expression of *KRAS* is significantly increased when pancreatic cancer cells are treated with H_2O_2, i.e., when the oxidative stress in the cell is increased (Fig. 3a; Cogoi et al. 2018). The rise of cellular ROS results in an increase of 8OG in the promoter region of *KRAS* containing the G4 motifs and of the recruitment of PARP-1, MAZ, and hnRNP A1. The co-localization of G4 and 8OG in the same promoter region (at 0.2 kb resolution) was confirmed by pull-down experiments of genomic DNA with biotinylated G4 ligand (b-6438) followed by ChIP with anti 8OG Ab (Cinque et al. 2020). Assuming that 8OG is present in the G4 motif due to its high guanine content,

H_2O_2 increases the transcription factor occupancy of the G4 promoter motif. This is indeed consistent with the pull-down and Western blot assays showing that the 32R motif forms a multiprotein complex with PARP-1, MAZ, and hnRNP A1, which is most likely the transcription pre-initialization complex. It is possible that 8OG acts as an epigenetic mark for the recruitment of transcription factors. The 32R motif of the *KRAS* promoter is in equilibrium with its folded form. Folding probably occurs spontaneously, as suggested by the polymerase stop assay performed with 32R inserted into the plasmid (Cogoi and Xodo 2006). 32R should fold into a G4 that is, according to NMR data, in equilibrium between two different forms, both of which are recognized by transcription factors essential for *KRAS*. Under increased oxidative stress, as occurs in cancer cells, including PDAC cells, certain guanines are oxidized because they have the lowest oxidation potential among DNA nucleobases (Saito et al. 1995). Since the guanines most susceptible to oxidation are those in G cluster, it is likely that 32R is oxidized. 8-Oxoguanine in oxidized 32R G4 behaves like an epigenetic marker that attracts PARP-1 to the *KRAS* promoter. When the protein binds to the G4, the folded DNA acts as a positive allosteric effector that increases the catalytic activity of PARP-1, which undergoes auto-PARylation. This was confirmed in vitro, while cell-based experiments indicated that only a few ADP-ribose units are present on PARylated PARP-1. Since each ADP-ribose unit contains a negative charge, PARylated PARP-1 becomes anionic and becomes a platform for the recruitment of cationic transcription factors. MAZ and hnRNP A1, which have an isoelectric point (pI) of 8.1 and 9.2, respectively, are indeed cationic under physiological conditions. Thus, the cationic transcription factors spatially accumulate in the promoter region of 32R, where the transcription-initialization complex should form. According to this model, *KRAS* transcription is expected to be inhibited when MAZ or hnRNP A1 are repressed. This has been demonstrated in several studies (Cogoi et al. 2013; Paramasivam et al. 2009). Given the important role attributed to PARP-1, suppression or inhibition of its catalytic activity represents another interesting strategy to inhibit *KRAS* in PDAC cells: some recent data obtained with olaparib and veliparib support this hypothesis.

Antigene Strategies Based on G4-Binding Small Molecules

A growing body of evidence suggests that G4 structures in the promoter of cancer-related genes serve as hubs for TFs (Cogoi et al. 2008; Spiegel et al. 2021; Ferino et al. 2021). This encouraged researchers to hypothesize that small molecules with high affinity for G4 DNA could compete away the interaction between TFs and the target G4 structures, thus representing a class of compounds with anticancer activity. One of the first G4-binding molecules showing the ability to inhibit transcription is TMPyP4 (Cogoi and Xodo 2006; Siddiqui-Jain et al. 2002). This cationic porphyrin was found to strongly reduce the expression of CAT directed by the murine *KRAS* promoter, to 20% of control (Cogoi and Xodo 2006), while a luciferase assay showed that binding of TMPyP4 to the Pu27-G4 motif of *c-MYC* reduced transcription by 50% (Siddiqui-Jain et al. 2002). More recently, Paulo and co-workers

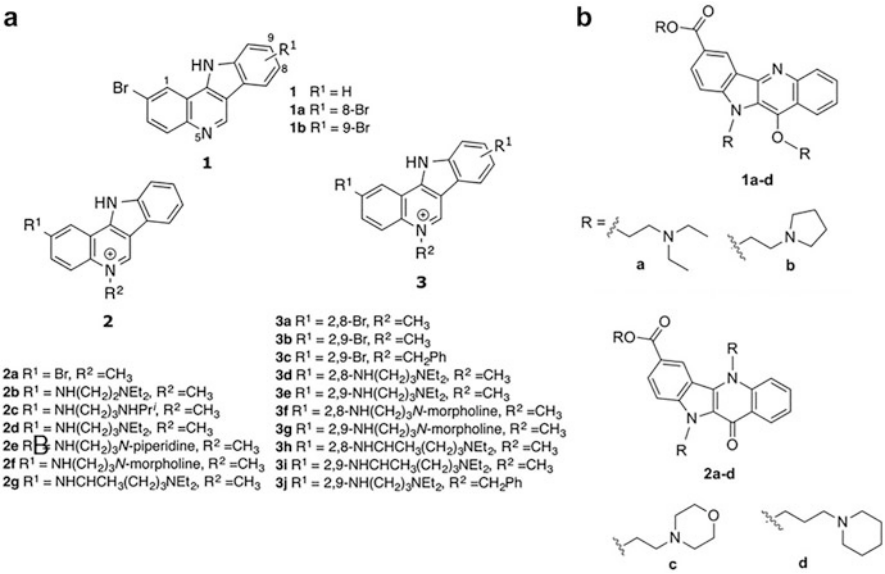

Fig. 4 (**a**) Structures of 5-methyl-indolo[3,2-c]quinoline derivatives (IQc) with a range of alkyldiamine side chains from Lavrado et al. (2015b). (**b**) Structures of 7-carboxylate indolo [3,2-*b*]quinoline tri-alkylamine derivatives from Brito et al. (2015)

developed a library of 5-methyl-indolo[3,2-c]quinoline IQc derivatives with a series of alkyldiamine side chains targeting DNA and RNA G4s located in the promoter and 5′-UTR mRNA of the *KRAS* gene (Lavrado et al. 2015a, b; Fig. 4a). The monosubstituted alkyldiamine IQc **2b-g** compounds stabilize the 21R G4 structure of *KRAS* and increase its T_M of 10–15 °C. The disubstituted alkyldiamine derivatives **3f–j** caused a similar G4 stabilization. While the disubstituted alkyldiamine derivatives **3d**, **e** caused strong stabilization with ΔT_M values between 12 and 22 °C (Lavrado et al. 2015b). Interestingly, IQc derivatives without alkyldiamine side chains (**1**, **2a**, **3c**) showed a lower ability to stabilize *KRAS* 21R G4. Moreover, the derivatives with a bulky benzyl N5 substituent (**3c** and **3j**) showed lower G4 stabilization compared to their monosubstituted counterparts **2a** and **3e**. All IQcs showed low affinity for ds-DNA ($1.5 < \Delta T_M < 9.1$ °C for **2b-g** and $1.6 < \Delta T_M < 6.5$ °C for **3d–j**), suggesting good selectivity of the IQcs for the 21R G4 as compared to ds-DNA. Compounds **3e** and **2d** were also tested for their ability to stabilize the G4s formed by the entire 32R motif of *KRAS*. The former increased the T_M of the G4s by 15 °C, the latter by 10.7 °C, suggesting that the IQcs can interact with both folded G4 structures of 32R.

The designed IQc molecules **2a**, **2d**, **3d**, and **3e** were found to inhibit the metabolic activity of cells harboring mutant *KRAS*. The compounds showed IC_{50} values between 0.4 and 1.45 μM in lung cancer cells A 594; 1.98–2.20 μM in pancreatic cancer cells MiaPaCa2; 0.22–4.80 μM in pancreatic cancer cells Panc-1; 0.14–3.46 μM in colon cancer cells HCT116; and 0.2–4.74 μM in SW620 cells.

The effect of the compounds on transcription was first investigated using a luciferase reporter assay. Two different sized *KRAS* promoter constructs containing the G4 motif were cloned into the *Firefly* luciferase pGL3 plasmid (pGL-Ras0.5 and pGL-Ras2.0). These plasmids were co-transfected in HEK293T cells with *Renilla* luciferase pRL-TK, and compounds **2d**, **3d**, and **3e** were found to reduce *Firefly* luciferase activity by ~25–50% compared to *Renilla* luciferase. The same decrease in promoter activity was observed with plasmids of different sizes (500 and 2000 bp), suggesting that the target region of the designed compounds is at most 500 bp upstream from the beginning of the coding region, which overlaps with the region where the G4 sequence is located.The effects of the IQc compounds on *KRAS* transcription in colon cancer cells (HCT116 and SW620) were examined by real-time RT-PCR. The results showed that the IQc compounds significantly reduced *KRAS* transcription in colon cancer cells to 20% (**2d**), 80% (**3d**), and 60% (**3e**) of control (DMSO treated cells). The results were confirmed by immunoblotting, which showed that the compounds reduced the KRAS protein to 40–70% of the control in both cancer cell lines, and the relative efficacy of the compounds followed the trend **3e** < **3d** < **2d** (Brito et al. 2015).

Subsequently, 7-carboxylate indolo[3,2-b]quinoline tri-alkylamine derivatives were found to be effective stabilizers of *KRAS* 21R G4 and potent anti-*KRAS* agents capable of inhibiting gene expression and inducing cell death by apoptosis in colon cancer cell lines (Lavrado et al. 2013; Fig. 4b). Calabrese et al. (2018) used a small molecule microarray (SMM) approach to identify preferential interaction between chlorhexidine and *KRAS* 21R G4 (Fig. 5a). Chlorhexidine showed a specific, low micromolar binding interaction with the *KRAS* G4. NMR and docking experiments suggest a binding mode determined by both aromatic stacking and groove binding interactions. Cancer cells with oncogenic mutations in the *KRAS* gene show increased sensitivity to chlorhexidine. Treatment of breast cancer cells with chlorhexidine leads to a downregulation of the KRAS protein level, whereas *KRAS*, transiently expressed by a promoter lacking G4, is not affected. Taken together, these studies provided strong evidence that G4 ligands can be promising anticancer drugs.

Recently, a trisubstituted naphthalenediimide quadruplex-binding compound [2,7-bis(3-morpholinopropyl)-4-((2-(pyrrolidin-1-yl)ethyl)amino)benzo[lmn][3,8] phenanthroline-1,3,6,8 (2H,7H)-tetraone] (CM03) was developed by computer modelling as an inhibitor of cell growth in PDAC cell lines (Fig. 5b; Marchetti et al. 2018). In vitro studies showed that CM03 stabilizes both *KRAS* 21R and 32R G4s by 11 and 9.6 °C, respectively. In contrast, it does not stabilize duplex DNA. The antiproliferative effect of CM03 was tested in lung adenocarcinomas (A549), breast adenocarcinomas (MCF7), and PDAC cell lines (MIA PaCa-2 and PANC-1), as well as in the fetal lung fibroblast-like non-oncogenic control cell line (WI-38). The compound showed strong growth inhibitory activity, particularly in the lung and pancreatic cancer cell lines, with IC_{50} values of 24, 159, 7, 18, and 1190 nM, respectively. In a mouse MIA PaCa-2 xenograft model for PDAC, CM03 showed a dose-dependent antitumor effect. The effect of CM03 was also tested in a genetically modified mouse model for PDAC. The KPC (Pdx1-Cre; LSLKrasG12D/+;

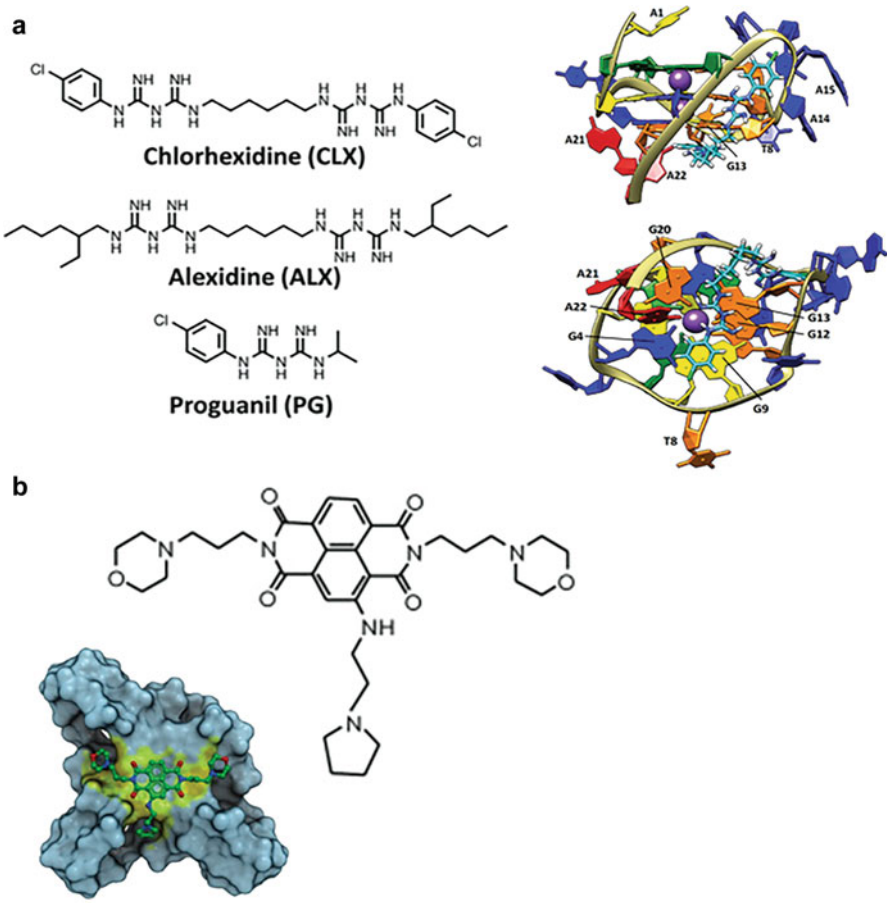

Fig. 5 (**a**) Structures of chlorhexidine, alexidine, and proguanil (Adapted from Calabrese et al. (2018)). (**b**) Trisubstituted naphthalene diimide quadruplex-binding compound 2,7-bis(3-morpholinopropyl)-4-((2-(pyrrolidin-1-yl)ethyl)amino)benzo[lmn][3,8]phenanthroline-1,3,6,8(2 H,7 H)-tetraone (CM03). Molecular model of CM03 bound to the native parallel human telomeric G4 structure from Marchetti et al. (2018)

LSL-Trp53R172H/+) mouse model develops tumors with genetic and pathological features of human PDAC. KPC mice treated twice a week with 15 mg/kg CM03 survived longer than the untreated animals, with two mice surviving more than twice as long. The effects of this quadruplex-binding small molecule on global gene expression were analyzed by RNA-Seq. The experiment showed that a large number of genes rich in G4 elements were downregulated, which are involved in essential signaling pathways for PDAC survival, metastasis, and drug resistance.

G4-Binding Compounds Binding to the 5′-UTR Region of the *KRAS* Gene

Recently, The author's laboratory, focused on the G4 motifs formed in the 5′-UTR of *KRAS* mRNA and used two types of G4-binding compounds to inhibit *KRAS* translation in PDAC cells.

The *KRAS* 5′-UTR forms three nonoverlapping RNA G4 structures (RG4s) stabilized by two G-tetrads, namely G4 utr-1, G4 utr-z, and G4 utr-c, which can serve as a platform for G4-binding compounds (Fig. 2b). UV-melting experiments showed that the RG4s melt cooperatively with T_M of 53 ± 0.5 (utr-1), 52 ± 0.5 (utr-c), and 64 ± 0.5 °C (utr-z), and ΔG values between −6.1 and −7.3 kcal/mol in 100 mM KCl (Miglietta et al. 2017). For comparison, the 254 nt 5′-UTR of *NRAS* mRNA is characterized by a G4 motif between −240 and −222 from ATG forming an RG4 with three G-tetrads and T_M of 74 °C in 20 mM KCl. The first compounds used in the author's laboratory to target the *KRAS* RG4s are anthrafurandiones (**1a**, **2a**) and anthrathiophenediones (**1b**, **2b**) (Miglietta et al. 2017; Fig. 6). At equimolar ratios, **2a** stabilizes RG4s of 10–15 °C, while **2b** of 4–10 °C. The compounds showed excellent ability to penetrate the cell membrane: **2a** and **2b** with aminoethyl side chains are taken up 20- and 4-fold more than the corresponding guanidino analogues **1a** and **1b**, respectively. This is because the positive charge of the guanidine group reduces the transport of the compounds through the lipid bilayer. Although **2a** differs from **2b** only by one atom in the five-member ring (oxygen versus sulfur), the ability of the former to penetrate the cell membrane is fivefold greater than that of the latter. This can possibly be explained by the higher polarizability of sulfur compared to oxygen. Luciferase experiments with a plasmid carrying *Renilla* driven by the *KRAS* promoter with the 5′-UTR element showed that **2a** and to a lesser extent **2b** reduce luciferase expression in a dose-response relationship. The ability of the compounds to inhibit also genomic *KRAS* was tested in Panc-1 cells. Consistent with the luciferase assay, anthrafuranedione **2a**, but not **2b**, was

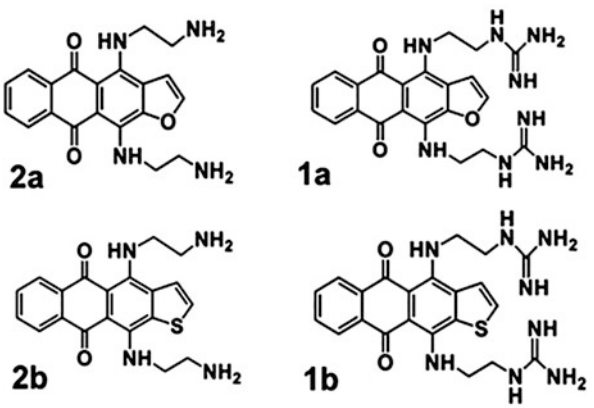

Fig. 6 Structures of 4,11-bis (2-aminoethylamino)anthra [2,3-b]furan-5,10-dione (**2a**), 4,11-bis(2-aminoethylamino) anthra[2,3-b]thiophene-5,10-dione (**2b**), and corresponding guanidino-modified derivatives **1a** and **1b**

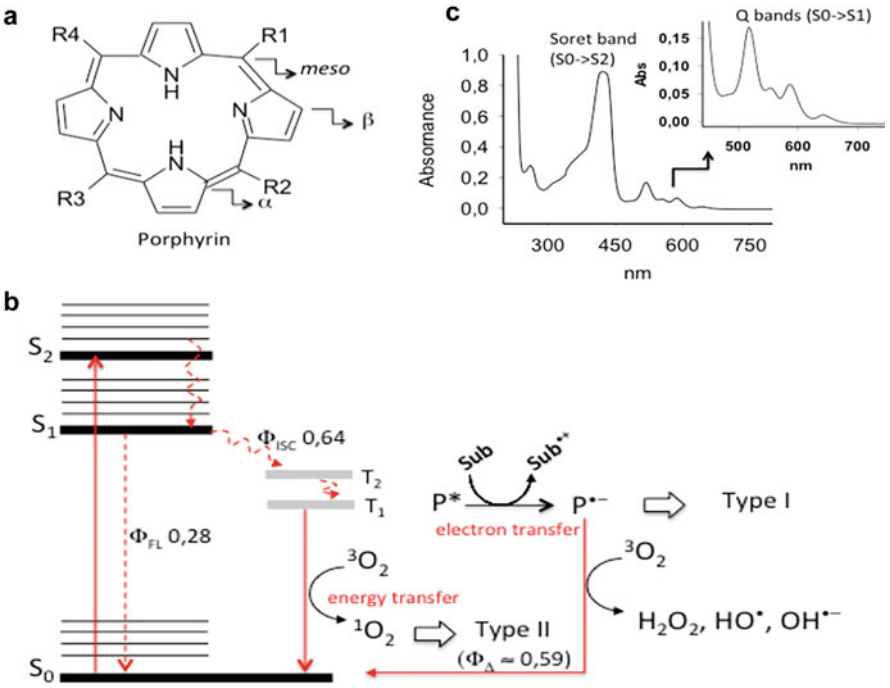

Fig. 7 (**a**) The porphyrin macrocycle. (**b**) Jablonski diagram of cationic porphyrins showing type-I and type-II processes from Xodo et al. (2016). (**c**) Absorption UV-visible spectrum of a porphyrin with typical Soret and Q-bands

found to downregulate *KRAS* by 50%, a result that confirms the efficacy of targeting the 5′-UTR RG4s to suppress the *KRAS* gene in PDAC cells. However, the designed compounds could have a complex behavior: besides binding to cytoplasmic RG4s, they could also target genomic G4 structures in gene promoters and cause undesirable side effects.

Therefore, the author's pursued a new strategy using cationic porphyrins, as they have the following interesting properties of (i) binding to RG4s with high affinity; (ii) producing reactive oxygen species and singlet oxygen $^1O_2$ when illuminated with light; and (iii) accumulating mainly in the cytoplasm.

Porphyrins are naturally occurring molecules that perform important functions in the human body as they are involved in the transport of oxygen and in the cellular respiration. They consist of four pyrrole rings that are connected to each other via a methine bridge.

The porphyrins that were used to target *KRAS* are synthetic and have been designed with the tetrapyrrole macrocycle substituted at the meso- or β-position (Fig. 7a–c). The π-electron system of the porphyrin absorbs strongly at ~400 nm (Soret band) and weakly at >500 nm (Q bands). When light is absorbed, an electron is transferred from the ground state (S_0) to an excited, short-lived state (S_1 or S_2).

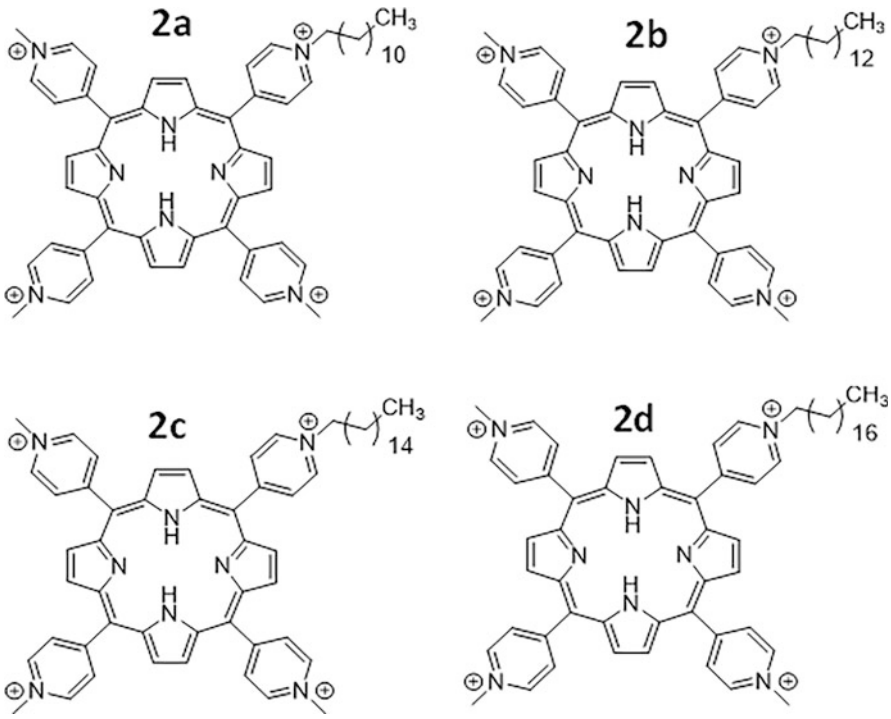

Fig. 8 (D) cationic alkyl-modified porphyrins tri-*meso*-(*N*-methyl-4-pyridyl)-*meso*-(*N*-(dodecadecyl, tetradecyl, hexadecyl, or octadecyl)-4-pyridyl) porphine (**2a**–**d**)

The Soret band at ~420 nm is due to the $S_0 \rightarrow S_2$ transition, while the Q bands between 550 and 700 nm are due to the $S_0 \rightarrow S_1$ transition (Xodo et al. 2016). While some of the excited-state molecules return to the ground state by fluorescence emission, the majority of the molecules undergo spin inversion (intersystem crossing, ISC) and populate triplet T states from which the excited porphyrins can interact with surrounding molecules (proteins, phospholipids, and nucleic acids) (type I process) or with molecular oxygen to generate singlet oxygen $^1O_2$ (type II). Contrary to common belief, $^1O_2$ has a relatively long lifetime (Skovsen et al. 2005), allowing it to diffuse over considerable distances within the cell. The reactive oxygen species generated by the porphyrins can oxidize DNA/RNA, especially the guanines, as they have the lowest redox potential among the nucleobases (Steenken and Jovanovic 1997). The quantum yield of singlet oxygen generation (Φ_Δ) of the designed cationic porphyrins is relatively high, ranging from 0.50 to 0.77, suggesting that the main photochemical reaction that takes place when they are in the excited triplex state is a type II process (Xodo et al. 2016).

To increase the ability to penetrate cell membranes, four analogues of porphyrin TMPyP4 bearing an alkyl side chain with 12, 14, 16, or 18 carbons, namely **2a**, **2b**, **2c**, and **2d** were developed (Fig. 8; Ferino et al. 2020). Although they carry four positive charges, the designed porphyrins are highly competent in penetrating the

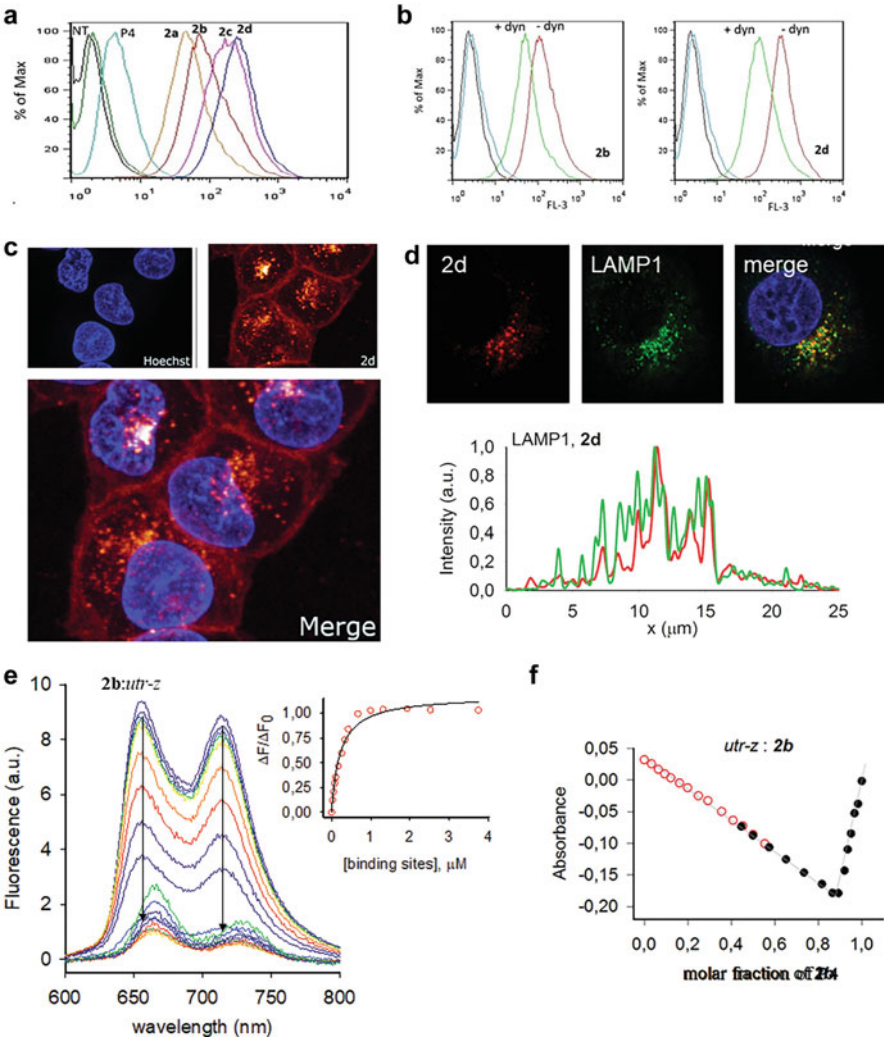

Fig. 9. (**a**, **b**) FACS analyses of Panc-1 cells treated with 5 μM **2a**–**d**, TMPyP2 (P2), or TMPyP4 (P4) for 6 h; (**b**) Effect of dynasore on the uptake of P4, **2b**, and **2d**, from Ferino et al. (2020); (**c**, **d**) Confocal microscopy images of Panc-1 cells treated with 5 μM **2d** for 6 h. The nuclei of the cells have been stained with Hoechst. Images show that the alkyl porphyrins co-localize with the lysosomes, from Di Giorgio et al. (2022); (**e**, **f**) Typical fluorescence titrations of 1.0 μM **2b** with *utr-z* RG4 in 50 mM Tris-HCl, pH 7.4, and 100 mM KCl. Right panel shows the fraction of bound porphyrin versus RG4 binding site concentration. The binding curve has been best fitted with a standard binding equation (Sigma Plot 11). The Job plot in 50 mM Tris-HCl, pH 7.4, 100 mM KCl, relative to the binding of **2b** to *utr-z* RG4 is shown. The ordinate reports the absorbance difference at 420 nm. Plots gave stoichiometries of 6 **2b** per RG4, from Ferino et al. (2020)

cell membrane as determined by cell cytometry and confocal microscopy. Porphyrins **2a**, **2b**, **2c**, and **2d** showed 8-, 14-, 40-, and 60-fold higher uptake than TMPyP4,

respectively (Fig. 9a, b). The mechanism of uptake was investigated using dynasore, a noncompetitive inhibitor of dynamin GTPase activity that blocks dynamin-dependent endocytosis in the cell. Dynasore was found to decrease the uptake of **2b** and **2d**, but not of TMPyP4, suggesting that the transport of alkyl porphyrins **2b** and **2d** occurs also via endocytosis. The confocal micrographs shown in Fig. 9c demonstrate that the endocytic vesicles in living cells occur in the cytoplasm with a punctate distribution. The vesicles co-localize with the lysosomes as lysotracker fluorescence (green) is strongly quenched by the porphyrin. Moreover, the fluorescence of the cells stained with LAMP-1 (green), an antibody specific for lysosomal-associated membrane protein 1, co-localizes with the porphyrin fluorescence (red), forming yellow foci indicating co-localization between **2d** and lysosomes. In addition to transport by endocytosis, cationic porphyrins fuse with the cell membrane, from which they are then released into the cytoplasm: a mechanism of internalization based on passive diffusion (see Fig. 9d).

The interaction between the *KRAS* RG4s and the cationic alkyl porphyrins was analyzed by UV-vis and fluorescence titration (Ferino et al. 2020). A typical fluorescence titration obtained by adding increasing amounts of *KRAS* utr-z RG4 to a solution of porphyrin **2b** is shown in Fig. 9e. After excitation at 420 nm (Soret band), the porphyrin emits between 660 and 730 nm. When the porphyrin binds to RG4, the fluorescence is quenched because the stacking interactions between the porphyrin and RG4 favor electron transfer from the excited singlet state of the porphyrin to guanines. Plotting fluorescence at 680 nm as a function of increasing amounts of RG4 yielded binding curves from which K_D values <1 μM were determined (Ferino et al. 2020). The data showed that the porphyrins have a high affinity for RG4, which increases with the length of the alkyl side chain. The interaction between the alkyl porphyrins and RG4 was studied by surface plasmon resonance (SPR). Although the sensorgrams were not so easy to interpret (due to the complex mechanism by which the alkyl porphyrins bind to RG4: stacking and aggregation), steady-state binding curves saturated at porphyrin concentrations <1 μM were obtained. They gave K_D values between 82 and 202 nM for utr-z, which are in agreement with the fluorescence titration data (Ferino et al. 2020). Binding stoichiometry determined by the continuous variation analysis method (Job plot) (Ferino et al. 2020) showed that the interaction between the utr-z RG4 and porphyrin TMPyP4 is characterized by a stoichiometric porphyrin/RG4 ratio of 4. In contrast, porphyrins 2b and 2d gave ratios of 6 and 9, respectively, indicating that there is a correlation between stoichiometry and alkyl chain length (Fig. 9f). To explain a stoichiometry of 4 TMPyP4 per G4, Sabharwal et al. (2016) suggested, based on light scattering experiments, that TMPyP4 first stacks at the G-tetrad ends of the structure. Then, excess porphyrins can stack over the two molecules already attached to the G4. With a one-carbon alkyl chain (a methyl as TMPyP4), only one porphyrin stacks over the RG4 ends because the electrostatic repulsion between the stacked porphyrins prevents further aggregation. When the porphyrin carries an extended alkyl chain (such as **2b** and **2d**), the forces that promote stacking are π-π-end stacking and hydrophobic interactions between the alkyl side chains. Long alkyl chains promote hydrophobic interactions that balance the repulsion between

stacked cationic porphyrins. TMPyP4 and its alkyl derivatives also bind to duplex DNA with comparable affinity. Job plots showed that the binding of TMPyP4 to a 20-mer RNA stem-loop hairpin has a stoichiometry of 2:1, which is different from the stoichiometry of 4:1 for a 20-mer RG4 such as utr-z RG4 (Ferino et al. 2020). This suggests that the RG4s in *KRAS* 5′-UTR form a kind of platform capable of efficiently attracting porphyrins, in greater quantity than mRNAs that have only a stem-loop secondary structure. Therefore, RG4-containing transcripts are more porphyrin-sensitive than non-RG4-containing transcripts. The higher amounts of porphyrins associated with RG4 transcripts produce more ROS and $^1O_2$ upon irradiation than stem-loop transcripts, and thus more photodegradation. A recent study showed that the fraction of porphyrins remaining trapped in the cell membrane generates lipids ROS upon illumination that activate a non-apoptotic type of cell death called ferroptosis (Di Giorgio et al. 2022). In addition, the photoactivated porphyrins bound to the RG4 structures should degrade the 5′-UTR region of mRNA (Ferino et al. 2020). This inhibits translation of *KRAS* mRNA, leading to cell death by apoptosis, as pancreatic cancer cells are addicted to the oncogenic *KRAS* and need its encoded protein to survive and proliferate. In short, the data collected so far show that the cationic alkylporphyrins act at three different levels to stop the proliferation of pancreatic cancer cells: apoptosis, ferroptosis, and *KRAS* suppression. Another important aspect of this therapeutic strategy used in vivo is that it is restricted to the area illuminated by light. Only in the presence of light are the porphyrins photoactivated and able to trigger the photoprocess that leads to cell death. The porphyrins in the tissues surrounding the illuminated area remain "mute" without producing cytotoxic effects.

The ability of the designed porphyrins to recognize and bind to *KRAS* RG4s within the transcriptome was demonstrated by a method based on a streptavidin-biotin pull-down assay with a biotinylated alkyl porphyrin and qRT-PCR. A detailed description of this experiment can be found in Ferino et al. (2020). In vitro experiments showed that alkyl porphyrins degrade the *KRAS* RG4 structures to which they are bound when activated by light. The degradation is mediated by ROS/$^1O_2$ as it is inhibited by N-acetylcysteine (NAC), a reducing agent that decreases the amount of ROS/$^1O_2$ (Sun 2010; Fig. 10a). Interestingly, the porphyrins showed a significantly lower ability to degrade RNA in the duplex or hairpin conformation. This might be due to the fact that a porphyrin stacked over a G-tetrad is in contact with four bases, whereas when intercalated into the double-stranded RNA is only in contact with two nucleobases. At the cellular level, the alkyl porphyrins photoactivated by light showed a very strong ability to suppress the *KRAS* gene, even at a concentration of 20 nM (Ferino et al. 2020). Indeed, qRT-PCR showed that the *KRAS* mRNA in both the Panc-1 and BxPC-3 cell lines was suppressed by porphyrin **2d** with a C18 alkyl chain in a dose-response manner. The alkyl porphyrin causes a strong suppression of *KRAS* transcript, to 30% of control (untreated cells) in Panc-1 cells and 40% of control in BxPC3 cells, at a concentration of only 20 nM, 24 h after photo-treatment (Fig. 10b). Western blot analysis showed that **2d** reduced the level of the KRAS protein to 3% of control. Porphyrin **2b** with a C14 chain reduced protein KRAS to 15% of control, while TMPyP4 with the alkyl chain replaced by a methyl

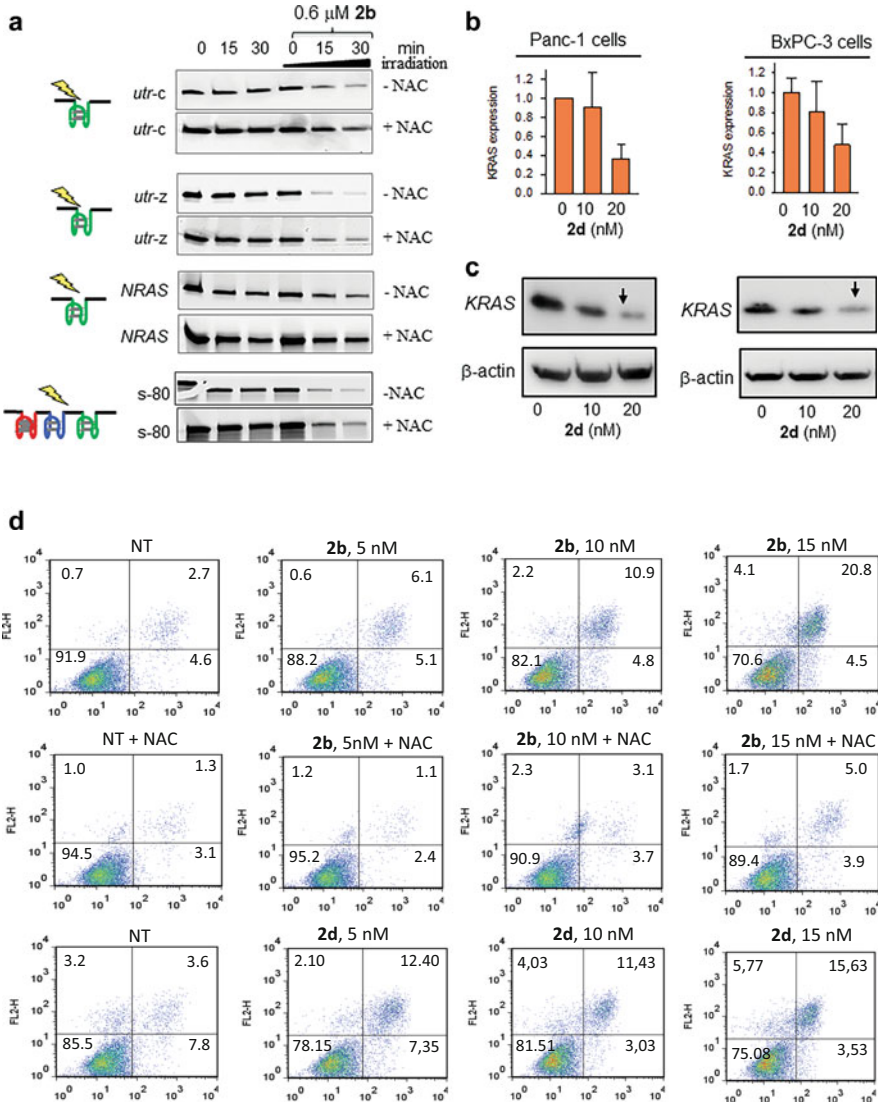

Fig. 10 (**a**) ROS produced by photoactivated alkyl porphyrin **2b** break down the *ras* RG4s. PAGE shows the residual RG4 as a function of increasing irradiation times; (**b**, **c**) Levels of KRAS mRNA and protein in Panc-1 cells photodynamically treated with 0, 10, and20 nM alkyl porphyrin 2d; (**d**) Annexin–propidium iodide experiment with Panc-1 photoirradiated with increasing amounts of **2b** (5, 10, and 15 nM) in the presence and absence of NAC (5 mM) and **2d** (5, 10, and 15 nM). Panels **a**, **b** are from Ferino et al. (2020) and panels **b**, **c** are from Di Giorgio et al. (2022)

chain reduced protein KRAS to <30% of control (Fig. 10c). In contrast, the porphyrin TMPyP2, which is unable to bind to RG4, showed no effect on the KRAS protein level (Rapozzi et al. 2014). The porphyrins TMPyP2 (control) and **2b** were also tested on SCID mice xenografted with a subcutaneous Panc-1 tumor. The mice were injected intratumorally with TMPyP2 (30 mg/Kg) or **2b** (3 mg/Kg) and the tumor was irradiated with a diode laser at 660 ± 5 nm (fluence 193 J/cm^2). Without irradiation, no effect on tumor growth was observed with either porphyrin. In contrast, irradiated porphyrin **2b** caused a strong delay in tumor growth, while irradiated TMPyP4 did not, as expected (Rapozzi et al. 2014).

RG4-Binding Alkyl Porphyrins Promote Cell Death by Apoptosis and Ferroptosis

Several studies have reported that suppression of oncogenic *KRAS* in pancreatic cancer cells leads to activation of apoptosis (Cogoi et al. 2013; Ferino et al. 2020; Sabharwal et al. 2016; Di Giorgio et al. 2022; Rapozzi et al. 2014), as PDAC cells cannot survive without the metabolic switch triggered by the oncogene. Apoptosis can be detected with annexin V and propidium iodide (PI). The assay is based on the observation that in early apoptosis, negatively charged phosphatidylserine (PS) is exposed at the outer surface of the plasma membrane so that PS is considered a marker of apoptosis. It binds specifically to annexin V, a cellular protein that, when conjugated to FITC, labels apoptotic cells with a fluorescent probe. Apoptotic cells marked with FITC-annexin can then be detected by flow cytometry. To detect necrotic or late apoptotic cells, characterized by loss of integrity of the plasma and nuclear membranes, PI is usually used. It is a fluorescent compound that binds to DNA by intercalating between bases with little or no sequence preference. After binding to DNA, the quantum yield increases from 20- to 30-fold. Since PI is not permeable to membranes, it is used to distinguish between necrotic, apoptotic, and healthy cells according to membrane integrity (Rapozzi et al. 2014). Figure 10d shows the results of the annexin V-PI assay of Panc-1 cells treated with **2b** and **2d** in the presence or absence of NAC. The photodynamic treatment with 5, 10, and 15 nM porphyrin increases the percentage of cells stained with both annexin V and PI in a dose-dependent manner, suggesting that up to 20% of cells are late apoptotic or necrotic. As expected for a process mediated by ROS, the percentage of apoptotic/necrotic cells are low when the experiment is performed in the presence of a reducing agent such as NAC, similar to that of untreated cells.

Recent data suggest that the mechanism of cell death induced by porphyrins is more complex and involves both apoptosis and ferroptosis (Sabharwal et al. 2016; Dixon et al. 2012). Although ferroptosis has only recently attracted the attention of researchers, it is known that the executioners of ferroptosis are lipid ROS, i.e., phospholipid hydroperoxides (PLOOHs), a form of lipid-based reactive oxygen species (Zhan et al. 2021; Conrad and Pratt 2019). In the cell, ferroptosis is normally suppressed by the xc-GSH-GPX4 pathway. GPX4 is an enzyme that lowers lipid ROS levels by converting PLOOHs to the corresponding nontoxic alcohols PLOHs

(Conrad and Friedmann Angeli 2015). As **2b** and **2d** are taken up into cells not only by endocytosis but also by passive diffusion, confocal microscopy showed that some of the porphyrins stack on the lipid bilayer of the membrane. Upon photoactivation, they produce ROS and $^1O_2$, which oxidize the phospholipids to form lipids ROS that trigger ferroptosis.

To show that the alkylporphyrins promote ferroptosis, the behavior of **2d** was compared with that of erastin, a potent ferroptosis inducer, in the presence and absence of ferrostatin 1 (Fer-1), an inhibitor of ferroptosis, or BocD-fmk, a widely used caspase inhibitor. Treatment with erastin (15 μM) resulted in a dramatic decrease in cell viability, which is due to cell death by ferroptosis. Moreover, the simultaneous treatment with erastin (15 μM) and Fer-1 (15 μM) leads to a complete restoration of cell viability, as expected. A similar behavior is observed in Panc-1 cells treated with 20 or 40 nM **2d**. This clearly indicates that alkylporphyrins also induce cell death by ferroptosis. However, the fact that Fer-1 did not fully restore cell viability after treatment with 40 nM **2d** implies that the porphyrin activates apoptosis in addition to ferroptosis. When apoptosis was inhibited by BocD-fmk, the percentage of viable cells after treatment with 20 and 40 nM **2d** was 80% and 50%, respectively, compared to control (untreated cells). This reduction in viability is due to ferroptosis. This result shows that **2d** causes cell death by both apoptosis and ferroptosis. Previous studies have shown that depletion of GPX4 leads to excessive lipid peroxidation and cell death by ferroptosis (Conrad and Friedmann Angeli 2015; Yang et al. 2014). GPX4 is a phospholipid hydrogen peroxide glutathione peroxidase that catalyzes the reduction of lipid hydrogen peroxides to protect cells from oxidative damage. The photoactivated porphyrin **2d** strongly suppresses GPX4 thus favoring ferroptosis.

Transcription Factor Decoy G-Quadruplex Oligonucleotides against the *KRAS* Gene

As illustrated in Fig. 3b, *KRAS* transcription is activated when TFs including PARP-1, MAZ, and hnRNPA1 are recruited to the critical promoter 32R motif to form the transcription complex recognized by RNA Pol II. One strategy to inhibit the expression of *KRAS* would be to hunt and sequester the TFs using synthetic decoy oligonucleotides that mimic the G4 structure of the promoter, which acts as a platform for TF recruitment. This strategy was tested several years ago to target STAT3, a TF involved in oncogenesis and cancer growth, using transcription factor decoy (TFD) oligonucleotides (Sen et al. 2012). The TFD oligonucleotides specific for STAT3 were designed as double-stranded DNA fragments mimicking the consensus DNA-binding site of STAT3, located in the *c-FOS* promoter region. Once these exogenous short double-stranded oligonucleotides are delivered to the cells, they should compete with the binding of STAT3 to its promoter site. Thus, the decoys should pull the TFs off the promoter and stop transcription (Fig. 11a). The effectiveness of the TFD oligonucleotides depends on their stability and their ability to penetrate the cell membrane. Grandis and co-workers developed a cyclic 15-mer

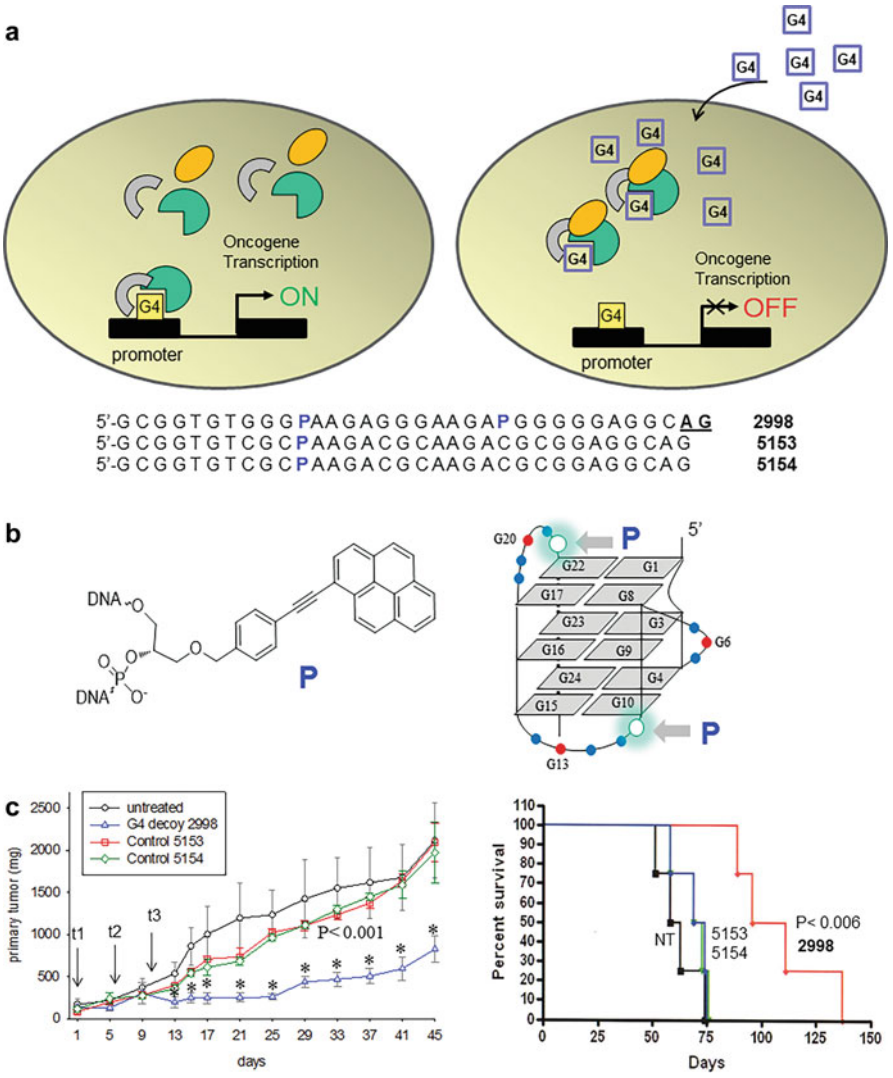

Fig. 11 (**a**) Schematic illustrating the decoy strategy and sequences of P-modified G4 decoys specific to KRAS. The underlined nucleotides are LNA-modified. The putative structure of the G4 decoys is also shown; (**b**) G4 decoy 2998 and control oligonucleotides 515/5154 were injected intratumorally into SCID mice bearing a subcutaneous Panc-1 xenograft. Tumor xenograft growth (mg) up to 45 days post-injection is shown in a graph. Oligonucleotide treatment (2 nmol/mouse) was given three times on days 1, 6, and 11 (t1, t2, and t3). From day 13, the Panc-1 xenograft grew more slowly in the 2998-treated group of mice than in the non-treated group of mice or the groups of mice treated with controls 5153 and 5154 ($P < 0.001$). Kaplan-Meier curves show the effect of decoy 2998 compared with the untreated group or the groups treated with 5153 or 5154. The median survival time of the 2998-treated group is 103.5 days, which is statistically higher than the median survival time of the control groups (71 and 71.5 days) ($P < 0.006$). (Data from Cogoi et al. (2013))

double-stranded oligonucleotide that inhibits transcription of STAT3-dependent genes such as c-*FOS*, *Bcl*-xL, and *cyclin* D1 in cancer cells, in xenograft mouse models of squamous cell carcinoma of the head and neck, and in human tumors (Sen et al. 2012). The TFD oligonucleotide was cyclized by hexaethylene glycol linkages at both ends to increase its stability and resistance to endogenous nucleases. The introduction of a point mutation into the cyclized double-stranded decoy resulted in an inactive decoy molecule that was unable to bind to STAT3 and had no effect on STAT3 target genes. The observation that the critical 32R motif located upstream of TSS in the *KRAS* promoter acts as a platform for TFs forming the transcription complex, makes the use of TFD oligonucleotides mimic the G4 of 32R an attractive strategy to downregulate the *KRAS* oncogene in cancer cells. By interrogating a publicly available microarray dataset (GSE15471), reporting the global gene expression from 36 pairs of normal and PDAC samples from the pancreas of cancer patients, it was found that the genes encoding PARP-1 and hnRNPA1, which recognize the 32R G4, are upregulated in PDAC tissues ($P < 0.007$) (Ferino et al. 2021). These TFs are therefore suitable targets for TFD oligonucleotides. In fact, biotin-streptavidin pull-down experiments showed that biotinylated 32R oligonucleotide used as decoy pulled down hnRNPA1, PARP-1 and MAZ from a Panc-1 total extract. Since these TFs are overexpressed in PDAC, the decoy approach should reduce the amount of free TFs that are recruited to the promoter. The decoy approach, based on the use of G4 oligonucleotides, were tested by the author's group in vitro and in vivo, the results obtained have been encouraging, and recently this strategy has been revisited for further investigation.

Since the *KRAS* -specific TFs recognize the G4 structure of the TFD oligonucleotides, their capacity to sequester TFs depends on their stability in the cellular media, i.e., their ability to maintain their solution structure and to resist to endogenous nucleases. To address these issues, the G4 decoys have been designed with a sequence corresponding to the G4 motif 32R. The decoys were designed with locked nucleic acid (LNA) modifications at the 3′ end to increase nuclease resistance and with polycyclic aromatic hydrocarbon insertions to stabilize the folded tertiary structure (Cogoi et al. 2013). The decoy molecule with two para-TINA (P) modifications, P = (R)-3-((4-(1-pyrenylethynyl) benzyl)oxy) propane-1,2-diol, capping the upper and lower G-quartets of the folded oligonucleotide (decoy 2998), showed promising in vitro and in vivo properties (Fig. 11b). Two oligonucleotides with five G → C mutations that prevent folding to a G4 structure were used as controls: the first with a P modification (5153), and the second with both P and LNA modifications (5154). Mobility shift, DMS footprinting, UV melting, and circular dichroism experiments showed that decoy 2998 should form a unimolecular folded G4 structure with a mixed parallel/antiparallel topology and $T_M = 79$ °C in 100 mM KCl, pH 7.4. EMSA showed that decoy 2998 strongly competed with the binding of MAZ to the G4 structure formed by the 32R sequence of the KRAS promoter, while the control sequences 5153 and 5154, which cannot form a G4 structure, did not. Quantitative RT-PCR and Western blot experiments showed that decoy 2998 dramatically reduced both the mRNA and protein of *KRAS* in Panc-1 pancreatic cancer cells to <10% of control (untreated cells or cells treated with control

G4-decoy	5' → 3' [a]	Mw calculated	Mw [b] Measured	ε (260 nm)	T_M [c] (°C)	Topology [d]
7213	TCGGGTTHCGGGCGCAGGGCHCGGGCGG	9044.78	9045.74	268.72	63.8	Antiparallel
7214	THGGGTTGCGGGCGCAGGGCACGGGHGG	9108.78	9109.64	278.62	56.8	mixed P/A
7215	THGGGTTGCGGGCHCAGGGCACGGGCGG	9040.82	9040.68	275.12	60.0	Antiparallel
7216	TCGGGTTGCGGGCHCAGGGCACGGGHGG	9040.82	9042.63	275.12	55.0	mixed P/A
7217	TCGGGTTGCGGGCGCAGGGCACGGGCGG	8852.52	8853.18	276.50	56.2	Antiparallel

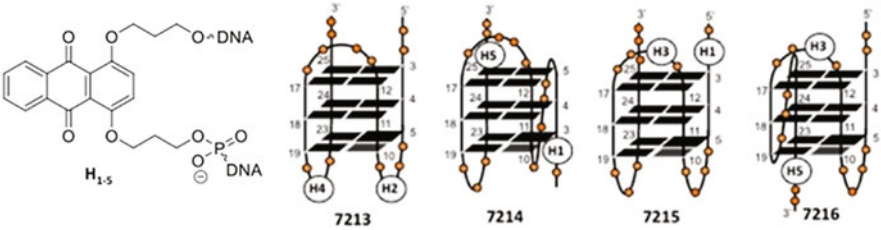

Fig. 12 Decoy G4 oligonucleotides with LNA modifications (underlined nucleotides) and anthraquinone insertions (H) to increase via π-stacking interactions the stability of the folded molecules. (Figure from Miglietta et al. (2015))

oligonucleotides) (Cogoi et al. 2013). Furthermore, Panc-1 cells treated with decoy 2998 were unable to form colonies compared to untreated cells. Since, according to propidium iodide-annexin V and caspase-3/7 assays, decoy oligonucleotide strongly activates apoptosis, whereas control oligonucleotides 5153 and 5154 do not.

The anticancer effect of decoy 2998 was also tested in vivo in SCID mice with a Panc-1 xenograft. Decoy 2998 and control molecules 5153 and 5154 were injected intratumorally with jet PEI (50 l solution containing 2 nmol oligonucleotide/mouse). Treatment was repeated three times (on days 1, 6 and 11), and tumor size was measured every 4 days using a caliper. The data presented in Fig. 11b show that G4 decoy 2998 dramatically reduced tumor xenograft growth (30% of control, $P < 0.001$) from day 13 after the first treatment compared to the non-treated or control-treated mice. The Kaplan-Meier survival curves showed that the median survival time of the mice treated with (5% glucose) was 60.5 days, of the mice treated with decoy 2998 was 103.5 days, of the mice treated with control 5153 was 71 days, and of the mice treated with control 5154 was 71.5 days. The median survival time of the 2998-treated mice increased by 70% compared to the control mice ($P < 0.006$) (Cogoi et al. 2013).

Promising results have also been obtained with TFD oligonucleotides designed to inhibit *HRAS* in T24 bladder cancer cells (Miglietta et al. 2015). The *HRAS* region upstream of the main transcription start site contains two G4 motifs, namely hras-1 and hras-2, which are involved in the regulation of transcription. The two G4 motifs overlap with the binding sites for MAZ and Sp1, two TFs essential for *HRAS* transcription. TFD oligonucleotides mimicking the hras-1 promoter motif were designed with LNA modifications and anthraquinone insertions to increase the stability of the folded oligonucleotides via π-stacking interactions. The TFDs were designed with either two or three LNA modifications and two anthraquinone

insertions, each replacing a nucleotide in different positions, as shown in Fig. 12: H2/H4 (7213), H1/H5 (7214), H1/H3 (7215), and H3/H5 (7216). Compound 7217 was instead engineered without anthraquinone insertions and with LNA modifications only. Dual-luciferase assays using a plasmid in which luciferase was driven by the entire HRAS promoter showed that all four designed TFD oligonucleotides reduced luciferase in a dose-response manner, further supporting the decoy strategy. The results were also confirmed by Western blots, which showed that decoys 7213, 7216, and 7217 strongly reduced the level of the HRAS protein.

To demonstrate that the designed TFD oligonucleotides act with a decoy mechanism, the authors used chromatin immunoprecipitation (ChIP) to investigate whether they attenuate the occupation of the *HRAS* promoter by MAZ. ChIP analysis using an antibody specific for MAZ showed that decoy 7214 reduced the occupancy of *HRAS* promoter by MAZ to about one-third of that observed in the untreated or control-treated cells.

Suppression of the *KRAS* Gene by miRNAs

miRNAs were first discovered by Ambros et al. in 1993 (Lee et al. 1993), and since then, 1917, miRNAs have been deposited in the miRNA database (http://www.mirbase.org/summary.shtml?org=hsa). miRNAs are small, noncoding, single-stranded RNA molecules that are usually 22 nucleotides long and are formed by either a canonical or noncanonical pathway (O'Brien et al. 2018). The canonical pathway forms a pre-miRNA using DGCR8, a double-stranded RNA-binding protein that interacts with Drosha and facilitates miRNA maturation. This pre-miRNA is further processed in the cytoplasm and loaded onto the Argonaute protein family (AGO) as a matured duplex miRNA.

In the noncanonical pathway, a small hairpin RNA (shRNA) undergoes either Dicer-dependent or Dicer-independent processing in the cytoplasm leading to its maturation. As a product of the two pathways, a miRNA-induced silencing complex (miRISC) is formed. The miRISC-mediated gene silencing occurs via the interaction of the miRISC complex with the miRNA response element (MRE) on the target mRNA, forming the miRISC:MRE complex. In many cases, this interaction occurs in the 5′ seed region (typically 2–8 nucleotides), with pairing at the 3′ end providing specificity and stability to the interaction. The miRISC:MRE complex is then degraded by removal of the m7G cap, and the uncapped mRNA undergoes 5′–3′ degradation in the presence of the exoribonucleases XRN1 (O'Brien et al. 2018).

A single miRNA can target a large number of mRNAs and vice versa. This has enabled the use of miRNAs in the diagnosis, prognosis, and therapy of various diseases. The present section focuses on the therapeutic aspect of miRNA in the context of pancreatic cancer.

Therapeutic strategies based on miRNAs can be categorized as either miRNA mimics or miRNA antagonists. The function/expression of the miRNA and the diseased target tissue are the two factors considered when classifying miRNAs as mimics or antagonists. With miRNA antagonists, one targets a miRNA that has a

gain of function in tumor disease. Silencing this miRNA leads to the expression of mRNA of tumor suppressor genes. Optimization of miRNA antagonists is important to protect them from endogenous nucleases, improve their in vivo delivery, and increase their binding affinity (Stenvang and Kauppinen 2008). This can be done by various chemical modifications, such as modifying the sugar moiety or the phosphodiester backbone and attaching small molecules and targeting only the seed region of the miRNA. The sugar bases can be modified at the 2′ position by 2′-O-methyl (2′-O-Me) (Davis et al. 2006), 2′-O-methoxyethyl (2′- MOE) (Stenvang and Kauppinen 2008), or 2′-fluoro (2′-F) (Davis et al. 2009). Other chemical modifications are LNA, locked nucleic acid, which consists of a 2′-O,4′-C-methylene bridge that locks the ribose in the 3′ endo conformation (Petersen and Wengel 2003), and UNA, unlocked nucleic acid, where the ribose ring lacks the C2′–C3′-bond (Fig. 13; Snead et al. 2013). Finally, the use of phosphorothioates, in which one oxygen of the phosphodiester backbone is replaced with sulfur, or morpholino oligonucleotides, in which the sugar moiety is replaced with a morpholine ring (Lima et al. 2018).

Numerous studies have been conducted on the prognostic and diagnostic aspect of miRNA in pancreatic cancer. This has led scientists to change their perspective of miRNA applications in therapy. The author's laboratory focused on targeting oncogenic *KRAS* by miR-216b, which is highly downregulated in PDAC. A miRNA mimic strategy was used to engineer miR-216b. miR-216b targets the 3′-UTR region of *KRAS* mRNA, whose sequence is complementary to the 5′-seed region. Two UNA (unlocked nucleic acid) modifications were introduced into miR-216b: in U1, one adenine was modified at the 3′ end, and in U2, two adenines were modified, one at the 3′ end and the other in the middle, just outside the seed region of the oligoribonucleotide. It was ensured that these modifications did not interfere with the hybridization of the miR-216b mimic to the mRNA.

The other modification introduced into miR-216b was achieved by appending a phosphate to the 5′ end. These designed miR-216b showed different results. The double-stranded miR-216, whose leading strand was modified with UNA, downregulated the expression of *KRAS*, but not *HRAS* or *NRAS* (Ferino et al. 2018).

As previously reported, the single-stranded miR-216b acts via the AGO2-dependent mechanism and can be used as a gene silencing agent. The 5′-phosphorylation did not affect the downregulation of KRAS, but the mimic with two UNA modifications showed a dramatic reduction in KRAS expression (by 90%). Finally, palmitoyl-oleyl-phosphatidylcholine POPC liposomes functionalized with ss-miR-216b conjugated with two palmityl chains and lipid-modified cell-penetrating peptide (TAT) was used to deliver the miRNA into the cells. Preliminary data showed that these nanoparticles induced a 70% decrease in colony formation compared to untreated cells or cells treated with naked POPC liposomes.

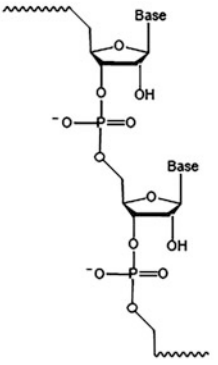
Base
OH
Base
OH

1

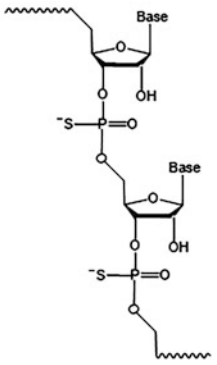
Base
OH
Base
OH

2

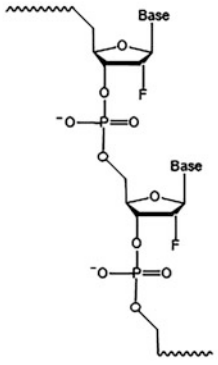
Base
F
Base
F

3

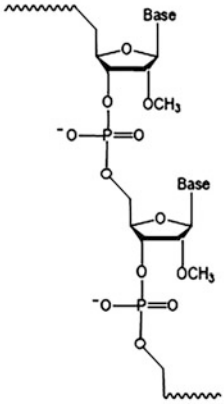
Base
OCH3
Base
OCH3

4

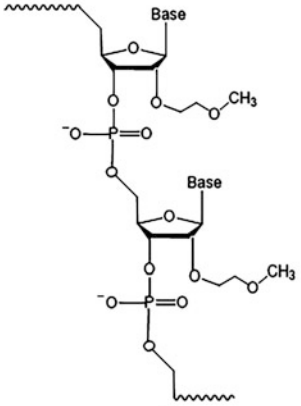
Base
CH3
Base
CH3

5

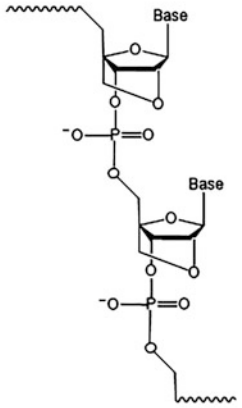
Base
Base

6

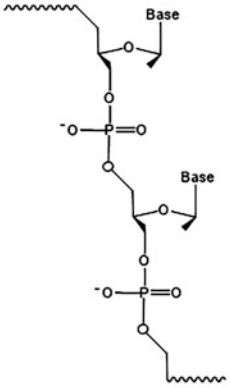
Base
Base

7

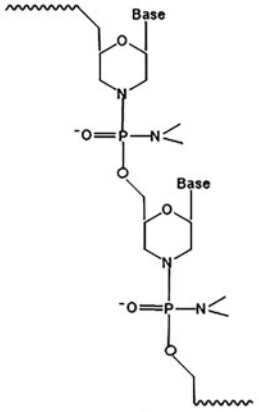
Base
Base

8

Conclusion

The first attempts to inhibit the RAS proteins, reported almost three decades ago, took advantage of the fact that they become active after farnesylation: a posttranslational lipid modification that anchors the RAS proteins to the plasma membrane. Although potent farnesyltransferase inhibitors were developed, they did not yield promising results, because, in the presence of farnesyl inhibitors, the proteins KRAS and NRAS can also be prenylated by geranylgeranyltransferases. Because of these problems, research focused on compounds that bind directly to the RAS proteins. These compounds were designed to bind to a shallow pocket on the protein surface to which GTP or GDP bind. Considering that GTP binds to the RAS protein with a very high affinity (K_D 10^{-11} M) and that its intracellular concentration is quite high (0.5 mM), the search for small molecules that can compete with the binding of GDP/GTP to the RAS proteins proved to be quite arduous. However, recently, pyridopyrimidine compounds (namely, sotorasib and adagrasib) that selectively alter cysteine 12 of the $KRAS^{G12C}$ protein and inhibit *KRAS*-dependent signaling pathways have produced encouraging results in patients with advanced non-small cell lung cancer. However, an alternative way to inhibit the *KRAS* pathways that drive tumor growth and metabolic switching is to directly target the *KRAS* oncogene. It is already known that its promoter sequence upstream TSS called 32R serves as a hub for transcription factor recruitment. It is also known that, 32R folds into two G4s, of which the one called G9T has a very particular structure characterized by a cleft that can be considered an ideal site for the specific binding of small molecules. Future work should therefore focus on using chemical libraries to select compounds that interact specifically with the *KRAS* G-quadruplex and compete with TFs binding to the promoter. In addition, the cationic alkyl porphyrins derived from TMPyP4 are a class of anticancer compounds with extraordinary potential for cancer therapy. Not only they bind with high affinity to G4 RNA, but they are also photosensitizers, meaning that when irradiated with light, they generate singlet oxygen capable of degrading the RNA sequence to which they are bound. The side effects caused by these compounds are limited compared to other cancer drugs. This is mainly due to the fact that they are used in nanomolar concentrations and are only activated in the tumor when irradiated with light. In contrast, the porphyrins remain inactive and noncytotoxic in the tissues surrounding the tumor that are not irradiated. Another important property of alkyl porphyrins is their ability to efficiently penetrate the cell membrane. They are transported by two mechanisms: clathrin-mediated endocytosis and passive diffusion. The endocytic vesicles localize mainly in the cytoplasm and only some of them reach the nucleus. In the cytoplasm, they are strongly co-localized with lysosomes, from which they spread in the cell. As they accumulate in the cytoplasm, they bind to RG4 structures, including those in the 5′-UTR of *KRAS*

Fig. 13 Comparison of miRNA structures: (1) unmodified sequence; (2) phosphorothioate sequence; (3) 2′-fluoro sequence; (4) 2′O-methyl sequence; (5) 2′O-methoxyethyl sequence; (6) locked nucleic acid sequence; (7) unlocked nucleic acid sequence; and (8) morpholino sequence

mRNA, for which they have a high affinity. After porphyrin sensitization with light, they produce $^1O_2$ that degrades *KRAS* mRNA and suppress translation. The biological activity of the alkyl-modified cationic porphyrins was demonstrated in pancreatic cancer cell lines as well as in a B78-H1 melanoma tumor xenograft model. After injection into the peritoneum of B57/BL6 mice, the amount of alkylporphyrins is higher in the tumor than in normal tissues, with the exception of liver and kidney. An interesting way to enhance uptake is to transport the porphyrins into the tumor using POPC liposomes. Alkyl porphyrins are easily fixed to the surface of POPC liposomes, forming functionalized nanoparticles with a diameter of 90 nm, which are efficiently taken up by cancer cells through endocytosis. In vivo, the liposomes reach the abnormal tumor tissue more than normal tissues through the enhanced permeability retention effect, by which the nanoparticles accumulate in cancer tissue, normally with increased vascular permeability. Overall, the authors of this chapter believe that cationic alkyl porphyrins and transcription decoy oligonucleotides represent a class of molecules with great potential as anticancer drugs. Future work in this field should focus on determining their effective antitumor capacity in human cancer models.

References

Alemasova EE, Lavrik OI (2019) Poly(ADP-ribosyl)ation by PARP1: reaction mechanism and regulatory proteins. Nucleic Acids Res 47:3811–3827

Awasthi N, Monahan S, Stefaniak A et al (2017) Inhibition of the MEK/ERK pathway augments nab-paclitaxel-based chemotherapy effects in preclinical models of pancreatic cancer. Oncotarget 9:5274–5286

Belotserkovskii BP, Liu R, Tornaletti S et al (2010) Mechanisms and implications of transcription blockage by guanine-rich DNA sequences. Proc Natl Acad Sci 107:12816–12821

Belotserkovskii BP, Soo Shin JH, Hanawalt PC (2017) Strong transcription blockage mediated by R-loop formation within a G-rich homopurine-homopyrimidine sequence localized in the vicinity of the promoter. Nucleic Acids Res 45:6589–6599

Brito H, Martins AC, Lavrado J et al (2015) Targeting KRAS oncogene in colon cancer cells with 7-carboxylate Indolo[3,2-b]quinoline tri-alkylamine derivatives. PLoS One 10:e0126891

Brummelkamp TR, Bernards R, Agami R (2002) Stable suppression of tumorigenicity by virus-mediated RNA interference. Cancer Cell 2:243–247

Calabrese DR, Zlotkowski K, Alden S et al (2018) Characterization of clinically used oral antiseptics as quadruplex-binding ligands. Nucleic Acids Res 46:2722–2732

Chen K, Zhang Y, Qian L et al (2021) Emerging strategies to target RAS signaling in human cancer therapy. J Hematol Oncol 14:116

Cinque G, Ferino A, Pedersen EB et al (2020) Role of poly [ADP-ribose] polymerase 1 in activating the *Kirsten ras* (*KRAS*) gene in response to oxidative stress. Int J Mol Sci 21:6237–6259

Cogoi S, Xodo LE (2006) G-quadruplex formation within the promoter of the *KRAS* proto-oncogene and its effect on transcription. Nucleic Acids Res 34:2536–2549

Cogoi S, Xodo LE (2016) G4 DNA in *ras* genes and its potential in cancer therapy. Biochim Biophys Acta 1859:663–674

Cogoi S, Paramasivam M, Spolaore B et al (2008) Structural polymorphism within a regulatory element of the human KRAS promoter: formation of G4-DNA recognized by nuclear proteins. Nucleic Acids Res 36:3765–3780

Cogoi S, Zorzet S, Rapozzi V et al (2013) MAZ-binding G4-decoy with locked nucleic acid and twisted intercalating nucleic acid modifications suppresses *KRAS* in pancreatic cancer cells and delays tumor growth in mice. Nucleic Acids Res 41:4049–4064

Cogoi S, Shchekotikhin AE, Xodo LE (2014) HRAS is silenced by two neighboring G-quadruplexes and activated by MAZ, a zinc-finger transcription factor with DNA unfolding property. Nucleic Acids Res 42:8379–8388

Cogoi S, Ferino A, Miglietta G et al (2018) The regulatory G4 motif of the Kirsten ras (*KRAS*) gene is sensitive to guanine oxidation: implications on transcription. Nucleic Acids Res 46:661–676

Collins MA, Bednar F, Zhang Y et al (2012) Oncogenic *KRAS* is required for both the initiation and maintenance of pancreatic cancer in mice. J Clin Invest 122:639–653

Conrad M, Friedmann Angeli JP (2015) Glutathione peroxidase 4 (Gpx4) and ferroptosis: what's so special about it? Mol Cell Oncol 2:e995047

Conrad M, Pratt DA (2019) The chemical basis of ferroptosis. Nat Chem Biol 15:1137–1147

Conroy T, Hammel P, Hebbar M et al (2018) FOLFIRINOX or gemcitabine as adjuvant therapy for pancreatic cancer. N Engl J Med 379:2395–2406

Cox AD, Der CJ, Philips MR (2015) Targeting RAS membrane association: back to the future for anti-RAS drug discovery? Clin Cancer Res 21:1819–1827

Davis S, Lollo B, Freier S, Esau C (2006) Improved targeting of miRNA with antisense oligonucleotides. Nucleic Acids Res 34:2294–2304

Davis S, Propp S, Freier SM et al (2009) Potent inhibition of microRNA in vivo without degradation. Nucleic Acids Res 37:70–77

Di Giorgio E, Ferino A, Choudhary H et al (2022) Photosensitization of pancreatic cancer cells by cationic alkyl-porphyrins in free form or engrafted into POPC liposomes: the relationship between delivery mode and mechanism of cell death. J Phochem Photobiol B 231:112449

Di Magliano MP, Logsdon CD (2013) Roles for KRAS in pancreatic tumor development and progression. Gastroenterology 144:1220–1229

Dixon SJ, Lemberg KM, Lamprecht MR et al (2012) Ferroptosis: an iron-dependent form of nonapoptotic cell death. Cell 149:1060–1072

Dunnett-Kane V, Burkitt-Wright E, Blackhall F et al (2020) Germline and sporadic cancers driven by the RAS pathway: parallels and contrasts. Ann Oncol 31:873–883

Eddy J, Vallur AC, Varma S et al (2011) G4 motifs correlate with promoter-proximal transcriptional pausing in human genes. Nucl Acids Res 39:4975–4983

Edwards AD, Marecki JC, Byrd AK et al (2021) G-Quadruplex loops regulate PARP-1 enzymatic activation. Nucleic Acids Res 49:416–431

Eser S, Reiff N, Messer M et al (2013) Selective requirement of PI3K/PDK1 signaling for Kras oncogene-driven pancreatic cell plasticity and cancer. Cancer Cell 23:406–420

Eser S, Schnieke A, Schneider G et al (2014) Oncogenic KRAS signalling in pancreatic cancer. Br J Cancer 111:817–822

Eustermann S, Videler H, Yang JC et al (2011) The DNA-binding domain of human PARP-1 interacts with DNA single-strand breaks as a monomer through its second zinc finger. J Mol Biol 407:149–170

Fan Z, Fan K, Yang C et al (2018) Critical role of KRAS mutation in pancreatic ductal adenocarcinoma. Transl Cancer Res 7:1728–1736

Ferino A, Miglietta G, Picco R et al (2018) MicroRNA therapeutics: design of single-stranded miR-216b mimics to target KRAS in pancreatic cancer cells. RNA Biol 15:1273–1285

Ferino A, Nicoletto G, D'Este F et al (2020) Photodynamic therapy for *ras*-driven cancers: targeting G-Quadruplex RNA structures with bifunctional alkyl-modified porphyrins. J Med Chem 63: 1245–1260

Ferino A, Marquevielle J, Choudhary H et al (2021) hnRNPA1/UP1 unfolds *KRAS* G-quadruplexes and feeds a regulatory axis controlling gene expression. ACS Omega 6:34092–34106

Gupte R, Liu Z, Kraus WL (2017) Parp and ADP-ribosylation: recent advances linking molecular functions to biological outcomes. Genes Dev 31:101–126

Huppert JL, Balasubramanian S (2007) G-quadruplexes in promoters throughout the human genome. Nucl Acids Res 35:406–413

Kanda M, Matthaei H, Wu J et al (2012) Presence of somatic mutations in most early-stage pancreatic intraepithelial neoplasia. Gastroenterology 142:730–733

Kerkour A, Marquevielle J, Ivashchenko S et al (2017) High-resolution three-dimensional NMR structure of the *KRAS* proto-oncogene promoter reveals key features of a G-quadruplex involved in transcriptional regulation. J Biol Chem 292:8082–8091

Lago S, Nadai M, Cernilogar FM et al (2021) Promoter G-quadruplexes and transcription factors cooperate to shape the cell type-specific transcriptome. Nat Commun 12:3885

Lavrado J, Borralho PM, Ohnmacht SA et al (2013) Synthesis, G-quadruplex stabilisation, docking studies, and effect on cancer cells of indolo[3,2-b]quinolones with one, two, or three basic side chains. Chem Med Chem 8:1648–1661

Lavrado J, Ohnmacht SA, Correia I et al (2015a) Indolo[3,2-c]quinoline G-quadruplex stabilizers: a structural analysis of binding to the human telomeric G-quadruplex. ChemMedChem 10: 836–849

Lavrado J, Brito H, Borralho PM et al (2015b) KRAS oncogene repression in colon cancer cell lines by G-quadruplex binding indolo[3,2-c]quinolines. Sci Rep 5:9696

Lee RC, Feinbaum RL, Ambros V (1993) The C. elegans heterochronic gene lin-4 encodes small RNAs with antisense complementarity to lin-14. Cell 75:843–854

Lima JF, Cerqueira L, Figueiredo C (2018) Anti-miRNA oligonucleotides: a comprehensive guide for design. RNA Biol 15:338–352

Lindsay CR, Blackhall FH (2019) Direct Ras G12C inhibitors: crossing the rubicon. Br J Cancer 121:197–198

Marchetti C, Zyner KG, Ohnmacht SA et al (2018) Targeting multiple effector pathways in pancreatic ductal adenocarcinoma with a G-quadruplex-binding small molecule. J Med Chem 61:2500–2517

Marquevielle J, Robert C, Lagrabette O et al (2020) Structure of two G-quadruplexes in equilibrium in the KRAS promoter. Nucleic Acids Res 48:9336–9345

Miglietta G, Gouda AS, Cogoi S et al (2015) Nucleic acid targeted therapy: G4 oligonucleotides downregulate HRAS in bladder cancer cells through a decoy mechanism. ACS Med Chem Lett 6:179–183

Miglietta G, Cogoi S, Marinello J et al (2017) RNA G-Quadruplexes in Kirsten Ras (KRAS) oncogene as targets for small molecules inhibiting translation. J Med Chem 60:9448–9461

Nayun K (2019) The interplay between G-quadruplex and transcription. Curr Med Chem 26: 2898–2917

O'Brien J, Hayder H, Zayed Y et al (2018) Overview of microRNA biogenesis, mechanisms of actions, and circulation. Front Endocrinol (Lausanne) 9:402

Ostrem JM, Peters U, Sos ML et al (2013) K-Ras(G12C) inhibitors allosterically control GTP affinity and effector interactions. Nature 503:548–551

Ou A, Schmidberger JW, Wilson KA et al (2020) High resolution crystal structure of a KRAS promoter G-quadruplex reveals a dimer with extensive poly-A pi-stacking interactions for small-molecule recognition. Nucleic Acids Res 48:5766–5776

Paramasivam M, Membrino A, Cogoi S et al (2009) Protein hnRNP A1 and its derivative Up1 unfold quadruplex DNA in the human *KRAS* promoter: implications for transcription. Nucleic Acids Res 37:2841–2853

Paramasivam M, Cogoi S, Xodo LE (2011) Primer extension reactions as a tool to uncover folding motifs within complex G-rich sequences: analysis of the human KRAS NHE. Chem Commun (Camb) 47:4965–4967

Petersen M, Wengel J (2003) LNA: a versatile tool for therapeutics and genomics. Trends Biotechnol 21:74–81

Rahib L, Wehner MR, Matrisian LM et al (2021) Estimated projection of US cancer incidence and death to 2040. JAMA Netw Open 4:e214708

Rapozzi V, Zorzet S, Zacchigna M et al (2014) Anticancer activity of cationic porphyrins in melanoma tumor-bearing mice and mechanistic in vitro studies. Mol Cancer 13:75
Rawla P, Sunkara T, Gaduputi V (2019) Epidemiology of pancreatic cancer: global trends, etiology and risk factors. World J Oncol 10:10–27
Sabharwal NC, Mendoza O, Nicoludis JM et al (2016) Investigation of the interactions between Pt (II) and Pd(II) derivatives of 5,10,15,20-tetrakis (*N*-methyl-4-pyridyl) porphyrin and G-quadruplex DNA. J Biol Inorg Chem 21(227–239):65
Saito I, Takayama M, Sugiyama H et al (1995) Photoinduced DNA cleavage via electron transfer: demonstration that guanine residues located 5' to guanine are the most electron-donating sites. J Am Chem Soc 117:6406–6407
Santana-Codina N, Roeth AA, Zhang Y et al (2018) Oncogenic KRAS supports pancreatic cancer through regulation of nucleotide synthesis. Nat Commun 9:4945
Sen M, Thomas SM, Kim S et al (2012) First-in-human trial of a STAT3 decoy oligonucleotide in head and neck tumors: implications for cancer therapy. Cancer Discov 2:694–705
Siddiqui-Jain A, Grand CL, Bearss DJ et al (2002) Direct evidence for a G-quadruplex in a promoter region and its targeting with a small molecule to repress c-*MYC* transcription. Proc Natl Acad Sci 99:11593–11598
Siegel RL, Miller KD, Jemal A (2018) Cancer Stat 68:7–30
Skovsen E, Snyder JW, Lambert JDC et al (2005) Lifetime and diffusion of singlet oxygen in a cell. J Phys Chem B 109:8570–8573
Snead NM, Escamilla-Powers JR, Rossi JJ et al (2013) 5'unlocked nucleic acid modifications improves siRNA targeting. Mol Ther Nucleic Acids 2:e103
Soldatenkov VA, Vetcher AA, Duka T et al (2008) First evidence of a functional interaction between DNA quadruplexes and poly(ADP-ribose) polymerase-1. ACS Chem Biol 3:214–219
Son J, Lyssiotis CA, Ying H et al (2013) Glutamine supports pancreatic cancer growth through a KRAS-regulated metabolic pathway. Nature 496:101–105
Spiegel J, Cuesta SM, Adhikari S et al (2021) G-quadruplexes are transcription factor binding hubs in human chromatin. Genome Biol 22:117
Steenken S, Jovanovic SV (1997) How easily oxidizable is DNA? One-electron reduction potentials of adenosine and guanosine radicals in aqueous solution. J Am Chem Soc 119:617–618
Stenvang J, Kauppinen S (2008) MicroRNAs as targets for antisense-based therapeutics. Expert Opin Biol Ther 8:59–81
Sun SY (2010) N-acetylcysteine, reactive oxygen species and beyond. Cancer Biol Ther 9:109–110
Todd AK, Neidle S (2008) The relationship of potential G-quadruplex sequences in *cis* -upstream regions of the human genome to SP1-binding elements. Nucleic Acids Res 36:2700–2704
Vallejo A, Perurena N, Guruceaga E et al (2017) An integrative approach unveils FOSL1 as an oncogene vulnerability in KRAS-driven lung and pancreatic cancer. Nat Commun 8(14294)
Von Hoff DD, Ervin T, Arena FP et al (2013) Increased survival in pancreatic cancer with nab-paclitaxel plus gemcitabine. N Engl J Med 369:1691–1703
Waters AM, Der CJ (2018) KRAS: the critical driver and therapeutic target for pancreatic cancer. Cold Spring Harb Perspect Med 8:a031435
Xodo LE, Cogoi S, Rapozzi V (2016) Photosensitizers binding to nucleic acids as anticancer agents. Future Med Chem 8:179–194
Yang WS, SriRamaratnam R, Welsch ME et al (2014) Regulation of ferroptotic cancer cell death by GPX4. Cell 156:317–331
Ying H, Kimmelman AC, Lyssiotis CA et al (2012) Oncogenic Kras maintains pancreatic tumors through regulation of anabolic glucose metabolism. Cell 149:656–760
Zhan G, Zhang Z, Yong T et al (2021) Manganese porphyrin-based metal-organic framework for synergistic sonodynamic therapy and ferroptosis in hypoxic tumors. Theranostics 11: 1937–1952
Zheng KW, Xiao S, Liu JQ et al (2013) Co-transcriptional formation of DNA: RNA hybridG-quadruplex and potential function as constitutional *cis*-element for transcription control. Nucleic Acids Res 41:5533–5541

Conclusion

Pancreatic cancer is driven by the activated mutant KRAS gene, which gives the tumour a metabolic plasticity that enables it to perform aerobic glycolysis and overcome nutrient deficiency by adapting the cell to use alternative energy sources. Aerobic glycolysis and glucose consumption are the traditional hallmarks of the Warburg effect, but now we know that tumours have high metabolic plasticity. The 5-year survival rate of patients with pancreatic ductal adenocarcinoma is less than 8% as the disease develops resistance to conventional chemotherapy. Due to this developed resistance, new therapeutic strategies are urgently needed. Studies have shown that expression of Nrf2 controlled by oncogenic KRAS leads to low intracellular ROS levels, thereby promoting tumorigenesis and metastasis in the pancreas. In contrast, inhibition of the KRAS -Nrf2 axis leads to upregulation of ROS and inhibition of proliferation and metastasis. In this work, we have investigated (i) how the expression of KRAS is regulated; (ii) what effects the KRAS -Nrf2 axis has on the metabolism of pancreatic cancer cells; and (iii) how new therapeutic approaches for PDAC can be developed.

In the first part of my PhD thesis, in collaboration with other researchers in the laboratory, we have studied the transcription factors that act on the G4 structure of the KRAS promoter. We have shown that hnRNPA1 and its proteolytic component UP1 interact with the KRAS G4s. Through NMR experiments by tracking the intensity of the imino protons of the G4 in the presence of hnRNP A1 and as a function of time, we found that the protein unfolds its structure after G4 binding. The KRAS G4 named G25T is virtually unfolded by hnRNP A1, while the other G4 named G9T is only partially unfolded. The two RRM domains of UP1 comprise the residues that undergo significant changes upon binding to the KRAS G4 conformer, as observed in the interaction between UP1 and telomeric G4. Given that hnRNPA1/UP1 can unfold G4 DNA, we believe that this protein is critical for controlling transcription. We discovered that hnRNPA1 is required for transcription of KRAS and for cell proliferation by using a Panc-1 knockout cell line in which hnRNPA1 was deleted using CRISPR/Cas9. Indeed, we found that the level of KRAS was lower in the Panc-1 cells with hnRNPA1 knockdown compared to the normal cells. Then, by pulldown and western blot assays, we discovered that the conformer G25T, and not the conformer G9T, serves as the platform for the assembly of the transcription pre-initiation complex with the nuclear proteins PARP1, Ku70, MAZ and

hnRNPA1. There is growing evidence that PDAC cells are addicted to KRAS, which activates mitogenic signalling, including the KRAS-ILK -hnRNP A1 axis. Its expression correlates with clinical outcome in PDAC patients. According to the Kaplan-Meier diagrams, PDAC patients with a high KRAS-ILK -hnRNPA1 axis have a significantly worse chance of survival than PDAC patients with low expression of the axis. Taken together, the results show that the KRAS-ILK -hnRNPA1 axis plays a crucial role in the maintenance of PDAC and imply that hnRNPA1 may be a desirable target for the development of new anticancer drugs to treat PDAC.

Next, we worked on the development of a molecular strategy to inhibit KRAS and thus downstream signal transduction. In collaboration with Prof. Andrey E. Shchekotikhin from Moscow University, we developed cationic porphyrins to stop PDAC cell proliferation by photodynamic action. The cationic alkyl porphyrins 2b and 2d, either as molecules in free form or embedded in POPC liposomes, showed a strong ability to stop cell growth in both mice and cell lines. While porphyrins grafted into liposomes are taken up exclusively by endocytosis, free alkyl porphyrins can also enter cells by membrane fusion and, to a lesser extent, by endocytosis.

According to confocal microscopy, porphyrin 2d colocalises with lysosomes before being released into the cytoplasm, where it binds to G4 RNA in the 5'-UTR of KRAS mRNA and destroys it upon illumination. However, when porphyrin is delivered engrafted into liposomes (L-2d), it is only partially colocalised with the lysosomes, which are likely to release a small amount of porphyrin into the cytoplasm, insufficient to inhibit KRAS. Interestingly, this behaviour affects the type of cell death mediated by the porphyrins. While liposome-engrafted porphyrins are taken up exclusively by endocytosis, free alkyl porphyrins can also enter cells by membrane fusion and, to a lesser extent, by endocytosis. In fact, only free cationic porphyrins down-regulate KRAS and the downstream Nrf2 and GPX4. The latter protein is important for cells as it prevents the production of the lipid ROS, which can trigger ferroptosis. Therefore, blocking the KRAS -Nrf2-GPX4 axis should significantly limit the cell's ability to control lipid peroxidation and protect membranes. Under stress conditions, GPX4 is essential for maintaining cell integrity by preventing oxidised membranes from releasing lipids ROS, which cause cell death by ferroptosis. In contrast, porphyrins bound to liposomes (L-2d) are internalised into cancer cells by endocytosis, leaving insufficient porphyrin molecules in the lipid bilayer to generate lipid ROS. L-2d does not release enough porphyrin

molecules into the cytoplasm to inhibit KRAS and its axis with Nrf2 and GPX4. On the other hand, it was discovered that L-2d effectively produces ROS upon illumination, which dramatically induces cell death by apoptosis. In summary, our results demonstrate the complexity of the ferroptosis- and apoptosis-based cell death pathway triggered by the cationic alkyl-modified porphyrins. The two forms of cell death coexist in porphyrin-treated cells, and the method of administration influences which type occurs more frequently: while free alkyl porphyrin mainly induces ferroptosis, liposomal anchored alkyl porphyrin mainly promotes apoptosis.

In the third and final phase of my PhD, I investigated what happens to pancreatic cancer cells when the KRAS -Nrf2 axis is switched off. To switch off this axis, we had two options: either inhibiting KRAS or inhibiting Nrf2. We tried the first approach but found that cells dependent on the KRAS oncogene did not survive when the oncogene was suppressed. Therefore, we decided to inhibit the axis by acting on Nrf2. We took a drastic approach and deleted Nrf2 in Panc-1 cells using CRISPR-Cas9 technology and succeeded in obtaining an Nrf2(-/-) knockout that could proliferate in DMEM medium. As expected, we discovered that suppression of the KRAS-Nrf2 axis leads to a significant increase of ROS in Nrf2(-/-) cells compared to normal Panc-1 cells. In addition to the increase in ROS, reduced glutathione and reduced total thiols in the cells were also reduced, consistent with the function of Nrf2 as a master regulator of ROS homeostasis. Next, we performed next-generation RNA sequencing analysis to investigate the effects of silencing the KRAS -Nrf2 axis on the whole transcriptome. The results showed that 1888 genes were down-regulated and 666 were up-regulated in Nrf2(-/-) cells compared to normal Panc-1 cells, assuming a threshold $|\log2\ F \geq 1|$, $P < 0.05$. Remarkably, Nrf2-deficient Panc-1 cells have lost their typical anaerobic properties and rely on aerobic metabolism using amino acids, especially arginine, and short-chain fatty acids as nutrients. RNA-seq showed that all key genes encoding glycolytic enzymes are down-regulated in the cells that have lost the KRAS -Nrf2 axis. In addition, the pentose phosphate and glutathione cycle are also severely suppressed in the knockout cells. These results were confirmed by quantitative analysis RT-PCR. Overall, the analysis show that the KRAS -Nrf2 axis in pancreatic cancer cells activates aerobic glycolysis, through which the cells feed glycolysis with a high glucose flux to generate ATP and biomass necessary to produce substrates for cell proliferation. Panc-1 cells are highly glycolytic, which was also confirmed by measuring

oxygen consumption using Seahorse. Aerobic glycolysis is particularly important in the early stages of cancer development, when the tumour mass has an insufficient vascular supply and resulting in an insufficient oxygen level. In addition, RNA-seq analysis revealed that loss of the KRAS -Nrf2 axis, which restricts the use of glucose, causes pancreatic cancer cells to switch to aerobic metabolism and use short-chain fatty acids and amino acids, especially arginine, as substrates. According to the GSEA, the KRAS signalling pathway is lost in Nrf2-deficient cells, while the CMYC pathway is enhanced to maintain malignancy. PDAC cells switch their metabolism from glucose to amino acids and fatty acids when aerobic glycolysis is suppressed. Arginine metabolism is adaptable to metabolic stress, as shown by unbiased functional enrichment analysis. In Nrf2(-/-) cells, where the KRAS G12D-Nrf2 axis is inactive, 8% of arginine is diverted to UC and 23% to creatine synthesis, depending on the number of metabolites derived from arginine. However, just 3% of the arginine in normal Panc-1 cells is directed to the UC, which is consistent with the fact that these cells are more glycolytic and require fewer amino acids to produce ATP. The *ckb* enzyme is not active in Panc-1 cells and < 1% % of creatine is converted to phosphocreatine. In contrast, *ckb* activity is three orders of magnitude greater in Nrf2(-/-) cells, in which 12% of the creatine pool is converted to phosphocreatine. As a result, an effective energy buffer is created from which PDAC cells draw ATP to support their growth and survival. The growth of Nrf2(-/-) and WT Panc-1 cells in Matrigel matrix 3D plates is inhibited by cyclocreatine and homoarginine, two molecules that inhibit the creatine-pathway.

Taken together, our results suggest that combination treatment focusing on both creatine metabolism and the KRAS -Nrf2 axis is likely to be more successful than monotherapy. Indeed, gemcitabine, oxaliplatin and anthrathiophenedione 2a, which are thought to interfere with the KRAS G12D-Nrf2 axis, dramatically increase their efficacy when used in combination with cyclocreatine. These drugs are based on the observation that PDAC cells respond to inhibition of the KRAS -Nrf2 axis by switching to aerobic metabolism and diverting arginine into the creatine pathway, which produces an energy-rich phosphate compound from which ATP is derived for cell growth. Thus, simultaneous suppression of the creatine pathway and the KRAS -Nrf2 axis makes PDAC cells more susceptible to combined therapy.

In summary, the work of this PhD focused on the role of KRAS and the KRAS -Nrf2 axis in

PDAC cells and may explain how pancreatic cancer cells become resistant to cancer treatments. We hypothesise that targeting KRAS and phosphocreatine is likely to be more effective than targeting the gene KRAS or its downstream signalling pathway alone. However, a more in-depth study is needed, as suppression of the KRAS -Nrf2 gene also activates the metabolism of medium-chain lipids, which may provide new metabolic targets for the treatment of PDAC.

References

1. Gittes GK. Developmental biology of the pancreas: A comprehensive review. Dev Biol. 2009;326(1):4-35. doi:10.1016/j.ydbio.2008.10.024.
2. Betts, J. G., Young, K. A., Wise, J. A., Johnson, E., Poe, B., Kruse, D. H., … De Saix, P. (2013). The endocrine pancreas. In Anatomy and Physiology. OpenStax.
3. Xodo LE. Quadruplex nucleic acids in KRAS targeted-cancer therapy. In: ; 2020:325-359. doi:10.1016/bs.armc.2020.04.004W
4. Bray F, Ferlay J, Soerjomataram I, Siegel RL, Torre LA, Jemal A. Global cancer statistics 2018: GLOBOCAN estimates of incidence and mortality worldwide for 36 cancers in 185 countries. CA Cancer J Clin. 2018;68(6):394-424. doi:10.3322/caac.21492W
5. Sung H, Ferlay J, Siegel RL, et al. Global Cancer Statistics 2020: GLOBOCAN Estimates of Incidence and Mortality Worldwide for 36 Cancers in 185 Countries. CA Cancer J Clin. 2021;71(3):209-249. doi:10.3322/caac.21660W
6. Ushio J, Kanno A, Ikeda E, et al. Pancreatic Ductal Adenocarcinoma: Epidemiology and Risk Factors. Diagnostics. 2021;11(3):562. doi:10.3390/diagnostics11030562W
7. Uccelli R, Mastrantonio M, Altavista P, Sciortino M, Carletti R. Pancreatic cancer mortality in Italy (1981–2015): a population-based study on geographic distribution and temporal trends. Ann Cancer Epidemiol. 2021;5:1-1. doi:10.21037/ace-20-23
8. H. Bekkali N, Oppong K. Pancreatic ductal adenocarcinoma epidemiology and risk assessment: Could we prevent? Possibility for an early diagnosis. Endosc Ultrasound. 2017;6(9):58. doi:10.4103/eus.eus_60_17
9. Kenner BJ, Chari ST, Maitra A, et al. Early Detection of Pancreatic Cancer—a Defined Future Using Lessons From Other Cancers. Pancreas. 2016;45(8):1073-1079. doi:10.1097/MPA.0000000000000701
10. Parkin DM, Boyd L, Walker LC. 16. The fraction of cancer attributable to lifestyle and environmental factors in the UK in 2010. Br J Cancer. 2011;105(S2):S77-S81. doi:10.1038/bjc.2011.489
11. Whitcomb DC, Shelton CA, Brand RE. Genetics and Genetic Testing in Pancreatic Cancer. Gastroenterology. 2015;149(5):1252-1264.e4. doi:10.1053/j.gastro.2015.07.057

12. Ulrich CD. Pancreatic Cancer in Hereditary Pancreatitis: Consensus Guidelines for Prevention, Screening and Treatment. Pancreatology. 2001;1(5):416-422. doi:10.1159/000055841
13. Matsubayashi H, Takaori K, Morizane C, et al. Familial pancreatic cancer: Concept, management and issues. World J Gastroenterol. 2017;23(6):935. doi:10.3748/wjg.v23.i6.935
14. Lami G. Endoscopic ultrasonography for surveillance of individuals at high risk for pancreatic cancer. World J Gastrointest Endosc. 2014;6(7):272. doi:10.4253/wjge.v6.i7.272
15. Amundadottir L, Kraft P, Stolzenberg-Solomon RZ, et al. Genome-wide association study identifies variants in the ABO locus associated with susceptibility to pancreatic cancer. Nat Genet. 2009;41(9):986-990. doi:10.1038/ng.429
16. Becker AE. Pancreatic ductal adenocarcinoma: Risk factors, screening, and early detection. World J Gastroenterol. 2014;20(32):11182. doi:10.3748/wjg.v20.i32.11182
17. Hruban RH, Adsay NV, Albores–Saavedra J, et al. Pancreatic Intraepithelial Neoplasia. Am J Surg Pathol. 2001;25(5):579-586. doi:10.1097/00000478-200105000-00003
18. Sohn TA, Yeo CJ, Cameron JL, et al. Intraductal Papillary Mucinous Neoplasms of the Pancreas. Ann Surg. 2004;239(6):788-799. doi:10.1097/01.sla.0000128306.90650.aa
19. Grant TJ, Hua K, Singh A. Molecular Pathogenesis of Pancreatic Cancer. In: Progress in Molecular Biology and Translational Science. Vol 144. ; 2016:241-275. doi:10.1016/bs.pmbts.2016.09.008.
20. Shinkawa T, Ohuchida K, Mochida Y, et al. Subtypes in pancreatic ductal adenocarcinoma based on niche factor dependency show distinct drug treatment responses. J Exp Clin Cancer Res. 2022;41(1):89. doi:10.1186/s13046-022-02301-9
21. Bailey P, Chang DK, Nones K, et al. Genomic analyses identify molecular subtypes of pancreatic cancer. Nature. 2016;531(7592):47-52. doi:10.1038/nature16965
22. Lomberk G, Blum Y, Nicolle R, et al. Distinct epigenetic landscapes underlie the pathobiology of pancreatic cancer subtypes. Nat Commun. 2018;9(1):1978. doi:10.1038/s41467-018-04383-6
23. Espiau-Romera P, Courtois S, Parejo-Alonso B, Sancho P. Molecular and Metabolic Subtypes Correspondence for Pancreatic Ductal Adenocarcinoma Classification. J Clin Med. 2020;9(12):4128. doi:10.3390/jcm9124128

24. Sakorafas GH, Tsiotou AG, Tsiotos GG. Molecular biology of pancreatic cancer; oncogenes, tumour suppressor genes, growth factors, and their receptors from a clinical perspective. Cancer Treat Rev. 2000;26(1):29-52. doi:10.1053/ctrv.1999.0144

25. Almoguera C, Shibata D, Forrester K, Martin J, Arnheim N, Perucho M. Most human carcinomas of the exocrine pancreas contain mutant c-K-ras genes. Cell. 1988;53(4):549-554. doi:10.1016/0092-8674(88)90571-5

26. Garcia PE, Adoumie M, Kim EC, et al. Differential Contribution of Pancreatic Fibroblast Subsets to the Pancreatic Cancer Stroma. Cell Mol Gastroenterol Hepatol. 2020;10(3):581-599. doi:10.1016/j.jcmgh.2020.05.004

27. Deramaudt T, Rustgi AK. Mutant KRAS in the initiation of pancreatic cancer. Biochim Biophys Acta - Rev Cancer. 2005;1756(2):97-101. doi:10.1016/j.bbcan.2005.08.003

28. Sirivatanauksorn V, Sirivatanauksorn Y, Lemoine NR. Molecular pattern of ductal pancreatic cancer. Langenbecks Arch Chir. 1998;383(2):105. doi:10.1007/s004230050101

29. Li D, Xie K, Wolff R, Abbruzzese JL. Pancreatic cancer. Lancet. 2004;363(9414):1049-1057. doi:10.1016/S0140-6736(04)15841-8

30. Caldas C, Hahn SA, da Costa LT, et al. Frequent somatic mutations and homozygous deletions of the p16 (MTS1) gene in pancreatic adenocarcinoma. Nat Genet. 1994;8(1):27-32. doi:10.1038/ng0994-27

31. Goggins M. Molecular Markers of Early Pancreatic Cancer. J Clin Oncol. 2005;23(20):4524-4531. doi:10.1200/JCO.2005.19.711

32. Hahn SA, Schutte M, Shamsul Hoque ATM, et al. DPC4 , A Candidate Tumor Suppressor Gene at Human Chromosome 18q21.1. Science (80-). 1996;271(5247):350-353. doi:10.1126/science.271.5247.350

33. Hansel DE, Kern SE, Hruban RH. Molecular Pathogenesis of Pancreatic Cancer. Annu Rev Genomics Hum Genet. 2003;4(1):237-256. doi:10.1146/annurev.genom.4.070802.110341

34. Belda-Iniesta C, De Cáceres II, Barriuso J, De Castro Carpeño J, Barón MG, Feliú J. Molecular biology of pancreatic cancer. Clin Transl Oncol. 2008;10(9):530-537. doi:10.1007/s12094-008-0247-6

35. Hochster HS, Haller DG, de Gramont A, et al. Consensus report of the International Society of Gastrointestinal Oncology on therapeutic progress in advanced pancreatic cancer. Cancer. 2006;107(4):676-685. doi:10.1002/cncr.22036
36. Hezel AF, Kimmelman AC, Stanger BZ, Bardeesy N, DePinho RA. Genetics and biology of pancreatic ductal adenocarcinoma. Genes Dev. 2006;20(10):1218-1249. doi:10.1101/gad.1415606
37. MacKenzie MJ. Molecular therapy in pancreatic adenocarcinoma. Lancet Oncol. 2004;5(9):541-549. doi:10.1016/S1470-2045(04)01565-7
38. Ram Makena M, Gatla H, Verlekar D, Sukhavasi S, K. Pandey M, C. Pramanik K. Wnt/β-Catenin Signaling: The Culprit in Pancreatic Carcinogenesis and Therapeutic Resistance. Int J Mol Sci. 2019;20(17):4242. doi:10.3390/ijms20174242
39. Nakamoto M, Hisaoka M. Clinicopathological Implications of Wingless/int1 (WNT) Signaling Pathway in Pancreatic Ductal Adenocarcinoma. J UOEH. 2016;38(1):1-8. doi:10.7888/juoeh.38.1
40. Morris JP, Cano DA, Sekine S, Wang SC, Hebrok M. β-catenin blocks Kras-dependent reprogramming of acini into pancreatic cancer precursor lesions in mice. J Clin Invest. 2010;120(2):508-520. doi:10.1172/JCI40045
41. Manegold P, Lai K, Wu Y, et al. Differentiation Therapy Targeting the β-Catenin/CBP Interaction in Pancreatic Cancer. Cancers (Basel). 2018;10(4):95. doi:10.3390/cancers10040095
42. Ercan G, Karlitepe A, Ozpolat B. Pancreatic Cancer Stem Cells and Therapeutic Approaches. Anticancer Res. 2017;37(6). doi:10.21873/anticanres.11628.
43. Zhang Y, Morris JP, Yan W, et al. Canonical Wnt Signaling Is Required for Pancreatic Carcinogenesis. Cancer Res. 2013;73(15):4909-4922. doi:10.1158/0008-5472.CAN-12-4384
44. Li H, Liu X, Jiang S, et al. WD repeat-containing protein 1 maintains β-Catenin activity to promote pancreatic cancer aggressiveness. Br J Cancer. 2020;123(6):1012-1023. doi:10.1038/s41416-020-0929-0
45. Jiang H, Li Q, He C, et al. Activation of the Wnt pathway through Wnt2 promotes metastasis in pancreatic cancer. Am J Cancer Res. 2014;4(5):537-544.

46. Bo H, Gao L, Chen Y, Zhang J, Zhu M. Upregulation of the expression of Wnt5a promotes the proliferation of pancreatic cancer cells in vitro and in a nude mouse model. Mol Med Rep. 2016;13(2):1163-1171. doi:10.3892/mmr.2015.4642

47. Liu X, Caffrey TC, Steele MM, et al. MUC1 regulates cyclin D1 gene expression through p120 catenin and β-catenin. Oncogenesis. 2014;3(6):e107-e107. doi:10.1038/oncsis.2014.19

48. Zhi X, Tao J, Xie K, et al. MUC4-induced nuclear translocation of β-catenin: A novel mechanism for growth, metastasis and angiogenesis in pancreatic cancer. Cancer Lett. 2014;346(1):104-113. doi:10.1016/j.canlet.2013.12.021

49. Chartier C, Raval J, Axelrod F, et al. Therapeutic Targeting of Tumor-Derived R-Spondin Attenuates β-Catenin Signaling and Tumorigenesis in Multiple Cancer Types. Cancer Res. 2016;76(3):713-723. doi:10.1158/0008-5472.CAN-15-0561

50. Fujioka S, Niu J, Schmidt C, et al. NF-κB and AP-1 Connection: Mechanism of NF-κB-Dependent Regulation of AP-1 Activity. Mol Cell Biol. 2004;24(17):7806-7819. doi:10.1128/MCB.24.17.7806-7819.2004

51. Liptay S, Weber CK, Ludwig L, Wagner M, Adler G, Schmid RM. Mitogenic and antiapoptotic role of constitutive NF-?B/Rel activity in pancreatic cancer. Int J Cancer. 2003;105(6):735-746. doi:10.1002/ijc.11081

52. Lawrence T. The Nuclear Factor NF- B Pathway in Inflammation. Cold Spring Harb Perspect Biol. 2009;1(6):a001651-a001651. doi:10.1101/cshperspect.a001651

53. Wang S, Zheng Y, Yang F, et al. The molecular biology of pancreatic adenocarcinoma: translational challenges and clinical perspectives. Signal Transduct Target Ther. 2021;6(1):249. doi:10.1038/s41392-021-00659-4

54. Turpin A, Neuzillet C, Colle E, et al. Therapeutic advances in metastatic pancreatic cancer: a focus on targeted therapies. Ther Adv Med Oncol. 2022;14:175883592211180. doi:10.1177/17588359221118019

55. Conroy T, Desseigne F, Ychou M, et al. FOLFIRINOX versus Gemcitabine for Metastatic Pancreatic Cancer. N Engl J Med. 2011;364(19):1817-1825. doi:10.1056/NEJMoa1011923

56. Von Hoff DD, Ervin T, Arena FP, et al. Increased Survival in Pancreatic Cancer with nab-Paclitaxel plus Gemcitabine. N Engl J Med. 2013;369(18):1691-1703. doi:10.1056/NEJMoa1304369

57. NCT03948763: A study of mRNA-5671/V941 as monotherapy and in combination with pembrolizumab (V941-001). https://clinicaltrials.gov/ct2/show/NCT03948763 (2019).
58. Hosein AN, Dougan SK, Aguirre AJ, Maitra A. Translational advances in pancreatic ductal adenocarcinoma therapy. Nat Cancer. 2022;3(3):272-286. doi:10.1038/s43018-022-00349-2
59. Aung KL, Fischer SE, Denroche RE, et al. Genomics-Driven Precision Medicine for Advanced Pancreatic Cancer: Early Results from the COMPASS Trial. Clin Cancer Res. 2018;24(6):1344-1354. doi:10.1158/1078-0432.CCR-17-2994
60. Canon J, Rex K, Saiki AY, et al. The clinical KRAS(G12C) inhibitor AMG 510 drives anti-tumour immunity. Nature. 2019;575(7781):217-223. doi:10.1038/s41586-019-1694-1
61. Anderson EM, Thomassian S, Gong J, Hendifar A, Osipov A. Advances in Pancreatic Ductal Adenocarcinoma Treatment. Cancers (Basel). 2021;13(21):5510. doi:10.3390/cancers13215510
62. Pishvaian MJ, Garrido-Laguna I, Liu S V., Multani PS, Chow-Maneval E, Rolfo C. Entrectinib in TRK and ROS1 Fusion-Positive Metastatic Pancreatic Cancer. JCO Precis Oncol. 2018;(2):1-7. doi:10.1200/PO.18.00039
63. Wennerberg K, Rossman KL, Der CJ. The Ras superfamily at a glance. J Cell Sci. 2005;118(5):843-846. doi:10.1242/jcs.01660
64. Paduch M, Jeleń F, Otlewski J. Structure of small G proteins and their regulators. Acta Biochim Pol. 2001;48(4):829-850. doi:10.18388/abp.2001_3850
65. Jančík S, Drábek J, Radzioch D, Hajdúch M. Clinical Relevance of KRAS in Human Cancers. J Biomed Biotechnol. 2010;2010:1-13. doi:10.1155/2010/150960
66. McGrath JP, Capon DJ, Smith DH, et al. Structure and organization of the human Ki-ras proto-oncogene and a related processed pseudogene. Nature. 1983;304(5926):501-506. doi:10.1038/304501a0
67. Hancock JF, Prior IA. Electron microscopic imaging of Ras signaling domains. Methods. 2005;37(2):165-172. doi:10.1016/j.ymeth.2005.05.018
68. Carta C, Pantaleoni F, Bocchinfuso G, et al. Germline Missense Mutations Affecting KRAS Isoform B Are Associated with a Severe Noonan Syndrome Phenotype. Am J Hum Genet. 2006;79(1):129-135. doi:10.1086/504394

69. Calin GA, Sevignani C, Dumitru CD, et al. Human microRNA genes are frequently located at fragile sites and genomic regions involved in cancers. Proc Natl Acad Sci. 2004;101(9):2999-3004. doi:10.1073/pnas.0307323101

70. Mann KM, Ying H, Juan J, Jenkins NA, Copeland NG. KRAS-related proteins in pancreatic cancer. Pharmacol Ther. 2016;168:29-42. doi:10.1016/j.pharmthera.2016.09.003

71. Eser S, Reiff N, Messer M, et al. Selective Requirement of PI3K/PDK1 Signaling for Kras Oncogene-Driven Pancreatic Cell Plasticity and Cancer. Cancer Cell. 2013;23(3):406-420. doi:10.1016/j.ccr.2013.01.023

72. Blasco RB, Francoz S, Santamaría D, et al. c-Raf, but Not B-Raf, Is Essential for Development of K-Ras Oncogene-Driven Non-Small Cell Lung Carcinoma. Cancer Cell. 2011;19(5):652-663. doi:10.1016/j.ccr.2011.04.002

73. Collisson EA, Trejo CL, Silva JM, et al. A Central Role for RAF→MEK→ERK Signaling in the Genesis of Pancreatic Ductal Adenocarcinoma. Cancer Discov. 2012;2(8):685-693. doi:10.1158/2159-8290.CD-11-0347

74. Maehama T, Dixon JE. The Tumor Suppressor, PTEN/MMAC1, Dephosphorylates the Lipid Second Messenger, Phosphatidylinositol 3,4,5-Trisphosphate. J Biol Chem. 1998;273(22):13375-13378. doi:10.1074/jbc.273.22.13375

75. Chardin P, Tavitian A. The ral gene: a new ras related gene isolated by the use of a synthetic probe. EMBO J. 1986;5(9):2203-2208. doi:10.1002/j.1460-2075.1986.tb04485.x

76. Lim K-H, Baines AT, Fiordalisi JJ, et al. Activation of RalA is critical for Ras-induced tumorigenesis of human cells. Cancer Cell. 2005;7(6):533-545. doi:10.1016/j.ccr.2005.04.030

77. Lim K-H, O'Hayer K, Adam SJ, et al. Divergent Roles for RalA and RalB in Malignant Growth of Human Pancreatic Carcinoma Cells. Curr Biol. 2006;16(24):2385-2394. doi:10.1016/j.cub.2006.10.023

78. Collins MA, Bednar F, Zhang Y, et al. Oncogenic Kras is required for both the initiation and maintenance of pancreatic cancer in mice. J Clin Invest. 2012;122(2):639-653. doi:10.1172/JCI59227

79. Ying H, Kimmelman AC, Lyssiotis CA, et al. Oncogenic Kras Maintains Pancreatic Tumors through Regulation of Anabolic Glucose Metabolism. Cell. 2012;149(3):656-670. doi:10.1016/j.cell.2012.01.058

80. Son J, Lyssiotis CA, Ying H, et al. Erratum: Corrigendum: Glutamine supports pancreatic cancer growth through a KRAS-regulated metabolic pathway. Nature. 2013;499(7459):504-504. doi:10.1038/nature12317

81. Weinstein IB, Joe AK. Mechanisms of Disease: oncogene addiction—a rationale for molecular targeting in cancer therapy. Nat Clin Pract Oncol. 2006;3(8):448-457. doi:10.1038/ncponc0558

82. Pagliarini R, Shao W, Sellers WR. Oncogene addiction: pathways of therapeutic response, resistance, and road maps toward a cure. EMBO Rep. 2015;16(3):280-296. doi:10.15252/embr.201439949

83. Pupo E, Avanzato D, Middonti E, Bussolino F, Lanzetti L. KRAS-Driven Metabolic Rewiring Reveals Novel Actionable Targets in Cancer. Front Oncol. 2019;9. doi:10.3389/fonc.2019.00848

84. Yan L, Raj P, Yao W, Ying H. Glucose Metabolism in Pancreatic Cancer. Cancers (Basel). 2019;11(10):1460. doi:10.3390/cancers11101460

85. Basso AD, Kirschmeier P, Bishop WR. Thematic review series: Lipid Posttranslational Modifications. Farnesyl transferase inhibitors. J Lipid Res. 2006;47(1):15-31. doi:10.1194/jlr.R500012-JLR200

86. Berndt N, Hamilton AD, Sebti SM. Targeting protein prenylation for cancer therapy. Nat Rev Cancer. 2011;11(11):775-791. doi:10.1038/nrc3151

87. Whyte DB, Kirschmeier P, Hockenberry TN, et al. K- and N-Ras Are Geranylgeranylated in Cells Treated with Farnesyl Protein Transferase Inhibitors. J Biol Chem. 1997;272(22):14459-14464. doi:10.1074/jbc.272.22.14459

88. Welsch ME, Kaplan A, Chambers JM, et al. Multivalent Small-Molecule Pan-RAS Inhibitors. Cell. 2017;168(5):878-889.e29. doi:10.1016/j.cell.2017.02.006

89. Patgiri A, Yadav KK, Arora PS, Bar-Sagi D. An orthosteric inhibitor of the Ras-Sos interaction. Nat Chem Biol. 2011;7(9):585-587. doi:10.1038/nchembio.612

90. Leshchiner ES, Parkhitko A, Bird GH, et al. Direct inhibition of oncogenic KRAS by hydrocarbon-stapled SOS1 helices. Proc Natl Acad Sci. 2015;112(6):1761-1766. doi:10.1073/pnas.1413185112

91. Mott HR, Owen D. Structures of Ras superfamily effector complexes: What have we learnt in two decades? Crit Rev Biochem Mol Biol. 2015;50(2):85-133. doi:10.3109/10409238.2014.999191

92. Hallin J, Engstrom LD, Hargis L, et al. The KRASG12C Inhibitor MRTX849 Provides Insight toward Therapeutic Susceptibility of KRAS-Mutant Cancers in Mouse Models and Patients. Cancer Discov. 2020;10(1):54-71. doi:10.1158/2159-8290.CD-19-1167

93. Bond MJ, Chu L, Nalawansha DA, Li K, Crews CM. Targeted Degradation of Oncogenic KRAS G12C by VHL-Recruiting PROTACs. ACS Cent Sci. 2020;6(8):1367-1375. doi:10.1021/acscentsci.0c00411

94. Sakamoto K, Lin B, Nunomura K, Izawa T, Nakagawa S. The K-Ras(G12D)-inhibitory peptide KS-58 suppresses growth of murine CT26 colorectal cancer cell-derived tumors. Sci Rep. 2022;12(1):8121. doi:10.1038/s41598-022-12401-3

95. Ferino A, Miglietta G, Picco R, Vogel S, Wengel J, Xodo LE. MicroRNA therapeutics: design of single-stranded miR-216b mimics to target KRAS in pancreatic cancer cells. RNA Biol. 2018;15(10):1273-1285. doi:10.1080/15476286.2018.1526536

96. Kumari S, Bugaut A, Huppert JL, Balasubramanian S. An RNA G-quadruplex in the 5′ UTR of the NRAS proto-oncogene modulates translation. Nat Chem Biol. 2007;3(4):218-221. doi:10.1038/nchembio864

97. Bugaut A, Balasubramanian S. 5′-UTR RNA G-quadruplexes: translation regulation and targeting. Nucleic Acids Res. 2012;40(11):4727-4741. doi:10.1093/nar/gks068

98. Miglietta G, Cogoi S, Marinello J, et al. RNA G-Quadruplexes in Kirsten Ras (KRAS) Oncogene as Targets for Small Molecules Inhibiting Translation. J Med Chem. 2017;60(23):9448-9461. doi:10.1021/acs.jmedchem.7b00622

99. Ferino A, Nicoletto G, D'Este F, et al. Photodynamic Therapy for ras -Driven Cancers: Targeting G-Quadruplex RNA Structures with Bifunctional Alkyl-Modified Porphyrins. J Med Chem. 2020;63(3):1245-1260. doi:10.1021/acs.jmedchem.9b01577

100. Jordano J, Perucho M. Chromatin structure of the promoter region of the human c-K-ras gene. Nucleic Acids Res. 1986;14(18):7361-7378. doi:10.1093/nar/14.18.7361

101. Jordano J, Perucho M. Initial characterization of a potential transcriptional enhancer for the human c-K-ras gene. Oncogene. 1988;2(4):359-366. http://www.ncbi.nlm.nih.gov/pubmed/3283654.

102. Cogoi S, Paramasivam M, Spolaore B, Xodo LE. Structural polymorphism within a regulatory element of the human KRAS promoter: formation of G4-DNA recognized by nuclear proteins. Nucleic Acids Res. 2008;36(11):3765-3780. doi:10.1093/nar/gkn120

103. Cogoi S, Zorzet S, Rapozzi V, Géci I, Pedersen EB, Xodo LE. MAZ-binding G4-decoy with locked nucleic acid and twisted intercalating nucleic acid modifications suppresses KRAS in pancreatic cancer cells and delays tumor growth in mice. Nucleic Acids Res. 2013;41(7):4049-4064. doi:10.1093/nar/gkt127

104. Bochman ML, Paeschke K, Zakian VA. DNA secondary structures: stability and function of G-quadruplex structures. Nat Rev Genet. 2012;13(11):770-780. doi:10.1038/nrg3296

105. Gellert M, Lipsett MN, Davies DR. HELIX FORMATION BY GUANYLIC ACID. Proc Natl Acad Sci. 1962;48(12):2013-2018. doi:10.1073/pnas.48.12.2013

106. Majee P, Kumar Mishra S, Pandya N, et al. Identification and characterization of two conserved G-quadruplex forming motifs in the Nipah virus genome and their interaction with G-quadruplex specific ligands. Sci Rep. 2020;10(1):1477. doi:10.1038/s41598-020-58406-8

107. Burge S, Parkinson GN, Hazel P, Todd AK, Neidle S. Quadruplex DNA: sequence, topology and structure. Nucleic Acids Res. 2006;34(19):5402-5415. doi:10.1093/nar/gkl655

108. Hazel P. Predictive modelling of topology and loop variations in dimeric DNA quadruplex structures. Nucleic Acids Res. 2006;34(7):2117-2127. doi:10.1093/nar/gkl182

109. Patel DJ, Phan AT, Kuryavyi V. Human telomere, oncogenic promoter and 5'-UTR G-quadruplexes: diverse higher order DNA and RNA targets for cancer therapeutics. Nucleic Acids Res. 2007;35(22):7429-7455. doi:10.1093/nar/gkm711

110. Huppert JL, Balasubramanian S. G-quadruplexes in promoters throughout the human genome. Nucleic Acids Res. 2007;35(2):406-413. doi:10.1093/nar/gkl1057

111. Yadav P, Harcy V, Argueso JL, Dominska M, Jinks-Robertson S, Kim N. Topoisomerase I Plays a Critical Role in Suppressing Genome Instability at a Highly Transcribed G-Quadruplex-Forming Sequence. Hanawalt PC, ed. PLoS Genet. 2014;10(12):e1004839. doi:10.1371/journal.pgen.1004839

112. Biffi G, Tannahill D, McCafferty J, Balasubramanian S. Quantitative visualization of DNA G-quadruplex structures in human cells. Nat Chem. 2013;5(3):182-186. doi:10.1038/nchem.1548

113. Chambers VS, Marsico G, Boutell JM, Di Antonio M, Smith GP, Balasubramanian S. High-throughput sequencing of DNA G-quadruplex structures in the human genome. Nat Biotechnol. 2015;33(8):877-881. doi:10.1038/nbt.3295

114. Hänsel-Hertsch R, Beraldi D, Lensing S V, et al. G-quadruplex structures mark human regulatory chromatin. Nat Genet. 2016;48(10):1267-1272. doi:10.1038/ng.3662

115. Cogoi S, Xodo LE. G-quadruplex formation within the promoter of the KRAS proto-oncogene and its effect on transcription. Nucleic Acids Res. 2006;34(9):2536-2549. doi:10.1093/nar/gkl286

116. Marquevielle J, Robert C, Lagrabette O, et al. Structure of two G-quadruplexes in equilibrium in the KRAS promoter. Nucleic Acids Res. 2020;48(16):9336-9345. doi:10.1093/nar/gkaa387

117. Eddy J, Vallur AC, Varma S, et al. G4 motifs correlate with promoter-proximal transcriptional pausing in human genes. Nucleic Acids Res. 2011;39(12):4975-4983. doi:10.1093/nar/gkr079

118. Kim N. The Interplay between G-quadruplex and Transcription. Curr Med Chem. 2019;26(16):2898-2917. doi:10.2174/0929867325666171229132619

119. Zheng K, Xiao S, Liu J, Zhang J, Hao Y, Tan Z. Co-transcriptional formation of DNA:RNA hybrid G-quadruplex and potential function as constitutional cis element for transcription control. Nucleic Acids Res. 2013;41(10):5533-5541. doi:10.1093/nar/gkt264

120. Belotserkovskii BP, Soo Shin JH, Hanawalt PC. Strong transcription blockage mediated by R-loop formation within a G-rich homopurine–homopyrimidine sequence localized in the vicinity of the promoter. Nucleic Acids Res. 2017;45(11):6589-6599. doi:10.1093/nar/gkx403

121. Cogoi S, Ferino A, Miglietta G, Pedersen EB, Xodo LE. The regulatory G4 motif of the Kirsten ras (KRAS) gene is sensitive to guanine oxidation: implications on transcription. Nucleic Acids Res. 2018;46(2):661-676. doi:10.1093/nar/gkx1142

122. Todd AK, Neidle S. The relationship of potential G-quadruplex sequences in cis-upstream regions of the human genome to SP1-binding elements. Nucleic Acids Res. 2008;36(8):2700-2704. doi:10.1093/nar/gkn078

123. Spiegel J, Cuesta SM, Adhikari S, Hänsel-Hertsch R, Tannahill D, Balasubramanian S. G-quadruplexes are transcription factor binding hubs in human chromatin. Genome Biol. 2021;22(1):117. doi:10.1186/s13059-021-02324-z

124. Edwards AD, Marecki JC, Byrd AK, Gao J, Raney KD. G-Quadruplex loops regulate PARP-1 enzymatic activation. Nucleic Acids Res. 2021;49(1):416-431. doi:10.1093/nar/gkaa1172

125. Cinque G, Ferino A, Pedersen EB, Xodo LE. Role of Poly [ADP-ribose] Polymerase 1 in Activating the Kirsten ras (KRAS) Gene in Response to Oxidative Stress. Int J Mol Sci. 2020;21(17):6237. doi:10.3390/ijms21176237

126. Pullman JM, Martin TE. Reconstitution of nucleoprotein complexes with mammalian heterogeneous nuclear ribonucleoprotein (hnRNP) core proteins. J Cell Biol. 1983;97(1):99-111. doi:10.1083/jcb.97.1.99

127. Krecic AM, Swanson MS. hnRNP complexes: composition, structure, and function. Curr Opin Cell Biol. 1999;11(3):363-371. doi:10.1016/S0955-0674(99)80051-9

128. Nadler SG, Merrill BM, Roberts WJ, et al. Interactions of the A1 heterogeneous nuclear ribonucleoprotein and its proteolytic derivative, UP1, with RNA and DNA: Evidence for multiple RNA binding domains and salt-dependent binding mode transitions. Biochemistry. 1991;30(11):2968-2976. doi:10.1021/bi00225a034

129. He Y, Smith R. Nuclear functions of heterogeneous nuclear ribonucleoproteins A/B. Cell Mol Life Sci. 2009;66(7):1239-1256. doi:10.1007/s00018-008-8532-1

130. Kamma H, Portman DS, Dreyfuss G. Cell Type-Specific Expression of hnRNP Proteins. Exp Cell Res. 1995;221(1):187-196. doi:10.1006/excr.1995.1366

131. He Y, Smith R. Nuclear functions of heterogeneous nuclear ribonucleoproteins A/B. Cell Mol Life Sci. 2009;66(7):1239-1256. doi:10.1007/s00018-008-8532-1

132. Görlach M, Wittekind M, Beckman RA, Mueller L, Dreyfuss G. Interaction of the RNA-binding domain of the hnRNP C proteins with RNA. EMBO J. 1992;11(9):3289-3295. doi:10.1002/j.1460-2075.1992.tb05407.x

133. Shamoo Y, Krueger U, Rice LM, Williams KR, Steitz TA. Crystal structure of the two RNA binding domains of human hnRNP A1 at 1.75 Å resolution. Nat Struct Biol. 1997;4(3):215-222. doi:10.1038/nsb0397-215

134. Clarke JP, Thibault PA, Salapa HE, Levin MC. A Comprehensive Analysis of the Role of hnRNP A1 Function and Dysfunction in the Pathogenesis of Neurodegenerative Disease. Front Mol Biosci. 2021;8. doi:10.3389/fmolb.2021.659610

135. Hay DC, Kemp GD, Dargemont C, Hay RT. Interaction between hnRNPA1 and IκBα Is Required for Maximal Activation of NF-κB-Dependent Transcription. Mol Cell Biol. 2001;21(10):3482-3490. doi:10.1128/MCB.21.10.3482-3490.2001

136. Das S, Ward SV, Markle D, Samuel CE. DNA Damage-binding Proteins and Heterogeneous Nuclear Ribonucleoprotein A1 Function as Constitutive KCS Element Components of the Interferon-inducible RNA-dependent Protein Kinase Promoter. J Biol Chem. 2004;279(8):7313-7321. doi:10.1074/jbc.M312585200

137. Paramasivam M, Membrino A, Cogoi S, Fukuda H, Nakagama H, Xodo LE. Protein hnRNP A1 and its derivative Up1 unfold quadruplex DNA in the human KRAS promoter: implications for transcription. Nucleic Acids Res. 2009;37(9):2841-2853. doi:10.1093/nar/gkp138

138. Ghosh M, Singh M. RGG-box in hnRNPA1 specifically recognizes the telomere G-quadruplex DNA and enhances the G-quadruplex unfolding ability of UP1 domain. Nucleic Acids Res. 2018;46(19):10246-10261. doi:10.1093/nar/gky854

139. Yang H, Zhu R, Zhao X, et al. Sirtuin-mediated deacetylation of hnRNP A1 suppresses glycolysis and growth in hepatocellular carcinoma. Oncogene. 2019;38(25):4915-4931. doi:10.1038/s41388-019-0764-z

140. Dolmans DEJGJ, Fukumura D, Jain RK. Photodynamic therapy for cancer. Nat Rev Cancer. 2003;3(5):380-387. doi:10.1038/nrc1071

141. Lee C-N, Hsu R, Chen H, Wong T-W. Daylight Photodynamic Therapy: An Update. Molecules. 2020;25(21):5195. doi:10.3390/molecules25215195

142. Correia JH, Rodrigues JA, Pimenta S, Dong T, Yang Z. Photodynamic Therapy Review: Principles, Photosensitizers, Applications, and Future Directions. Pharmaceutics. 2021;13(9):1332. doi:10.3390/pharmaceutics13091332

143. Hua S, Wu SY. The use of lipid-based nanocarriers for targeted pain therapies. Front Pharmacol. 2013;4. doi:10.3389/fphar.2013.00143

144. Allen TM, Cullis PR. Liposomal drug delivery systems: From concept to clinical applications. Adv Drug Deliv Rev. 2013;65(1):36-48. doi:10.1016/j.addr.2012.09.037

145. Pattni BS, Chupin V V., Torchilin VP. New Developments in Liposomal Drug Delivery. Chem Rev. 2015;115(19):10938-10966. doi:10.1021/acs.chemrev.5b00046
146. Akbarzadeh A, Rezaei-Sadabady R, Davaran S, et al. Liposome: classification, preparation, and applications. Nanoscale Res Lett. 2013;8(1):102. doi:10.1186/1556-276X-8-102
147. Oku N, Doi K, Namba Y, Okada S. Therapeutic effect of adriamycin encapsulated in long-circulating liposomes on meth-a-sarcoma-bearing mice. Int J Cancer. 1994;58(3):415-419. doi:10.1002/ijc.2910580318
148. Golombek SK, May J-N, Theek B, et al. Tumor targeting via EPR: Strategies to enhance patient responses. Adv Drug Deliv Rev. 2018;130:17-38. doi:10.1016/j.addr.2018.07.007
149. Kuimova MK, Yahioglu G, Ogilby PR. Singlet Oxygen in a Cell: Spatially Dependent Lifetimes and Quenching Rate Constants. J Am Chem Soc. 2009;131(1):332-340. doi:10.1021/ja807484b
150. Liou G-Y, Storz P. Reactive oxygen species in cancer. Free Radic Res. 2010;44(5):479-496. doi:10.3109/10715761003667554
151. Bedard K, Krause K-H. The NOX Family of ROS-Generating NADPH Oxidases: Physiology and Pathophysiology. Physiol Rev. 2007;87(1):245-313. doi:10.1152/physrev.00044.2005
152. Zhang L, Li J, Zong L, et al. Reactive Oxygen Species and Targeted Therapy for Pancreatic Cancer. Oxid Med Cell Longev. 2016;2016:1-9. doi:10.1155/2016/1616781
153. Sosa V, Moliné T, Somoza R, Paciucci R, Kondoh H, LLeonart ME. Oxidative stress and cancer: An overview. Ageing Res Rev. 2013;12(1):376-390. doi:10.1016/j.arr.2012.10.004
154. Martinez-Useros J, Li W, Cabeza-Morales M, Garcia-Foncillas J. Oxidative Stress: A New Target for Pancreatic Cancer Prognosis and Treatment. J Clin Med. 2017;6(3):29. doi:10.3390/jcm6030029
155. van Zandwijk N. EUROSCAN, a Randomized Trial of Vitamin A and N-Acetylcysteine in Patients With Head and Neck Cancer or Lung Cancer. J Natl Cancer Inst. 2000;92(12):977-986. doi:10.1093/jnci/92.12.977

156. Vurusaner B, Poli G, Basaga H. Tumor suppressor genes and ROS: complex networks of interactions. Free Radic Biol Med. 2012;52(1):7-18. doi:10.1016/j.freeradbiomed.2011.09.035

157. Cichon MA, Radisky DC. ROS-induced epithelial-mesenchymal transition in mammary epithelial cells is mediated by NF-κB-dependent activation of Snail. Oncotarget. 2014;5(9):2827-2838. doi:10.18632/oncotarget.1940

158. Morgan MJ, Liu Z. Crosstalk of reactive oxygen species and NF-κB signaling. Cell Res. 2011;21(1):103-115. doi:10.1038/cr.2010.178

159. Son Y, Kim S, Chung H-T, Pae H-O. Reactive Oxygen Species in the Activation of MAP Kinases. In: ; 2013:27-48. doi:10.1016/B978-0-12-405881-1.00002-1

160. Durand N, Storz P. Targeting reactive oxygen species in development and progression of pancreatic cancer. Expert Rev Anticancer Ther. 2017;17(1):19-31. doi:10.1080/14737140.2017.1261017

161. Lister A, Nedjadi T, Kitteringham NR, et al. Nrf2 is overexpressed in pancreatic cancer: implications for cell proliferation and therapy. Mol Cancer. 2011;10(1):37. doi:10.1186/1476-4598-10-37

162. Buelna-Chontal M, Zazueta C. Redox activation of Nrf2 & NF-κB: A double end sword? Cell Signal. 2013;25(12):2548-2557. doi:10.1016/j.cellsig.2013.08.007

163. Moon EJ, Giaccia A. Dual roles of NRF2 in tumor prevention and progression: Possible implications in cancer treatment. Free Radic Biol Med. 2015;79:292-299. doi:10.1016/j.freeradbiomed.2014.11.009

164. Hayes AJ, Skouras C, Haugk B, Charnley RM. Keap1–Nrf2 signalling in pancreatic cancer. Int J Biochem Cell Biol. 2015;65:288-299. doi:10.1016/j.biocel.2015.06.017

165. Arlt A, Schäfer H, Kalthoff H. The 'N-factors' in pancreatic cancer: functional relevance of NF-κB, NFAT and Nrf2 in pancreatic cancer. Oncogenesis. 2012;1(11):e35-e35. doi:10.1038/oncsis.2012.35

166. Lau A, Villeneuve N, Sun Z, Wong P, Zhang D. Dual roles of Nrf2 in cancer. Pharmacol Res. 2008;58(5-6):262-270. doi:10.1016/j.phrs.2008.09.003

167. Purohit V, Wang L, Yang H, et al. ATDC binds to KEAP1 to drive NRF2-mediated tumorigenesis and chemoresistance in pancreatic cancer. Genes Dev. 2021;35(3-4):218-233. doi:10.1101/gad.344184.120

168. Wang X-J, Sun Z, Villeneuve NF, et al. Nrf2 enhances resistance of cancer cells to chemotherapeutic drugs, the dark side of Nrf2. Carcinogenesis. 2008;29(6):1235-1243. doi:10.1093/carcin/bgn095

169. Jagust P, Alcalá S, Jr BS, Heeschen C, Sancho P. Glutathione metabolism is essential for self-renewal and chemoresistance of pancreatic cancer stem cells. World J Stem Cells. 2020;12(11):1410-1428. doi:10.4252/wjsc.v12.i11.1410

170. Ferino A, Rapozzi V, Xodo LE. The ROS-KRAS-Nrf2 axis in the control of the redox homeostasis and the intersection with survival-apoptosis pathways: Implications for photodynamic therapy. J Photochem Photobiol B Biol. 2020;202:111672. doi:10.1016/j.jphotobiol.2019.111672

171. Jaramillo MC, Zhang DD. The emerging role of the Nrf2–Keap1 signaling pathway in cancer. Genes Dev. 2013;27(20):2179-2191. doi:10.1101/gad.225680.113

172. Taguchi K, Yamamoto M. The KEAP1–NRF2 System in Cancer. Front Oncol. 2017;7. doi:10.3389/fonc.2017.00085

173. Canning P, Sorrell FJ, Bullock AN. Structural basis of Keap1 interactions with Nrf2. Free Radic Biol Med. 2015;88:101-107. doi:10.1016/j.freeradbiomed.2015.05.034

174. McMahon M, Thomas N, Itoh K, Yamamoto M, Hayes JD. Redox-regulated Turnover of Nrf2 Is Determined by at Least Two Separate Protein Domains, the Redox-sensitive Neh2 Degron and the Redox-insensitive Neh6 Degron. J Biol Chem. 2004;279(30):31556-31567. doi:10.1074/jbc.M403061200

175. Wang H, Liu K, Geng M, et al. RXRα Inhibits the NRF2-ARE Signaling Pathway through a Direct Interaction with the Neh7 Domain of NRF2. Cancer Res. 2013;73(10):3097-3108. doi:10.1158/0008-5472.CAN-12-3386

176. He F, Ru X, Wen T. NRF2, a Transcription Factor for Stress Response and Beyond. Int J Mol Sci. 2020;21(13):4777. doi:10.3390/ijms21134777

177. Kansanen E, Kivelä AM, Levonen A-L. Regulation of Nrf2-dependent gene expression by 15-deoxy-Δ12,14-prostaglandin J2. Free Radic Biol Med. 2009;47(9):1310-1317. doi:10.1016/j.freeradbiomed.2009.06.030

178. Ogura T, Tong KI, Mio K, et al. Keap1 is a forked-stem dimer structure with two large spheres enclosing the intervening, double glycine repeat, and C-terminal domains. Proc Natl Acad Sci. 2010;107(7):2842-2847. doi:10.1073/pnas.0914036107

179. Zipper LM, Mulcahy RT. The Keap1 BTB/POZ Dimerization Function Is Required to Sequester Nrf2 in Cytoplasm. J Biol Chem. 2002;277(39):36544-36552. doi:10.1074/jbc.M206530200

180. Hayes JD, McMahon M. NRF2 and KEAP1 mutations: permanent activation of an adaptive response in cancer. Trends Biochem Sci. 2009;34(4):176-188. doi:10.1016/j.tibs.2008.12.008

181. Komatsu M, Kurokawa H, Waguri S, et al. The selective autophagy substrate p62 activates the stress responsive transcription factor Nrf2 through inactivation of Keap1. Nat Cell Biol. 2010;12(3):213-223. doi:10.1038/ncb2021

182. Taguchi K, Motohashi H, Yamamoto M. Molecular mechanisms of the Keap1-Nrf2 pathway in stress response and cancer evolution. Genes to Cells. 2011;16(2):123-140. doi:10.1111/j.1365-2443.2010.01473.x

183. Um H-C, Jang J-H, Kim D-H, Lee C, Surh Y-J. Nitric oxide activates Nrf2 through S-nitrosylation of Keap1 in PC12 cells. Nitric Oxide. 2011;25(2):161-168. doi:10.1016/j.niox.2011.06.001

184. Yang G, Zhao K, Ju Y, et al. Hydrogen Sulfide Protects Against Cellular Senescence via S -Sulfhydration of Keap1 and Activation of Nrf2. Antioxid Redox Signal. 2013;18(15):1906-1919. doi:10.1089/ars.2012.4645

185. Kansanen E, Jyrkkänen H-K, Levonen A-L. Activation of stress signaling pathways by electrophilic oxidized and nitrated lipids. Free Radic Biol Med. 2012;52(6):973-982. doi:10.1016/j.freeradbiomed.2011.11.038

186. Kim J-H, Yu S, Chen JD, Kong AN. The nuclear cofactor RAC3/AIB1/SRC-3 enhances Nrf2 signaling by interacting with transactivation domains. Oncogene. 2013;32(4):514-527. doi:10.1038/onc.2012.59

187. Chowdhry S, Zhang Y, McMahon M, Sutherland C, Cuadrado A, Hayes JD. Nrf2 is controlled by two distinct β-TrCP recognition motifs in its Neh6 domain, one of which can be modulated by GSK-3 activity. Oncogene. 2013;32(32):3765-3781. doi:10.1038/onc.2012.388

188. Rada P, Rojo AI, Chowdhry S, McMahon M, Hayes JD, Cuadrado A. SCF/β-TrCP Promotes Glycogen Synthase Kinase 3-Dependent Degradation of the Nrf2 Transcription Factor in a Keap1-Independent Manner. Mol Cell Biol. 2011;31(6):1121-1133. doi:10.1128/MCB.01204-10

189. Hayes JD, Dinkova-Kostova AT. The Nrf2 regulatory network provides an interface between redox and intermediary metabolism. Trends Biochem Sci. 2014;39(4):199-218. doi:10.1016/j.tibs.2014.02.002

190. Wu KC, Cui JY, Klaassen CD. Effect of Graded Nrf2 Activation on Phase-I and -II Drug Metabolizing Enzymes and Transporters in Mouse Liver. Rodrigues-Lima F, ed. PLoS One. 2012;7(7):e39006. doi:10.1371/journal.pone.0039006

191. Zhan X, Li J, Zhou T. Targeting Nrf2-Mediated Oxidative Stress Response Signaling Pathways as New Therapeutic Strategy for Pituitary Adenomas. Front Pharmacol. 2021;12. doi:10.3389/fphar.2021.565748

192. Rojo de la Vega M, Chapman E, Zhang DD. NRF2 and the Hallmarks of Cancer. Cancer Cell. 2018;34(1):21-43. doi:10.1016/j.ccell.2018.03.022

193. Mukaigasa K, Tsujita T, Nguyen VT, et al. Nrf2 activation attenuates genetic endoplasmic reticulum stress induced by a mutation in the phosphomannomutase 2 gene in zebrafish. Proc Natl Acad Sci. 2018;115(11):2758-2763. doi:10.1073/pnas.1714056115

194. Glover-Cutter KM, Lin S, Blackwell TK. Integration of the Unfolded Protein and Oxidative Stress Responses through SKN-1/Nrf. Garsin DA, ed. PLoS Genet. 2013;9(9):e1003701. doi:10.1371/journal.pgen.1003701

195. Kwak M-K, Wakabayashi N, Greenlaw JL, Yamamoto M, Kensler TW. Antioxidants Enhance Mammalian Proteasome Expression through the Keap1-Nrf2 Signaling Pathway. Mol Cell Biol. 2003;23(23):8786-8794. doi:10.1128/MCB.23.23.8786-8794.2003

196. Li B, Fu J, Chen P, et al. The Nuclear Factor (Erythroid-derived 2)-like 2 and Proteasome Maturation Protein Axis Mediate Bortezomib Resistance in Multiple Myeloma. J Biol Chem. 2015;290(50):29854-29868. doi:10.1074/jbc.M115.664953

197. Clarke R, Cook KL, Hu R, et al. Endoplasmic Reticulum Stress, the Unfolded Protein Response, Autophagy, and the Integrated Regulation of Breast Cancer Cell Fate. Cancer Res. 2012;72(6):1321-1331. doi:10.1158/0008-5472.CAN-11-3213

198. Pajares M, Jiménez-Moreno N, García-Yagüe ÁJ, et al. Transcription factor NFE2L2/NRF2 is a regulator of macroautophagy genes. Autophagy. 2016;12(10):1902-1916. doi:10.1080/15548627.2016.1208889

199. Holmström KM, Baird L, Zhang Y, et al. Nrf2 impacts cellular bioenergetics by controlling substrate availability for mitochondrial respiration. Biol Open. 2013;2(8):761-770. doi:10.1242/bio.20134853

200. Ludtmann MHR, Angelova PR, Zhang Y, Abramov AY, Dinkova-Kostova AT. Nrf2 affects the efficiency of mitochondrial fatty acid oxidation. Biochem J. 2014;457(3):415-424. doi:10.1042/BJ20130863

201. Holmström KM, Kostov R V., Dinkova-Kostova AT. The multifaceted role of Nrf2 in mitochondrial function. Curr Opin Toxicol. 2016;1:80-91. doi:10.1016/j.cotox.2016.10.002

202. Sazanov LA. A giant molecular proton pump: structure and mechanism of respiratory complex I. Nat Rev Mol Cell Biol. 2015;16(6):375-388. doi:10.1038/nrm3997

203. Piantadosi CA, Carraway MS, Babiker A, Suliman HB. Heme Oxygenase-1 Regulates Cardiac Mitochondrial Biogenesis via Nrf2-Mediated Transcriptional Control of Nuclear Respiratory Factor-1. Circ Res. 2008;103(11):1232-1240. doi:10.1161/01.RES.0000338597.71702.ad

204. Gureev AP, Sadovnikova IS, Starkov NN, Starkov AA, Popov VN. p62-Nrf2-p62 Mitophagy Regulatory Loop as a Target for Preventive Therapy of Neurodegenerative Diseases. Brain Sci. 2020;10(11):847. doi:10.3390/brainsci10110847

205. He F, Antonucci L, Karin M. NRF2 as a regulator of cell metabolism and inflammation in cancer. Carcinogenesis. 2020;41(4):405-416. doi:10.1093/carcin/bgaa039

206. Fu J, Xiong Z, Huang C, et al. Hyperactivity of the transcription factor Nrf2 causes metabolic reprogramming in mouse esophagus. J Biol Chem. 2019;294(1):327-340. doi:10.1074/jbc.RA118.005963

207. Zahra K, Dey T, Ashish, Mishra SP, Pandey U. Pyruvate Kinase M2 and Cancer: The Role of PKM2 in Promoting Tumorigenesis. Front Oncol. 2020;10. doi:10.3389/fonc.2020.00159

208. Yates MS, Tran QT, Dolan PM, et al. Genetic versus chemoprotective activation of Nrf2 signaling: overlapping yet distinct gene expression profiles between Keap1 knockout and triterpenoid-treated mice. Carcinogenesis. 2009;30(6):1024-1031. doi:10.1093/carcin/bgp100

209. Uruno A, Furusawa Y, Yagishita Y, et al. The Keap1-Nrf2 System Prevents Onset of Diabetes Mellitus. Mol Cell Biol. 2013;33(15):2996-3010. doi:10.1128/MCB.00225-13

210. He F, Antonucci L, Yamachika S, et al. NRF2 activates growth factor genes and downstream AKT signaling to induce mouse and human hepatomegaly. J Hepatol. 2020;72(6):1182-1195. doi:10.1016/j.jhep.2020.01.023

211. Mitsuishi Y, Taguchi K, Kawatani Y, et al. Nrf2 Redirects Glucose and Glutamine into Anabolic Pathways in Metabolic Reprogramming. Cancer Cell. 2012;22(1):66-79. doi:10.1016/j.ccr.2012.05.016

212. Uruno A, Yagishita Y, Katsuoka F, et al. Nrf2-Mediated Regulation of Skeletal Muscle Glycogen Metabolism. Mol Cell Biol. 2016;36(11):1655-1672. doi:10.1128/MCB.01095-15

213. Singh A, Happel C, Manna SK, et al. Transcription factor NRF2 regulates miR-1 and miR-206 to drive tumorigenesis. J Clin Invest. 2013;123(7):2921-2934. doi:10.1172/JCI66353

214. Chorley BN, Campbell MR, Wang X, et al. Identification of novel NRF2-regulated genes by ChIP-Seq: influence on retinoid X receptor alpha. Nucleic Acids Res. 2012;40(15):7416-7429. doi:10.1093/nar/gks409

215. Sunami Y, Rebelo A, Kleeff J. Lipid Metabolism and Lipid Droplets in Pancreatic Cancer and Stellate Cells. Cancers (Basel). 2017;10(1):3. doi:10.3390/cancers10010003

216. Daemen A, Peterson D, Sahu N, et al. Metabolite profiling stratifies pancreatic ductal adenocarcinomas into subtypes with distinct sensitivities to metabolic inhibitors. Proc Natl Acad Sci. 2015;112(32). doi:10.1073/pnas.1501605112

217. Karasinska JM, Topham JT, Kalloger SE, et al. Altered Gene Expression along the Glycolysis–Cholesterol Synthesis Axis Is Associated with Outcome in Pancreatic Cancer. Clin Cancer Res. 2020;26(1):135-146. doi:10.1158/1078-0432.CCR-19-1543

218. Zhao L, Zhao H, Yan H. Gene expression profiling of 1200 pancreatic ductal adenocarcinoma reveals novel subtypes. BMC Cancer. 2018;18(1):603. doi:10.1186/s12885-018-4546-8

219. Rozeveld CN, Johnson KM, Zhang L, Razidlo GL. KRAS Controls Pancreatic Cancer Cell Lipid Metabolism and Invasive Potential through the Lipase HSL. Cancer Res. 2020;80(22):4932-4945. doi:10.1158/0008-5472.CAN-20-1255

220. Yabushita S, Fukamachi K, Tanaka H, et al. Metabolomic and transcriptomic profiling of human K- ras oncogene transgenic rats with pancreatic ductal adenocarcinomas. Carcinogenesis. 2013;34(6):1251-1259. doi:10.1093/carcin/bgt053

221. Tadros S, Shukla SK, King RJ, et al. De Novo Lipid Synthesis Facilitates Gemcitabine Resistance through Endoplasmic Reticulum Stress in Pancreatic Cancer. Cancer Res. 2017;77(20):5503-5517. doi:10.1158/0008-5472.CAN-16-3062
222. Hatzivassiliou G, Zhao F, Bauer DE, et al. ATP citrate lyase inhibition can suppress tumor cell growth. Cancer Cell. 2005;8(4):311-321. doi:10.1016/j.ccr.2005.09.008
223. Kamphorst JJ, Cross JR, Fan J, et al. Hypoxic and Ras-transformed cells support growth by scavenging unsaturated fatty acids from lysophospholipids. Proc Natl Acad Sci. 2013;110(22):8882-8887. doi:10.1073/pnas.1307237110
224. Guillaumond F, Bidaut G, Ouaissi M, et al. Cholesterol uptake disruption, in association with chemotherapy, is a promising combined metabolic therapy for pancreatic adenocarcinoma. Proc Natl Acad Sci. 2015;112(8):2473-2478. doi:10.1073/pnas.1421601112
225. Moffitt RA, Marayati R, Flate EL, et al. Virtual microdissection identifies distinct tumor- and stroma-specific subtypes of pancreatic ductal adenocarcinoma. Nat Genet. 2015;47(10):1168-1178. doi:10.1038/ng.3398
226. Gabitova-Cornell L, Surumbayeva A, Peri S, et al. Cholesterol Pathway Inhibition Induces TGF-β Signaling to Promote Basal Differentiation in Pancreatic Cancer. Cancer Cell. 2020;38(4):567-583.e11. doi:10.1016/j.ccell.2020.08.015
227. Kimmelman AC. Metabolic Dependencies in RAS -Driven Cancers. Clin Cancer Res. 2015;21(8):1828-1834. doi:10.1158/1078-0432.CCR-14-2425
228. Kaira K, Sunose Y, Arakawa K, et al. Prognostic significance of L-type amino-acid transporter 1 expression in surgically resected pancreatic cancer. Br J Cancer. 2012;107(4):632-638. doi:10.1038/bjc.2012.310
229. Coothankandaswamy V, Cao S, Xu Y, et al. Amino acid transporter SLC6A14 is a novel and effective drug target for pancreatic cancer. Br J Pharmacol. 2016;173(23):3292-3306. doi:10.1111/bph.13616
230. Wise DR, Thompson CB. Glutamine addiction: a new therapeutic target in cancer. Trends Biochem Sci. 2010;35(8):427-433. doi:10.1016/j.tibs.2010.05.003
231. Hensley CT, Wasti AT, DeBerardinis RJ. Glutamine and cancer: cell biology, physiology, and clinical opportunities. J Clin Invest. 2013;123(9):3678-3684. doi:10.1172/JCI69600

232. Guillaumond F, Leca J, Olivares O, et al. Strengthened glycolysis under hypoxia supports tumor symbiosis and hexosamine biosynthesis in pancreatic adenocarcinoma. Proc Natl Acad Sci. 2013;110(10):3919-3924. doi:10.1073/pnas.1219555110

233. Pupo E, Avanzato D, Middonti E, Bussolino F, Lanzetti L. KRAS-Driven Metabolic Rewiring Reveals Novel Actionable Targets in Cancer. Front Oncol. 2019;9. doi:10.3389/fonc.2019.00848

234. Son J, Lyssiotis CA, Ying H, et al. Glutamine supports pancreatic cancer growth through a KRAS-regulated metabolic pathway. Nature. 2013;496(7443):101-105. doi:10.1038/nature12040

235. Abrego J, Gunda V, Vernucci E, et al. GOT1-mediated anaplerotic glutamine metabolism regulates chronic acidosis stress in pancreatic cancer cells. Cancer Lett. 2017;400:37-46. doi:10.1016/j.canlet.2017.04.029

236. Pastore A, Piemonte F, Locatelli M, et al. Determination of Blood Total, Reduced, and Oxidized Glutathione in Pediatric Subjects. Clin Chem. 2001;47(8):1467-1469. doi:10.1093/clinchem/47.8.1467

237. Wang VM-Y, Ferreira RMM, Almagro J, et al. CD9 identifies pancreatic cancer stem cells and modulates glutamine metabolism to fuel tumour growth. Nat Cell Biol. 2019;21(11):1425-1435. doi:10.1038/s41556-019-0407-1

238. Commisso C, Davidson SM, Soydaner-Azeloglu RG, et al. Macropinocytosis of protein is an amino acid supply route in Ras-transformed cells. Nature. 2013;497(7451):633-637. doi:10.1038/nature12138

239. Mayers JR, Wu C, Clish CB, et al. Elevation of circulating branched-chain amino acids is an early event in human pancreatic adenocarcinoma development. Nat Med. 2014;20(10):1193-1198. doi:10.1038/nm.3686

240. Daher B, Parks SK, Durivault J, et al. Genetic Ablation of the Cystine Transporter xCT in PDAC Cells Inhibits mTORC1, Growth, Survival, and Tumor Formation via Nutrient and Oxidative Stresses. Cancer Res. 2019;79(15):3877-3890. doi:10.1158/0008-5472.CAN-18-3855

241. Olivares O, Mayers JR, Gouirand V, et al. Collagen-derived proline promotes pancreatic ductal adenocarcinoma cell survival under nutrient limited conditions. Nat Commun. 2017;8(1):16031. doi:10.1038/ncomms16031

242. Zaytouni T, Tsai P-Y, Hitchcock DS, et al. Critical role for arginase 2 in obesity-associated pancreatic cancer. Nat Commun. 2017;8(1):242. doi:10.1038/s41467-017-00331-y

243. Wu G. Amino acids: metabolism, functions, and nutrition. Amino Acids. 2009;37(1):1-17. doi:10.1007/s00726-009-0269-0

244. Eagle H. Amino Acid Metabolism in Mammalian Cell Cultures. Science (80-). 1959;130(3373):432-437. doi:10.1126/science.130.3373.432

245. Jackson MJ, Beaudet AL, O'Brien WE. MAMMALIAN UREA CYCLE ENZYMES. Annu Rev Genet. 1986;20(1):431-464. doi:10.1146/annurev.ge.20.120186.002243

246. Windmueller HG, Spaeth AE. Source and fate of circulating citrulline. Am J Physiol Metab. 1981;241(6):E473-E480. doi:10.1152/ajpendo.1981.241.6.E473

247. RYALL J, NGUYEN M, BENDAYAN M, SHORE GC. Expression of nuclear genes encoding the urea cycle enzymes, carbamoyl-phosphate synthetase I and ornithine carbamoyl transferase, in rat liver and intestinal mucosa. Eur J Biochem. 1985;152(2):287-292. doi:10.1111/j.1432-1033.1985.tb09196.x

248. Featherston W, Rogers Q, Freedland R. Relative importance of kidney and liver in synthesis of arginine by the rat. Am J Physiol Content. 1973;224(1):127-129. doi:10.1152/ajplegacy.1973.224.1.127

249. Levillain O, Hus-Citharel A, Morel F, Bankir L. Localization of arginine synthesis along rat nephron. Am J Physiol Physiol. 1990;259(6):F916-F923. doi:10.1152/ajprenal.1990.259.6.F916

250. Flynn N., Meininger C., Haynes T., Wu G. The metabolic basis of arginine nutrition and pharmacotherapy. Biomed Pharmacother. 2002;56(9):427-438. doi:10.1016/S0753-3322(02)00273-1

251. Barbul A. Arginine: Biochemistry, Physiology, and Therapeutic Implications. J Parenter Enter Nutr. 1986;10(2):227-238. doi:10.1177/0148607186010002227

252. Aulak KS, Mishra R, Zhou L, et al. Post-transcriptional Regulation of the Arginine Transporter Cat-1 by Amino Acid Availability. J Biol Chem. 1999;274(43):30424-30432. doi:10.1074/jbc.274.43.30424

253. Husson A, Brasse-Lagnel C, Fairand A, Renouf S, Lavoinne A. Argininosuccinate synthetase from the urea cycle to the citrulline-NO cycle. Eur J Biochem. 2003;270(9):1887-1899. doi:10.1046/j.1432-1033.2003.03559.x

254. Hammermann R, Dreißig MDM, Mössner J, et al. Nuclear Factor-κB Mediates Simultaneous Induction of Inducible Nitric-Oxide Synthase and Up-Regulation of the Cationic Amino Acid Transporter CAT-2B in Rat Alveolar Macrophages. Mol Pharmacol. 2000;58(6):1294-1302. doi:10.1124/mol.58.6.1294

255. Kakuda DK, Sweet MJ, MacLeod CL, Hume DA, Markovich D. CAT2-mediated L-arginine transport and nitric oxide production in activated macrophages. Biochem J. 1999;340(2):549-553. doi:10.1042/0264-6021:3400549

256. Hatzoglou M, Fernandez J, Yaman I, Closs E. REGULATION OF CATIONIC AMINO ACID TRANSPORT: The Story of the CAT-1 Transporter. Annu Rev Nutr. 2004;24(1):377-399. doi:10.1146/annurev.nutr.23.011702.073120

257. Lopez AB, Wang C, Huang CC, et al. A feedback transcriptional mechanism controls the level of the arginine/lysine transporter cat-1 during amino acid starvation. Biochem J. 2007;402(1):163-173. doi:10.1042/BJ20060941

258. Martín L, Comalada M, Marti L, et al. Granulocyte-macrophage colony-stimulating factor increases <scp>l</scp> -arginine transport through the induction of CAT2 in bone marrow-derived macrophages. Am J Physiol Physiol. 2006;290(5):C1364-C1372. doi:10.1152/ajpcell.00520.2005

259. Manner CK, Nicholson B, MacLeod CL. CAT2 arginine transporter deficiency significantly reduces iNOS-mediated NO production in astrocytes. J Neurochem. 2003;85(2):476-482. doi:10.1046/j.1471-4159.2003.01695.x

260. Nicholson B, Manner CK, Kleeman J, MacLeod CL. Sustained Nitric Oxide Production in Macrophages Requires the Arginine Transporter CAT2. J Biol Chem. 2001;276(19):15881-15885. doi:10.1074/jbc.M010030200

261. Nicholson B, Manner CK, MacLeod CL. Cat2 l-arginine transporter-deficient fibroblasts can sustain nitric oxide production. Nitric Oxide. 2002;7(4):236-243. doi:10.1016/S1089-8603(02)00116-7

262. Simon A, Plies L, Habermeier A, Martiné U, Reining M, Closs EI. Role of Neutral Amino Acid Transport and Protein Breakdown for Substrate Supply of Nitric Oxide Synthase in Human Endothelial Cells. Circ Res. 2003;93(9):813-820. doi:10.1161/01.RES.0000097761.19223.0D

263. Chen C-L, Hsu S-C, Ann DK, Yen Y, Kung H-J. Arginine Signaling and Cancer Metabolism. Cancers (Basel). 2021;13(14):3541. doi:10.3390/cancers13143541

264. Qiu F, Chen Y-R, Liu X, et al. Arginine Starvation Impairs Mitochondrial Respiratory Function in ASS1-Deficient Breast Cancer Cells. Sci Signal. 2014;7(319). doi:10.1126/scisignal.2004761

265. Changou CA, Chen Y-R, Xing L, et al. Arginine starvation-associated atypical cellular death involves mitochondrial dysfunction, nuclear DNA leakage, and chromatin autophagy. Proc Natl Acad Sci. 2014;111(39):14147-14152. doi:10.1073/pnas.1404171111

266. Cheng C-T, Qi Y, Wang Y-C, et al. Arginine starvation kills tumor cells through aspartate exhaustion and mitochondrial dysfunction. Commun Biol. 2018;1(1):178. doi:10.1038/s42003-018-0178-4

267. Chu C-Y, Lee Y-C, Hsieh C-H, et al. Genome-wide CRISPR/Cas9 knockout screening uncovers a novel inflammatory pathway critical for resistance to arginine-deprivation therapy. Theranostics. 2021;11(8):3624-3641. doi:10.7150/thno.51795

268. Chen C-L, Hsu S-C, Chung T-Y, et al. Arginine is an epigenetic regulator targeting TEAD4 to modulate OXPHOS in prostate cancer cells. Nat Commun. 2021;12(1):2398. doi:10.1038/s41467-021-22652-9

269. Hsu S-C, Chen C-L, Cheng M-L, et al. Arginine starvation elicits chromatin leakage and cGAS-STING activation via epigenetic silencing of metabolic and DNA-repair genes. Theranostics. 2021;11(15):7527-7545. doi:10.7150/thno.54695

270. Cheng C-T, Kuo C-Y, Ouyang C, et al. Metabolic Stress-Induced Phosphorylation of KAP1 Ser473 Blocks Mitochondrial Fusion in Breast Cancer Cells. Cancer Res. 2016;76(17):5006-5018. doi:10.1158/0008-5472.CAN-15-2921

271. Kremer JC, Prudner BC, Lange SES, et al. Arginine Deprivation Inhibits the Warburg Effect and Upregulates Glutamine Anaplerosis and Serine Biosynthesis in ASS1-Deficient Cancers. Cell Rep. 2017;18(4):991-1004. doi:10.1016/j.celrep.2016.12.077

272. Long Y, Tsai W-B, Wangpaichitr M, et al. Arginine Deiminase Resistance in Melanoma Cells Is Associated with Metabolic Reprogramming, Glucose Dependence, and Glutamine Addiction. Mol Cancer Ther. 2013;12(11):2581-2590. doi:10.1158/1535-7163.MCT-13-0302

273. Tsai W-B, Aiba I, Long Y, et al. Activation of Ras/PI3K/ERK Pathway Induces c-Myc Stabilization to Upregulate Argininosuccinate Synthetase, Leading to Arginine

Deiminase Resistance in Melanoma Cells. Cancer Res. 2012;72(10):2622-2633. doi:10.1158/0008-5472.CAN-11-3605

274. Brashears CB, Barlin M, Ehrhardt WR, et al. Systems level profiling of arginine starvation reveals MYC and ERK adaptive metabolic reprogramming. Cell Death Dis. 2020;11(8):662. doi:10.1038/s41419-020-02899-8

275. Gao P, Tchernyshyov I, Chang T-C, et al. c-Myc suppression of miR-23a/b enhances mitochondrial glutaminase expression and glutamine metabolism. Nature. 2009;458(7239):762-765. doi:10.1038/nature07823

276. Liu J, Ma J, Wu Z, et al. Arginine deiminase augments the chemosensitivity of argininosuccinate synthetase-deficient pancreatic cancer cells to gemcitabine via inhibition of NF-κB signaling. BMC Cancer. 2014;14(1):686. doi:10.1186/1471-2407-14-686

277. Wang H, Li Q-F, Chow H, Choi S, Leung Y-C. Arginine deprivation inhibits pancreatic cancer cell migration, invasion and EMT via the down regulation of Snail, Slug, Twist, and MMP1/9. J Physiol Biochem. 2020;76(1):73-83. doi:10.1007/s13105-019-00716-1

278. Wyant GA, Abu-Remaileh M, Wolfson RL, et al. mTORC1 Activator SLC38A9 Is Required to Efflux Essential Amino Acids from Lysosomes and Use Protein as a Nutrient. Cell. 2017;171(3):642-654.e12. doi:10.1016/j.cell.2017.09.046

279. Bonavida B, Garban H. Nitric oxide-mediated sensitization of resistant tumor cells to apoptosis by chemo-immunotherapeutics. Redox Biol. 2015;6:486-494. doi:10.1016/j.redox.2015.08.013

280. Chang C-F, Diers AR, Hogg N. Cancer cell metabolism and the modulating effects of nitric oxide. Free Radic Biol Med. 2015;79:324-336. doi:10.1016/j.freeradbiomed.2014.11.012

281. Khalil N, Abi-Habib RJ. [HuArgI (co)-PEG5000]-induced arginine deprivation leads to autophagy dependent cell death in pancreatic cancer cells. Invest New Drugs. 2020;38(5):1236-1246. doi:10.1007/s10637-019-00883-4

282. Hernandez CP, Morrow K, Lopez-Barcons LA, et al. Pegylated arginase I: a potential therapeutic approach in T-ALL. Blood. 2010;115(25):5214-5221. doi:10.1182/blood-2009-12-258822

283. Bowles TL, Kim R, Galante J, et al. Pancreatic cancer cell lines deficient in argininosuccinate synthetase are sensitive to arginine deprivation by arginine deiminase. Int J Cancer. 2008;123(8):1950-1955. doi:10.1002/ijc.23723

284. Nussler AK, Gansauge S, Gansauge F, et al. Overexpression of endothelium-derived nitric oxide synthase isoform 3 in the vasculature of human pancreatic tumor biopsies. Langenbeck's Arch Surg. 1998;383(6):474-480. doi:10.1007/s004230050163

285. Camp ER, Yang A, Liu W, et al. Roles of Nitric Oxide Synthase Inhibition and Vascular Endothelial Growth Factor Receptor-2 Inhibition on Vascular Morphology and Function in an In vivo Model of Pancreatic Cancer. Clin Cancer Res. 2006;12(8):2628-2633. doi:10.1158/1078-0432.CCR-05-225.

Acknowledgement

To my father, the first and most important person I want to thank for believing in me and supporting me against all odds. Then I would like to thank my mother for always encouraging me to dream big. Without her, I would never have thought of doing a PhD and that too in a foreign country.

My second thanks go to Prof. Xodo who put his trust in me and chose me as a PhD student. I have learnt so much about research under his guidance. I will always remember what you taught me and focusing me on becoming a better researcher every day.

Eros Di Giorgio has played the role of an angel in disguise for me. I want to thank you for your trust and support in every failed experiment and for showing me the way. Without you I would never have learned to direct my energy in the right direction.

Stefano Beinat, living alone abroad is not easy, especially when I came to Italy from India. Everything was at stake, from my confidence to my work efficiency. For anyone, such a change of environment is overwhelming and not everyone can understand. It can make you either break or make it. I am glad I found you, gave helped me gaining back confidence in myself and made me realise why I travelled thousands of miles away from home. Thank you for having my back every time I had a nervous breakdown, never leaving me alone and being there for me like family.

And finally, to all my friends and colleagues with whom I have shared moments of joy and sorrow. For being present in my life, both personally and professionally, and helping me to grow and learn.

I do not know what the future holds for me and each of us, but each of us has played a role in the past three years and I will be grateful for all of them because good moments have made me laugh and bad moments have made me strong.

Every disease has a strong impact on families and society. Finally, I would like to thank all the family members of people battling terminal illnesses. Without your patience and serenity, the fight for them would not have been possible for them.